ILMATIETEEN LAITOS
METEOROLOGISKA INSTITUTET
FINNISH METEOROLOGICAL INSTITUTE

134
CONTRIBUTIONS

WIND GUSTS IN THE ATMOSPHERIC BOUNDARY LAYER

IRENE SUOMI

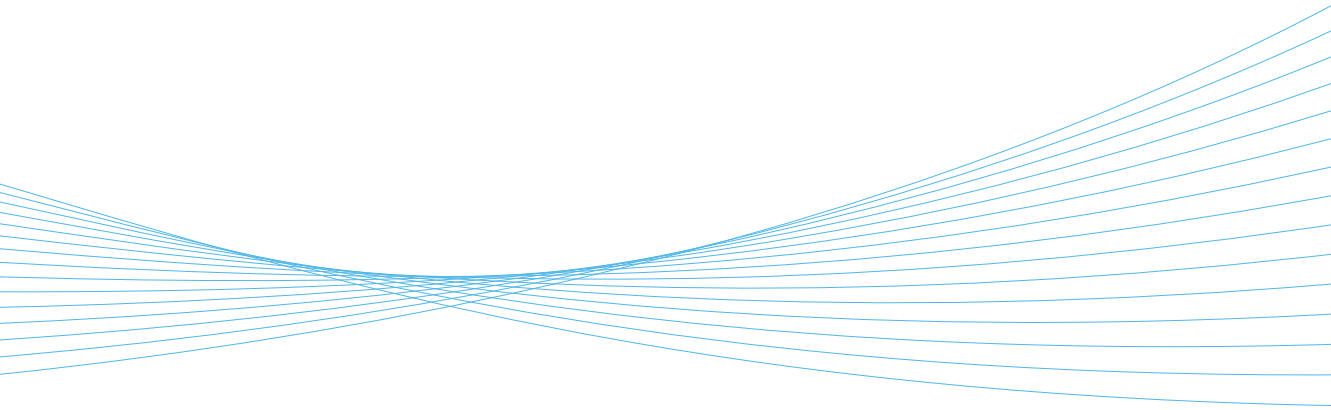

FINNISH METEOROLOGICAL INSTITUTE
CONTRIBUTIONS

No. 134

WIND GUSTS IN THE ATMOSPHERIC BOUNDARY LAYER

Irene Suomi

Department of Physics
Faculty of Science
University of Helsinki
Helsinki, Finland

ACADEMIC DISSERTATION in meteorology

To be presented, with the permission of the Faculty of Science of the University of Helsinki, for public criticism in E204 auditorium at Physicum (Gustaf Hällströmin katu 2 A, Helsinki) on August 25th, 2017, at 12 noon.

Finnish Meteorological Institute
Helsinki, 2017

Supervisors Professor Timo Vihma
Meteorological Research, Polar Meteorology and Climatology
Finnish Meteorological Institute, Finland

DSc. Sven-Erik Gryning
Department of Wind Energy
Technical University of Denmark

Dr. Carl Fortelius
Meteorological Research, Numerical Weather Prediction
Finnish Meteorological Institute, Finland

Reviewers Associate Professor Boris Galperin
College of Marine Science
University of South Florida, USA

Professor Haraldur Ólafsson
Faculty of Physical Sciences
University of Iceland

Custos Professor Heikki Järvinen
Department of Physics
University of Helsinki, Finland

Opponent Professor A. A. M. (Bert) Holtslag
Department of Environmental Sciences
Wageningen University, The Netherlands

ISBN 978-952-336-024-2 (paperback)
ISBN 978-952-336-025-9 (pdf)
ISSN 0782-6117

Erweko
Helsinki 2017

FINNISH METEOROLOGICAL INSTITUTE

Published by Finnish Meteorological Institute
(Erik Palménin aukio 1), PL 503
00101 Helsinki

Series title, number and report code of publication
Finnish Meteorological Institute
Contributions 134, FMI-CONT-134
Date
August 2017

Author
Irene Suomi

Title
Wind gusts in the atmospheric boundary layer

Abstract

Wind gusts, which are short duration (typically 3 s) wind speed maxima, are representative of the extreme wind conditions. They are very important for human activity, because the strongest gusts associated with storms are the most significant single cause of natural hazards. The impact of wind gusts on different structures depends on the characteristics of each structure. For example for wind energy, it is important to know both the probability of extreme maximum gusts in time scales of decades for the design of power plants and in the shorter term to support wind turbine operations.

For wind gust forecasting it is essential to have reliable wind gust observations. Traditionally, observations have only been available from weather stations where the wind is usually measured at a reference height of 10 m. For wind energy, information is needed at greater heights, as the hub heights of the largest turbines extend even above 150 m. The main aim of this work has been to investigate wind gusts across the entire atmospheric boundary layer based on observations from tall meteorological masts as well as applying new measurement methods developed in this dissertation. The novel methods are based on turbulence measurements taken onboard a research aircraft and by a Doppler lidar.

The research aircraft can fly long distances in a short time, so the measured wind speeds do not represent wind speed variation in time but they are a function of flight distance. The new method developed in this dissertation to compare temporal and spatial scales allows the measurement of wind gusts from a research aircraft. Then, observations can be obtained from places where traditional weather stations or meteorological masts cannot be deployed. Applying the new method, the observed wind gusts from the marine Arctic matched well with those observed at a meteorological mast in the Baltic Sea, although also differences were observed between these environments.

Doppler lidar provides radial wind speed measurements along a laser beam transmitted by the instrument. When data from at least three lines of sight are combined, the three-dimensional wind vector can be derived. However, the measurements from multiple lines of sight take several seconds, and the different beams represent different measurement volumes. For these reasons, the measured wind speed maxima from the Doppler lidar used in this work were higher than the corresponding wind gusts from the nearby meteorological mast. In this dissertation, we developed a new theoretical method that significantly reduced this positive bias. Wind gust measurements are usually prone to measurement errors, called outliers. The use of a spike removal algorithm typically applied in traditional turbulence measurements, resulted in significantly improved Doppler lidar data quality. The method performed even better than the traditional data quality assurance methods based on carrier-to-noise ratio, by removing the unrealistic outliers present in the time series.

Based on the above wind gust measurements, it was found that in the lowest part of the atmospheric boundary layer the ratio of the wind gust speed and the mean wind speed, called the gust factor, decreases strongly with measurement height. The higher the aerodynamic roughness of the surface, the greater is the change. Moreover, the static stability of the atmosphere affects the gust factor: the decrease of the gust factor with height is clearly smaller in unstable than in stable conditions. The gust parameterizations used in numerical weather prediction models were originally designed for the reference measurement height of 10 m. A new parameterization was developed that takes into account not only the effects of surface roughness and atmospheric stability but also the height above the surface. Based on meteorological mast and research aircraft measurements, the new parametrization yielded better results than previous methods.

Publishing unit
Finnish Meteorological Institute

Classification (UDC)	Keywords	
551.55, 551.551, 551.554, 551.556	Wind gust, atmospheric boundary layer, wind energy, meteorological mast, research aircraft, Doppler lidar, comparison of temporal and spatial scales, spike removal, parameterization	
ISSN and series title		
0782-6117 Finnish Meteorological Institute Contributions		
ISBN	Language	Pages
ISBN 978-952-336-024-2 (paperback), 978-952-336-025-9 (pdf)	English	118

FINNISH METEOROLOGICAL INSTITUTE

Julkaisija
Ilmatieteen laitos
(Erik Palménin aukio 1), PL 503
00101 Helsinki

Julkaisun sarja, numero ja raporttikoodi
Finnish Meteorological Institute
Contributions 134, FMI-CONT-134
Julkaisuaika
Elokuu 2017

Tekijä
Irene Suomi

Nimike
Tuulen puuskat ilmakehän rajakerroksessa

Tiivistelmä

Tuulen puuskat, eli tuulen nopeuden hetkelliset (kestoltaan noin 3 s) maksimit kertovat tuulen ääriolosuhteista. Ne ovat ihmisen toiminnan kannalta erittäin tärkeitä, sillä voimakkaat myrskypuuskat ovat suurin yksittäinen luonnon aikaansaamien tuhojen ja vaaratilanteiden aiheuttaja. Puuskien vaikutus eri rakenteille riippuu paljon tarkasteltavan rakenteen ominaisuuksista. Esimerkiksi tuulienergian kannalta on tärkeää tietää sekä todennäköisyys äärimmäisille puuskaoloille vuosikymmenien aikaskaalassa voimaloiden suunnittelun kannalta että lyhyemmällä aikavälillä voimaloiden operatiivisen toiminnan tueksi.

Puuskien ennustamisen kannalta luotettavat puuskahavainnot ovat ensisijaisen tärkeitä. Perinteisesti puuskahavaintoja on ollut saatavilla vain säähavaintoasemilta, joissa tuulta tyypillisesti mitataan 10 m referenssikorkeudella. Tuulivoimaloiden kannalta tietoa tarvitaan ylempää, sillä suurimpien voimaloiden napakorkeus on nykyisin jopa yli 150 m. Tässä väitöskirjatyössä on tarkasteltu tuulen puuskaisuutta koko ilmakehän rajakerroksessa perustuen korkeiden meteorologisten mastojen havaintoihin sekä tässä väitöskirjatyössä kehitettyjen uusien mittausmenetelmien avulla. Uudet menetelmät perustuvat tutkimuslentokoneella ja Doppler lidarilla tehtyihin mittauksiin.

Tutkimuslentokone pystyy lyhyessä ajassa lentämään pitkiä matkoja, jolloin mitattu tuulen nopeuden aikasarja ei edusta tuulen ajallista vaihtelua vaan tuulen nopeuden vaihtelua lentomatkan suhteen. Väitöskirjatyössä kehitetty uusi menetelmä tuulen nopeuden ajallisen ja paikallisen vaihtelun vertaamiseen mahdollistaa puuskien mittaamisen tutkimuslentokoneesta, jolloin havaintoja saadaan myös paikoista, joissa ei ole säähavaintoasemia tai meteorologisia mastoja. Uutta menetelmää soveltaen arktisilla merillä tehdyt puuskaisuusmittaukset vastasivat hyvin Itämerellä meteorologisesta mastosta käsin tehtyjä mittauksia, vaikka erojakin havaittiin näiden ympäristöjen välillä.

Doppler lidarilla voidaan mitata lasersäteen avulla säteen suuntaista tuulen nopeutta. Yhdistämällä tietoa vähintään kolmelta eri suuntaan suunnatulta säteeltä, saadaan mittauksista johdettua kolmiulotteinen tuulivektori. Usean säteen mittaamiseen kuluu kuitenkin aikaa useita sekunteja, ja eri säteet edustavat eri mittaustilavuuksia. Tämän vuoksi tässä työssä käytetyn Doppler lidarin mittaamat tuulen nopeuden maksimit olivat korkeampia kuin vastaavat meteorologisesta mastosta mitatut puuskanopeudet. Tässä väitöskirjatyössä kehitettiin uusi teoreettinen menetelmä, joka pienentää huomattavasti tätä positiivista harhaa. Puuskien mittaus on altis mittausvirheille. Käyttämällä perinteisissä turbulenssimittauksissa usein sovellettua piikkien poistoalgoritmia, pystyttiin Doppler lidarin puuskamittauksia parantamaan huomattavasti. Menetelmä toimi jopa paremmin kuin perinteiset Doppler lidarin signaalin voimakkuuteen perustuvat laadunvarmistusmenetelmät, sillä sen avulla pystyttiin poistamaan yksittäisiä epärealistisen suuria arvoja mitatusta tuulen nopeuden aikasarjasta.

Saatujen mittaustulosten perusteella havaittiin, että rajakerroksen alaosassa puuskanopeuden ja tuulen nopeuden suhde, puuskakerroin, pienenee voimakkaasti mittauskorkeuden funktiona. Muutos on sitä voimakkaampaa mitä suurempi on alustan aerodynaaminen rosoisuus. Myös ilmakehän staattinen stabiilisuus vaikuttaa puuskakertoimeen: kertoimen muutos mittauskorkeuden funktiona on selvästi pienempi epästabiileissa kuin stabiileissa olosuhteissa. Puuskien ennustamiseen käytetyt puuskaparametrisoinnit on alunperin suunniteltu 10 m referenssimittauskorkeudelle. Työssä kehitettiin uusi parametrisointi, joka ottaa huomioon alustan rosoisuuden ja ilmakehän stabiiliuden lisäksi myös mittauskorkeuden. Vertailut meteorologisista mastoista ja tutkimuslentokoneilla tehtyihin mittauksiin vahvistivat, että uusi parametrisointi tuotti parempia tuloksia kuin aikaisemmat menetelmät.

Julkaisijayksikkö
Ilmatieteen laitos

Luokitus (UDK)
551.55, 551.551,
551.554, 551.556

Asiasanat
Tuulen puuska, ilmakehän rajakerros,
tuulienergia, meteorologinen masto, tutkimuslento-
kone, Doppler lidar, ajallisen ja paikallisen vaihtelun
vertailu, piikkien poisto, parametrisointi

ISSN ja avainnimike
0782-6117 Finnish Meteorological Institute
Contributions

ISBN	Kieli	Sivumäärä
ISBN 978-952-336-024-2 (nid.), 978-952-336-025-9 (pdf)	Englanti	118

Preface

The work for this dissertation has been a long but rewarding process. As I mention in the summary of this thesis, the idea to study wind gusts was originated from the needs of the Finnish Wind Atlas. The first aim was to compare the simulated wind gusts from a numerical weather prediction model with those from observations from tall meteorological masts. Even though the task seemed quite straightforward in the beginning, it later turned out to be not as simple as we first thought: the Wind Atlas was published much before my first article of this dissertation. One may see this as a failure, for me it has become my main motivation to do science. I think the beauty is that you start from something and end up with something else that you really could not imagine in the first place. In the beginning, I did not plan to write a thesis about measuring wind gusts. I just ended up writing four papers about it. And now, after finishing this thesis I realize how these small studies have complemented each other.

I have not achieved these results alone. I owe my gratitude to my excellent supervisors, Timo Vihma, Carl Fortelius and Sven-Erik Gryning, who have supported me in a perfect way. They have allowed me to work independently from day to day, but whenever I have needed help, they have been there. I thank Timo Vihma for all the support and guidance through the work. I have learned a lot from you not only in science but also in life in general. I admire your enthusiastic attitude towards science and I never stop being amazed by your effective way of working. I am also very grateful to Carl Fortelius especially for the long and sometimes intensive discussions on some aspects of my work: these have advanced my understanding greatly. I want to direct my special thanks to Sven-Erik Gryning. I appreciate your help in showing me what is relevant in my work and what is not. I am also grateful to you for providing me the opportunities to visit the world leading institute on wind energy, the Department of Wind Energy at the Technical University of Denmark (DTU).

I value the support from the work community at the Finnish Meterological Institute (FMI). I want to thank all the leaders at FMI, especially the head of the Research and Development, Yrjö Viisanen, and the heads of the Meteorological Research Unit (MET), Sylvain Joffre and Sami Niemelä for providing me the best possible facilities to conduct the work for this thesis. I especially want to thank Sylvain Joffre, who had the key role in the beginning of this work, when he introduced me to Sven-Erik Gryning and challenged me to travel to DTU. In MET, I have worked in three different groups, first in the Meteorological Research Applications group led by Pertti Nurmi, then in the Numerical Weather Prediction Models group then led by Sami Niemelä, and since 2014 in the Polar Meteorology and Climatology group led by Timo Vihma. I thank all the group leaders for the nice and friendly environment you have been able to create, and special thanks to all the colleagues and friends in our Unit and elsewhere at FMI for refreshing chats during coffee and lunch breaks. The warm, homely atmosphere amongst the people at FMI makes it very nice place to come to work even if there were gusty winds outside.

I thank all the co-authors and people who have helped me during this work. I especially want thank Reijo Hyvönen, who helped me in the very beginning of the work to find past wind gust data sets from meteorological masts in Finland. I also thank Rogier Floors who kindly accompanied me to visit the National Test Site for Large Wind Turbines at Høvsøre. I will always remember that trip with the studless snow tires through the wintery landscapes of Denmark. I am also thankful to Christof Lüpkes and Jörg Hartmann for the fruitful discussions and sharing of their expertise during my visit to Bremerhaven. I thank Ewan O'Connor for helping me to understand Doppler lidars better. I also appreciate his work on improving the language of Paper IV, as well as the help from Victoria Sinclair for improving the language of Paper I. I thank Antti Hellsten for helping me to understand the engineering aspect of wind gusts better when finalizing this thesis. I also thank the two reviewers of the thesis, Boris Galperin and Haraldur Ólafsson for their constructive and positive feedback.

This dissertation has received funding from the Vilho, Yrjö ja Kalle Väisälä Foundation, the ERC FP7 project PBL-PMES, whose coordinator was Sergej Zilitinkevich, and from two Academy of Finland projects CACSI and TWASE coordinated by Timo Vihma. In addition, the work has been supported by altogether four short term scientific missions funded by EU COST Actions WIRE and TOPROF.

In my case, life has not always been a bed of roses, and no one else knows that better than my family. There are no words to describe the meaning of their support to reach this point. I am most grateful to my wonderful children, Iida and Aaro, and my caring husband Pasi for their love. I feel privileged to have both, a marvellous family and a career.

Irene Suomi
Helsinki, May 2017

Contents

List of original publications

I Suomi, I., T. Vihma, S.-E. Gryning, and C. Fortelius, 2013: Wind-gust parametrizations at heights relevant for wind energy: a study based on mast observations. *Quarterly Journal of the Royal Meteorological Society*, **139**(674), 1298–1310. doi:10.1002/qj.2039

II Suomi, I., S.-E. Gryning, R. Floors, T. Vihma, and C. Fortelius, 2015: On the vertical structure of wind gusts. *Quarterly Journal of the Royal Meteorological Society*, **141**(690), 1658–1670. doi:10.1002/qj.2468

III Suomi, I., C. Lüpkes, J. Hartmann, T. Vihma, S.-E. Gryning, and C. Fortelius, 2016: Gust factor based on research aircraft measurements: a new methodology applied to the Arctic marine boundary layer. *Quarterly Journal of the Royal Meteorological Society*, **142**(701), 2985–3000. doi:10.1002/qj.2880

IV Suomi, I., S.-E. Gryning, E. J. O'Connor, and T. Vihma, 2017: Methodology for obtaining wind gusts using Doppler lidar. *Quarterly Journal of the Royal Meteorological Society*. (published online). doi:10.1002/qj.3059

The author is responsible for most of the work related to Papers **I**–**IV**. This includes data analyses and the writing process. In Paper **III**, the author developed the peak factor method to compare wind gust observations from a research aircraft with those from a meteorological mast, and in Paper **IV**, the author developed the scaling method for lidar wind gusts.

1. Introduction

Storms with extreme wind gust conditions have a major contribution to damage caused by natural hazards. During 1980 – 2009, storms were the most expensive natural hazards in Europe, with about a 32% share of overall losses (amounting to about 132 billion euros) and 59% of insured losses (about 71 billion euros). The costs of even one single storm event can exceed billions of euros. For example, the most significant storms in Europe during 1998 – 2009, the winter storms Lothar and Martin in late December 1999 and Kyrill in January 2007 caused overall losses of 15.5 billion and 7.7 billion euros, respectively (Wehrli et al., 2010).

In Finland and in other boreal regions, extreme winds typically cause damage to forests, but usually the indirect damage caused by felled trees has a larger economic impact than the actual losses in terms of lost timber. For example, trees falling on power lines cause typically long-lasting (even weeks in remote locations) and wide-ranging (hundreds of square kilometres) power outages that can affect tens of thousands of households. These extreme events not only occupy rescue services, power companies and distribution network maintenance, they also cause massive costs to insurance companies (e.g. Prahl et al., 2015).

Strong gusts are a risk to safety. For aviation, the risks are not only related to take-off and landing (Chan, 2012) but also to the safety during flight (Shi et al., 2015). For shipping, the risks are mostly related to the conditions at the port area. Strong winds may reduce the efficiency of port operations or even cause downtime, but they can also be a safety risk for workers handling containers (e.g. Solari et al., 2012). In Finland, the heterogeneous coastline creates challenges for shipping, because the routes are often narrow and complex, and the numerous islands and other features of the complex coastline can enhance the extreme winds by chanelling the flow.

For wind energy, wind information is needed in different time horizons. In the planning phase, the wind turbine designers need to account for local wind climate and turbulence conditions but also the expected return levels of extreme gusts to ensure the strength of the turbine structure (e.g. Burton et al., 2011). When operating wind turbines, the time scales of interest vary from minutes to multiple days ahead (Wang et al., 2011). Wind power production forecasts in the short-range (hours up to a day) and in long-term (up to 2 days) give guidance to system operators to plan the unit commitment and scheduling with the ultimate aim to increase the profits of the electricity traders. On the other hand, the very short-term wind speed forecasts with a time span of minutes can be used to recognize patterns of oncoming wind speed and/or direction changes which may lead to extreme load on the turbine structure and cause enhanced fatigue or even broken turbine components. This type of gust information can be derived from dynamic-stochastic modelling (Kanev and van Engelen, 2010) combined with measurements from nacelle-based Doppler lidars (Towers and Jones,

2016; Bos et al., 2016).

The impact the wind has on structures depends strongly on the structure or on the environment of interest. For example, the impact of strong winds on the aircraft at airports depend on many factors such as the orientation of the runways, the characteristics of the surrounding environment and on the type and design of the aircraft. Moreover, damage to forests is not only governed by the actual wind gust extremes, but also by the state of the environmental conditions at the forest site. These include various factors such as the type, height, age and density of trees, the soil type and the possible snow load and ground frost (e.g. Peltola, 2006; Gregow, 2013; James et al., 2014; Jung et al., 2016). The landscape may also have a strong effect on the wind locally. In mountainous terrain the slope angle and the orientation of the slope can affect the wind climate by enhancing - or shadowing - the wind speed locally (e.g. Rife et al., 2004; Horvath et al., 2012; Tiriolo et al., 2015).

Modern extreme wind warning systems not only predict the wind extremes based on the predicted state of the atmosphere, but also take into account their expected impact on the built or non-built environment. Besides issuing general warnings to society, the forecasts can be tailored to take into account the needs of each end-user group and thereby user oriented services can be provided. Examples of such systems are the one by Solari et al. (2012) for port areas, and the system by Prahl et al. (2015) which aims in assessing the severity of wind events based on the insured losses. These systems, called reforecasts, combine information from statistical/dynamical approaches and traditional numerical weather prediction (NWP) techniques. They can provide realistic wind forecasts locally, and take into account also the processes not represented by the NWP models, such as orographic effects causing channeling/shadowing of the wind and gravity wave formation, terrain/land use characteristics, even gusts of convective origin, but their disadvantage is the requirement of a long period of data on which the statistical model is based. Moreover, the results from such models lack an understanding of the actual physical processes underlying the predicted gust events, because different factors may contribute simultaneously and therefore the evaluation and further improvements of the model can be difficult (e.g. Sheridan, 2011). In other words, despite the advantages of the reforecasting methods, it is important to understand and develop the physical description of wind gusts in NWP models. Then, the reforecasting methods become powerful tools to downscale and interpret the gust forecasts to a form easily accessible and applicable by the end users.

Wind gust forecasts in NWP models are based on parameterizations, because the spatial and temporal resolution of the models are insufficient to represent all the scales of turbulent flow contributing to wind gusts, those from metres to kilometres and from seconds to hours (e.g. Seity et al., 2011; Honnert and Masson, 2014). Most of

the parameterizations aim at predicting the gust factor (G), which is the ratio of the wind gust speed (U_{max}) to the mean wind speed (U)

$$G = \frac{U_{max}}{U}. \tag{1}$$

The gust factor can be used to estimate the wind gust speed when a forecast for the mean wind speed is provided. Gust factor parameterizations usually take into account various parameters describing the state of the atmosphere (surface-layer stability, boundary-layer height, potential contribution of convective gusts) and the characteristics of the surface (aerodynamic roughness, subgrid scale orography).

The majority of wind gust parameterizations, including the methods by Woetmann Nielsen and Petersen (2001), Brasseur (2001) and Wichers Schreur and Geertsema (2008) have originally been developed to estimate wind gusts at 10 m height, which is the reference measurement height for surface winds (WMO, 2008). However, for many practical applications, such as wind energy, this height is usually too low (e.g. Emeis, 2014). Moreover, also from the point of view of the observations, the reference 10 m height is sometimes problematic. The conditions at weather stations are often less than ideal, and for practical reasons the wind measurement height may deviate from the 10 m height. Wind records can also suffer from the impact of local roughness elements surrounding the anemometer, and therefore measurements may not be representative of large scales. Methods proposed to correct the measured mean wind speed for suboptimal site environment have been called exposure correction (Wieringa, 1986, 1996; Verkaik, 2000). These methods are based on turbulence measurements, but if those are not available, information about gusts is used instead, which means that the correction can only be applied to correct the mean wind speed, not the wind gust speed.

When the gust observations are representative only locally, the validation of gust forecasts from NWP models becomes a challenge, as the model represents the average conditions in the scale of the grid-cell, which is typically from a few hundred meters to kilometers (Honnert and Masson, 2014). If the observations were available from 50 to 100 m heights, the measured wind gusts would become representative on the scale of a few kilometers (Wieringa, 1986, 1996). For high structures and especially for wind energy, it is not only relevant to know the wind gusts at certain levels, but information from the whole profile up to 200 – 300 m heights is needed to understand the effects of wind variability in the scale of the area swept by the blades, which can be as large as 100 m or more in diameter for the largest turbines (with hub heights reaching above 150 m).

To validate and further develop wind gust forecasting methods it is important to have:

1. representative, systematic gust observations from long periods (years, preferably decades) from different environments

2. parameterizations in NWP models to provide good estimates for the gusts, which can be further applied in reforecasting methods to downscale the information to meet the end-user requirements

The key motivations in this thesis have been to develop methodologies to measure wind gusts and, based on those, to test and further develop the gust parameterizations applied in NWP models. The new methodologies include measurements taken onboard a research aircraft (Paper III) and those by a Doppler lidar (Paper IV). Research aircraft can provide gust measurements from regions and heights where standard in situ measurement techniques cannot be applied or the deployment of instruments is either challenging or costly, as in the marine Arctic. Doppler lidar data can provide valuable information on gust profiles potentially within the whole boundary layer and thereby increase our understanding on the physical processes contributing to the gusts.

In this thesis, new information is presented on the structure of the wind gusts up to heights of about 150 m based on meteorological mast data (Papers I and II) and up to 300 m based on a Doppler wind lidar data (Paper IV). The measurements from a research aircraft provide information from the entire boundary layer and potentially at any height in the atmosphere (Paper III). Dependence of a gust factor on the height above the surface (all papers), on surface roughness and the static stability of the atmosphere (Papers I – III), as well as on the gust length scales in terms of time (seconds, all papers) and distance (Paper III) are introduced.

2. Theoretical background

In this Section, we will start with the gust definition (Section 2.1.) and the impact of wind gusts in terms of the dynamic pressure loads they pose on obstacles (Section 2.2.) and compare that to the traditional meteorological approach where the aim is to estimate frictional effects of the surface on the atmospheric flow. Then, in Section 2.3., we will discuss the methodologies to parameterize wind gusts in NWP models, by introducing the statistical theory of maxima (Section 2.3.1.), which is applied in surface-based parameterizations introduced in Section 2.3.2.

2.1. Definition of a gust

In meteorology, and throughout this work, a wind gust is defined as a short-duration wind speed maximum during a longer sampling period (T). Mathematically it is expressed as the maximum of the moving averages with a moving average window length equal to the gust duration (t_g)

$$U_{max} = \max\left(\left[\frac{1}{n}\sum_{j=i}^{i+n-1} u_j\right]_{i=1}^{N-n+1}\right), \tag{2}$$

where U_{max} is the wind gust speed, u the horizontal wind speed, n the number of observations during t_g and N the total number of samples during the entire sampling period denoted as T. Traditionally in meteorological applications, the gusts are measured and the wind forecasts issued using a gust duration t_g = 3 s and a sample length T = 600 s (WMO, 2008). However, sometimes other durations are used as well. For example, peak gusts in the automated surface observing system (ASOS) network of the US National Weather Service (NWS) are based on hourly (T = 1 h) records of t_g = 5 s wind gusts (Lombardo et al., 2009).

Figure 1 shows an example of a wind speed time series as measured by a sonic anemometer (a) and after applying a 3 s (b) and 15 s (c) moving average to it. The wind gusts are highlighted as red boxes. The width of each box represents the duration of the gust (t_g) and the height of the box the strength of the gust relative to the mean wind speed ($U_{max} - U$).

Wind speed time series can also be estimated from spatially distributed measurements collected onboard a fast-moving platform, such as a research aircraft (Paper III). Then a long distance can be covered within a fairly short time period. For the gust definition it means that gusts can no longer be based on temporal averaging but on spatial averaging. Then, in terms of Equation 2, n corresponds to the number of samples within the gust length x_g and N is the total number of observations corresponding to the length of the entire sample X. In Paper III,

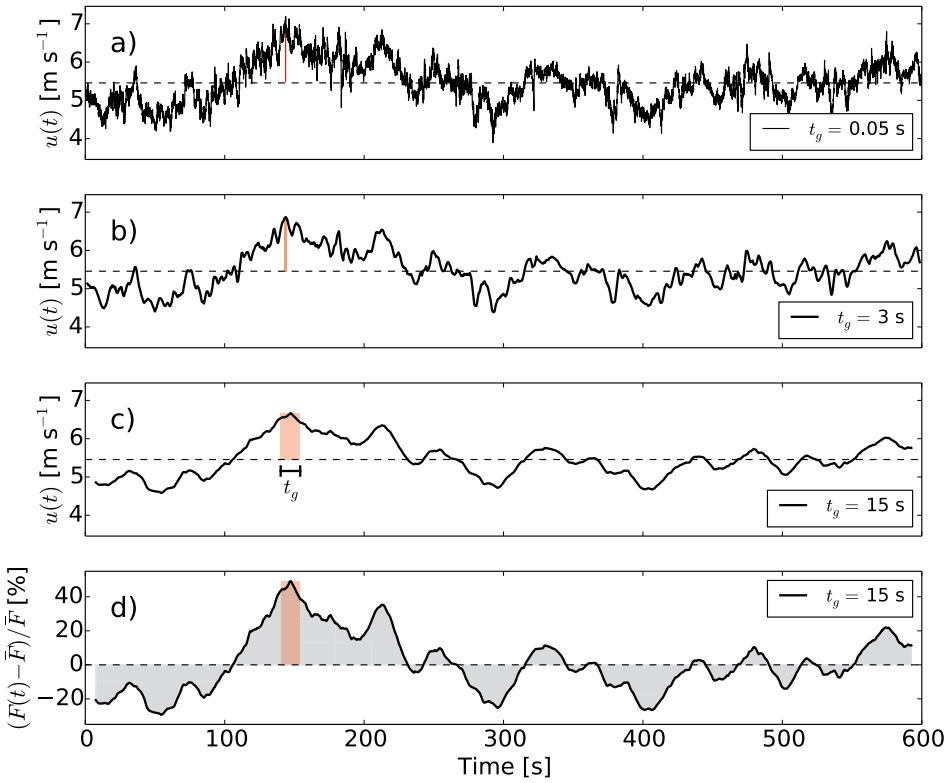

Figure 1: Example of a wind speed time series. Panel (a) shows the raw data with 20 Hz sampling frequency, and panels (b) and (c) the time series after applying a 3 s and 15 s moving average, respectively. In panel (d), the dynamic force ($F \propto u^2$)) caused by the wind is shown relative to the mean force over the sample for the moving averaged ($t_g = 15$ s) wind speed signal. In all panels, the gust (its magnitude and duration) is indicated by a red line or a box.

different methodologies to determine the length scales [x_g,X] are introduced to obtain gusts from turbulence measurements from a research aircraft such that these gust measurements can be compared with those observed at weather stations.

2.2. Wind loads vs frictional effects on the atmospheric flow

The main aim of measuring and forecasting wind gusts is to estimate the effects of the aerodynamic loads they cause on structures. Often these loads are considered to

be destructive, causing risk to safety or losses in energy production, but they can also contribute to the movement of sea ice or on the suspension of particles (dust, sea spray) from the surface (Zeng et al., 2010; Veron et al., 2012). In this section, we begin with a short description of the flow dynamics in the lowest part of the atmospheric boundary layer, followed by a more detailed discussion on how the gusts affect forests (Section 2.2.1.), wind turbines operation (Section 2.2.2.), aviation safety (Section 2.2.3.), and flows over sea ice (Section 2.2.4.).

The dynamic pressure, the force (F) per unit area (A) caused by the wind on an obstacle if the wind is stopped by the obstacle is

$$\frac{F}{A} = \frac{1}{2}\rho_a V_a^2, \tag{3}$$

where ρ_a is the density of air and V_a the wind speed. In other words the dynamic pressure is proportional to the square of the wind velocity. Equation 3 represents the energy available in the wind per unit volume. In reality, the actual force exerted on a body depends on the aerodynamical properties of the body, such as the shape, size, characteristics (surface roughness, elasticity, permeability, etc) of the structure (e.g. Madsen et al., 1986), and on the characteristics of the wind itself. The effect of the dynamic force F on a body is often divided into components of drag and lift (and side) forces, which are directed along and perpendicular to the flow, respectively. The lift forces are important especially for aviation balancing the weight of the aircraft and for wind energy by resulting in the rotation of a turbine rotor. The drag force, on the other hand, is a resistance force that acts against the wind in the direction of the wind. It is caused by the pressure differences across the body and by the shear stress in the vicinity of the surface of the body.

In meteorology, the aim is at estimating the average frictional effects of the underlying Earth's surface on the atmospheric flow. The drag force caused by the surface on the wind is typically considered in terms of the so-called Reynolds shear stress which is given per unit area of the Earth's surface as

$$\tau = -\rho u_*^2, \tag{4}$$

where the friction velocity $u_* = (\overline{u'w'}^2 + \overline{v'w'}^2)^{1/4}$ is determined by the covariances of the fluctuating parts of the vertical wind (w') with those of the horizontal wind components along (u') and perpendicular (v') to the mean wind. The minus sign in Equation 4 indicates that the flux is from the atmosphere to the surface, i.e. the surface friction decelerates the atmospheric flow.

The lowest part of the atmospheric boundary layer (ABL), called the surface layer can be divided vertically into three separate regimes, known as the viscous sublayer, the roughness sublayer (RSL) and the inertial sublayer (ISL), respectively. The viscous

sublayer is a thin (a millimetre or less) layer near the surface, where viscous dissipation is responsible for the frictional effects on the flow. Over natural surfaces this layer is much thinner than the height of the roughness elements contributing to the Reynolds stress (e.g. Garratt, 1992). Therefore, the viscous sublayer is typically neglected from considerations. The RSL encompasses roughness elements and the airspace right above them, up to about 2-5 times (sometimes even 10 times) the height of the roughness elements. The RSL depth is called the blending height (there exist other definitions of the blending height too). Above that, up to about 10% of the height of the ABL, there is the ISL, where the Reynolds stress is assumed to be nearly constant with height, and the wind profile is logarithmic and can be determined by flux-profile relationships; to account for the buoyancy effects, the Monin-Obukhov similarity theory (MOST) can be applied. Within the RSL, the wind profile deviates from a logarithimic profile and the similarity theories usually do not apply. Turbulence is affected by local effects of individual roughness elements increasing turbulence levels relative to the mean wind speed (high turbulence intensity). Moreover, turbulence is often characterized by large coherent structures.

In traditional ISL theories, the boundary-layer is usually considered to be horizontally homogeneous. In reality, however, large variations exist in the surface properties (surface roughness, temperature, moisture content). When there is a well-defined boundary between two surface types, such as a coastline, a new boundary layer develops downwind of the edge, called the internal boundary layer (IBL, Garratt, 1990). Within the IBL, the wind profile is modified by the underlying surface, whereas above, it is determined by the conditions of the upwind surface. The depth of the IBL increases by downwind distance from the edge, and after some distance a new ISL, called the new equilibrium layer (NEL), can develop near the surface within the IBL. The formation of NEL depends on the distance from the boundary and on the static stability of the atmosphere and the surface roughness. In neutral conditions over mostly flat grassland terrain Floors et al. (2011) estimated that NEL reached a height of about 13-21 m at a horizontal distance of about 2.2 km from the coastline. When the surface is heterogeneous and the surface conditions are patchy, distinct IBLs are difficult or even impossible to distinguish, then the net effect of varying roughness conditions can be estimated by determining an effective roughness length (e.g. Vihma and Savijärvi, 1991).

Traditional meteorological boundary-layer theories aim at estimating the average momentum flux from the atmosphere to the surface on time scales typically ranging from half an hour to one hour, or in a kilometre-scale. For extreme wind loads caused by wind gusts, the relevant scales are from seconds to minutes. When considering forests and sea ice, the interaction between the atmosphere and the roughness elements takes place within the RSL, whereas in wind energy the aim is to avoid/reduce the

effects of local roughness elements by the optimal siting and design of wind turbines. Aviation safety, on the other hand, concerns not only the conditions within the boundary layer but also in the free atmosphere. In the following subsections we will discuss these aspects in more detail.

2.2.1. Forests

Over a homogeneous dense canopy, where the trees are closely spaced, the top of the trees ideally acts like a displaced surface (Stull, 2009). However, this kind of simplification is not usually valid in reality due to large variations in canopy height, type and density. The flow across the sharp edge of a horizontally uniform forest can to a first approximation be described by the IBL concept. In addition, at the edge, the mean streamlines can be tilted upwards (upwind edge) or downwards (downwind edge) and over the forest up to about 20-30 tree heights from the edges, the canopy-top flow can experience a jet-like enhancement (upwind edge) or deceleration (downwind edge) (Dellwik et al., 2010; Emeis, 2014).

Coherent structures in the RSL within and above the canopy are often divided into periods of sweeps (high wind ($u' > 0$), downward motion ($w' < 0$)) and ejections (low wind ($u' < 0$), upward motion ($w' > 0$)), thus both contribute to the total momentum flux. Based on our results in Paper II, gusts (U_{max}) occur typically during sweeps ($w' < 0$). In the RSL, sweeps have been found to be infrequent penetrations of high momentum air into the canopy layer in ejection-dominated flow near the canopy top whereas higher above, within the ISL sweeps dominate over ejections (Finnigan et al., 2009), but also the opposite has been observed, sweeps dominating over ejections within the canopy top (Thomas and Foken, 2007). The horizontal scale of coherent patterns in the horizontal wind speed is close to that of the ABL height both within ISL and near the canopy top. Moreover, in strong wind conditions, patterns are elongated in the streamwise direction (Patton et al., 2016). The turbulence integral length scale (the distance after which the autocorrelation function of the wind speed falls to e^{-1}) is about 3 times the height of the trees (Patton et al., 2016), and based on observations by Eder et al. (2013), a typical duration of a coherent structure is 10-40 s. In other words, the coherent fluctuations in horizontal wind speed at the canopy top are typically larger than the size of individual trees.

Due to the complex nature of interactions between trees and the atmospheric flow, estimation of the potential wind induced damage on a forest stand is typically based on probabilistic approaches, which take into account the expected critical wind speed and the average conditions of the forest stand (James et al., 2014).

2.2.2. Wind energy

This section is mainly based on Burton et al. (2011). Wind turbines harvest energy from the wind. The power output from a wind turbine is given by

$$P = \frac{1}{2} C_p \rho_a A_R U^3, \tag{5}$$

where C_p is the power coefficient and A_R is the area swept by the blades. The wind power is thus proportional to the cube of the horizontal wind speed (U), and to the square of the length of the blades ($A_R = \pi R^2$, where R is the length of the blades). In other words, taking into account the extended logarithmic wind profile (Gryning et al., 2007, 2014), the higher the hub height and the longer the blades, the more power can be produced.

The wind turbine design parameters in Equation 5 are C_p and R. The power coefficient C_p is the ratio of the extracted power (P_{out}) relative to the power available in the air, $C_p = \frac{P_{out}}{\frac{1}{2}\rho A_R U^3}$. There exists a theoretical maximum for this ratio, the Betz limit, which is $C_{p,max}$ =0.593, but in reality the maximum value is smaller and depends on the design characteristics of the turbine. C_p can be expressed as a function of the tip speed ratio $\lambda = \frac{\Omega R}{U}$, where Ω is the angular speed of the blades. λ depends on the pitch angle of the blades (the angle between the blade direction and the normal to the wind direction) and on the yaw angle (the angle between the rotor disc and the normal to the wind direction).

The main objective of wind turbines is to optimize energy capture from the swept area of the rotor. Two types of wind turbines are currently in large scale operations, fixed speed and variable speed turbines. A fixed-speed turbine has a constant rotational speed Ω as the system is directly connected to the network, while variable speed turbines are decoupled from the network using power electronics. The airfoils can either be bolted at a specific pitch angle, or be pitch controlled. Passive bolted blades use stall regulation to achieve a constant rotational speed and are thus often used in fixed-speed turbines, while pitch regulated airfoils enable the tracking of a fixed tip speed ratio λ. Most old turbines are stall regulated whereas pitch regulation has become more common during the last decade. The advantage of pitch regulation is that the power output above the rated speed is fairly constant over a larger wind speed range (C_p close to its maximum) compared to stall-regulated systems.

In extreme wind conditions, to avoid damage, stall-regulated turbines are stopped whereas pitch-regulated systems are turned off from the wind ('feathered') by setting the pitch angle to 90°. Therefore, stall-regulated turbines must be designed stronger to bear the extreme loads. In pitch-regulated systems, where the blades can be lighter, the blade costs are in general lower, but on the other hand the costs due to the more complicated control system are higher and the turbine structure has generally lower

reliability.

Besides the extreme loads, the life-time of a turbine depends on fatigue loads caused by e.g. the wind shear, direction change (yaw error) and turbulence. A high turbulence intensity may cause resonant vibrations in the wind turbine structure. Extreme operational loads causing fatigue and/or even broken components are typically related to peak gusts, extreme rise-time events and/or extreme changes in wind direction. Turbine control systems with pitch regulation can potentially take these into account when observations of the incoming wind are available (e.g. Towers and Jones, 2016; Bos et al., 2016; Schlipf and Raach, 2016). In this study, we have analysed wind gusts based on the meteorological definition of a gust. Based on Figure 1, the gust factor G of the example wind speed time series after a 15 s moving average is about 1.2. In terms of Equation 3, this gust causes a pressure load that is 1.5 times the magnitude of the average load caused by the mean wind speed. In other words, gust loads associated with even a fairly small gust factor can be high relative to the mean wind loading. Information about gust factors can be useful in estimation of the maximum loads on the wind turbines when the mean wind speed is known.

2.2.3. Aviation safety

Aviation safety encompasses safety at airports and during flight. Turbulence is the leading cause of injuries during flights. There are different mechanisms that create turbulence, including thunderstorms (convectively-induced turbulence, CIT), clear air turbulence (CAT) associated with jet streams, fronts and other regimes of strong wind shear, turbulence caused by mountain waves and the wake turbulence caused by another aircraft (e.g. Williams, 2014). The gusts experienced by aircraft are mainly due to changes in the lift, which is caused by the change in the vertical wind speed rather than in the horizontal wind speed (Shi et al., 2015). The same applies also to safety during take-off and landing, where a sudden change in the lift can risk cabin safety and in the worst cases cause a tail strike (Chan, 2012) or even a plane crash. Hazardous conditions at airports are mainly caused by sudden changes in either wind direction and/or speed related to a peak gust or a lull. The impact of such events depends on the size and the aerodynamical characteristics of the aircraft. At airports with high density air traffic, the turbulence caused by aircraft wake vortices may also pose a risk to safety (Barbaresco et al., 2013).

In this study, the meteorological wind gust measured by the research aircraft is different from the gusts causing risk to aircraft safety. However, information about the expected extreme gusts conditions, a high gust factor G associated with a strong mean wind speed, can be used to estimate the risks to aviation safety.

2.2.4. Sea ice

Sea ice has an important role in the Arctic climate system, and an understanding of the interaction between the atmosphere, ocean and the sea ice is crucial for parameterization of physical processes in climate models (Vihma et al., 2014). The sea ice surface has unique characteristics compared to the other surfaces on Earth. The general wintertime stable stratification typical over Arctic sea ice can change drastically to very unstable conditions due to an opening of a lead or a polynya. Moreover, roughness over sea ice can also be highly variable as the size and the shape of the floes varies, resulting from both thermodynamical (melting, freezing) and mechanical (rafting, ridging) processes.

The momentum flux from the atmosphere to the surface is parameterized in terms of a drag coefficient (C_d) as $\tau = -\rho C_d |U| U$ using flux-profile relationships and MOST. Over the fractional sea ice, the drag coefficient is first determined separately for ice and open water surfaces and then combined as an area-weighted average corresponding to the sea ice concentration. In addition, the effects of floe edges, melt bond edges and ice ridges are accounted for in terms of a form drag (Lüpkes et al., 2012; Lüpkes and Gryanik, 2015).

As pointed out in Section 2.2.1., the momentum flux encompasses periods of sweeps and ejections. So far their relative contribution to the sea ice motion has not yet been investigated, but we hypothesize that sweeps are the most important ones. However, even though the gusts occur typically during sweeps (Paper II), the contribution of a single short-duration (seconds) gust event is unimportant for the time-averaged momentum flux which is typically taken as an average over 30 min to 1 h. Instead, the impact of maximum loads, caused by coherent structures could potentially be taken into account similar to parameterization of dust emissions from a land surface (Zeng et al., 2010).

2.3. Wind gust forecasting

Wind gust forecasts in NWP models are based on parameterizations. These parameterizations can be divided into two groups, surface-based methodologies and profile methods. In surface-based methods, the wind gust speed (U_{max}) is typically divided into the parts of a mean wind speed (U) and a positive fluctuation, which is taken proportional to the standard deviation of the wind speed (σ_u)

$$U_{max} = U + g_x \sigma_u, \tag{6}$$

where the coefficient of proportionality is called the peak factor

$$g_x = \frac{U_{max} - U}{\sigma_u}. \tag{7}$$

The gust factor (Equation 1) then becomes

$$G = 1 + g_x \frac{\sigma_u}{U} = 1 + g_x I_u, \tag{8}$$

where $I_u = \frac{\sigma_u}{U}$ is the turbulence intensity. In a typical gust parameterization, the peak factor (g_x) is derived from statistical considerations and I_u is based on surface-layer similarities. In Section 2.3.1., we will first discuss the methodology to estimate g_x based on the statistical theory of extremes (Rice, 1944, 1945), and then in Section 2.3.2. the actual parameterizations will be presented. In this study, we have only applied methods based on the surface-based parameterizations, but for comparison we will also present the well-known profile method by Brasseur (2001) at the end of Section 2.3.2.

2.3.1. Statistical approach to parameterize gusts

In this section we will present the statistical approach to estimate the maximum value in the time series (the peak factor, Equation 7) when the mean statistical properties (U, σ_u, power spectrum) of the wind speed are known. The statistical theory of maxima, often called the Rice theory, was first proposed by Rice (1944, 1945). Since then, the theory has been applied in various studies with small modifications (Davenport, 1964; Greenway, 1979; Beljaars, 1987; Kristensen et al., 1991; Wichers Schreur and Geertsema, 2008, Papers II-IV). Davenport (1964) applied the Rice theory to wind speed measurements. Greenway (1979) tested the method against wind tunnel measurements and evaluated the effect of filtering on the gust factor to estimate loads on structures. Beljaars (1987) used the method to derive a parameterization for NWP models. His approach is still used in the operational Integrated Forecasting System (IFS) of the European Centre for Medium-Range Weather Forecasts (ECMWF) with a small modification to account for convective gusts (Bechtold and Bidlot, 2009). Kristensen et al. (1991) compared the method to the Gumbel theory of extremes, and suggested that these theories are equivalent. Wichers Schreur and Geertsema (2008) took one step further and combined the Rice theory to include turbulence kinetic energy (TKE) from a weather model when it is available. In Paper II, the theory is validated against observations from a 100-m-high meteorological mast. In papers III and IV the method is applied to relate observations of wind speed maxima from instrumention onboard a research aircraft and from a Doppler lidar. Both instrumentations have the potential to provide wind gust measurements from heights and regions yet unreachable by the traditional in-situ anemometers.

According to the Rice theory, the probability that the horizontal wind speed u performs one up-crossing (the time derivative $\dot{u} > 0$) of the level U_x is

$$\int_0^\infty d\dot{u} \int_{U_x - \dot{u}\Delta t}^{U_x} P(u, \dot{u}) du \approx \Delta t \int_0^\infty \dot{u} P(U_x, \dot{u}) d\dot{u}, \tag{9}$$

where $P(u, \dot{u})$ is the joint probability of the wind speed and its time derivative. The covariance of u and $\dot{u}$ is

$$\langle (u - U)\dot{u} \rangle = \frac{1}{2} \frac{d}{dt} \left\langle u^2 \right\rangle . \tag{10}$$

If the variance of u is stationary (does not depend on time), i.e. $\frac{d}{dt} \left\langle u^2 \right\rangle = 0$, u and $\dot{u}$ will be uncorrelated and hence statistically independent

$$P(u, \dot{u}) = P(u)P(\dot{u}). \tag{11}$$

Following Kristensen et al. (1991), both probabilities, $P(u)$ and $P(\dot{u})$, are assumed Gaussian

$$\begin{aligned} P(u) &= \frac{1}{\sqrt{2\pi}\sigma_u} e^{-\frac{(u-U)^2}{2\sigma_u^2}} \\ P(\dot{u}) &= \frac{1}{\sqrt{2\pi}\sigma_{\dot{u}}} e^{-\frac{\dot{u}^2}{2\sigma_{\dot{u}}^2}}, \end{aligned} \tag{12}$$

even though real atmospheric turbulence is typically non-Gaussian, because higher order statistical moments contribute to the probability density function (e.g. McComb, 1990). To estimate those, quasi-Gaussian turbulence models have been developed (e.g. the QNSE method by Sukoriansky et al., 2005, 2006), which are, however, beyond the scope of this work. For strong gusts (for which $U >> 0$), the two probabilities in Equation 12 are fairly good approximations.

Following from Equations 9, 11 and 12 the average rate η of up-crossing the level U_x is

$$\eta(U_x) = P(U_x) \int_0^\infty \dot{u} P(\dot{u}) d\dot{u} = \frac{\sigma_{\dot{u}}}{2\pi\sigma_u} e^{-\frac{(U_x-U)^2}{2\sigma_u^2}}. \tag{13}$$

The expectation value for the number of upcrossings of the level U_x within a time series of length T is $N(U_x) = \eta(U_x)T$. The probability for upcrossing the level U_x k times within the time interval T can be estimated by using the Poisson distribution

$$P(k, N) = \frac{N(U_x)^k}{k!} e^{-N(U_x)}. \tag{14}$$

As we are interested in estimating the maxima of the wind speed time series, we will set $k = 0$, which gives the probability of u not exceeding U_x in period T

$$P(0, N) = \exp\left(-N(U_x)\right). \tag{15}$$

Now combining Equations 13 and 15 yields

$$P(u < U_x) = \exp\left(-\frac{T}{2\pi\tau} e^{-\frac{(U_x-U)^2}{2\sigma_u^2}} \right), \tag{16}$$

where $\tau = \frac{\sigma_u}{\sigma_{\dot{u}}}$ is the turbulent time scale. From Equation 16 we can estimate the peak factor as $g_x \approx \frac{U_x - U}{\sigma_u}$ yielding

$$g_x = \left[2 \ln \left\{ \frac{T}{2\pi\tau} \frac{1}{\ln\left(\frac{1}{P}\right)} \right\} \right]^{0.5}, \tag{17}$$

where P is the probability of a peak factor not exceeding the value g_x in an ensemble of samples. Thus, the median peak factor in an ensemble of samples corresponds to a probability $P = 0.5$.

The turbulent time scale τ in Equation 17 can be estimated using information on the (one-sided) turbulence power spectrum ($S(f)$, where f is the frequency)

$$\tau = \frac{1}{2\pi} \left(\frac{\int_0^\infty S(f) df}{\int_0^\infty f^2 S(f) df} \right)^{1/2}. \tag{18}$$

The advantage of Rice theory is that it provides the theoretical basis to estimate the relationship between the gust duration and the wind gust speed (Section 2.1.). Equation 18 provides the turbulent time scale of the continuous wind speed signal including all scales of turbulent motion beyond the sample length T.

When a moving average (Equation 2) is applied to the time series, the statistical properties of the time series change. This can be described by introducing a filter $|H(f)|^2$ to the spectrum as

$$S_f(f) = |H(f)|^2 S(f), \tag{19}$$

where $S_f(f)$ is the filtered spectrum. The filter function for a traditional cup anemometer instrumentation is

$$|H(f)|^2 = \left(\frac{sin(\pi f t_g)}{\pi f t_g} \right)^2 \left(\frac{sin(\pi f \Delta t_o)}{\pi f \Delta t_o} \right)^2 \frac{1}{1 + (2\pi f \frac{l}{U})^2} \tag{20}$$

where the first component on the right hand side is the moving average filter with an averaging window length of t_g, which is the gust duration. The other two components are typically used when the aim is to describe the effect of the measuring chain on the resulting wind speed time series. The second component on the right hand side of Equation 20 expresses the effect of sampling frequency f_o, where the interval between individual measurements $\Delta t_o = 1/f_o$. The last component on the right hand side is the filtering caused by the anemometer inertia in case of a cup or a propeller anemometer with a response length l. Anemometer response depends on the mean wind speed: at low wind speeds a cup/propeller anemometer responds slower than at high wind speeds. The response of a sonic anemometer to wind speed variations depends mainly

on the dimensions of the instrument, because for a typical instrument set-up, the sampling frequency is 10 – 20 Hz, i.e. $\Delta t_o << t_g$. The effect of anemometer dimensions on the measured turbulence can be estimated in the same way as the third component on the right hand side of Equation 20. However, this component is less important for sonic anemometers than for cup anemometers, because the dimensions of a sonic anemometer (i.e. the distance between the transducers transmitting and receiving the acoustic signal carried by the wind from one transmitter to the other) are typically small, of the order of about 20 cm, whereas for a typical cup anemometer the distance constant is $l \approx 2$ m. Moreover, wind gust measurements are meaningful usually only at high wind speeds, when l/U is typically small.

After filtering (replacing $S(f)$ in Equation 18 by $S_f(f)$ from Equation 19) the resulting peak factor from Equation 17 provides an estimate of the peak of the filtered (moving averaged) wind speed relative to the standard deviation of this filtered signal. To estimate the gust factor using Equation 17, we are interested in the peak factor relative to the true turbulence, not to that of the filtered signal. Therefore, we need to multiply the peak factor from Equation 17 by an additional coefficient, r_σ, which is the ratio of the filtered and the true turbulence

$$r_\sigma = \left(\frac{\int_0^\infty |H(f)|^2 S(f) df}{\int_0^\infty S(f) df} \right)^{1/2} . \tag{21}$$

2.3.2. Gust factor parameterizations in NWP models

In this section we will first introduce four different versions of surface-based parameterizations, including the one developed in this study, Papers I and III. Then, in the end we will present the well-known profile method by Brasseur (2001), which was not applied in this work but has been evaluated in various NWP model studies (e.g. Goyette et al., 2003; Belušić and Klaić, 2004; Ágústsson and Ólafsson, 2009; Pinto et al., 2009; Tammelin et al., 2013).

The surface-based parameterizations aim at estimating the gust factor using Equation 8, where the gust factor is divided into components of the peak factor and the turbulence intensity. The parameterizations used in this study are shown in Table 1, where they are also divided into the components of the peak factor and the turbulence (σ_u) in order to simplify their intercomparison.

The methods by Woetmann Nielsen and Petersen (2001) and Wichers Schreur and Geertsema (2008) as well as the one from Papers I and III assume a constant peak factor, which can be determined by application for example by applying the statistical theory introduced in Section 2.3.1. By contrast, the method by Wieringa (1973) uses another formulation for the peak factor, where the product Ut_g represents the gust length scale. This formulation is valid for a sample length T =10 min, but the method can also be

Table 1: Surface-based gust factor parameterizations divided into components of a peak factor (g_x) and turbulence (σ_u) as in Equation 8. The methods are called W73: Wieringa (1973); WNP01: Woetmann Nielsen and Petersen (2001); WSG08: Wichers Schreur and Geertsema (2008). u_* is the friction velocity, w_* convective velocity scale, L Obukhov length, z_i the boundary-layer height, and f_T a coefficient determining the effect of sample length T on G ($G_{3600s} = f_T G_{600s}$, $f_T = 1.1$).

Method	g_x	σ_u	other terms
W73	$1.42 + 0.3013 \ln(\frac{990}{U t_g} - 4)$	$2.5 u_{*0}$	f_T
WNP01	1.7	$1.8 u_{*0} + \gamma_u 0.5 w_*$, $\begin{cases} \gamma_u = 1 \text{ for } L < 0 \\ \gamma_u = 0 \text{ for } L >= 0 \end{cases}$	-
WSG08	g_x (Equation 17)	$\sqrt{2\text{TKE}}$ or $2.185 u_{*0}$	-
Papers I, III	g_x (Equation 17)	$\begin{cases} u_{*0}\left[0.35\left(-\frac{z_i}{\kappa L}\right)^{2/3} + 4\left(1 - \frac{z}{z_i}\right)\right]^{1/2} & \text{for } L < 0 \\ 2u_{*0}\left(1 - \frac{z}{z_i}\right)^{1/2} & \text{for } L \geq 0 \end{cases}$	-

applied for T =1 h by multiplying the gust factor by an additional coefficient f_T = 1.1 (Wieringa, 1973).

There are clear differencies between the methods. In Table 1 we show instead of the turbulence intensity ($\frac{\sigma_u}{U}$) only the parameterization for the standard deviation of the horizontal wind speed, because when applied to the NWP model, the mean wind speed is provided by the model. All methods include the friction velocity within the ISL, u_{*0}, to parameterize σ_u. In addition, the method by Wichers Schreur and Geertsema (2008) provides a possibility to use turbulence kinetic energy (TKE), when it is available from the NWP model. The coefficients in front of u_{*0} vary from 1.8 to 2.5, the highest one is in the Wieringa (1973) method whereas the smallest one in the method by Woetmann Nielsen and Petersen (2001). The Wieringa (1973) method and the Wichers Schreur and Geertsema (2008) version based on u_{*0} assume near neutral conditions, which are typical during extreme winds. The methods by Woetmann Nielsen and Petersen (2001) and our method include an additional component for unstable conditions. Also, the TKE-based version of Wichers Schreur and Geertsema (2008) method accounts for stability effects as they are included in the TKE estimate from the NWP model. Our new method (Papers I and III) takes into account the effect of height above surface by assuming a linearly decreasing momentum flux from the surface to the boundary-layer top. The height effect is also accounted for in the Wichers Schreur and Geertsema (2008) method when TKE is available from all levels of a NWP model.

The profile method by Brasseur (2001), also called the wind gust estimate (WGE) method, estimates the wind gust speed at 10 m level based on the mean wind speed profile within the whole boundary-layer, taking into account also the profiles of TKE and buoyancy. This method has been described as the most physically-based parameterization (e.g. Sheridan, 2011), because its basic idea is that the gusts result from turbulent eddies bringing fast-moving air parcels down to surface while retaining their original momentum. The heights (z_p) from where the parcels can originate, depends on the buoyancy and the TKE profiles. First, the depth of the layer from which the gust can originate is determined by integration

$$\frac{1}{z_p}\int_0^{z_p} \mathrm{TKE}(z)dz \geq \int_0^{z_p} g\frac{\Delta\theta_v(z)}{\Theta_v(z)}dz, \tag{22}$$

where the height z_p is the height of the parcel, g gravitational acceleration, Θ_v the virtual potential temperature and $\Delta\theta_v(z)$ its variation over a given layer. On the left hand side of Equation 22 there is the mean kinetic energy integrated from the surface up to height z_p whereas on the right hand side there is the potential energy of buoyancy. When all levels z_p for which Equation 22 is valid are found, the WGE is the maximum

of the mean wind speeds within these heights

$$\mathrm{WGE} = \max|U(z_p)|. \tag{23}$$

In addition to the WGE, the method also provides lower and upper bounds for this estimate. The lower bound is obtained by including the TKE profile without integration on the left hand side of Equation 22 as $\frac{2.5}{11}\mathrm{TKE}(z)$, and by applying Equation 23 again to these new z_p values. The upper bound is just the maximum wind speed within the boundary layer. Besides the 10-m-level wind gust speed, the Brasseur (2001) method can be extended to provide an estimate for U_{max} (i.e. WGE) at any level within the boundary layer, for example the model levels of a wind atlas (Tammelin et al., 2013).

3. Measurements

To measure the maxima of the fluctuating wind speed, a high temporal (or spatial) resolution of the measurements is required. This requirement has limited the available wind gust observations to traditional in-situ measurements based on cup, propeller and sonic anemometers. As discussed in Section 2.3.1, the characteristics of the instrumentation, the sampling frequency and the anemometer inertia of cup and propeller anemometers or the dimensions of the sonic anemometer affect the measured wind gusts. Today, anemometers are designed such that these factors are practically unimportant for measuring (strong) wind gusts that last for a second or longer, but old wind gust records may suffer from the slow response of the anemometer, or from an inadequate sampling frequency. In fact, the reference gust duration in meteorology, t_g = 3 s, was originally chosen because the response times of old anemometers were about 2-5 s (Greenway, 1979).

The research of this dissertation is based on measurements. These are illustrated in Figure 2. Papers I and II are based on traditional meteorological mast measurements using cup and sonic anemometers, but in Papers III and IV new methodologies to measure wind gust are developed, applying the statistical theory of extremes (Section 2.3.1.). These include measurements collected onboard a research aircraft and from a Doppler lidar. There is in Figure 2 an example of a 1-min-long time series measured by a Doppler lidar (green) and a meteorological mast (blue). With Taylor's hypothesis (Taylor, 1938) and a 10 m s^{-1} advection speed this 1 min period of data would correspond roughly to about 600 m in distance. This distance can be covered by a research aircraft within about 9 s. Research aircraft and Doppler lidars can provide information from heights and regions which have not been possible to reach with traditional in-situ measurement techniques.

In this section, we will first introduce the meteorological mast measurements, which were taken at the southern coast of Finland and near the west coast of Denmark, where also the Doppler lidar measurements were obtained. The research aircraft data is from the marine Arctic around the Svalbard archipelago.

3.1. Meteorological mast measurements

Meteorological mast measurements were available from three sites, Isosaari, Loviisa and Høvsøre. The first two are located in the southern coast of Finland and the third near the western coast of Denmark. Paper I was based on data from Isosaari and Loviisa. The majority of paper II is about Høvsøre, but an insight to the results from Loviisa and Isosaari is also provided. In Papers III and IV, the mast measurements from Høvsøre were used as the reference gust measurements in the comparisons with the research aircraft (Paper III) and Doppler lidar (Paper IV) gusts.

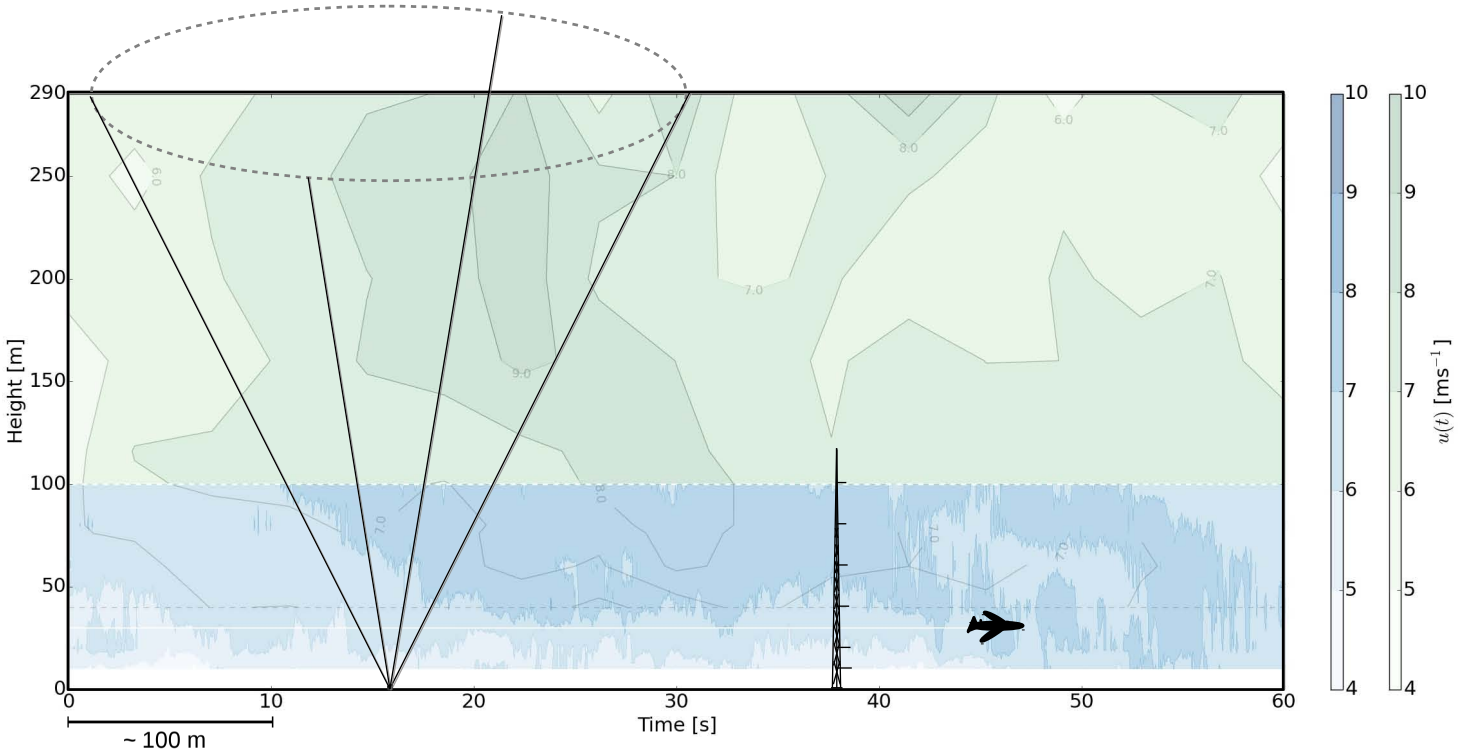

Figure 2: Illustration of the measurements used in this study: a Doppler lidar, a meteorological mast and a research aircraft. In the background, an example of a 2D wind field is shown from a Doppler lidar (green) and the sonic anemometers at 10-100 m heights (blue) at Høvsøre.

3.1.1. Isosaari, Finland

Isosaari is a fairly big (about 0.76 km^2) island located about 8 km southeast of Helsinki city centre. The meteorological mast was situated in the northeastern part of the island. The measurements were analysed from two sectors, southeastern sector (65°-225°) and southwestern (225°-280°). The first represented a marine sector with a long fetch over open water and the latter covered the Isosaari Island that reaches up to about 2 to 3 km from the mast behind which there is open water. The Isosaari Island has a fairly flat terrain and the surface roughness is characterized by a sparse mixed forest. The mast was equiped with Vaisala WAA151 cup anemometers at three heights (42, 62 and 83 m) and WAV151 wind vanes at 40 and 81 m levels. In addition, there were available temperature and humidity observations from the height of 42 and 83 m. The recorded parameters included 10 min mean wind speed, its standard deviation, the mean wind direction as well as the maximum 3 s gust during each 10 min period. Temperature and humidity were also recorded as 10 min averages. Data covers the period 1 April 2009 – 30 November 2009.

3.1.2. Loviisa, Finland

The Loviisa mast is located about 80 km east of Helsinki, on a peninsula south of the town Loviisa. The meteorological mast is in the middle of the peninsula, which is covered by a sparse, mainly coniferous forest with an average tree height of about 12-15 m. Two sectors were considered also from this site, one pointing to the north (330°...20°) and another towards the southwest (180°-240°). The northern sector represents land covered by forest. The shoreline is at about 500 m southwest of the mast, but there are some islands between the shoreline and the open water. The wind measurements were collected from 30, 103 and 143 m heights of the meteorological mast. At the two lower levels there were Gill sonic instruments, wereas at the highest level the instrument was a Metek USA-1. Temperature was measured at five levels (2, 10, 40, 100, 140 m) and the pressure and humidity were also measured at a height of 2 m. All instruments were operated by a Vaisala MILOS-520 data collection and processing system, and all parameters were recorded as hourly averages and the gusts were provided as 1 s maximum during each hour. The data was collected between 1 April 2009 – 31 March 2010, but from the marine southwestern sector only the period without sea ice was chosen, i.e. 1 April 2009 – 30 November 2009.

3.1.3. Høvsøre, Denmark

The Danish National Test Station for Large Wind Turbines is located at Høvsøre near the western coast of Denmark, at about 1.7 km from the shoreline. The 100 m meteorological mast is situated at the southern end of a row of wind turbine test stands,

the nearest one at a distance of about 120 m. A detailed description of the site and its instrumentation is provided by Peña et al. (2016). Here, in this dissertation we have used data from the ultrasonic anemometers (Metek Scientific USA-1) deployed at six levels (10, 20, 40, 60, 80, 100 m) on booms pointing towards the north. The 3D wind velocity components and the sonic temperature were recorded at 20 Hz resolution. The data was processed following several steps, which included data quality assurance, coordinate rotation along and perpendicular to the mean wind direction, correction of the sonic temperature for side-wind effects and application of the eddy covariance technique to obtain an estimate for the surface layer stability. Various combinations of wind speeds were computed, including the mean wind speed over a 10-60 min periods and gusts with varying durations from 1 to 30 s.

Only the eastern sector of the meteorological mast was chosen for the analysis, because it represents the most undisturbed and homogeneous surface conditions characterized by flat grassland terrain, i.e. ideal for reference conditions to investigate wind gusts. In Paper II, the study period covered all of 2010. The comparison of research aircraft measurements with mast measurements in Paper III was also based on this data set. In Paper IV, a two-day period, 10 – 11 October 2015, was chosen for the comparisons with Doppler lidar measurements.

3.2. Doppler lidar measurements from Høvsøre, Denmark

A Windcube V2 Doppler lidar by Leosphere was operated next to the meteorological mast at Høvsøre. It measures radial wind speeds along five lines of sight, four inclined and one vertical beams. The inclined beams have a 28° zenith angle and they are at 90° azimuth angles relative to each other. To measure one set of lidar beams takes about 3.8 s. To investigate the applicability of Doppler lidar measurements to obtain reliable estimates for wind gusts in Paper IV, a period covering 10 – 11 October 2015 was chosen. During the whole period, the wind direction was easterly. Both days were characterized by a clear diurnal cycle in the boundary-layer structure with stable conditions during the nights and unstable ones during the days. On the second day there was some rain, which is usually a challenge to lidars, but for this study it provided a good test case to investigate the effects of lidar data quality on gusts.

3.3. Research aircraft observations in the marine Arctic

Research aircraft measurements in Paper III were collected over the marine Arctic around Svalbard archipelago as part of the ARTIST measurement campaign in March and April 1998 (Hartmann et al., 1999). This data set is well documented and analysed in previous studies. None of the analyses had, however, assessed the wind gusts. The research aircraft was the German Polar 2 aircraft owned by the Alfred Wegener

Institute. Turbulence measurements were taken by a five-hole probe and they were recorded at 120 Hz. With the average speed of the research aircraft about 70 m s^{-1} relative to the Earth's surface, the spatial resolution was about 0.6 m.

The flights included low-level horizontal legs over open water and (fractional) sea ice, under various stability conditions. In addition, there were horizontal flight legs at multiple heights over the same track over open water with a long over-water fetch and in extremely unstable conditions over open water during periods with a cold-air outbreak (CAO) originating over the Arctic sea ice.

4. Summary of the results

The key results of this thesis will be presented in the following three sections. The first two sections will answer to the main motivations of the dissertation, on the measurement of the gust factor and on the development of parameterizations to estimate it. The third section will focus on the new methodologies to measure wind gusts (Papers III and IV).

4.1. Observed gust factors

Mean gust factor profiles were analysed based on data from three meteorological masts introduced in Section 3.1. The high frequency measurements from Høvsøre allowed calculation of gusts with different durations t_g and reference periods T, whereas from Finnish stations (Isosaari and Loviisa) only the gusts and mean wind speeds were available with predefined time scales, which differed from each other. Therefore, a direct comparison of the absolute values of the gust factors is not possible. In Figure 3 the mean G profiles are shown relative to the value at the lowest observation level. In panel (a) over a relatively rough surface (both sectors from Loviisa, southwestern sector from Isosaari), G decreases strongly with height. The overall decrease is about 25-35%, and the decrease is slightly stronger in the southwestern sectors of both sites than in the northern sector of Loviisa. The lowest observation level, 30 m, of Loviisa mast is within the RSL, because the average tree height was about 12-15 m. The measured gust factors at this level are strongly affected by the roughness of the forest canopy in all sectors. The two upper levels, 103 m and 143 m, are above the RSL and therefore they are probably more representative of the large scale (kilometre-scale) flow. In the southwest, there is a long fetch over a fairly smooth sea surface before the flow approaches the coast, whereas in the north the flow has travelled a long distance over a rough (forested) land surface. These differences between the sectors are probably reflected in the observed G being somewhat higher in the northern than in the southwestern sector.

In Figure 3b, the overall decrease of G is much smaller than in Figure 3a because the surface roughness at Høvsøre (flat grassland) and in the marine sector of Isosaari is smaller than in the southwestern sector of Isosaari and in Loviisa. G decreases only by about 10% or less within the 100 m layer above the surface. At all sites, Loviisa, Isosaari and Høvsøre, the rate of decrease of G is smallest in unstable and strongest in stable conditions. However, the effect of stability on the G profile is much weaker than the effect of surface roughness. The stability dependence of G profiles is related to the stability effects on the mean wind speed profile, i.e. stronger vertical gradients are expected under stable and near neutral than in unstable conditions.

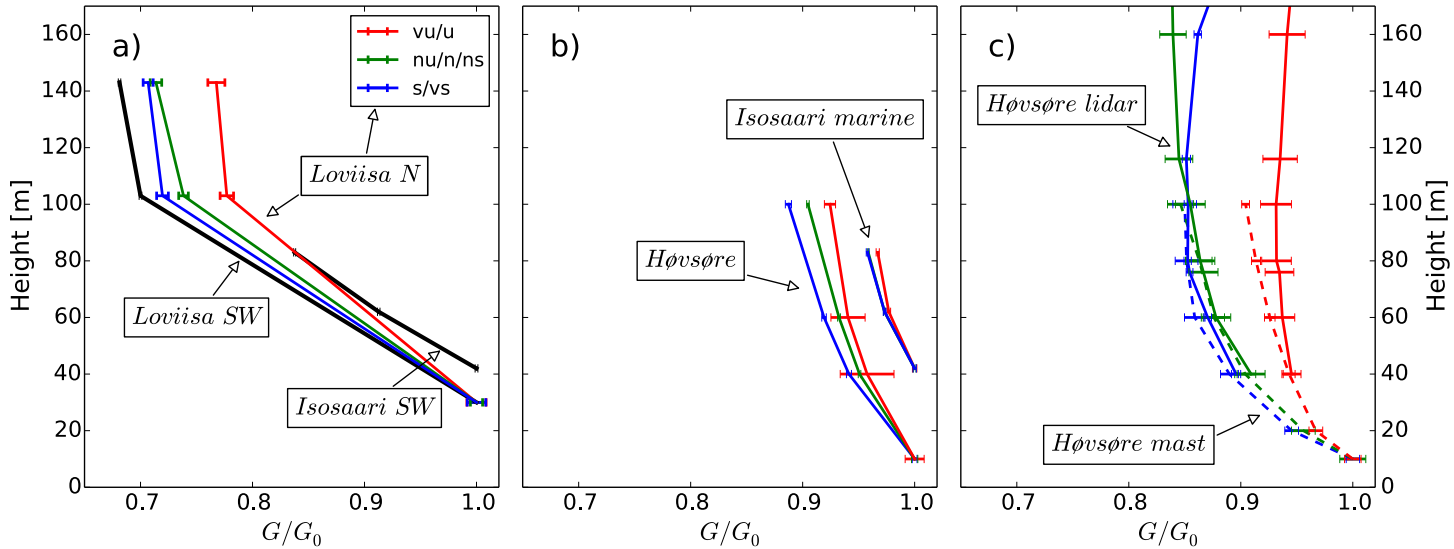

Figure 3: Mean gust factor profiles from a) Loviisa southwest sector (SW), Isosaari SW and from Loviisa north (N) sector (Paper I), and b) Høvsøre and Isosaari marine sector (Papers I and II), and c) from Høvsøre mast and lidar on October 10 2015 (Paper IV). Gust factors are normalized by the value at the lowest observation level. Error bars show the standard error of the mean. Stability groups (Loviisa N in panel (a) and panels (b) and (c)) are defined as vu/u: unstable (-200< L <-50), nu/n/ns: near neutral $|L|$ >200 and vs/s: stable (10< L <200).

Based on Figure 3a, the measurement height has a large impact on the resulting gust factors over a rough surface. Within the RSL, the measured wind gusts are representative only in the immediate vicinity of the mast, whereas above it they represent larger scales. Based on the available measurement levels of the meteorological masts at Isosaari and Loviisa, it is not possible to estimate the average RSL height. In other words, the linear profile from the 30 m level to the 103 m level at Loviisa is probably not representative of the true G profile. However, it illustrates that within this layer, a small change in the measurement height leads to a fairly large change in the gust factor. This also affects comparisons with model results, when the model gust factors are based on the average surface conditions in the grid-size scale, i.e. in the scale of a kilometre or more. When the measurements are taken at higher altitudes, at about 100 m level, the gust factors would still retain the characteristics caused by the static stability of the atmosphere, but they would be more homogeneous in space, and thereby possibly allow a better validation with the NWP model winds and gusts.

Traditionally gust factor profiles have only been available from the lower parts of the boundary layer where meteorological masts can reach. Lidars can provide information from higher using the methodology developed in Paper IV. The resulting profiles in Figure 3c show a fairly good correspondence with mast measurements especially in stable and neutral conditions. These profiles deviate from those in Figure 3b, because these are based only on a 2-day period on 10-11 October 2015, whereas the median profiles of Figure 3b are based on a full year (2010) of data.

In Paper III, gusts were investigated within the whole depth of the boundary layer based on research aircraft measurements. The profiles are shown in Figure 4. In panel (c), the gust factors measured during a cold-air outbreak were through the entire boundary layer slightly higher than those during a flow parallel to the ice edge, although the ABL was unstable also in the latter case. For comparison, also the mean G profile from the Isosaari marine sector is shown in Figure 4c. The results show that during CAOs, G was also higher than the mean G in Isosaari marine sector.

Besides profiles, gust factors were also observed over (fractional) sea ice and open water in the Arctic based on low-level horizontal flights (Paper III). Figure 5 shows the observed histograms of G from the Isosaari marine sector and from these Arctic flights. Overall, there are more stable and near neutral conditions than unstable ones in both data sets. This is typical for marine environments in mid-latitudes and in the Arctic where unstable conditions are mainly caused by cold air advection over a relatively warm sea surface and not by the diurnal cycle in the surface energy budget. In both environments the gust factors are mainly between 1.0 and 1.4. In Isosaari, the majority of the stable and near-neutral conditions are related to gust factors below 1.2, whereas in the marine Arctic most of the near-neutral conditions have G's higher than 1.2.

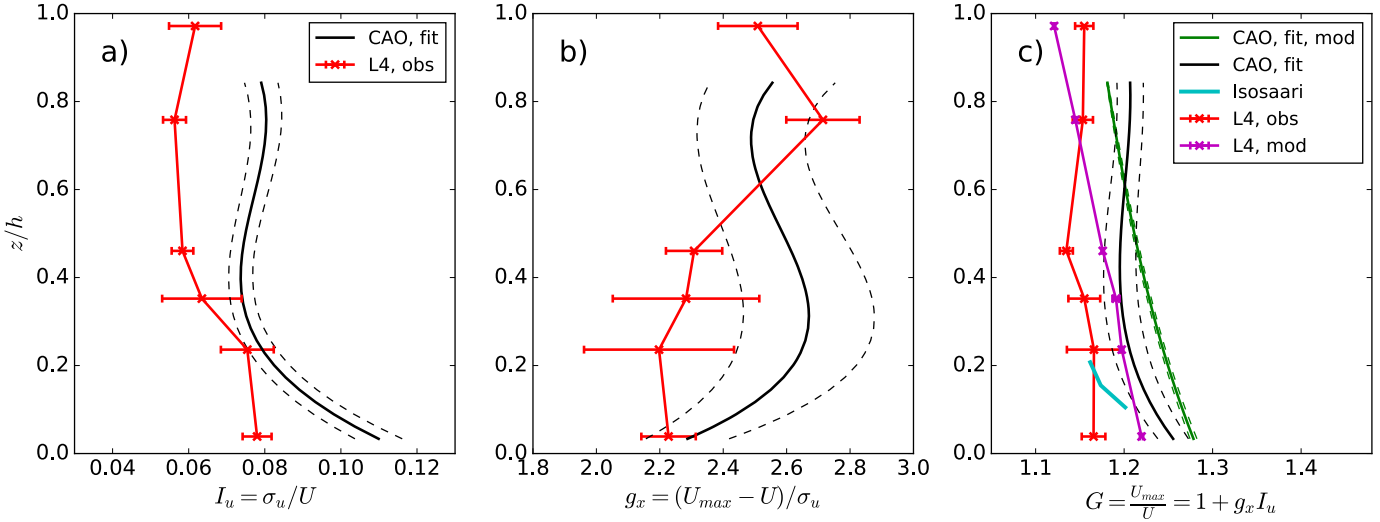

Figure 4: Turbulence intensity I_u (a), the peak factor g_x (b) and the gust factor G (c) based on research aircraft data in extremely unstable conditions over open water during cold air outbreaks (CAO) and in unstable conditions over open water when the flow is parallel to the sea ice edge (L4). The error bars and the dashed lines show the standard error of the mean. The profiles during CAO represent a cubic fit to the original observed profiles. Panel (c) shows also the parameterized G using the method of Paper I as well as the mean unstable G profile from Isosaari marine sector. The diagram is redrawn after Paper III. The Isosaari G profile is from Paper I.

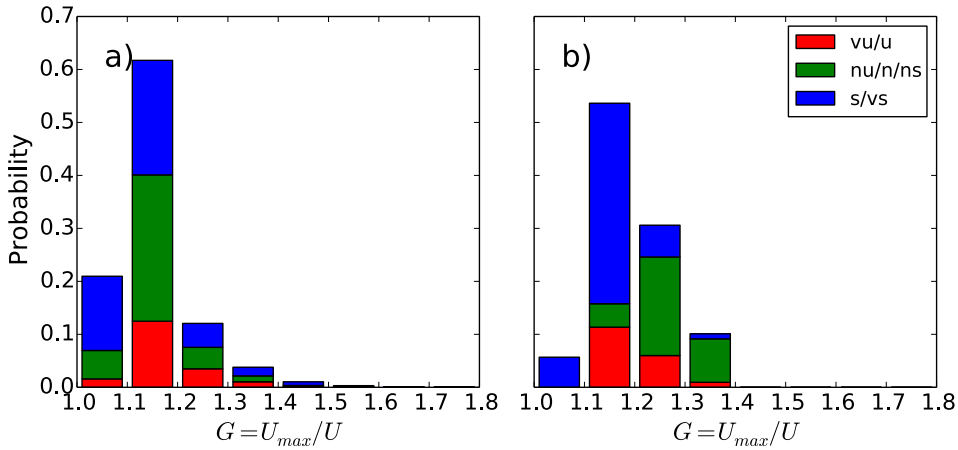

Figure 5: Histograms of G at 62 m level in the Isosaari marine sector (a) and G based on horizontal low-level flights over Arctic sea ice and open water (b). Stability groups are presented as in Figure 3.

Isosaari data cover only the ice-free period whereas from the Arctic there were also observations over sea ice. This explains the differences between the distributions in stable and neutral conditions.

In Paper II, the vertical structure of gust events was studied in a selection of 15 strongest wind cases from the eastern sector of Høvsøre mast during 2010. These included near-neutral, unstable and stable conditions. In each case, the location of a local maximum at each mast level relative to the maximum gust (U_{max}) at 10 m (or 100 m) level was detected within a time window of ±1 min around the maximum gust. In an ensemble of samples the local maxima appeared on average before U_{max} was observed at the 10 m level, and after the 100-m-level maximum gust. The same feature has also been observed in LES results over a vegetation canopy. Finnigan et al. (2009) investigated the mean structure of static pressure peaks at the canopy top, and found that these consisted of paired sweep and ejection events in the direction of the mean flow. During the sweep events, the maxima also propagated on average from higher levels to lower ones in the direction of the mean wind speed as in our study.

4.2. Development of gust factor parameterizations

In a typical surface-layer gust parametrization, the gust factor is composed of a peak factor and the turbulence intensity (Equation 8). The former defines the effects of the gust length-scales on the gust factor and the latter determines the effects of stability

and surface roughness (Paper II).

Peak factors are typically fairly constant with height or they decrease slightly in the lowest part of the ABL (Papers I-III), but in extreme unstable conditions like during CAOs in Figure 4b the peak factor can also increase with height even though the turbulence intensity decreases. This means that, even though the velocity variance decreases with height, strong deviations (gusts) from the mean occur occasionally. This feature can be important, for example, for wind turbine operations and/or aircraft safety during take-off and landing. The peak factors near the boundary layer top were also higher than in the middle (Figure 4b). That is probably due to the entrainment processes in the upper part of the boundary layer.

A theoretical methodology to estimate peak factor using the statistical theory of maxima (Section 2.3.1.) was tested in Paper II using different formulations for the turbulence spectrum. The theoretical estimates, however, did not reproduce the observed vertical decrease of g_x typical in near-neutral and stable conditions and near-constant peak factor with height in unstable conditions. Despite these discrepancies, the theoretical method is applicable for practical applications when the aim is to convert gust factors between the time-scales [t_g,T] = [1 s,1 h] and [t_g,T] = [3 s,10 min].

In this work, altogether four different gust factor parameterizations were applied (Wieringa, 1973; Woetmann Nielsen and Petersen, 2001; Wichers Schreur and Geertsema, 2008, Papers I, III). The method by Wieringa (1973) takes into account only the surface roughness, whereas the other methods also take into account the stability effects. However, it was found that the method by Woetmann Nielsen and Petersen (2001) overestimates G in unstable conditions both in the coastal Finland (Paper I) and over the marine Arctic (Paper III).

The parameterization by Wichers Schreur and Geertsema (2008) is based on estimation of the turbulence intensity in terms of TKE when it is available from a model. The advantage of this method is that when TKE is provided, no other parameterization of turbulence is needed, and the gust factor estimate can be calculated for all model levels. We tested this method based on the research aircraft data from the Arctic, and found that the assumption $I = \sqrt{2\mathrm{TKE}}/U$ overestimates the gust factor and so $I = \sqrt{\mathrm{TKE}}/U$ should be used instead (Paper III). This method provided the best correlations (R^2 = 0.88) compared to the other methods (R^2 from 0.52 to 0.8), where the estimation of σ_u was based on u_*.

The new method developed in Paper I to parameterize G outperformed the methods by Wieringa (1973) and Woetmann Nielsen and Petersen (2001) in Isosaari and Loviisa, and also good results were obtained for the marine Arctic (Paper III). Overall, there is a small underestimation of G in stable and neutral conditions, and in unstable conditions the gust factors were slightly too high. However, the RMSE values

were almost as good as for the Wichers Schreur and Geertsema (2008) method (Paper III). The height dependence of G was fairly well reproduced by all parametrizations. In the Wieringa (1973) method, the variations with height come from assuming a logarithmic wind profile, while in the modified version of the Woetmann Nielsen and Petersen (2001) method, and in the new method (Papers I and III), we assumed a linearly decreasing momentum flux from the surface to zero at the top of the boundary layer.

As this study is fully based on observations, it was not possible to evaluate the WGE method by Brasseur (2001), which requires information on the profiles of the mean wind speed, potential temperature and TKE within the entire ABL, neither of which were available. Instead, in Paper II, we investigated the spectra of mean wind speed (U) and wind gust speed (U_{max}) at the 10 m and 100 m levels. The results showed that gusts at the 10 m level ($U_{max,10}$) have almost the same amount of kinetic energy as the mean wind speed at the 100 m level (U_{100}). Moreover, there was a peak in $U_{max,10}$ in the diurnal cycle, which rose above the U_{100} and $U_{max,100}$ curves. The distributions of the difference $U_{100} - U_{max,10}$ revealed that, under unstable conditions, $U_{max,10}$ was mostly higher than U_{100}. This means that according to the method by Brasseur (2001), in unstable conditions the wind speed maxima originate from above the mast heights. On the contrary, in very stable consitions where the $U_{max,10}$ was mostly smaller than U_{100}, the surface maxima are produced within a very shallow near-surface layer. In near-neutral conditions $U_{max,10}$ was either higher or lower than U_{100}. In other words, based on the measurements from a 100 m meteorological mast it is not possible to assess the performance of the Brasseur (2001) method in near-neutral conditions typical for high impact strong winds.

4.3. New methodologies to obtain wind gusts

4.3.1. Research aircraft measurements

In Paper III we investigated the possibilities of estimating wind gusts from turbulence measurements taken onboard a research aircraft under the assumption that the gusts can be produced by many different factors, for instance, turbulent fluctuations or intermittency. Research aircraft measure over a fairly large distance during a short time interval. Therefore, the definition of a gust can no more be based on temporal but is instead based on spatial averaging. To derive the length scales x_g and X corresponding the time scales t_g and T (Equation 2), four different methods were tested. One of the methods was based on Taylor's hypothesis of frozen turbulence (Taylor, 1938), which assumes that a stationary wind field is advected past a fixed point by the mean wind speed U. Then the relationship between the distance and the time becomes $x = Ut$. Another method to convert between the scales was to assume that the

sampling frequencies represent the same scales of motion. If the sampling frequency of the five-hole probe onboard the research aircraft was f_c and the sampling frequency at a fixed point f_o, then with a flight speed of V_c the length scale becomes $x = \frac{f_o}{f_c} V_c t$. The third method to derive the length scales was just to assume that the ratio of t_g and T is equal to the ratio of x_g and X.

We developed a new, fourth method to convert between temporal and spatial scales. It is based on comparison of median peak factors from a research aircraft and from a meteorological mast. Although the data sets used in Paper III were from different locations (research aircraft measurements from the marine Arctic and the meteorological mast measurements from over flat grassland terrain in Denmark) and periods (spring 1998, full year 2010, respectively), it was possible to apply the method, because it is assumed that statistically, the behaviour of the time series in an ensemble of samples does not depend on location or on the period if the conditions are homogeneous and stationary (Section 2.3.1.).

To compare the statistical behaviour of peak factors from both data sources, median peak factors were computed with different combinations of [x_g,X] and [t_g,T] from the research aircraft data and from the meteorological mast measurements, denoted here as $g_x(x_g, X)$ and $g_x(t_g, T)$, respectively. A fixed range of temporal averages was set for t_g from 1 to 10 s and for T from 5 to 30 min. Corresponding ranges of the length scales x_g and X, that minimize the difference between $g_x(x_g, X)$ and $g_x(t_g, T)$ in the least squared sense, were then determined. One of the resulting fitted field pairs is shown in Figure 6. From this, it is possible to find the length scale counterparts for any pair of gust time scales. For example, in Figure 6, the time scales t_g = 3 s and T = 10 min have the length scale counterparts x_g = 15.6 m and X = 4.7 km.

In this new method, the median peak factors were calculated using data from all horizontal low level flights and separately from three different levels of the meteorological mast. The results for these different mast heights are summarized in Table 2. The gust length x_g increases with increasing mast height, whereas the sample length X decreases with increasing height. The increase in x_g is in line with the results by Patton et al. (2016), where they found based on the LES results above (and within) a forest canopy, that the integral length scale of the horizontal wind speed increases with height above a canopy. However, here the canopy height (of grassland) was much smaller than in their study (20-m high forest canopy).

Based on the peak factor method, the sample length X decreases with height above surface (Table 2). As discussed by Emeis (2014), because the turbulence length-scale is small close to the surface and increases with height, a longer sampling period is typically required in eddy covariance calculations at higher altitudes. Also the results by Patton et al. (2016) support this idea. In eddy covariance calculations, the aim is to cover all the scales of turbulent motion that contribute to the turbulent

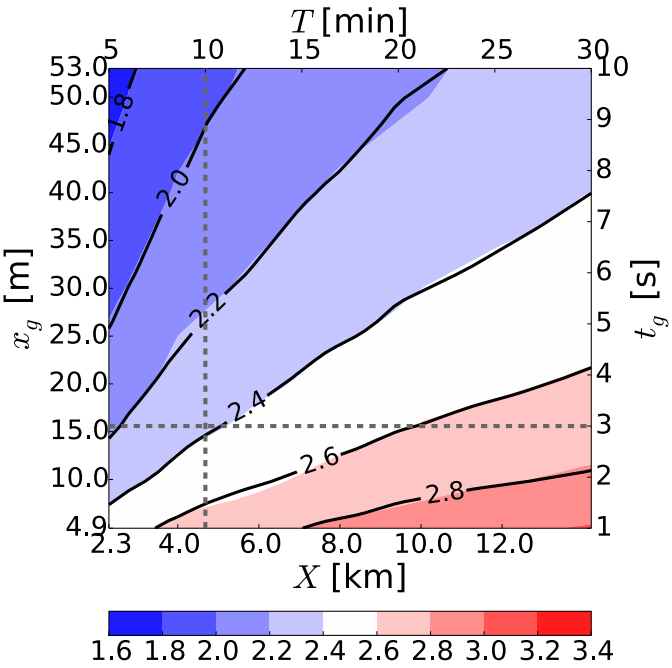

Figure 6: Median peak factor distribution as a function of the time scales t_g and T (contours) and the length scales x_g and X (colors). The mast measurements shown as function of the time scales were taken at the 40 m level of the Høvsøre meteorological mast. The length scale counterparts were derived from all the low level flights during the research aircraft campaign. The optimal length scales [x_g,X] corresponding to the time scales [t_g,T] are [15.6 m,4.7 km].

fluxes. With an increasing sample length the probability of breaking the stationarity assumption invoked in the statistical theory of maxima (Section 2.3.1.) increases. The low level flights in Paper III were mostly characterized by increasingly heterogeneous conditions as a function of the distance. This increases the probability of a relatively higher peak factor as a function of increasing sample length compared to stationary conditions. At Høvsøre, where the data covers a full year over a fairly uniform terrain, it is probable that the median peak factors are more representative for stationary conditions, especially above the 10 m level. This may also explain the decreasing sample length with height in Table 2.

In Paper III, we did not use the results from the peak factor method to calculate the wind gust speed, but instead used the results following from Taylor's hypothesis of frozen turbulence with a constant advection speed of 10 m s^{-1}. These length scales were x_g = 30 m and X = 6 km. As seen in Sections 4.1. and 4.2., the results

Table 2: The gust length scales [x_g,X] resulting from the peak factor method using data from the research aircraft and from three different heights (z) of the meteorological mast (Paper III).

z (m)	x_g (m)	X (km)
10	13.3	6.0
40	15.6	4.7
60	15.7	4.2

on G compared well with independent mast measurements from the marine sector of the Isosaari meteorological mast. In other words, the length scales were chosen successfully. However, the difference to the results from the peak factor method (x_g = 15.6 m and X = 4.7 km) are not large in terms of G. Using the median peak factors from both length scale pairs and assuming a turbulence intensity $I = 0.2$, which is a very high value (Emeis, 2014), the difference in G (resulting from Equation 8) is only about 1.7%, which is small compared to the other factors affecting G: the surface roughness, stability and height above the surface (Figure 3).

4.3.2. Wind gusts based on Doppler lidar measurements

In Paper IV, a scaling method for obtaining wind gusts from Doppler lidar measurements was developed. The method efficiently reduces the positive bias of the Doppler lidar wind speed maxima found in the comparison with meteorological mast measurements. This novel method not only scales the lidar gusts but also provides estimates for wind gusts with variable gust durations including the shorter durations (of the order of a second) which are beyond the limits of the lidar measurement frequency. The input parameters for the scaling method include the wind gust speed, mean wind speed and the standard deviation of the horizontal wind speed from the lidar. The wind gust speed is calculated as the maximum of the moving-averaged horizontal wind speed. For the WindCube V2 Doppler lidar used in this study, an average over 5 samples (corresponding to gust duration t_g = 19 s) was found to be adequate, but this depends on the lidar type and the scanning technique and must be tuned separately for each lidar set-up. Using Doppler lidar data only for the scaling method will provide reasonable gust factor estimates, with a small positive bias (about 0.03) and RMSE of about 0.06, but it is possible to reduce this bias by better estimates of the velocity variance. The improved performance of the scaling method was most noticeable in turbulent daytime conditions, but it also improved the estimation of gustiness in precipitating conditions.

The data quality is crucial for a successful scaling. We applied a spike detection method similar to that typically used in sonic anemometer data processing, and it

was found to effectively remove outliers from the data. The spikes were replaced by linear interpolation using neighbouring non-spike values. This removal of spikes improves the gust factor estimation the most in cases when only a few outliers exist. When unrealistically high wind speed values (poor data quality) start to dominate the time series, the performance of the spike detection deteriorates. For measuring wind gusts, the spike detection algorithm performed better than a traditional Carrier-to-Noise-Ratio-based (CNR) data quality assurance method.

Figure 3c shows that gust factors from the lidar match those from the meteorological mast in neutral and stable conditions, but in unstable conditions they are overestimated at the 60 m level and above. As the lidar combines data from four lines of sight to construct the 3D wind vector, the heterogeneity of the wind field at the scale of the cone defined by the lidar measuring beams (scales of about 100 – 300 m in this case) propagate to the wind vector estimate. In turbulent daytime conditions, where the wind is strongly variable, the measured wind gust is affected by these wind fluctuations, this leads to the overestimation of the gust factor.

5. Conclusions and future perspectives

The work for this thesis started at the time the Finnish Wind Atlas (Tammelin et al., 2013) was under preparation. One task was to provide estimates for the gust factor at the heights of the final output, from 50 to 400 m. Measurements available at that time (from Isosaari and Loviisa, Paper I), only covered heights up to 150 m. Furthermore, most of the available parameterizations were developed for surface conditions. The method of Wichers Schreur and Geertsema (2008) could have been applied to the output levels, but the method of Brasseur (2001) was chosen, as being more physically-based, and slightly modified to provide estimates for all the required heights (Tammelin et al., 2013).

During this work we have gained new knowledge on wind gusts within the whole boundary layer. Near the surface, the gust factor is mostly determined by the height above the surface and by the surface roughness, the static stability being also important, but not as important as the roughness. Existing parameterizations have been tested and further developed, and we have proposed a new parameterization to take into account the effects of height above the surface on the gust factor in addition to the roughness and stability effects. We obtained good results not only for the boreal and coastal environments of Finland but also for the marine Arctic. However, based on the measurements used in this study, it was not possible to compare our method with the well-known profile method by Brasseur (2001), which has been evaluated in various other studies based on NWP model results rather than observations only, because it requires simultaneous profiles of the mean wind speed, TKE and buoyancy (temperature, humidity). In the future, Doppler lidar technology may provide a possibility for direct evaluation of the method with observations, provided that a temperature profile is available simultaneously, for example from a tethered balloon or from an unmanned aerial vehicle (UAV, e.g. Jonassen et al., 2015).

In this work, new methodologies were developed to obtain gusts from research aircraft and Doppler lidar measurements. Research aircraft can provide information from remote locations where deployment of other type of wind instrumentation is challenging or even impossible. Doppler lidars, on the other hand, can provide information on gust profiles. In the future, comparison of gusts from a lidar with LES results can potentially provide a possibility to better understand the mechanisms by which the gusts are generated in the atmosphere, and thereby, also new parameterizations for NWP models can potentially be developed.

The peak factor method developed in Paper III provides a new approach to compare the statistical behaviour of wind speed time series as a function of temporal and spatial scales. Its application does not require assumptions about the advection speed, which are needed for applying Taylor's hypothesis (Taylor, 1938), even though Taylor's hypothesis can be applied to express the theoretical statistical behaviour of

extremes as a function of distance (Appendix B of Paper III). An open question is, could the peak factor method provide new information on how the turbulent time and length scales compare in non-stationarity wind speed conditions in different environments and stability conditions, provided that the time series from a fixed point represents the same environment (and period) as the data in terms of distance. These types of tests could be based on LES results or on measurements from a wind tunnel where the degree of nonstationarity in the flow field can be controlled.

The scaling methodology for Doppler lidar wind gusts in Paper IV was developed for one particular lidar type and scanning technique. In the future, the next step will be to test the applicability of the method to other lidar types and scanning sequences, such as conical scans with many more beams. An open question is, for example, what is a sufficient Doppler lidar measurement frequency for obtaining reliable wind gust estimates? And, furthermore, it is important to understand how the horizontal heterogeneity affects the measurements. To understand that, measurements from various environments are needed.

In this study, we found that over a forest, within the RSL, gust factors are much higher than above, within the ISL. This means that strong, infrequent, gusts can penetrate towards the surface while high turbulence levels caused by the rough surface below retard the mean wind speed only, leading to a high G. This is in line with the results on coherent structures within and above a forest canopy (Thomas and Foken, 2007; Finnigan et al., 2009; Eder et al., 2013; Patton et al., 2016). However, most of these meteorological studies have focused on the flux-profile relationships and the parameterization of the surface frictional effects as well as on the exchanges of trace gases and temperature and humidity, which are also important aspects of the atmosphere-canopy interactions because of the ongoing climate change. To develop methodologies to model the dynamic response of trees to wind speed fluctuations, we require realistic information about the flow above and within the canopy. Such information can be provided by LES models, but more focus is needed on understanding the length, the frequency and the dynamic structure of coherent extreme wind load events within the canopy also based on measurements. A consequence of this aspect may be that the definition of a gust may also require revision. The gust factor only provides information on the magnitude of the instantaneous (3-5 s) maximum wind speed deviation from the mean, but not on the duration, shape, and frequency of occurrence of the deviation, which could be useful information for practical purposes.

References

Ágústsson, H., and H. Ólafsson, 2009: Forecasting wind gusts in complex terrain. *Meteorology and Atmospheric Physics*, **103**(1), 173–185.

Barbaresco, F., P. Juge, M. Klein, D. Canal, Y. Ricci, J.-Y. Schneider, J.-F. Moneuse, E. Lavergne, and L. Mutuel, 2013: Wake vortex detection, prediction and decision support tools in SESAR program. *Digital Avionics Systems Conference (DASC), 2013 IEEE/AIAA 32nd*, IEEE, 6B1–1.

Bechtold, P., and J. Bidlot, 2009: Parametrization of convective gusts. *ECMWF Newsletter*, **119**, 15–18.

Beljaars, A., 1987: The influence of sampling and filtering on measured wind gusts. *Journal of Atmospheric and Oceanic Technology*, **4**(4), 613–626.

Belušić, D., and Z. B. Klaić, 2004: Estimation of bora wind gusts using a limited area model. *Tellus A*, **56**(4), 296–307.

Bos, R., A. Giyanani, and W. Bierbooms, 2016: Assessing the severity of wind gusts with lidar. *Remote Sensing*, **8**(758), 1–13.

Brasseur, O., 2001: Development and application of a physical approach to estimating wind gusts. *Monthly Weather Review*, **129**(1), 5–25.

Burton, T., D. Sharpe, N. Jenkins, and E. Bossanyi, 2011: *Wind Energy Handbook*. John Wiley & Sons, Chichester, UK, 742 pp, 2 edition.

Chan, P., 2012: An event of tail strike of an aircraft due to terrain-induced wind shear at the Hong Kong International Airport. *Meteorological Applications*, **19**(3), 325–333.

Davenport, A. G., 1964: Note on the distribution of the largest value of a random function with application to gust loading. *Proceedings, Institution of Civil Engineering*, volume 28, 187–196.

Dellwik, E., J. Mann, and K. S. Larsen, 2010: Flow tilt angles near forest edges – Part 1: Sonic anemometry. *Biogeosciences*, **7**(5), 1745–1757.

Eder, F., A. Serafimovich, and T. Foken, 2013: Coherent structures at a forest edge: properties, coupling and impact of secondary circulations. *Boundary-layer meteorology*, **148**(2), 285–308.

Emeis, S., 2014: Current issues in wind energy meteorology. *Meteorological Applications*, **21**(4), 803–819.

Finnigan, J. J., R. H. Shaw, and E. G. Patton, 2009: Turbulence structure above a vegetation canopy. *Journal of Fluid Mechanics*, **637**, 387–424.

Floors, R., S.-E. Gryning, A. Peña, and E. Batchvarova, 2011: Analysis of diabatic flow modification in the internal boundary layer. *Meteorologische Zeitschrift*, **20**(6), 649–659.

Garratt, J., 1990: The internal boundary layer – a review. *Boundary-Layer Meteorology*, **50**(1-4), 171–203.

Garratt, J., 1992: *The Atmospheric Boundary Layer*. Cambridge Atmospheric and Space Science Series. Cambridge University Press, UK, 316 pp.

Goyette, S., O. Brasseur, and M. Beniston, 2003: Application of a new wind gust parameterization: Multiscale case studies performed with the Canadian regional climate model. *Journal of Geophysical Research: Atmospheres*, **108**(D13).

Greenway, M., 1979: An analytical approach to wind velocity gust factors. *Journal of Wind Engineering and Industrial Aerodynamics*, **5**(1-2), 61–91.

Gregow, H., 2013: *Impact of strong winds, heavy snow loads and soil frost conditions on the risks to forests in Northern Europe*, volume 94 of *Finnish Meteorological Institute Contributions*. Unigrafia Oy, Helsinki, Finland, 51 pp.

Gryning, S.-E., E. Batchvarova, B. Brümmer, H. Jørgensen, and S. Larsen, 2007: On the extension of the wind profile over homogeneous terrain beyond the surface boundary layer. *Boundary-Layer Meteorology*, **124**(2), 251–268.

Gryning, S.-E., E. Batchvarova, R. Floors, A. Peña, B. Brümmer, A. N. Hahmann, and T. Mikkelsen, 2014: Long-term profiles of wind and Weibull distribution parameters up to 600 m in a rural coastal and an inland suburban area. *Boundary-layer meteorology*, **150**(2), 167–184.

Hartmann, J., F. Albers, S. Argentini, A. Bochert, U. Bonafé, W. Cohrs, A. Conidi, D. Freese, T. Georgiadis, A. Ippoliti, L. Kaleschke, C. Lüpkes, U. Maixner, G. Mastrantonio, F. Ravegnani, A. Reuter, G. Trivellone, and A. Viola, 1999: Arctic radiation and turbulence interaction study (ARTIST). *Berichte zur Polarforschung (Reports on Polar Research)*, **305**.

Honnert, R., and V. Masson, 2014: What is the smallest physically acceptable scale for 1D turbulence schemes? *Frontiers in Earth Science*, **2**(27), 1–5.

Horvath, K., D. Koracin, R. Vellore, J. Jiang, and R. Belu, 2012: Sub-kilometer dynamical downscaling of near-surface winds in complex terrain using WRF and MM5 mesoscale models. *Journal of Geophysical Research: Atmospheres*, **117**(D11).

James, K. R., G. A. Dahle, J. Grabosky, B. Kane, and A. Detter, 2014: Tree biomechanics literature review: Dynamics. *Journal of Arboriculture and Urban Forestry*, **40**, 1–15.

Jonassen, M. O., P. Tisler, B. Altstädter, A. Scholtz, T. Vihma, A. Lampert, G. König-Langlo, and C. Lüpkes, 2015: Application of remotely piloted aircraft systems in observing the atmospheric boundary layer over Antarctic sea ice in winter. *Polar Research*, **34**(1).

Jung, C., D. Schindler, A. T. Albrecht, and A. Buchholz, 2016: The role of highly-resolved gust speed in simulations of storm damage in forests at the landscape scale: A case study from southwest Germany. *Atmosphere*, **7**(1), 7.

Kanev, S., and T. van Engelen, 2010: Wind turbine extreme gust control. *Wind Energy*, **13**(1), 18–35.

Kristensen, L., M. Casanova, M. Courtney, and I. Troen, 1991: In search of a gust definition. *Boundary-Layer Meteorology*, **55**(1), 91–107.

Lombardo, F. T., J. A. Main, and E. Simiu, 2009: Automated extraction and classification of thunderstorm and non-thunderstorm wind data for extreme-value analysis. *Journal of Wind Engineering and Industrial Aerodynamics*, **97**(3), 120–131.

Lüpkes, C., and V. M. Gryanik, 2015: A stability-dependent parametrization of transfer coefficients for momentum and heat over polar sea ice to be used in climate models. *Journal of Geophysical Research: Atmospheres*, **120**(2), 552–581.

Lüpkes, C., V. M. Gryanik, J. Hartmann, and E. L. Andreas, 2012: A parametrization, based on sea ice morphology, of the neutral atmospheric drag coefficients for weather prediction and climate models. *Journal of Geophysical Research: Atmospheres*, **117**(D13).

Madsen, H. O., S. Krenk, and N. C. Lind, 1986: *Methods of structural safety*. Prentice-Hall International Series in Civil Engineering and Engineering Mechanics. Prentice-Hall, New Jersey, USA, 403 pp.

McComb, W. D., 1996 [1990]: *The Physics of Fluid Turbulence*, volume 25 of *Oxford Engineering Science Series*. Clarendon Press, 572 pp.

Patton, E. G., P. P. Sullivan, R. H. Shaw, J. J. Finnigan, and J. C. Weil, 2016: Atmospheric stability influences on coupled boundary layer and canopy turbulence. *Journal of the Atmospheric Sciences*, **73**(4), 1621–1647.

Peltola, H. M., 2006: Mechanical stability of trees under static loads. *American Journal of Botany*, **93**(10), 1501–1511.

Peña, A., R. Floors, A. Sathe, S.-E. Gryning, R. Wagner, M. S. Courtney, X. G. Larsén, A. N. Hahmann, and C. B. Hasager, 2016: Ten years of boundary-layer and wind-power meteorology at Høvsøre, Denmark. *Boundary-Layer Meteorology*, **158**(1), 1–26.

Pinto, J. G., C. P. Neuhaus, A. Krüger, and M. Kerschgens, 2009: Assessment of the wind gust estimate method in mesoscale modelling of storm events over West Germany. *Meteorologische Zeitschrift*, **18**(5), 495–506.

Prahl, B., D. Rybski, O. Burghoff, and J. Kropp, 2015: Comparison of storm damage functions and their performance. *Natural Hazards and Earth System Sciences*, **15**(4), 769–788.

Rice, S. O., 1944: Mathematical analysis of random noise. *Bell System Technical Journal*, **23**(3), 282–332.

Rice, S. O., 1945: Mathematical analysis of random noise. *Bell System Technical Journal*, **24**(1), 46–156.

Rife, D. L., C. A. Davis, Y. Liu, and T. T. Warner, 2004: Predictability of low-level winds by mesoscale meteorological models. *Monthly Weather Review*, **132**(11), 2553–2569.

Schlipf, D., and S. Raach, 2016: Turbulent extreme event simulations for lidar-assisted wind turbine control. *Journal of Physics: Conference Series*, volume 753(5), IOP Publishing.

Seity, Y., P. Brousseau, S. Malardel, G. Hello, P. Bénard, F. Bouttier, C. Lac, and V. Masson, 2011: The AROME-France convective-scale operational model. *Monthly Weather Review*, **139**(3), 976–991.

Sheridan, P., 2011: Review of techniques and research for gust forecasting and parameterisation. Forecasting Research Technical Report 570, Met Office, UK.

Shi, X.-k., J.-w. Liu, Y.-d. Li, B. Huang, and Y.-q. Tan, 2015: A diagnostic method for aircraft turbulence based on high-resolution numerical weather prediction products. *Natural Hazards*, **77**(2), 867–881.

Solari, G., M. P. Repetto, M. Burlando, P. De Gaetano, M. Pizzo, M. Tizzi, and M. Parodi, 2012: The wind forecast for safety management of port areas. *Journal of Wind Engineering and Industrial Aerodynamics*, **104**, 266–277.

Stull, R. B., 2009: *An introduction to boundary layer meteorology*, volume 13. Springer Science & Business Media, 670 pp.

Sukoriansky, S., B. Galperin, and V. Perov, 2005: Application of a new spectral theory of stably stratified turbulence to the atmospheric boundary layer over sea ice. *Boundary-Layer Meteorology*, **117**(2), 231–257.

Sukoriansky, S., B. Galperin, and V. Perov, 2006: A quasi-normal scale elimination model of turbulence and its application to stably stratified flows. *Nonlinear Processes in Geophysics*, **13**(1), 9–22.

Tammelin, B., T. Vihma, E. Atlaskin, J. Badger, C. Fortelius, H. Gregow, M. Horttanainen, R. Hyvönen, J. Kilpinen, J. Latikka, K. Ljungberg, N. G. Mortensen, S. Niemelä, K. Ruosteenoja, K. Salonen, I. Suomi, and A. Venäläinen, 2013: Production of the Finnish wind atlas. *Wind Energy*, **16**(1), 19–35.

Taylor, G. I., 1938: The spectrum of turbulence. *Proceedings of the Royal Society of London*, **164**, 476–490.

Thomas, C., and T. Foken, 2007: Flux contribution of coherent structures and its implications for the exchange of energy and matter in a tall spruce canopy. *Boundary-Layer Meteorology*, **123**(2), 317–337.

Tiriolo, L., R. C. Torcasio, S. Montesanti, A. M. Sempreviva, C. R. Calidonna, C. Transerici, and S. Federico, 2015: Forecasting wind power production from a wind farm using the RAMS model. *Advances in Science and Research*, **12**, 37–44.

Towers, P., and B. L. Jones, 2016: Real-time wind field reconstruction from LiDAR measurements using a dynamic wind model and state estimation. *Wind Energy*, **19**(1), 133–150.

Verkaik, J., 2000: Evaluation of two gustiness models for exposure correction calculations. *Journal of Applied Meteorology*, **39**(9), 1613–1626.

Veron, F., C. Hopkins, E. Harrison, and J. Mueller, 2012: Sea spray spume droplet production in high wind speeds. *Geophysical Research Letters*, **39**(16).

Vihma, T., R. Pirazzini, I. Fer, I. A. Renfrew, J. Sedlar, M. Tjernström, C. Lüpkes, T. Nygard, D. Notz, J. Weiss, et al., 2014: Advances in understanding and

parameterization of small-scale physical processes in the marine Arctic climate system: a review. *Atmospheric Chemistry and Physics (ACP)*, **14**(17), 9403–9450.

Vihma, T., and H. Savijärvi, 1991: On the effective roughness length for heterogeneous terrain. *Quarterly Journal of the Royal Meteorological Society*, **117**(498), 399–407.

Wang, X., P. Guo, and X. Huang, 2011: A review of wind power forecasting models. *Energy procedia*, **12**, 770–778.

Wehrli, A., J. Herkendell, and A. Jol, 2010: Mapping the impacts of natural hazards and technological accidents in Europe. Technical Report 13/2010, European Environment Agency (EEA), Copenhagen, Denmark.

Wichers Schreur, B., and G. Geertsema, 2008: Theory for a TKE based parameterization of wind gusts. *HIRLAM Newsletter*, **54**, 177–188.

Wieringa, J., 1973: Gust factors over open water and built-up country. *Boundary-Layer Meteorology*, **3**(4), 424–441.

Wieringa, J., 1986: Roughness-dependent geographical interpolation of surface wind speed averages. *Quarterly Journal of the Royal Meteorological Society*, **112**(473), 867–889.

Wieringa, J., 1996: Does representative wind information exist? *Journal of Wind Engineering and Industrial Aerodynamics*, **65**(1-3), 1–12.

Williams, J. K., 2014: Using random forests to diagnose aviation turbulence. *Machine Learning*, **95**(1), 51–70.

WMO, 2008: Measurement of surface wind. *Guide to meteorological instruments and methods of observation*, volume WMO No. 8 (7th edn). World Meteorological Organisation, Geneva, Switzerland. `http://www.wmo.int/pages/prog/gcos/documents/gruanmanuals/CIMO/CIMO_Guide-7th_Edition-2008.pdf` (accessed 19 December 2016).

Woetmann Nielsen, N., and C. Petersen, 2001: Calculation of wind gusts in DMI-HIRLAM. *Scientific Report 01-03*. Danish Meteorological Institute, Copenhagen, Denmark.

Zeng, Q., X. Cheng, F. Hu, and Z. Peng, 2010: Gustiness and coherent structure of strong winds and their role in dust emission and entrainment. *Advances in Atmospheric Sciences*, **27**(1), 1–13.

I

Reprinted, with permission, from
Quarterly Journal of Royal Meteorological Society, 139, 1298–1310,
doi:10.1002/qj.2039

RMetS
Royal Meteorological Society

Wind-gust parametrizations at heights relevant for wind energy: a study based on mast observations

I. Suomi,[a]* T. Vihma,[a] S.-E. Gryning[b] and C. Fortelius[a]
[a]*Finnish Meteorological Institute, Helsinki, Finland*
[b]*Technical University of Denmark, Roskilde, Denmark*

*Correspondence to: I. Suomi, Finnish Meteorological Institute, PO Box 503, FI-00101 Helsinki, Finland.
E-mail: irene.suomi@fmi.fi

Wind gusts are traditionally observed and reported at the reference height of 10 m and most gust parametrization methods have been developed only for this height. In many practical applications, e.g. in wind energy, the relevant heights are, however, up to a few hundred metres. In this study, mean gustiness conditions were studied using observations from two coastal/archipelago weather masts in the Gulf of Finland (northern Europe) with observation heights between 30 and 143 m. Only moderate and strong wind cases were addressed. Both masts were located over relatively flat terrain but the local environment, and hence the surface roughness length, differed between the mast locations. The observations showed that above all the gust factor depended on the surface roughness. Stability had a more pronounced effect over the rough forested surface than over the smooth sea surface. At both locations the stability had a larger effect on gusts than the observation height. Two existing parametrization methods, developed for a 10 m reference height, were validated against the observations and a new parametrization was proposed. In the new method, the gust factor depends on the standard deviation of the wind speed, which is parametrized on the basis of the surface friction velocity, the Obukhov length and height and the boundary-layer height. The new gust parametrization method outperformed the two older methods: the effects of surface roughness, stability and the height above the surface were well represented by the new method.

Key Words: atmospheric boundary layer; coastal meteorology; gust factor

Received 30 December 2011; Revised 8 June 2012; Accepted 16 August 2012; Published online in Wiley Online Library 7 January 2013

Citation: Suomi I, Vihma T, Gryning S-E, Fortelius C. 2013. Wind-gust parametrizations at heights relevant for wind energy: a study based on mast observations. *Q. J. R. Meteorol. Soc.* **139**: 1298–1310. DOI:10.1002/qj.2039

1. Introduction

A wind gust (or peak gust) is, by definition, a maximum wind speed of short duration t during a sampling interval T (WMO, 2008). The sampling interval is quite often the same as the averaging period for the mean wind. To describe the ratio of the gust wind speed and the mean wind speed, a gust factor is defined:

$$G_{t,T} = \frac{u_{t,T}}{u_T}, \tag{1}$$

where $u_{t,T}$ is the gust wind speed of duration t during a period T and u_T is the mean wind speed averaged over T. Following from this definition, any maximum wind speed during a time period from a fraction of a second (10–20 Hz is a typical measurement frequency of fast-response sonic anemometers) up to 10 min can be called a gust (Brook and Spillane, 1968; WMO, 2008; Harper *et al.*, 2010). The typical averaging period T for the mean wind varies from a few minutes in aviation applications (Young and Kristensen, 1992) to an hour or longer for climate studies (WMO,

2008). The WMO (2008) recommendation is 3 s for the gust duration t and 10 min for the mean wind averaging period T. Several studies have focused on the effect of different gust durations and averaging period lengths on gusts (Durst, 1960; Deacon, 1965). Statistical approaches have also been proposed to estimate the effect of gust observing practices (Brook and Spillane, 1968; Beljaars, 1987; Kristensen *et al.*, 1991; Wichers Schreur and Geertsema, 2008).

Extreme gusts–the gusts that are located in the upper tail in the gust wind-speed distribution–may cause damage to buildings and other structures. In a boreal region, like Finland, gusts of $15\,\mathrm{m\,s^{-1}}$ or more can be considered as extreme over land areas and they may cause damage to forests and extensive power cuts as trees fall on to power lines (Rauhala and Juga, 2010). Besides the damage caused by extreme gusts, gustiness is of concern in various sectors of society from aviation (e.g. Young and Kristensen, 1992; Guan and Yong, 2002) to air-pollution dispersion studies (Arya, 1999) and wind-energy production (Petersen *et al.*, 1998). The wind-energy sector requires information on gustiness for two reasons: (a) siting of turbines and construction planning; and (b) turbine management. In siting, both the return times of extreme gusts (for the strength analysis of the structures) and the local gustiness conditions are important: strong fluctuations in wind speed and direction may cause power losses and/or extra load on structures (e.g. Petersen *et al.*, 1998).

Wind gusts are, unlike the standard deviation of the mean wind speed, commonly included in reports from synoptic and automatic weather stations (WMO, 2008) and often constitute the only information about turbulence conditions given by these stations. The advantage of reporting gusts is that they are relatively easy for the general public to interpret, in contrast to, for example, turbulence intensity, which is widely used in wind-energy applications. However, the wind observation height at synoptic weather stations is 10 m (WMO, 2008), while today's wind turbines have hub heights of about 100 m or more and the arc swept by the blades of a turbine can be as large as 100 m or more in diameter. Hence, for the purposes of wind-energy production, it is clear that information, especially concerning the gust profiles, is also needed for higher levels. Most parametrization methods for wind gusts have been developed for the 10 m height (e.g. Woetman Nielsen and Petersen, 2001; Brasseur, 2001; Wichers Schreur and Geertsema, 2008), although the method by Brasseur (2001) can be applied to higher elevations too (Tammelin *et al.*, 2011).

The impact of gust profiles on high structures had been recognized by the middle of the 20th century (e.g. Deacon, 1955). Originally, the height dependence of gusts was estimated using power-law relations, where the ratio of the wind speed at some height above the surface to the wind speed at 10 m equals the ratio of the corresponding heights to a power of p: $u(z)/u(10\,\mathrm{m}) = (z/10\,\mathrm{m})^p$. Different values for p have been suggested: for example, Deacon (1955) found that p for the gust wind speed ($p \approx 0.085$) is smaller than that for the mean wind speed ($p \approx 0.2$) at heights between 10 and 100 m, which means that the gust wind speed changes less with height than the mean wind speed. This is due to the fact that close to the surface there is typically more turbulence, i.e. the wind speed usually fluctuates more than aloft. In other words, the difference between the gust wind speed and the mean wind speed decreases with height.

Gusts are generated mainly by two mechanisms: wind shear and buoyancy (e.g. Woetman Nielsen and Petersen, 2001). Wind shear dominates in near-neutral conditions. In unstable conditions both mechanisms apply and the gustiness is enhanced by large turbulent eddies produced by thermals, which develop over warm surfaces when strong upward heat fluxes exist and can encompass the whole depth of the boundary layer. In the context of rain showers and deep convection we may observe extreme near-surface gusts caused by downbursts, but they are usually considered separately from traditional boundary-layer gusts (Nakamura *et al.*, 1996). Kim *et al.* (2007) simulated downbursts of different sizes using a computational fluid dynamics (CFD) model and found that gusts due to downbursts with diameters greater than 2000 m could no longer be estimated using 10 m wind gusts and a typical boundary-layer wind profile. Under stable stratification, buoyancy tends to damp gusts and hence acts against wind shear in the production of gusts.

On the other hand, under stable conditions gusts may also be generated by gravity waves, as was observed by Ágústsson and Ólafsson (2004) in the vicinity of high mountains in Iceland. Extreme gusts caused by gravity waves were also observed and modelled by Belusić and Klaić (2004) for Bora winds and by Meyers *et al.* (2003) over the Rocky Mountains. In the latter study, extreme gust wind speeds were related to very stable conditions. On the lee side of mountains the wind can also be very gusty due to breaking gravity waves. However, in the case of vertically propagating gravity waves the gust factor close to the surface may remain small (Valkonen *et al.*, 2010). Due to the irregular nature of gravity waves, they are typically excluded from gust theories. On the other hand, if a numerical model is able to reproduce the flow over a mountain barrier realistically, the gust forecasts may succeed (Meyers *et al.*, 2003; Goyette *et al.*, 2003; Belusić and Klaić, 2004).

Forecasting gusts relies heavily on the post-processing of numerical weather prediction (NWP) model products because today's models still have far too coarse spatial and temporal resolution to resolve gusts explicitly. Therefore, parametrizations for gusts are needed. Several types of gust parametrization methods are described in the literature. In its simplest form, a gust parametrization can consist of a table of mean gust factors categorized by surface type, as in the method used by the UK Met Office in the 1990s (Brasseur, 2001, his table 6). Many gust parametrizations are based on Monin–Obukhov theory. Although the strongest gusts are usually observed concurrent with strong mean wind speed and thus neutral stratification (Wieringa, 1973; Wichers Schreur and Geertsema, 2008; Harper *et al.*, 2010), gustiness is strongly affected by stability in conditions of light winds (Young and Kristensen, 1992; Woetman Nielsen and Petersen, 2001). Some gust parametrization methods (Brasseur, 2001; Wichers Schreur and Geertsema, 2008) use NWP model output of the turbulence kinetic energy (TKE). Wichers Schreur and Geertsema's method is based on Monin–Obukhov similarity theory, whereas Brasseur (2001) assumes that surface gusts result from descent of air parcels towards the surface by turbulent eddies. These parcels retain their initial speed during this process and hence induce a gust at the surface. The method has been applied by several authors, for example Goyette *et al.* (2003), Belusić and Klaić (2004), Ágústsson and Ólafsson (2009), Pinto *et al.* (2009) and Tammelin *et al.* (2011).

Table 1. Factors determining the gust factor (G) in different parametrizations. Here z_0 is the roughness length, U the mean wind speed, z refers to the height above the surface and T and t are the averaging period lengths for the mean wind speed and the gust wind speed, respectively. θ is the potential temperature and θ_v the virtual potential temperature. E is the turbulent kinetic energy, u_{*0} is the surface friction velocity and w_* is the convective velocity scale.

Method	Gust factor
UK Met Office (table 6 from Brasseur, 2001)	$G = f(z_0)$
Wieringa (1973)	$G = f(U, t, T, z, z_0)$
Brasseur (2001)	$G = f(U(z), z, \theta, \theta_v(z), E(z))$
Woetman Nielsen and Petersen (2001)	$G = f(U, u_{*0}, w_*)$
Wichers Schreur and Geertsema (2008)	$G = f(U, t, T, z, E)$

Table 1 lists some widely applied parametrizations that are based on meteorological data, some of which include the effect of gust duration. Because the gust wind speed is strongly correlated with the mean wind speed, it is included in almost all methods. Surface roughness is taken into account either directly (Wieringa, 1973; Woetman Nielsen and Petersen, 2001) or indirectly via TKE (Brasseur, 2001; Wichers Schreur and Geertsema, 2008), as is the effect of stability, except in the method of Wieringa (1973) which assumes neutral stability conditions. All of the methods in Table 1 were originally developed for surface gusts only, referring to a standard 10 m measurement height. Only Wieringa (1973) argues that his method is applicable up to heights of 50 m, but even this is below the heights relevant for wind-energy production today. It is also possible to modify the method by Brasseur (2001) such that it can be used to estimate gusts at different heights within the boundary layer, as was done by Tammelin *et al.* (2011).

In this study we will test existing gust parametrizations at heights between 30 and 143 m, using observations from two weather masts. Only cases where the mean wind speed was 5 m s^{-1} or more are considered (at 30 m, a 3 m s^{-1} criterion was used). Both masts are located on the southern coast of Finland, in a region where wind turbines could potentially be located in the future. The stations represent relatively flat terrain with two different types of roughness environment: marine and inland with forest. Since this study concentrates on observations, we will apply only those methods for which input parameters are available from observations: Wieringa (1973, hereafter W73) and Woetman Nielsen and Petersen (2001, hereafter WNP01). The aim of this study is to take a step forward in understanding what type of parametrization is optimal for gusts at altitudes relevant for wind-energy production. To this aim we develop a new gust parametrization, combining different approaches from the literature, and show that this new method outperforms the two older ones.

2. Gust parametrization methods

2.1. Method of Wieringa (1973)

Based on observations, gustiness is known to be a function of the mean wind speed and the height above the surface (e.g. Deacon, 1955; Davis and Newstein, 1968). These two parameters, as well as the surface roughness, form the basis for the gustiness parametrization method suggested by W73:

$$G_{t,T} = f_T\left[1 + \frac{1.42 + 0.3013\ln\{(990/(u_T t) - 4\}}{\ln(z/z_0)}\right], \quad (2)$$

where z is the height above the surface and z_0 is the aerodynamic roughness length. The product $u_T t$ represents a gust wavelength, which can be up to approximately 200 m. In this parametrization method, gusts are also expressed as a function of gust duration t, and two sampling period lengths are taken into account by introducing a coefficient f_T: $f_T = 1.0$ when $T = 10$ min and $f_T = 1.1$ for $T = 1$ h. This coefficient represents the effect of a possible trend in the wind-speed measurements during a one-hour sampling period, whereas W73 had removed the trend from the 10 min observations before deriving the equations. This method was developed for neutral stability conditions in a near-surface layer of depth about 50 m, where the shear stress variation is less than 10%. Though the gustiness method is based on observations from only one station, W73 demonstrated the applicability of the method to several other locations with different measurement heights and surface roughness conditions.

The W73 method is simple and easy to apply to both observations and model output. The formulation is, however, limited to the surface layer only. Also, W73 highlight that the method is not a good approximation at low wind speeds.

2.2. Method of Woetman Nielsen and Petersen (2001)

Whereas the W73 parametrization is limited to neutral conditions, WNP01 introduced a gustiness formulation that accounts for atmospheric stability. Gustiness is assumed to result from wind shear and buoyant production of turbulence. The equation for $G_{t,T}$ is

$$G_{t,T} = 1 + \gamma_u\left(c_b\frac{w_*}{u_T} + c_n\frac{u_{*0}}{u_T}\right) + \gamma_s c_n\frac{u_{*0}}{u_T}, \quad (3)$$

where $\gamma_u = 1 - \gamma_s$ with $\gamma_s = 1$ for stably and $\gamma_s = 0$ for unstably stratified surface layers, u_{*0} is the surface friction velocity and the convective velocity scale is $w_* = \left(B_p h\right)^{1/3}$, where h is the height of the boundary layer and B_p is the buoyant production of turbulent kinetic energy. Constants c_n and c_b are defined as $c_n = c_t\sigma_U/u_{*0} \approx 3.06c_t$ and $c_b = c_t\sigma_U/w_* \approx 0.85c_t$, where σ_U is the standard deviation of the horizontal wind speed and the constant of proportionality c_t is determined statistically in WNP01. When applying this method to higher altitudes, we assume that the momentum flux (τ) decreases linearly with height, so that for friction velocity we have $\tau(z)/\rho = u_*^2 = u_{*0}^2(1 - z/h)$.

2.3. A new gust parametrization

Gusts can be expressed as a function of turbulence intensity. For example, Wieringa (1973) and Harper *et al.* (2010) presented the gust speed as a sum of the mean wind speed and a fluctuating component proportional to the standard deviation of the mean wind speed,

$$u_{t,T} = u_T + k\sigma_U, \quad (4)$$

where k is a constant of proportionality. We can derive a similar expression by substituting Eq. (4) into the definition of the gust factor (Eq. (1)), which can be written as

$$G_{t,T} = 1 + g_{t,T}\frac{\sigma_U}{u_T}. \quad (5)$$

Here, the ratio σ_U/u_T is the turbulence intensity and $g_{t,T}$ is a normalized gust (or peak factor in some studies, e.g. Harper *et al.*, 2010), defined as

$$g_{t,T} = \frac{u_{t,T} - u_T}{\sigma_U}. \tag{6}$$

Now we have three variables that determine the gust factor. They are the normalized gust, the standard deviation of the horizontal wind speed and the mean wind speed. The normalized gust can be derived from observations (see section 3). The average normalized gust observed at Isosaari, at all heights, was $g_{3,600} = 2.9$ and that at Loviisa was $g_{1,3600} = 1.9$ at the two uppermost levels and $g_{1,3600} = 2.1$ for the lowest level (t and T are given in s).

Often σ_U is not available from observations, but several options for the parametrization of the standard deviation of the mean wind speed exist in the literature and can be utilized. For this study we tested the methods introduced in Cenedese *et al.* (1998). A comparison of methods (section 3.4) suggests the following formulations modified from Gryning *et al.* (1987):

$$\sigma_U = u_{*0}\left\{0.35\left(-\frac{h}{\kappa L}\right)^{2/3} + \left(2 - \frac{z}{h}\right)\right\}^{1/2} \tag{7}$$

for unstable conditions, and

$$\sigma_U = 2u_{*0}\left(1 - \frac{z}{h}\right)^{1/2} \tag{8}$$

for stable stratifications. Here, $\kappa = 0.4$ is the von Karman constant, h is the boundary-layer height and L is the Obukhov length.

2.4. Theoretical comparison of the methods

To illustrate the similarity between the new gust parametrization and the method by WNP01, Eq. (3) can be written as

$$G_{t,T} = 1 + c_\mathrm{b}\frac{w_*}{u_T} + c_\mathrm{n}\frac{u_{*0}}{u_T} \tag{9}$$

for unstable and

$$G_{t,T} = 1 + c_\mathrm{n}\frac{u_{*0}}{u_T} \tag{10}$$

for stable and neutral conditions. The coefficients c_b and c_n, using a common coefficient of proportionality c_t (in WNP01: $c_t = 1.7$) are $c_\mathrm{b} = c_t\sigma_U/w_* \approx 0.85c_t$ and $c_\mathrm{n} = c_t\sigma_U/u_{*0} \approx 3.06c_t$. Now we recognize that $c_t = g_{t,T}$. If we substitute these into Eqs (9) and (10) and use the identity $w_* = u_{*0}[-h/(\kappa L)]^{1/3}$ (e.g. Kaimal and Finnigan, 1994, p. 22), we obtain

$$G_{t,T} = 1 + g_{t,T}\left\{0.85\left(-\frac{h}{\kappa L}\right)^{1/3} + 3.06\right\}\frac{u_{*0}}{u_T} \tag{11}$$

for unstable and

$$G_{t,T} = 1 + c_\mathrm{n}\frac{u_{*0}}{u_T} \tag{12}$$

for stable and neutral conditions. We see that in both methods (the new method of Eqs (5)–(8) and the reformulated WNP01 method of Eqs (11) and (12)) σ_U is expressed as a function of the friction velocity. In Eqs (7) and (8), σ_U is, in addition, a function of the height above the surface relative to the boundary-layer height. Close to the surface ($z \to 0$) in neutral conditions ($L \to \infty$ or $L \to -\infty$), Eqs (7) and (8) reduce to $\sigma_U = 2u_{*0}$, whereas the WNP01 method of Eqs (11) and (12) gives $\sigma_U = 3.06u_{*0}$. In unstable conditions, when the effect of buoyancy overcomes the effect of shear in the production of turbulence, Eq. (7) reduces to

$$\begin{aligned}\sigma_U &= u_{*0}\left\{0.35\left(-\frac{h}{\kappa L}\right)^{2/3}\right\}^{1/2} \\ &\cong 0.6u_{*0}\left(-\frac{h}{\kappa L}\right)^{1/3} = 0.6w_*,\end{aligned} \tag{13}$$

and Eq. (11) to

$$\sigma_U = 0.85u_{*0}\left(-\frac{h}{\kappa L}\right)^{1/3} = 0.85w_*. \tag{14}$$

Hence, in both stable and unstable cases, the WNP01 method gives larger σ_U values than Eqs (7) and (8), but the difference is smaller in unstable than in stable conditions.

The method by W73 also has similarities with the other methods. Using the same notation as above, the normalized gust of W73 is given by

$$g_{t,T} = 1.42 + 0.3013\ln(990/u_T t) - 4. \tag{15}$$

W73 assumes $\sigma_U \approx 2.5u_{*0}$ and neutral stability conditions with a logarithmic wind profile: $u_T = u_{*0}\kappa^{-1}\{\ln(z/z_0)\}^{-1}$, yielding $G_{t,T} = 1 + g_{t,T}\{\ln(z/z_0)\}^{-1}$, which is identical to Eq. (2) when $f_{T=3600} = 1$. Hence, we can immediately see that G in this case is not a function of stability and it should be applied only at near-surface levels where the friction velocity is close to its surface value. W73 estimated the method to be applicable to heights up to about 50 m.

3. Observations and derived quantities

3.1. Observations

The gust parametrization methods were tested using observations from two meteorological masts, located on the southern coast of Finland (Figure 1). One mast was situated on the fairly large island of Isosaari (25.06698°E, 60.103875°N), about 8 km southeast of Helsinki city centre. The second mast was located on a peninsula (26.32524°E, 60.37754°N) south of the town of Loviisa, about 80 km east of Helsinki. Both stations are located in regions with fairly flat terrain; typical elevations are only of order a few metres a.s.l. The datasets cover a full year, from 1 April 2009–March 31 2010. However, when the wind was from the marine sectors (Isosaari east/south and southwest, Loviisa southwest) we only used the time period when there was no sea ice present, i.e. 1 April 2009–30 November 2009.

The Isosaari mast stands in the northeastern part of the Isosaari island, immediately southwest of a narrow peninsula (Figure 1). There is open sea in the northern sector between Isosaari and the mainland, which is approximately 4 km away. In the eastern and southern sectors there is approximately 70 km of open sea between Isosaari and the Estonian coast. The observations are mainly affected by the surface roughness of the island (sparse mixed forest)

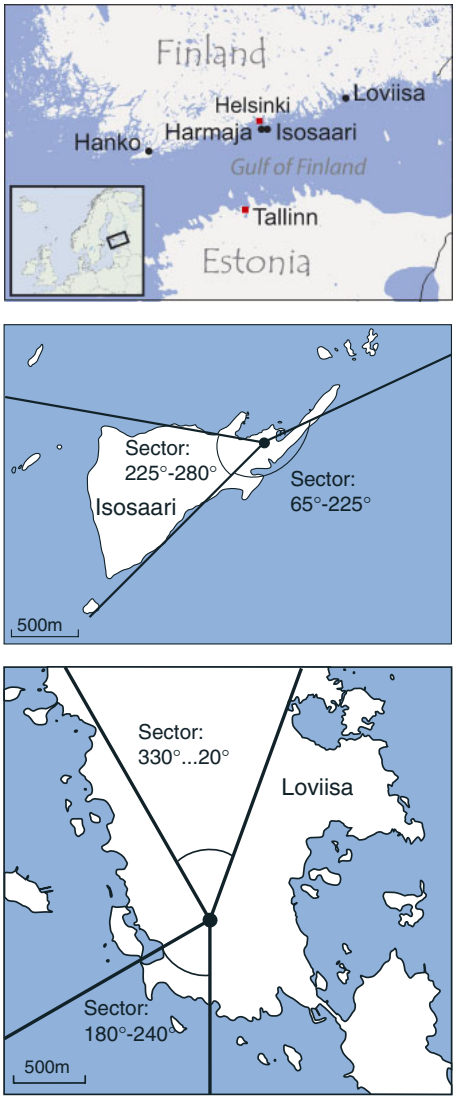

Figure 1. Gulf of Finland (top) and Isosaari island (middle) with the main marine sector (65°–225°) and the additional sector (225°–280°), and Loviisa peninsula (bottom) with the land sector pointing towards north (330°–20°) and the marine sector (180°–240°) in the southwest. This figure is available in colour online at wileyonlinelibrary.com/journal/qj

when the winds are from the west/southwest. Wind-speed measurements were made at three levels (42, 62 and 83 m) with Vaisala WAA151 cup anemometers. The wind direction was recorded at 40 and 81 m using WAV151 wind vanes. Temperature and humidity observations were available at two levels as well (42 and 83 m) from Vaisala HMP45D temperature and humidity sensors. The recorded parameters include 10 min mean wind speed and direction, standard deviation of wind speed and direction and a maximum and minimum 3 s wind speed (gust) during each 10 min period. Temperature and humidity are also recorded as 10 min averages.

The Loviisa mast is located in the middle of a peninsula, about 500 m from the coastline in all directions except towards the north, where there is continuous land (Figure 1). In the marine sectors, there are varying numbers of additional islands in all directions. In the vicinity of the mast there is a sparse, mainly coniferous, forest with an average tree height of about 12–15 m. At Loviisa, the wind measurements were available at three levels: 30, 103 and 143 m. Wind speed and direction were measured with sonic anemometers: Gill sonic instruments at 30 and 103 m and a Metek USA-1 at 143 m, all operated by a Vaisala MILOS-520 data collection and processing system. Temperature was measured at five levels: 2, 10, 40, 100 and 140 m. At the 2 m level, pressure and relative humidity were also observed. All parameters were recorded as hourly averages and the gust was given as a maximum of 1 s averages during each hour.

In this study we are interested in moderate and strong wind conditions. Therefore, we excluded all cases where the mean wind speed at the highest level was less than 5.0 m s^{-1}. In addition, at Loviisa the cases where the 30 m mean wind speed was less than 3.0 m s^{-1} were excluded. The average mean wind speed (gust wind speed) of the remaining observations at the highest observation level was 9.2 m s^{-1} (11.7 m s^{-1}) for the northern sector of Loviisa, 9.4 m s^{-1} (11.5 m s^{-1}) for the southwestern sector of Loviisa, and 8.1 m s^{-1} (9.9 m s^{-1}) and 9.0 m s^{-1} (10.8 m s^{-1}) for the south/east and southwest sectors of Isosaari, respectively. The maximum gust at the highest level at Loviisa was 23.6 m s^{-1} and that at Isosaari was 21.9 m s^{-1}.

To test the gust parametrization methods, two sectors, one from Isosaari and one from Loviisa, were selected that have the most homogeneous surface conditions. By doing this, we reduce any possible effects due to the internal boundary layers that may form when the surface type changes dramatically, for example in the southwestern sector of Isosaari and in all marine sectors of the Loviisa mast, where there is a sea–land boundary and other islands nearby. The selected sector in Isosaari, 65°–225°, points to the east and south as seen in Figure 1 and is characterized by open sea. In contrast, the Loviisa sector, 330°–20°, represents a forested land surface.

The total number of observations from Isosaari (excluding the winter months and weak wind conditions) is about 22 000, from which nearly 6900 observations were selected from the east/south sector and 5800 from the southwest. The sampling was performed every 10 min. The total number of 1 hourly observations from Loviisa was nearly 4500 (excluding the weak winds), of which 323 cases were selected from the northern sector and 502 from the southwest (during ice-free conditions).

The boundary-layer (BL) height was not available from measurement. We therefore used operational forecasts from the High-Resolution Limited-Area Model (HIRLAM) system, which is used by the Finnish Meteorological Institute. The reference model version (V72) was used with a horizontal resolution of approximately 16 km. The BL height is calculated in the model based on the bulk Richardson number Ri_b method proposed by Vogelezang and Holtslag (1996).

3.2. *Calculation of surface fluxes and stability*

The flux data from the sonic anemometers were not archived by the power company operating the Loviisa mast. Therefore, we calculated the fluxes and the Obukhov length

both at Loviisa and Isosaari using the methodology described by Launianen and Vihma (1990), which is based on the Monin–Obukhov theory. At Loviisa, we used temperature measurements at 10 and 40 m and wind speed at 30 m. At Isosaari, we applied the data on wind speed and air temperature at 42 m and sea-surface temperature (SST) measured at the nearest synoptic weather station Harmaja (WMO: 02795), which is located about 4 km west of Isosaari. On the basis of the calculated Obukhov length, the data from both masts were divided into stability classes.

The Harmaja SST measurements were taken approximately 1 m below the mean sea level. The observed water temperature may, however, differ significantly from the skin temperature of the sea surface, which is in direct contact with the atmosphere. To investigate this effect we compared the Harmaja SST observations with SST observations derived from satellite data (a product of Finnish Environment Institute using AVHRR (NOAA), TERRA MODIS (NASA) and ENVISAT MERIS (ESA) data). In the spring, early summer and autumn the satellite and *in situ* observations agreed well, but in the middle of the summer the Harmaja *in situ* observations were higher than the temperatures obtained from satellite data. We therefore introduced a correction function to the Harmaja data which had a sinusoidal form: no correction was applied during the spring and autumn and a maximum correction of 0.5 °C was applied in the middle of summer. The effect of the correction on the results for G was, however, minimal.

3.3. Determination of the normalized gust based on observations

The normalized gust $g_{t,T}$ (Eq. (6)) was determined from observations. Figure 2 shows that at both Isosaari and Loviisa the difference between the gust and the mean wind speed ($u_{t,T}$–u_T) can be expressed by a linear relationship with standard deviation σ_U. Hence, it is convenient to use an average value for $g_{t,T}$. In our data, the normalized gust was fairly constant with wind speed. This finding contradicts the assumptions made by W73, Eq. (15). The normalized gust did not vary much with height as only at the lowest measurement level at Loviisa was the mean $g_{t,T}$ larger than at the two upper levels. The scatter in $g_{t,T}$ was larger when winds were weak (not shown), which is in agreement with Harper *et al.* (2010), who studied gusts in tropical cyclones. They suggest that this is due to a constant eddy integral length-scale, which means that a larger number of observations with higher wind speeds improves the accuracy of the gust-factor estimate.

3.4. Standard deviation of horizontal wind speed

The new gust parametrization requires a parametrization for the standard deviation of wind speed. In Cenedese *et al.* (1998), four different formulations for the standard deviation of the cross-wind component of the wind velocity σ_v were given for unstable (Panofsky *et al.*, 1977; Paumier *et al.*, 1986; Wilczak and Phillips, 1986; Gryning *et al.*, 1987) and three for stable conditions (Hanna, 1982; Paumier *et al.*, 1986; Gryning *et al.*, 1987). We tested these methods assuming that σ_v is the same order of magnitude as the standard deviation of the horizontal (scalar) wind speed σ_U. The results are shown in Table 2 for Isosaari and in Table 3 for Loviisa. The best scores are highlighted with bold. In general, correlations at Isosaari were much smaller than at Loviisa. This was probably because the stochastic nature of wind speed was reflected more in the results when the averaging period was shorter (10 min in Isosaari; 1 h in Loviisa). All methods except that of Wilczak and Phillips (1986) performed almost equally well.

All methods (except that of Panofsky *et al.* (1977) when applied at Isosaari) showed a negative bias. It was probably because the assumption that σ_U and σ_v are equal is a poor approximation. In addition, the standard deviation of the along-wind component (σ_u) contributes to σ_U, which is often defined as $\sigma_U = \sqrt{\sigma_u^2 + \sigma_v^2}$. The relative importance of the along- and cross-wind components has been discussed previously (e.g. Garrat, 1992). Pragmatically, we assume that in stable conditions $\sigma_v = \sigma_u$, which means that $\sigma_U = \sqrt{2}\sigma_v$. Hence, this assumption is the cause by which Eq. (8), originally by Gryning *et al.* (1987), obtained its current form for stable conditions. The results after this modification show improvement (Tables 2 and 3; the method called 'modified Gryning *et al.* (1987)'). The standard deviation derived from the WNP01 gustiness method already included the effect of both horizontal wind velocity components, but σ_U was overestimated in all cases in Tables 2 and 3, showing larger (positive) bias than the other methods.

4. Results

4.1. Isosaari marine sector and Loviisa land sector

The methods by W73, WNP01 and the new method are compared in this section. Figure 3 shows the observed and parametrized gust-factor distributions for the lowest height level at Isosaari. All methods have a large peak in the gust-factor distribution between 1.1 and 1.2. In the observations, this range of gust-factor values includes all stability categories, as do the W73 method and the new method. In WNP01, there were almost no gust factors between 1.1 and 1.2 when unstable conditions were present and, instead, unstable conditions usually resulted in larger gust factors. Even though the WNP01-based gust-factor distribution as a whole (regardless of stability) looks most similar to the observed distribution, the method overestimates the effect of stability: this is clearly seen in Figure 4, which demonstrates the differences in the mean gust-factor profiles. Here, it is noteworthy that the W73 method performs almost as well as the other methods, even though it assumes neutral stability. The mean gust-factor profiles, however, are most realistic with the new method. According to the observations, WNP01 and the new method, a height difference between 42 and 83 m as well as a stratification difference between stable and unstable has a statistically significant (99% confidence level) effect on the gust factor (Figure 4).

At Loviisa, stability has a larger effect on gustiness than at Isosaari. The observed gust-factor distribution in Figure 5(a) is wider than that at Isosaari (Figure 3(a)) and at Loviisa the mean gust-factor profiles vary more with stability (Figure 6(a)) than at Isosaari. Here, the W73 method overestimates the gust factors in general. The WNP01 method, again, exaggerates the effect of stability, which is especially visible in Figure 5(c) where the gust-factor distribution has two peaks. The new method produces the most realistic gust-factor distribution, though the distribution is not as wide as observed, especially at

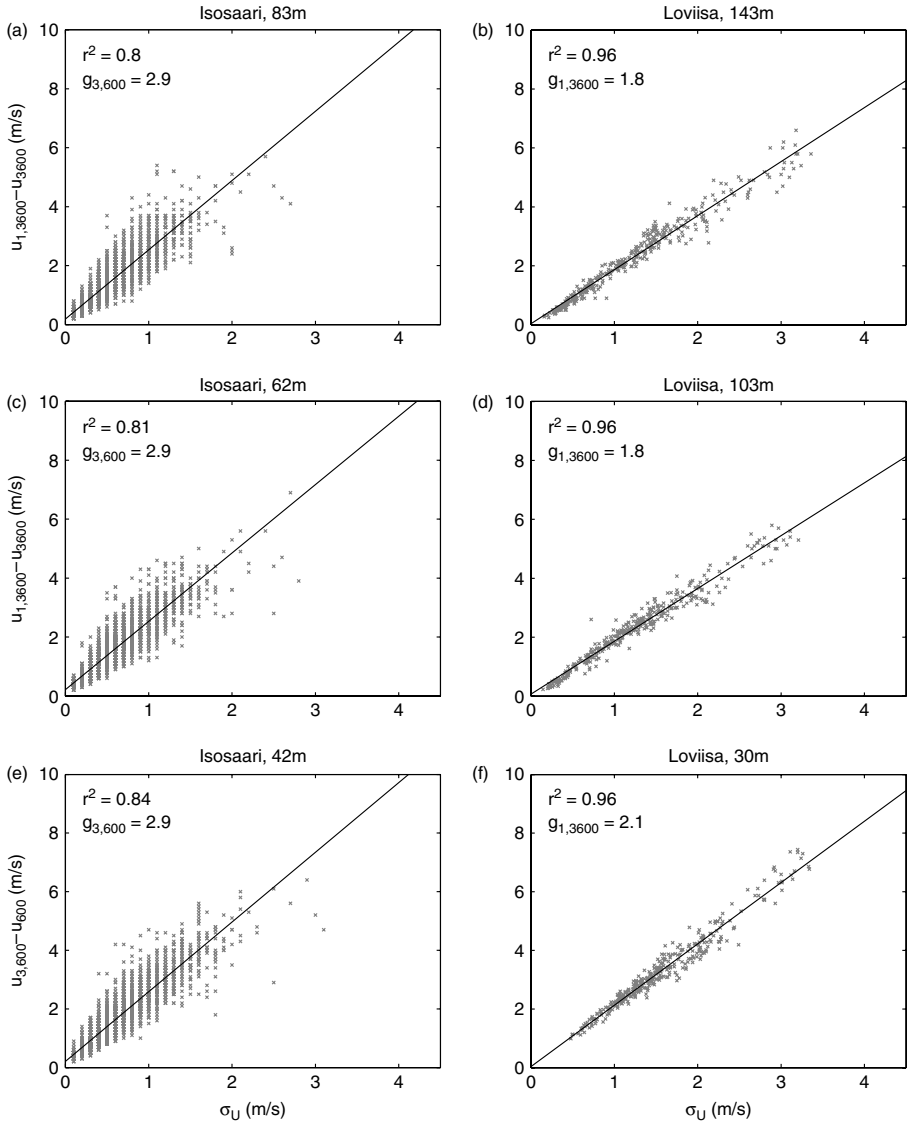

Figure 2. Maximum deviation from the mean wind speed as a function of standard deviation of wind speed for Isosaari and Loviisa. The straight line represents a linear least-squares fit to the data.

Table 2. Correlation coefficient (r^2), root-mean-square error (*RMSE*), bias and standard error (*SE*) for different σ_U parametrization methods at Isosaari. The best scores are highlighted in bold.

	Unstable				Stable			
	r^2	*SE*	*RMSE*	*BIAS*	r^2	*SE*	*RMSE*	*BIAS*
Panofsky *et al.* (1977)	**0.41**	**0.24**	0.06	0.15	–	–	–	–
Hanna (1982)	–	–	–	–	0.35	**0.21**	0.05	−0.21
Paumier *et al.* (1986)	0.38	**0.24**	**0.05**	**0.00**	**0.36**	**0.21**	0.05	−0.18
Wilczak and Phillips (1986)	0.14	0.30	0.06	−0.16	–	–	–	–
Gryning *et al.* (1987)	0.35	**0.24**	**0.05**	−0.02	0.33	**0.21**	0.05	−0.15
Modified Gryning *et al.* (1987)	–	–	–	–	0.33	0.22	**0.04**	**−0.03**
Woetman Nielsen and Petersen (2001)	0.37	0.38	0.10	0.88	0.26	0.29	0.06	0.30

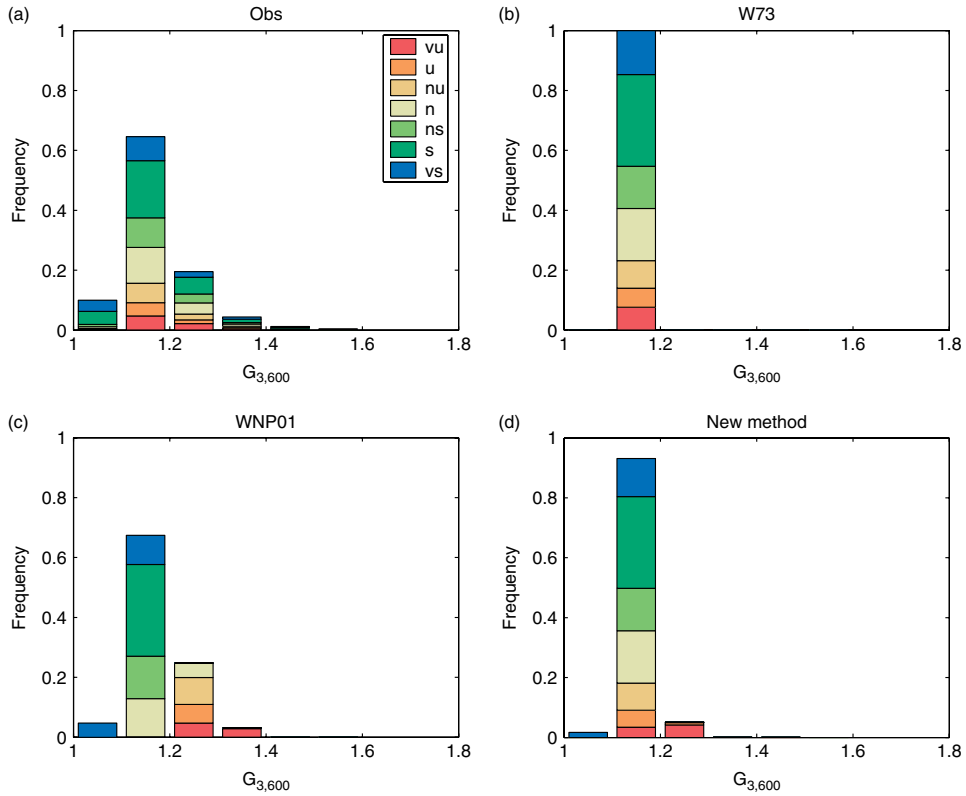

Figure 3. Gust-factor distributions at the lowest level (42 m) in Isosaari. The stability classes in the legend are defined as very unstable (vu): $-100 < L < -50$; unstable (u): $-200 < L < -100$; near-neutral unstable (nu): $-500 < L < -200$; neutral (n): $|L| > 500$; near-neutral stable (ns): $200 < L < 500$; stable (s): $50 < L < 200$; very stable (vs): $10 < L < 50$. This figure is available in colour online at wileyonlinelibrary.com/journal/qj

Table 3. Same as Table 2 but for Loviisa.

	Unstable				Stable			
	r^2	*SE*	*RMSE*	*BIAS*	r^2	*SE*	*RMSE*	*BIAS*
Panofsky *et al.* (1977)	**0.80**	**0.32**	**0.13**	**−0.08**	–	–	–	–
Hanna (1982)	–	–	–	–	**0.68**	0.34	0.17	−0.60
Paumier *et al.* (1986)	0.75	0.35	0.18	−0.52	**0.68**	**0.31**	0.17	−0.54
Wilczak and Phillips (1986)	0.39	0.53	0.25	−1.06	–	–	–	–
Gryning *et al.* (1987)	0.72	0.38	0.19	−0.59	0.66	0.35	0.16	−0.49
Modified Gryning *et al.* (1987)	–	–	–	–	0.66	**0.31**	**0.13**	**−0.24**
Woetman Nielsen and Petersen (2001)	0.71	0.63	0.29	1.48	0.45	0.37	0.16	0.45

the upper end (right-hand side) of the distribution. The effect of stability on gusts is quite similar at all levels in Loviisa, even though the gust factor decreases clearly from the 30 m level. The decrease is quite well captured by all methods.

The W73 method gives almost no variation of median G with stability (Figures 3(b) and 5(b)). This is as expected, since the method assumes neutral conditions and a logarithmic wind profile. Other parameters in W73 are the surface roughness and wind speed, but they have only a minor effect on results: an increase in the wind speed from 0–30 m s^{-1} only causes a 20–30% decrease in G at Loviisa (z_0 = 1.9 m); over a smooth surface, such as at Isosaari, the change is even smaller (not shown). Moreover, most of the change takes place at low wind speeds (< 5 m s^{-1}), which are not important in the prediction of maximum wind conditions and were excluded from this study.

The WNP01 method is too sensitive to stability. At both Isosaari and Loviisa, the method overestimates G in unstable cases. WNP01 does not explicitly take into account the dependence of G on height, but we incorporated the height dependence by decreasing the friction velocity with height. The height dependence also enters the results via differences in the mean wind speed.

The new parametrization method gives the best results at both Loviisa and Isosaari (Figures 4(d) and 6(d)). At Isosaari, the profiles of G are very close to the observed ones, though the profiles for very unstable and stable cases are

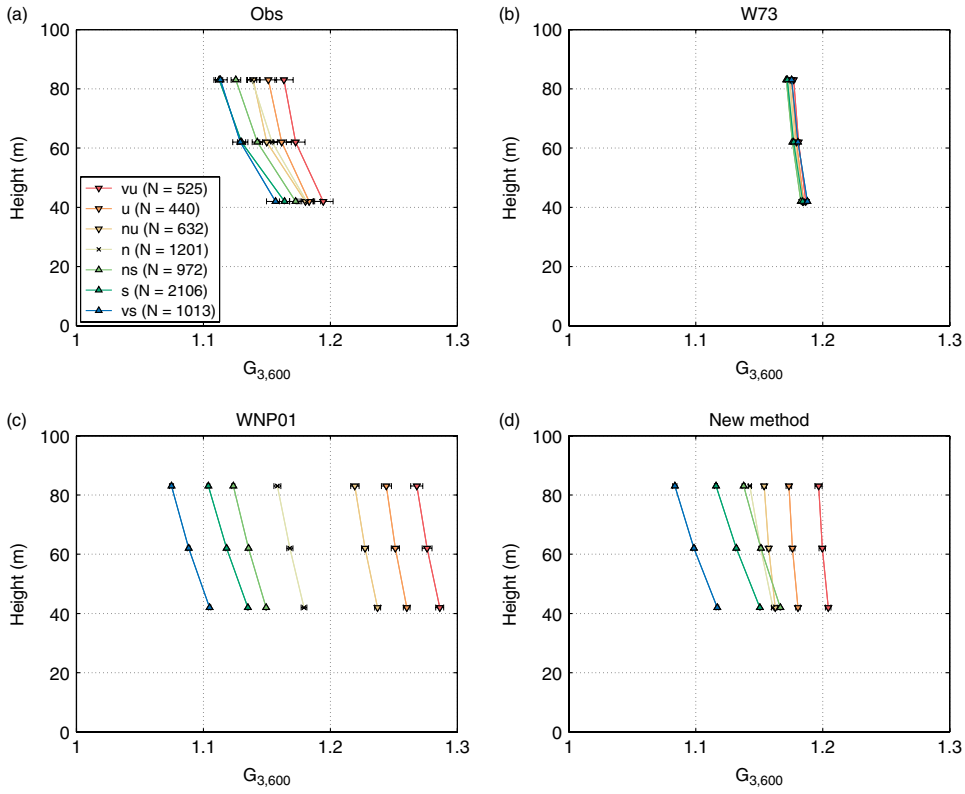

Figure 4. Mean gust-factor profiles in Isosaari. Stability classes are defined as in Figure 3. The horizontal error bars represent 99% confidence intervals. The number of observations (N) within each stability group is given in the legend. This figure is available in colour online at wileyonlinelibrary.com/journal/qj

somewhat too far away from the neutral profile. At Loviisa the new method clearly outperforms the other methods.

4.2. *Comparison of similar sectors from Isosaari and Loviisa*

Since the Isosaari and Loviisa masts represent different environments, the measurement heights differ and the instruments and observation practices are different, a direct comparison of the data is difficult. The most similar conditions are found in the southwestern sectors of the masts: in Isosaari at 225°–280° and in Loviisa at 180°–240°. The vegetation is of similar type, sparse forest, and the changes in elevation are small. At Isosaari, the coastline is at about 1000–1500 m from the mast and in Loviisa it is about 600–800 m away. The sector angles are such that they allow the same weather conditions to be included in both datasets. However, it must be noted that the masts will not experience exactly the same weather conditions due to their differing locations. The main difference between these sectors is that at Isosaari there is open sea for several hundred km while at Loviisa there are islands with a typical area of 1–10 km^2 within a distance of 3 km or more off the coastline. We compared these sectors using data only from the period when the sea was ice-free, i.e. 1 April 2009–30 November 2009.

The comparison results are shown in Figure 7, where both the original sectors studied in section 4.1 (note the small difference compared with the profiles in Figure 6(a), due to the different time period) and the southwestern sectors of both masts are presented. When the original sectors are considered (Figure 7(a)), large differences exist between the two masts, but when the two southwestern sectors are compared the differences are much smaller, not even statistically significant (at 99% level), in all cases (Figure 7(b)).

Also, a comparison of Figure 7(a) and (b) shows that at Loviisa there is no similar variation between the mean gust factors in different stability conditions in the southwestern sector to that in the northern sector. At Isosaari, the mean gust factors are clearly larger in the southwestern sector than in the east/south. There is also a clear gap in mean gust factors between stable and unstable conditions. These features are probably related to complex effects of the land–sea boundary and the islands near Loviisa.

It can be seen from Figure 7 that gust factors in the southwestern sector are smaller at Isosaari than at Loviisa. This is as expected, because the recorded gust duration is smaller and the sampling period larger at Loviisa than at Isosaari. Both these changes lead to a larger gust factor at Loviisa. The difference is large between the original sectors of each mast (Figure 7(a)), but not as large between the southwestern sectors. The difference is actually so small that it can be explained in the light of previous studies. For example, W73 estimated that the gust factor within 1 h is about 10% larger than that within 10 min close to the surface; also the change in gust duration from 3 s to 1 s increases the gust factor (e.g. Wieringa, 1973; Brook and

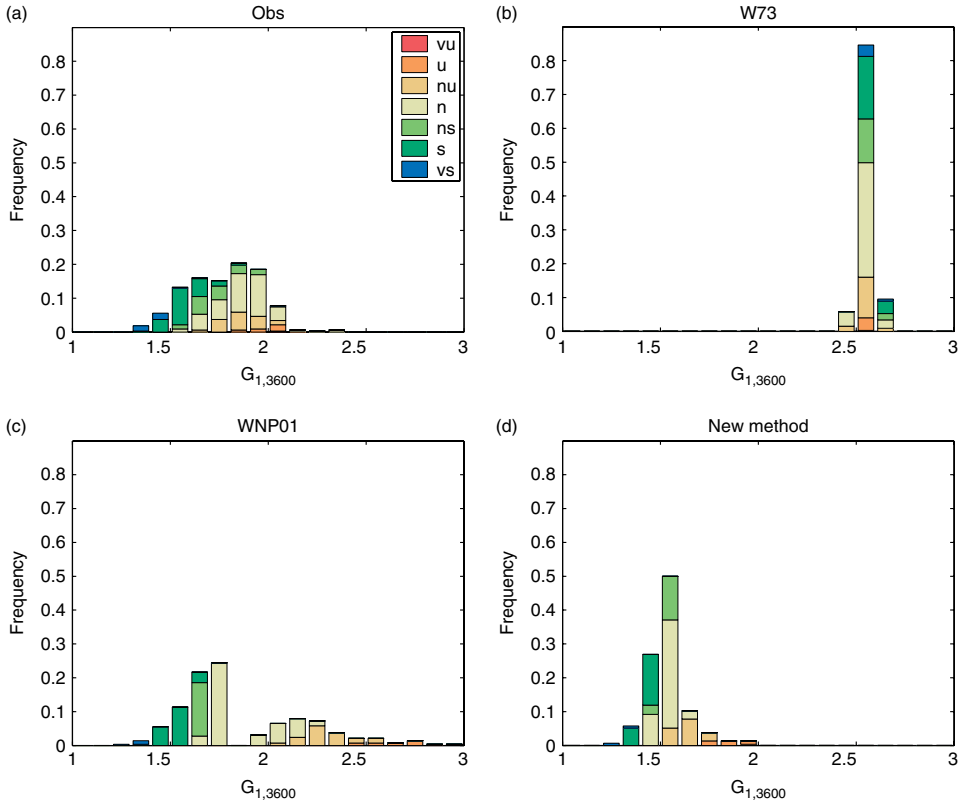

Figure 5. Gust-factor distributions at the lowest level (30 m) in Loviisa. Stability classes are defined as in Figure 3. This figure is available in colour online at wileyonlinelibrary.com/journal/qj

Spillane, 1968). The height dependence of this difference is, however, unknown.

5. Discussion

In this section we will discuss the components that were used to derive the new gust parametrization method: the standard deviation of wind speed σ_U and the normalized gust $g_{t,T}$. Also the possible effects of inaccuracy of the boundary-layer height on the results are discussed.

5.1. *Standard deviation of wind speed, σ_U*

The standard deviation of wind speed is not identical for sonic and cup anemometers, as sonic anemometers give both along- and cross-wind components, σ_u and σ_v, whereas cup anemometers and wind vanes give the standard deviation of the scalar wind speed σ_U and the standard deviation of the wind direction σ_θ. However, our data from the sonic anemometers on the Loviisa mast was converted by the power company to a form that corresponds to the measurements available from cup anemometers. Thus, we can assume that both datasets represent the scalar σ_U. Differences in the length of the averaging period and sampling frequency, however, need to be taken into account. The larger the period T over which the standard deviation is calculated, the larger the standard deviation expected. Durst (1960) indicate that the difference in σ_U measured over 1 h compared with that measured over 10 min can be about 2%. The effect of the sampling frequency can on average cause differences of about 5% (Beljaars, 1987).

When the data obtained for the southwestern sectors are considered (as in section 4.2), the mean σ_U at Loviisa at 103 m was 1.0 m s^{-1} whereas at Isosaari at 83 m it was 0.7 m s^{-1}. At the lowest levels (30 m at Loviisa and 42 m at Isosaari) the values were 1.9 and 1.1 m s^{-1} respectively. The differences between the two masts at both upper and lower levels are larger than expected. The differences were even larger between the northern sector of Loviisa and the eastern / southern sector of Isosaari, with mean σ_U values at higher levels (103 and 83 m) of 1.5 and 0.5 m s^{-1} and at lower levels (30 and 42 m) of 1.7 and 0.6 m s^{-1} for Loviisa and Isosaari respectively. While the differences in the mean values between similar sectors are of order 30–80%, the differences between the land and marine sectors are of order 200–300%. The latter cannot be explained by the different measurement and averaging practices and it is evident that the different environments within the sectors must have an effect.

5.2. *Normalized gust $g_{t,T}$*

Different formulations for the normalized gust are available in the literature. Durst (1960) introduced a selection of coefficients (normalized gusts) to calculate gusts of different durations from the standard deviation of wind speed. For a

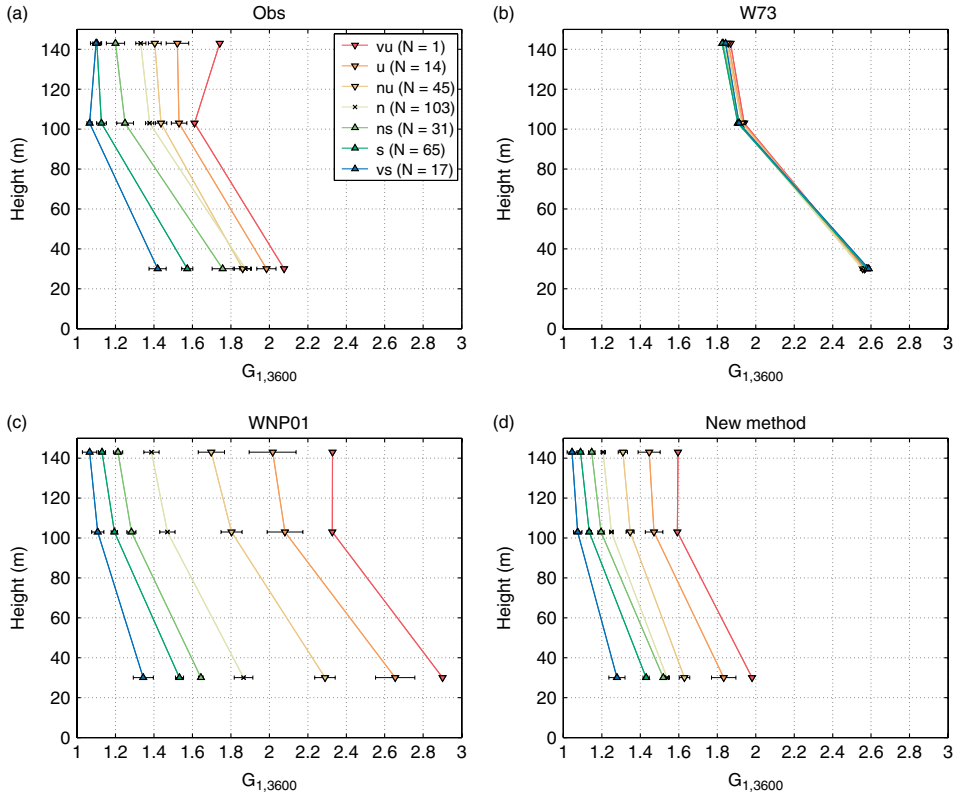

Figure 6. Mean gust-factor profiles in Loviisa. Stability classes are defined as in Figure 3, and error bars and the number of observations (N) are given as in Figure 4. This figure is available in colour online at wileyonlinelibrary.com/journal/qj

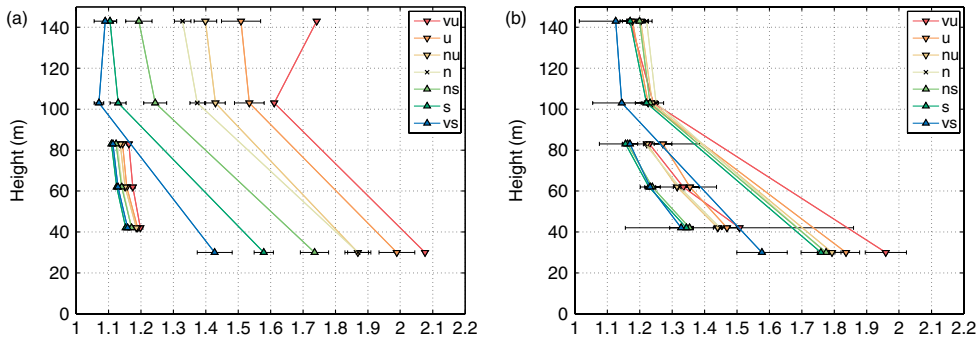

Figure 7. Mean gust-factor profiles (a) in the Isosaari eastern/southern sector and Loviisa northern sector and (b) in the southwestern sectors of Isosaari and Loviisa. Stability classes are defined as in Figure 3 and the error bars as in Figure 4. This figure is available in colour online at wileyonlinelibrary.com/journal/qj

5 s gust this coefficient was 3.0. Durst (1960) assumed, while deriving the coefficients, that a Gaussian distribution of wind fluctuations around the mean wind existed, but he noted that using, for instance, the Gumbel distribution would yield slightly larger coefficients. Deacon (1965) derived an empirical equation for the ratio of a wind gust with arbitrary duration and a gust with 2 s duration. He found that this ratio is a function of surface roughness. Brook and Spillane (1968) further developed the methodology of Durst (1960) and extended the idea of Deacon (1965) to derive an equation for the ratio of gusts with different time-scales T and t. In this process they introduced a function for the velocity spectrum, which they then used to estimate the variance of the fluctuations. Their results suggest that gusts with 1 s duration are about 10–15% larger than gusts with a duration of 3 s. The effect of the sampling period (T) is smaller: gusts during 1 h are about 1–5% larger than gusts during 10 min if the gust duration is kept constant.

Wieringa (1973) estimated the normalized gust using Eq. (15). The change in gust duration from 3 s to 1 s causes an

increase of about 15% in $g_{t,T}$ which is of the same order of magnitude as in the results of Brook and Spillane (1968). However, Wieringa (1973) estimated the influence of the sampling period length to be 10% when going from 10 min to 1 h, which is larger than the estimates by Brook and Spillane (1968). Beljaars (1987) also studied the effect of sampling and filtering on gusts. He used a similar approach to Brook and Spillane (1968), but applied two known wind-velocity spectra (Højstrup, 1982; Kaimal, 1978), both defined as a function of stability. The results showed that changing the gust duration from 1–3 s causes a decrease of about 10% in normalized gust. The effect of the sampling period length (T) on the normalized gust has received much less attention than that of the gust duration (t) in gust-related papers.

The mean normalized gust in both sectors of Loviisa was close to 2: in the northern sector $g_{1,3600} = 2.1$ at the lowest level and $g_{1,3600} = 1.9$ at the upper two levels, and in the southwest sector the normalized gusts were 2.1 and 2.0 respectively. In the eastern/southern sector of Isosaari $g_{3,600} = 2.9$, while in the southwest sector $g_{3,600} = 2.7$ at all levels. It appears that the deviation of the gust wind speed from the mean wind speed behaves in a similar way to the standard deviation; hence a change in surface roughness, like that between the Isosaari east/south and southwest sectors, does not affect the normalized gust estimates. This suggests that the differences between observation practices (instruments and averaging period lengths) would be the main factor in determining the normalized gust. However, previous studies suggest that $g_{1,3600} > g_{3,600}$, which was not the case here as $g_{t,T}$ at Loviisa was less than at Isosaari: $g_{1,3600} < g_{3,600}$. Based on the data used in this study, it is not possible to explain where this contradiction comes from.

5.3. *Sensitivity to the boundary-layer height*

In general, the results are not very sensitive to the BL height. In unstable conditions the BL height is used to calculate the convective velocity scale, which is required in the calculation of the gust factor estimate. However, the convective velocity scale is proportional to the cubic root of the BL height, which means that in practice a 50% error in the BL height corresponds to only a 20% error in the convective velocity scale.

The BL height is also used in estimating the height dependence of the friction velocity. We assume that the turbulent momentum flux decreases linearly with height to the top of the boundary layer. Hence, the friction velocity decreases with the square root of the height relative to the BL height. The change close to the surface is small, but it gradually increases towards the top of the BL. With large BL heights (relative to the height of the mast), the error in the BL height causes only a small error in the friction velocity profile at the height of the mast. However, when the BL height is small, for example twice the mast height or less ($\sim$ 300–400 m), the error in the BL height may cause a fairly large error in the friction velocity profile. A comparison study of HIRLAM boundary-layer heights with SODAR measurements in Helsinki (Kouznetsov *et al.*, 2010) showed that shallow BL heights are predicted well at the Finnish coast of the Gulf of Finland.

6. Conclusions

In this study we have tested two wind-gust parametrizations with application to heights relevant for wind energy. In addition, a new wind-gust parametrization was derived. All three methods were compared using data from two weather masts located on the Finnish coast of the Gulf of Finland, in a potential region for wind power plants. One of the masts, Isosaari, represented marine, open water conditions, while the other, Loviisa, represented a rough, forested area. Both stations were located on a fairly flat terrain.

The results showed that the surface roughness was the most important factor controlling the gustiness: the differences in the gust factor between Loviisa land sector and Isosaari marine sector were much larger than the differences related to variations in stability and observation height. The effect of stability was more pronounced over a rough surface than over the smooth marine one. At both masts, within the range of our observations, the stability affected the gustiness more than the observation height did. Young and Kristensen (1992) demonstrated the strong effects of stability in the case of weak winds ($3\,\mathrm{m\,s^{-1}}$). In our study, however, cases of weak winds were excluded, which means that stability is also important during moderate winds. Both the WNP01 method and the new method included a stability dependence, but in the case of WNP01 the effect of stability was too pronounced in unstable conditions, especially over a rough land surface.

The height dependence of gusts was fairly well produced by all parametrization methods. In the W73 method, the variations with height come from assuming a logarithmic wind profile, while in WNP01 and the new method we assumed that the momentum flux decreases linearly to zero at the top of the boundary layer.

The new gust parametrization method was derived using existing parametrizations for the standard deviation of wind speed. This makes the method applicable to various environments, as was shown here for the two sites with different surface roughness and thermal environments. Furthermore, we found that the relationship between the gust and the standard deviation of wind speed, described as a normalized gust, was fairly linear and that a constant value for the normalized gust can be used for a specific observation site and height.

The comparison of the two masts using observations from sectors that have more similar roughness conditions showed that even though the measurement practices and the instruments differ between the masts, the gust factors are comparable if the sectors are similar enough.

The new gust parametrization method was superior compared with the methods of W73 and WNP01, especially over a rough surface, when the stability had a strong effect on results. The new method did not exaggerate the effect of stability as was the case in the WNP01 method. Furthermore, the new method could be used at different heights above the surface, which made it applicable up to a couple of hundred metres above the surface, at heights relevant for wind energy and other engineering applications.

Acknowledgements

This research has received funding from the European Research Council under the European Community's 7th

Framework Programme (FP7/2007-2013)/ERC grant agreement number 227915, project PBL-PMES, Sergej Zilitinkevich, coordinator, and from the Danish Council for Strategic Research, Sagsnr. 2104-08-0025 (Tall Wind project). We acknowledge Fortum Corporation for providing us with the observations from the Loviisa weather mast and the Finnish Environment Institute for the satellite SST data. We thank Victoria Sinclair for improving the English language. We also thank the two anonymous reviewers for constructive comments on the manuscript.

References

Ágústsson H, Ólafsson H. 2004. Mean gust factors in complex terrain. *Meteorol. Z.* **13**: 149–155.

Ágústsson H, Ólafsson H. 2009. Forecasting wind gusts in complex terrain. *Meteorol. Atmos. Phys.* **103**: 173–185.

Arya SP. 1999. *Air pollution meteorology and dispersion*. Oxford University Press: New York.

Beljaars ACM. 1987. The influence of sampling and filtering on measured wind gusts. *J. Atmos. Ocean. Technol.* **4**: 613–626.

Belusić D, Klaić ZB. 2004. Estimation of bora wind gusts using a limited area model. *Tellus* **56A**: 296–307.

Brasseur O. 2001. Development and application of a physical approach to estimating wind gusts. *Mon. Weather Rev.* **129**: 5–25.

Brook RR, Spillane T. 1968. The effect of averaging time and sample duration on estimation and measurement of maximum wind gusts. *J. Appl. Meteorol.* **7**: 567–574.

Cenedese A, Cosemans G, Erbrink H, Stubi R. 1998. 'Vertical profiles of wind, temperature and turbulence.' In *COST Action 710 – Final Report*, European Commission: Luxembourg, Belgium.

Davis FK, Newstein H. 1968. The variation of gust factors with mean wind speed and with height. *J. Appl. Meteorol.* **7**: 372–378.

Deacon EL. 1955. Gust variation with height up to 150 m. *Q. J. R. Meteorol. Soc.* **81**: 562–573.

Deacon EL. 1965. Wind gust speed: averaging time relationship. *Aust. Meteorol. Mag.* **52**: 11–14.

Durst CS. 1960. Wind speeds over short periods of time. *Meteorol. Mag.* **89**: 181–186.

Garrat JR. 1992. *The Atmospheric Boundary Layer*. Cambridge University Press: Cambridge, UK.

Goyette S, Brasseur O, Beniston M. 2003. Application of a new wind-gust parametrization: Multiscale case studies performed with the Canadian regional climate model. *J Geophys Res.* **108**(D13): 4374.

Gryning SE, Holtslag AAM, Irwin JS, Sivertsen B. 1987. Applied dispersion modelling based on meteorological scaling parameters. *Atmos. Environ.* **21**: 79–89.

Guan WL, Yong K. 2002. '*Review of aciation accidents caused by wind shear and identification methods*', Publications of the Aviation Safety Council, Taiwan. Available at http://www.asc.gov.tw/author_files/WINSHEAR.pdf (accessed 28 December2011).

Hanna SR. 1982. Applications in air pollution modelling. In *Atmospheric turbulence and air pollution modelling*, Nieuwstadt FTM, van Dop H (eds). Reidel: Boston, MA.

Harper BA, Kepert JD, Ginger JD. 2010. '*Guidelines for converting between various wind averaging periods in tropical cyclone conditions*', WMO/TD-No. 1555, World Meteorological Organization: Geneva, Switzerland.

Højstrup J. 1982. Velocity spectra in the unstable planetary boundary layer. *J Atmos. Sci.* **39**: 2239–2248.

Kaimal JC. 1978. Horizontal velocity spectra in an unstable surface layer. *J Atmos. Sci.* **35**: 18–24.

Kaimal JC, Finnigan JJ. 1994. *Atmospheric Boundary Layer Flows: Their Structure and Measurement*. Oxford University Press: New York.

Kim J, Hangan H, Ho TCE. 2007. Downburst versus boundary layer induced loads for tall buildings. *Wind Struct.* **10**: 481–494.

Kouznetsov R, Sofiev M, Soares J, Fortelius C. 2010. 'The height of a shallow mixing layer in models: performance of different schemes'. *Proc. 15th International Symposium for the Advancement of Boundary Layer Remote Sensing,* University of Versailles Saint-Quentin-en-Yvelines, Paris, France.

Kristensen L, Casanova M, Courtney MS, Troen I. 1991. In search of a gust definition. *Boundary-Layer Meteorol.* **55**: 91–107.

Launiainen J, Vihma T. 1990. Derivation of turbulent surface fluxes – an iterative flux-profile method allowing arbitrary observing heights. *Environ. Software* **5**: 113–124.

Meyers MP, Snook JS, Wesley DA, Poulos GS. 2003. A Rocky Mountain Storm. Part II: The forest blowdown over the west slope of the northern Colorado mountains – observations, analysis and modeling. *Weather Forecast.* **18**: 662–674.

Nakamura K, Kershaw R, Gait N. 1996. Prediction of near-surface gusts generated by deep convection. *Meteorol. Appl.* **3**: 157–167.

Panofsky HA, Tennekes H, Lenschow DD, Wyngaard JC. 1977. The characteristics of turbulent velocity components in the surface layer under convective conditions. *Boundary-Layer Meteorol.* **11**: 355–361.

Paumier J, Stinson D, Kelly T, Bollinger C, Irwin JS. 1986. '*MPDA-1.1: a meteorological processor for diffusion analysis*', Report EPA/600/8-86/011. EPA: Research Triangle Park, NC.

Petersen EL, Mortensen NG, Landberg L, Højstrup J, Frank HP. 1998. Wind power meteorology. Part I: climate and turbulence. *Wind Energy* **1**: 25–45.

Pinto JG, Neuhaus CP, Krüger A, Kerschgens M. 2009. Assessment of the wind gust estimate method in mesoscale modelling of storm events over West Germany. *Meteorol. Z.* **18**: 495–506.

Rauhala J, Juga I. 2010. 'Wind and snow storm impacts on society'. *15th International Road Weather Conference*, Quebec City, Canada, 5–7 February 2010, Standing International Road Weather Commission, University of Birmingham, UK.

Tammelin B, Vihma T, Atlaskin E, Badger J, Fortelius C, Gregow H, Horttanainen M, Hyvnen R, Kilpinen J, Latikka J, Ljungberg K, Mortensen NG, Niemelä S, Ruosteenoja K, Salonen K, Suomi I, Venäläinen A. 2011. Production of the Finnish Wind Atlas. *Wind Energy*. DOI:10.1002/we.517.

Valkonen T, Vihma T, Kirkwood S, Johansson MM. 2010. Fine-scale model simulation of gravity waves generated by Basen nunatak in Antarctica. *Tellus* **62A**: 319–332.

Vogelezang DHP, Holtslag AAM. 1996. Evaluation and model impacts of alternative boundary-layer height formulations. *Boundary-Layer Meteorol.* **81**: 245–269.

Wichers Schreur B, Geertsema G. 2008. Theory for a TKE based parametrization of wind gusts. *HIRLAM Newsletter* **54**: .

Wieringa J. 1973. Gust factors over open water and built-up country. *Boundary-Layer Meteorol.* **3**: 424–441.

Wilczak JM, Phillips MS. 1986. An indirect estimation of convective boundary layer structure for use in pollution dispersion models. *J. Clim. Appl. Meteorol.* **25**: 1609–1624.

World Meteorological Organization (WMO). 2008. Measurement of surface wind. In *Guide to Meteorological Instruments and Methods of Observation*, WMO-No. 8, 7th edn, World Meteorological Organization, Geneva, Switzerland.

Woetmann Nielsen N, Petersen C. 2001. *Calculation of wind gusts in DMI-HIRLAM*, Scientific Report, 01–03, Danish Meteorological Institute, Copenhagen, Denmark.

Young GS, Kristensen L. 1992. Surface-layer gusts for aircraft operation. *Boundary-Layer Meteorol.* **59**: 231–242.

Reprinted, with permission, from
Quarterly Journal of Royal Meteorological Society, 141, 1658–1670,
doi:10.1002/qj.2468

II

 Q. J. R. Meteorol. Soc. 141: 1658–1670, July 2015 A DOI:10.1002/qj.2468

RMetS
Royal Meteorological Society

On the vertical structure of wind gusts

I. Suomi,[a]* S.-E. Gryning,[b] R. Floors,[b] T. Vihma[a] and C. Fortelius[a]
[a]*Finnish Meteorological Institute, Helsinki, Finland*
[b]*Technical University of Denmark, Roskilde, Denmark*

*Correspondence to: I. Suomi, Finnish Meteorological Institute, PO Box 503, FI-00101 Helsinki, Finland.
E-mail: irene.suomi@fmi.fi

The increasing size of wind turbines, their height and the area swept by their blades have revised the need for understanding the vertical structure of wind gusts. Information is needed for the whole profile. In this study, we analyzed turbulence measurements from a 100 m high meteorological mast at the Danish National Test Station for Large Wind Turbines at Høvsøre in Denmark. The site represents flat, homogeneous grassland with an average gust factor of 1.4 at 10 m and 1.2 at 100 m level. In a typical surface-layer gust parametrization, the gust factor is composed of two components, the peak factor and the turbulence intensity, of which the turbulence intensity was found to dominate over the peak factor in determining the effects of stability and height above the surface on the gust factor. The peak factor only explained 15% or less of the vertical decrease of the gust factor, but determined the effect of gust duration on the gust factor. The statistical method to estimate the peak factor did not reproduce the observed vertical decrease in near-neutral and stable conditions and near-constant situation in unstable conditions. Despite this inconsistency, the theoretical method provides estimates for the peak factor when comparing gust durations of 1 and 3 s with averaging period lengths of 10 min and 1 h. A new technique to study the timing of maxima at different levels relative to the maximum gust at some level was developed. Results showed that a 10 m level maximum gust was typically preceded by maxima at higher levels and vice versa: a 100 m gust was usually followed by a maximum at lower levels.

Key Words: atmospheric boundary layer; weather mast measurements; wind gust profile
Received 19 May 2014; Revised 17 September 2014; Accepted 20 September 2014; Published online in Wiley Online Library 05 December 2014

1. Introduction

Wind gusts, defined as short-duration wind-speed maxima, are relevant from various aspects. Severe wind gusts may cause damage to buildings and other structures and, especially in boreal regions, they typically cut large areas of forest and thereby often cause wide and long-lasting power cuts in rural areas. The direct and indirect costs together can rise to several millions of euros, even for a single storm event alone. For industries like wind energy and aerospace, wind gusts may cause limitations to operations. For aviation, gusty wind can become a safety risk in take-off and landing. For wind turbines, gustiness can reduce the efficiency by causing uneven, extra load on the turbine structures. The trend in increasing size of wind turbines has revised the need for turbulence and wind gust data. While the hub heights can reach up to 100 m or more, the blade diameters can also be as large as 100 m. Therefore, it is not enough to study gusts at a single height, but information on the entire vertical profile of gusts is also needed.

Peak gusts represent the high extremes in a turbulent wind field. Gusts are a statistical measure, for which the probability density function can be derived from the spectrum of wind-speed variations (e.g. Beljaars, 1987; Kristensen *et al.*, 1991; Wichers Schreur and Geertsema, 2008). For observational purposes, the World Meteorological Organization (WMO, 2008) recommends defining a gust as the maximum of 3 s averages during a 10 min sampling period. Beljaars (1987) showed that gusts with different durations are comparable with each other, provided that the characteristics of the instrumentation are known.

Prediction of wind gusts today still relies on parametrizations, even though the horizontal resolution of numerical weather prediction (NWP) models has increased to kilometre scale during the last decade (e.g. Seity *et al.*, 2011). The highest resolution NWP models can simulate mesoscale convective structures, but cannot solve all the scales of eddies responsible for gusts, namely spatial scales up to 1 km and temporal scales from a fraction of a second to a few minutes.

There are basically two types of gust parametrization: those based on surface-layer similarity theories and the so-called profile method. The main idea of a surface-layer gust parametrization is to estimate the gust factor (G), i.e. the ratio of the gust wind speed, $U_{\max}$, and the mean horizontal wind speed, U:

$$G = \frac{U_{\max}}{U} = 1 + \frac{U_{\max} - U}{\sigma_u} \frac{\sigma_u}{U} = 1 + g_x I, \qquad (1)$$

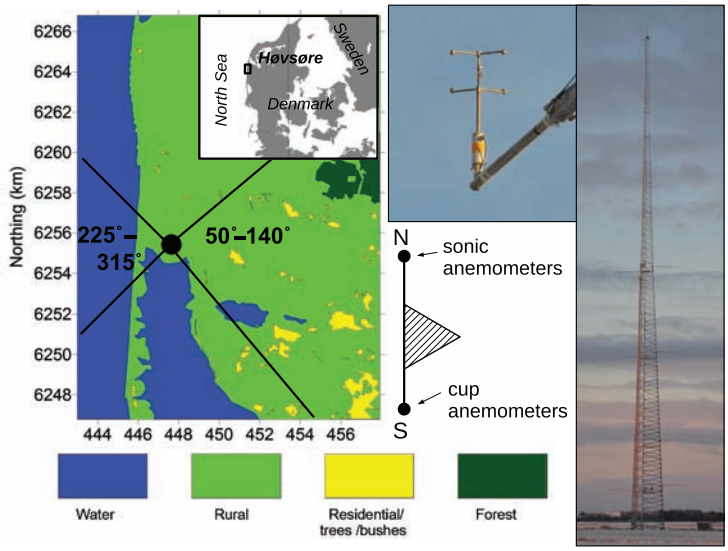

Figure 1. The meteorological mast of the Danish National Test Station for Large Wind Turbines located at Høvsøre in northwest Denmark. The east (50°–140°) and west (225°–315°) sectors are shown at the top of the land-use map. The coordinate system refers to UTM32. The ultrasonic anemometers are mounted on booms pointing towards the north.

where σ_u is the standard deviation of the horizontal wind velocity, g_x is a peak factor (sometimes also called the normalized gust) and I is the turbulence intensity of the horizontal wind velocity. The peak factor can be estimated through statistical considerations. The probability for one upcrossing of a level g_x can be derived using the joint (Gaussian) probability of a wind signal and its derivative. Both probabilities can be expressed in terms of the spectra of horizontal wind-velocity fluctuations. The peak factor also depends on the length of the moving average window used to determine the wind gust speed. Also, the ability of an anemometer (or a numerical model) to detect small-scale variations in wind speed affects the peak factor. These factors can be described by filtering the spectrum equation. This probabilistic method also provides a basis for estimating the average duration of a gust.

In Eq. (1), σ_u can be estimated from the turbulent kinetic energy (TKE) whenever it is available from a NWP model (e.g. Wichers Schreur and Geertsema, 2008). When the TKE is not available, σ_u is typically parametrized using Monin–Obukhov similarity theory. For instance, Wieringa (1973) assumes that the strongest gusts are always observed in near-neutral conditions and hence $\sigma_u \propto u_*$, where u_* is the friction velocity. Woetman Nielsen and Petersen (2001) used the convective velocity scale to describe the effect of buoyancy on gusts in unstable conditions. However, recently it has been found that this type of parametrization can easily overestimate the buoyancy effects on the gust factor in unstable conditions (Suomi *et al.*, 2013).

The profile method for gust parametrization was first introduced by Brasseur (2001). The estimated gust at 10 m height is equal to the mean wind speed at some height above the surface, within the boundary layer. This height depends on the stability conditions and on the TKE within the layer considered. Besides giving an estimate for wind gust speed, this method also provides a lower and upper limit for the gust, which is an advantage compared with other methods. This method by Brasseur (2001) has been widely tested in many different environments over flat and complex terrain (e.g. Goyette *et al.*, 2003; Ágústsson and Ólafsson, 2009), in the vicinity of high mountains (e.g. Belusić and Klaić, 2004) and in the production of a wind atlas (Tammelin *et al.*, 2013). However, many operational models such as the operational Integrated Forecast System (IFS, cycle 38r1) of the European Centre for Medium-Range Weather Forecasts (ECMWF) and the latest HIgh Resolution Limited Area Model (HIRLAM) version 7.4rc1 use surface-layer methods to estimate wind gust speed. The method by Wichers Schreur and Geertsema (2008) is used in HIRLAM, whereas the IFS model uses the methodology presented in ECMWF (2012). In the latter, wind-profile characteristics are taken into account, but only in convective conditions, when the deep convection parametrization is activated. A review of techniques and research for gust forecasting and parametrization has been presented by Sheridan (2011).

The vertical structure of gusts has not received much attention, but it is relevant for wind energy, for example. It is obvious that the method by Brasseur (2001) can be applied to estimate gusts at any level within the boundary layer (e.g. Tammelin *et al.*, 2013), but the surface-layer methods represent the conditions near the surface only. Suomi *et al.* (2013) found that a simple assumption of linearly decreasing momentum flux from the surface to the top of the boundary layer gives a good estimate for the height dependence of gusts up to 143 m height.

To investigate the vertical structure of wind gusts, we will use observations from the Danish National Test Station for Large Wind Turbines, located in Høvsøre in northwest Denmark (Figure 1). First, in section 2, we will briefly review the statistical methods used to estimate the peak factor. In section 3, we will introduce the measurements, data processing methods and definition of the gust in this study. The results in section 4 will start with an investigation of the factors that determine the gusts, as presented in Eq. (1). We will establish the relative effect of the peak factor and turbulence intensity on the gust factor in different stability conditions and with respect to height above the surface within the lowest 100 m of the atmosphere. Then, we will study gusts with durations from 1–30 s with two reference periods: 10 min and an hour. Both the vertical differences between the 10 and 100 m heights and different stability conditions will be considered. The results will then be compared with theoretical peak factor estimates. Finally, in section 4.2 we will take a closer look at the vertical structure of individual gust events in a set of 15 example cases. To end, a summary is provided in section 5.

2. Statistical approaches to defining the gust

The peak factor g_x in Eq. (1) can be derived from statistical considerations. The basis for the statistical theory of extremes was first presented by Rice (1944, 1945) and is therefore often called the 'Rice theory'. Beljaars (1987), Kristensen *et al.* (1991) and Wichers Schreur and Geertsema (2008) present the application

of the theory to predict gusts. Assuming that the probability (P) of a normalized wind speed to exceed some level is Poisson-distributed, then its probability for not crossing a level g_x can be expressed as

$$P\left(\frac{u(t)-U}{\sigma_u} < g_x, T\right) = \mathrm{e}^{[-N_x(g_x,T)]}, \tag{2}$$

where $u(t)$ is the horizontal wind speed, U its mean and σ_u^2 its variance during a sampling period T. $N_x(g_x, T)$ is the average number of upcrossings of level g_x during T. The number of upcrossings can be estimated assuming a joint Gaussian probability of the horizontal wind speed (u) and its time derivative ($\dot{u}$), yielding

$$N_x(g_x, T) = \frac{T}{2\pi}\frac{\sigma_{\dot{u}}}{\sigma_u}\mathrm{e}^{(-g_x^2/2)}, \tag{3}$$

where $\sigma_{\dot{u}}^2$ is the variance of the derivative $\dot{u}$. The variances of u and $\dot{u}$ can both be further expressed as $\sigma_u^2 = \int_0^\infty S(\omega)\,\mathrm{d}\omega$ and $\sigma_{\dot{u}}^2 = \int_0^\infty \omega^2 S(\omega)\,\mathrm{d}\omega$, where $S(\omega)$ is the power spectrum of the wind-speed signal and ω the angular frequency $\omega = 2\pi f$, where f is the frequency. For a detailed description of the method, see Kristensen *et al.* (1991).

Kristensen *et al.* (1991) define the (normalized) gust as 'the wind speed deviation from the mean which, on average, is exceeded once during the reference period T', i.e. $N_x(g_x, T) = 1$. Hence their equation for the average normalized gust reads

$$< g_x >= \left[2\ln\left(\frac{T}{2\pi}\frac{\sigma_{\dot{u}}}{\sigma_u}\right)\right]^{1/2}. \tag{4}$$

Wichers Schreur and Geertsema (2008) leave the probability of a gust event open to the user and give the gust equation as

$$< g_x >= \left[2\ln\left(\frac{T}{\tau}\frac{1}{\sqrt{2\pi\ln(1/P)}}\right)\right]^{1/2}, \tag{5}$$

where τ is a characteristic time-scale of the spectrum:

$$\tau = \sqrt{2\pi}\frac{\sigma_u}{\sigma_{\dot{u}}}.$$

Note that, with $P = \mathrm{e}^{-1}$, Eq. (5) equates to Eq. (4). In this study, we will use $P = 0.5$, which corresponds to the theoretical median peak factor.

Beljaars (1987) estimates the normalized gust as

$$< g_x >= [2\ln(\nu T)]^{1/2} + \gamma[2\ln(\nu T)]^{-1/2}, \tag{6}$$

where $\gamma = 0.5772$ is Euler's constant and ν is the characteristic frequency representing the width of the spectrum:

$$\nu = \frac{1}{2\pi}\frac{\sigma_{\dot{u}}}{\sigma_u}.$$

The probabilistic approach above provides a theoretical estimate for the peak factor, which is a function of the sampling period length T and the variances of u and $\dot{u}$. The variances can be expressed in terms of the turbulence spectrum, for which different empirical formulations exist. In this study we will test four of them: Kaimal *et al.* (1972), Kaimal (1978), Højstrup (1982) and Højstrup *et al.* (1990). The first is the simplest one and assumes neutral conditions:

$$\frac{fS(f)}{u_*^2} = \frac{105f^+}{(1+33f^+)^{5/3}}, \tag{7}$$

where $f^+ = fz/U$ is the normalized frequency and z the height above the surface. All formulations are applicable to unstable conditions, but Højstrup (1982) cannot be used in stable conditions. In addition to the stability effects, the effect of the height above the surface on the peak factor is also described by the turbulence spectrum.

The spectrum equations mentioned above represent all scales of turbulent fluctuation. In practice, the measured wind velocity signal is always affected by the characteristics of the anemometer and the sampling strategy. Traditionally, for cup anemometers, these effects have been taken into account by introducing a filter function (e.g. Wichers Schreur and Geertsema, 2008):

$$|H(f)|^2 = \left(\frac{\sin(\pi f t_\mathrm{g})}{\pi f t_\mathrm{g}}\right)^2\left(\frac{\sin(\pi f\Delta t)}{\pi f\Delta t}\right)^2\frac{1}{1+(2\pi fl/U)^2}. \tag{8}$$

The three filter components, from left to right, are the moving average filter with a window length equal to the gust duration t_g, a sampling frequency $(1/\Delta t)$ filter and the anemometer response filter with a length constant l. With a sonic anemometer, for practical purposes only the first one really matters. The sampling frequency, here 20 Hz, is so high that it does not have any practical relevance for gusts. The dimensions of the sonic anemometer may become important at very low wind speeds, because the instrument cannot measure wind-speed fluctuations on scales smaller than twice the path length between the transducers, which is about 20 cm, i.e. $l \approx 0.4$ m. However, it is clearly smaller than a typical cup anemometer response length of about 1–3 m.

Using the filter function of Eq. (8) to filter the turbulence spectrum $S(f)$, Eq. (5) will become

$$< g_x >= \left[2\ln\left\{\frac{T}{\ln(1/P)}\left(\frac{\int_0^\infty f^2|H(f)|^2S(f)\,\mathrm{d}f}{(\int_0^\infty |H(f)|^2S(f)\,\mathrm{d}f}\right)^{1/2}\right\}\right]^{1/2}. \tag{9}$$

This equation now provides an estimate for the peak factor of an averaged/filtered signal. What we are actually interested in is the peak factor determined as the ratio of the maximum deviation $(U_\mathrm{max} - U)$ and the true standard deviation $(\sigma_{u,\mathrm{true}})$:

$$g_x = \frac{U_\mathrm{max}-U}{\sigma_{u,\mathrm{true}}}.$$

To calculate this, we must multiply Eq. (9) by the ratio of the standard deviations of the measured/filtered signal $(\sigma_{u,\mathrm{meas}})$ and the true/unfiltered signal $(\sigma_{u,\mathrm{true}})$, as in Wichers Schreur and Geertsema (2008):

$$r_\sigma = \frac{\sigma_{u,\mathrm{meas}}}{\sigma_{u,\mathrm{true}}} = \left(\frac{\int_0^\infty |H(f)|^2S(f)\,\mathrm{d}f}{\int_0^\infty S(f)\,\mathrm{d}f}\right)^{1/2}. \tag{10}$$

3. Data and methods

3.1. Measurements

Wind and turbulence observations used in this study were taken at the Danish National Test Station for Large Wind Turbines located at Høvsøre in northwest Denmark, about 1.7 km from the coast of the North Sea (Figure 1). A well-equipped meteorological mast is situated at the southern end of a row of five wind turbines, the nearest one about 120 m north of the tower. The mast is surrounded by flat, open grassland (Figure 1). The shoreline in the west and a bay in the south cause some heterogeneities in the surface conditions. There are some sparse bushes and a few small buildings in the east but their effect on surface conditions is small.

The mast is equipped with ultrasonic anemometers (Metek Scientific USA-1, sampling rate 20 Hz) on booms pointing towards the north at six heights: 10, 20, 40, 60, 80 and 100 m.

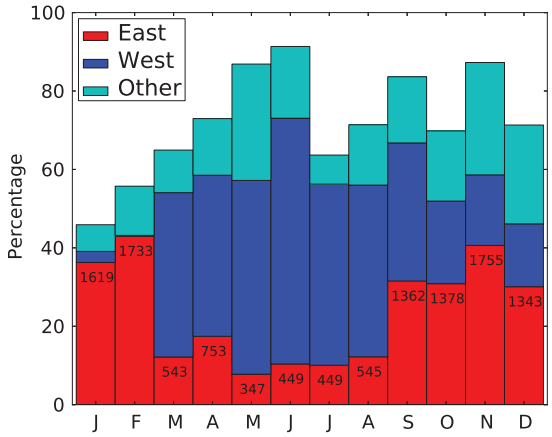

Figure 2. Coverage of full profiles (simultaneous data from levels 10, 40, 60 and 100 m) from the ultrasonic anemometers in each month in the east, west and combined south–north (= other) sectors, based on wind direction from the sonic anemometer at the 10 m level. The numbers at the top of the east sector columns show the actual number of full profiles for that sector.

The data were divided into east (50–140°) and west (225–315°) sectors (Figure 1) based on wind direction measured with the sonic anemometer at 10 m level. All of the analyses in this article are based on data from the east sector only, since it is the least disturbed by surface inhomogeneities and wake effects of the wind turbines and the structure of the mast itself. When data from other sectors is used, this is mentioned separately.

The study period covers the year 2010. The maximum possible number of 10 min data from one instrument is 52 560 during the whole year. Figure 2 shows the coverage of full profiles (i.e. those 10 min periods from which data were available from all levels simultaneously) in each month. The coverage does not reach 100%, because we take into account only full profiles, i.e. simultaneous data from all levels. Because data from the sonic anemometer at the 20 m level was missing at the end of the year (October–December) and there were some discrepancies in the data from the 80 m level after 1 July 2010, we excluded these levels from analysis of the mean conditions (and from Figure 2). In the case studies of section 4.2, however, these are included, i.e. the 20 m level before October and 80 m level where applicable.

3.2. *Data processing*

First, the high-frequency (20 Hz) data from ultrasonic anemometers were checked for unphysical values and spikes. The validity ranges were $(-50, +50)$ m s^{-1} for the longitudinal and latitudinal wind velocity components, $(-10, +10)$ m s^{-1} for the vertical component and $(-20, +50)$ °C for the sonic temperature. For the vertical velocity, Vickers and Mahrt (1997) used 5 m s^{-1} criteria, but they found after further inspection that some of the flagged values were physical. The spikes were removed using the following criteria: any measured value of each wind velocity component (temperature) that exceeds 4.5 (5.0) times the standard deviation of that velocity component (temperature) in a window of 15 values was labelled as a spike. This procedure was repeated three times with an increasing threshold of standard deviation in steps of +0.1 for the wind velocity components and +0.5 for the temperature.

The unphysical values, the detected spikes and the missing values were then removed from the time series. Mean variables and gusts were calculated only if an averaging period consisted of at least 99% good quality data. After the quality checks, we used the ECPACK library package (version 2.5.23) described by Van Dijk *et al.* (2004) to process the data further.

Table 1. Stability groups and their criteria in terms of the Obukhov length (Gryning *et al.*, 2007).

Stability	Range in L
Very unstable (vu)	$-100 < L \leq -50$
Unstable (u)	$-200 < L \leq -100$
Near-neutral, unstable (nu)	$-500 < L \leq -200$
Neutral (n)	$\lvert L\rvert \geq 500$
Near-neutral, stable (ns)	$200 \leq L < 500$
Stable (s)	$50 \leq L < 200$
Very stable (vs)	$10 \leq L < 50$

To obtain the wind velocity components, the coordinate axes were transformed using a planar fit method (Wilczak *et al.*, 2001). The planar fit angles were calculated using data from both easterly and westerly sectors (Figure 1). We used the mean wind speed range 2–12 m s^{-1}, because the uncertainty in the measurements becomes high at low wind speeds. The angles were determined using all 10 min means from easterly and westerly sectors in 2010; at the 80 m level, we used six-month periods instead, since the instrument was changed at the beginning of July. In addition to the planar fit coordinate rotation, the u and v components were rotated such that they were aligned with and perpendicular to the mean wind ($\bar{v} = 0$, where the overbar denotes the mean over a 10 min period).

The above calculations were also performed with 30 and 60 min averaging periods. The first was used for flux calculations and the second to investigate the effects of different time-scales on gust factor. After the coordinate transformation, the sonic temperature was corrected for cross-wind effects (Liu *et al.*, 2001) and a linear trend was removed from the 30 and 60 min time series. We did not remove the trend from the 10 min periods, because then we might lose information about coherent structures that can have time-scales up to a few minutes (e.g. Thomas and Foken, 2005) and can partly be responsible for the formation of peak gusts, especially in a convective boundary layer. The trend in a 30 or 60 min period may be related to longer time-scales like the diurnal variation typical for summertime, which cannot be described with a statistical gust model.

A 30 min averaging period was used to calculate the friction velocity and the Obukhov length. The friction velocity was calculated as $u_* = (\overline{u'w'}^2 + \overline{v'w'}^2)^{1/4}$ and the Obukhov length as $L = -u_*^3 \left(\kappa(g/\bar{T}_S)\overline{w'T'_S}\right)^{-1}$, where the prime refers to the fluctuating part of a variable, $\kappa = 0.4$ is the von Kármán constant, g is the acceleration due to gravity and T_S the temperature from a sonic anemometer. The data were divided into stability groups based on the Obukhov length at 10 m (Table 1).

3.3. *Calculation of gusts*

Sonic anemometers provide wind speed measurements as a three-component vector. In this study, the wind gust speed is calculated as

$$U_{\max} = \max(\sqrt{u_m^2 + v_m^2}), \tag{11}$$

where the subscript m refers to a moving average with window length equal to the gust duration t_g. The effect of different gust durations, from 1 up to 30 s, on gusts during a 10 and 60 min period will be studied in section 4.1.3. To ensure stationarity in the data, the 60 min periods that were used in gust time-scale analysis were chosen such that all six 10 min periods were also included in the 10 min dataset (i.e. good data quality, full profiles, east sector). For the standard deviation of wind speed, we use the standard deviation of the along-wind component only. This choice is based on the result that the gust wind speed $U_{\max}$ is very close to the along-wind velocity u_m, as will be shown in section 4.1.1.

Table 2. Cases with strong wind conditions. The time is GMT + 1.

CASE	Date	Time	Length (h)
C1	10 January	0500–1100	6
C2	10–11 January	1900–0100	6
C3	11 January	0400–0900	5
C4	16 January	1200–1800	6
C5	7 May	0300–0700	4
C6	7 May	1100–1800	7
C7	7 September	1100–1700	5
C8	7 September	1730–2030	3
C9	7–8 September	2200–0600	8
C10	8 September	0630–0900	2.5
C11	8 September	1100–1400	3
C12	2 October	0200–1200	10
C13	3 October	1030–1830	8
C14	29 November	0400–1000	6
C15	29 November	1400–1900	5

3.4. *Case studies*

The vertical structure of gust events will be studied in 15 example cases with strong wind conditions. The cases are listed in Table 2. From the easterly sector, there were 38 days when the mean wind speed at 100 m exceeded 13 m s^{-1}. We arranged these dates by the number of 10 min periods satisfying the wind speed (>13 m s^{-1} at 100 m level) and direction (50–140° at 10 m level) criteria and selected nine days that had the highest number for further analysis. Based on stability and stationarity, we selected from each day one or more cases of several hours duration, which then composed the 15 cases of Table 2. Cases C1 and C3 represent winter-time stable conditions, case C9 nocturnal stable conditions and cases C7 and C11 unstable conditions. All of them have stationary wind conditions. As a contrast, situations with an increasing (C4 and C10) and decreasing (C6, C8 and C15) trend were also chosen. The rest of the cases, C2, C5 C12, C13 and C14, represent near-neutral or slightly stable stationary conditions.

4. Results

This section has two parts. The first, section 4.1, will include analysis based on the whole dataset from the eastern sector and the second, section 4.2, only on the cases in Table 2.

4.1. *Sensitivity of gust profiles to stability and gust time-scales*

4.1.1. *Gust velocity components*

The relative contributions of u and v to the maximum gust at 10 m level are shown in Figure 3. The cross-wind component during the maximum gust is evenly distributed around zero. Its median is slightly positive, about 1.2% of the wind gust speed. The magnitude of the cross-wind component is generally less than 30% of the maximum gust and the magnitude of the along-wind component during the maximum gust is very close to that of the gust wind speed.

In addition, the mean vertical velocity during the maximum and minimum gust (w_{max}, w_{min}) was calculated. The minimum gust is defined as in Eq. (11), but using a 3 s minimum instead of a maximum. If there were several equally low minima, we considered only the first one. Figure 4 shows the mean vertical wind component during maximum and minimum gust as a median of all profiles. w_{max} is mainly negative and its magnitude has a maximum at around 40–60 m (Figure 4), while w_{min} is mainly positive. These vertical wind velocity results during maximum and minimum gusts suggest that gusts are strongly related to up- and downdraughts in the boundary layer.

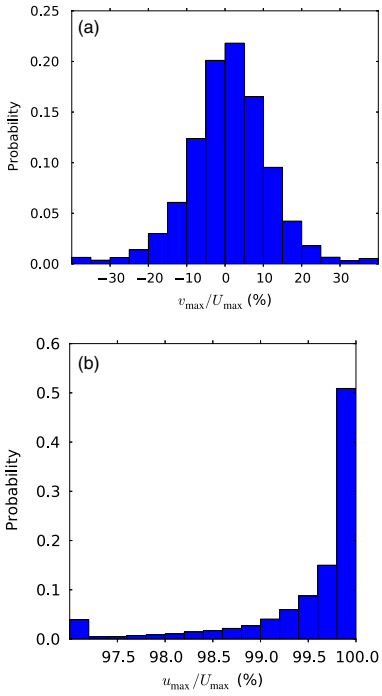

Figure 3. Distributions of mean (a) cross-wind and (b) along-wind velocity components, averaged over the duration of the maximum gust (t_g = 3 s, T = 10 min) at 10 m level.

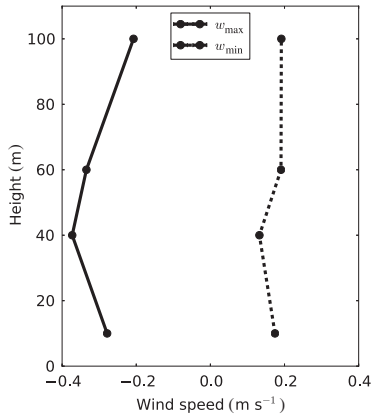

Figure 4. Median profile of the vertical wind velocity component during maximum (w_{max}) and minimum (w_{min}) gusts (t_g = 3 s).

4.1.2. *Effects of stability and height on the gust factor*

The gust factor is known to be a function of stability and height above the surface (e.g. Suomi *et al.*, 2013). The strongest mean wind and wind gust speeds are observed in near-neutral conditions and the weakest ones in very stable and very unstable conditions (not shown). However, the gust factors are lower than average only in stable conditions, whereas in unstable conditions the gust factors are of similar magnitude to those in near-neutral conditions. The median gust factor profiles in Figure 5 shows that this feature can be seen at all levels within the lowest 100 m of the atmosphere. However, there are also differences in the profiles. In stable (vs/s) conditions, the gust factor decreases with height more than in neutral or unstable conditions. As shown in Table 3, the difference in the median gust factors between 10 and 100 m levels is

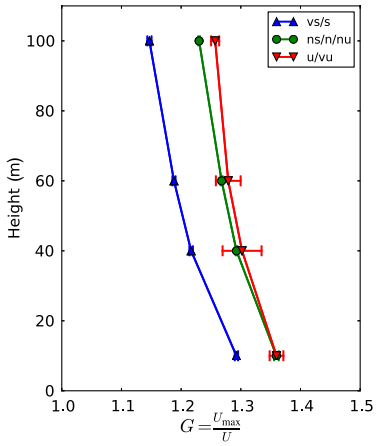

Figure 5. Median gust factor profiles for three combined stability groups that represent stable (vs, s), (near-) neutral (ns, n, nu) and unstable (vu, u) conditions. Error bars represent the standard error.

about −0.15 in combined stable (vs/s) conditions, whereas in combined unstable (vu/u) conditions it is only about −0.10.

Eq. (1) shows that the gust factor can be expressed in terms of a peak factor and turbulence intensity. We examined their relative effect on the gust factor profile by keeping one of them constant with height and allowed the other to vary with height: $G = 1 + g_x I_{\text{constant}}$ or $G = 1 + g_{x,\text{constant}} I$, where the constant refers to a median over all heights. The results are shown in Table 3. Turbulence intensity is the primary factor in determining the height dependence of a gust factor. The height dependence of the peak factor has minor influence, but it depends strongly on stability conditions.

4.1.3. *Gust time-scales*

The load that gusts cause on structures like wind turbines depends, besides on the strength of a gust, also on gust duration. In this section, we will compare gusts with different durations during a 10 and 60 min sampling period and compare them with the theoretical estimates calculated using the methodology described in section 2.

Figure 6 shows the effect of gust duration on the wind gust speed and gust factor. In panels (a) and (b), $U_{\max}$ is normalized by the 1 s maximum wind gust speed $U_{\max,1s}$. The ratio $U_{\max}/U_{\max,1s}$ decreases with increasing gust duration by about 5% at the 10 m level and about 3% at the 100 m level, when the gust duration changes from 1 to 5 s. The main reason for the different decrease rate of the ratio between the levels is due to the higher $U_{\max,1s}$ at 100 m than at 10 m. The sampling period length does not affect this result: changes within 10 and 60 min periods are very similar. Instead, atmospheric stability does affect the results. The decrease rate of the ratio is largest in stable and near-neutral conditions at the 10 m level and smallest in stable conditions at the 100 m level (Figure 6(b)). The difference between the 10 and 100 m level curves is smallest in unstable and largest in stable conditions.

The median gust factors in Figure 6(c) are, on average, higher during the 60 min sampling period than during the 10 min period. At both levels, 10 and 100 m, the gust factors decrease with increasing gust duration. The decrease is strongest at short durations (from 1 to 5 s) and it levels out at higher durations. The difference between the 10 and 100 m level curves is smaller with the 10 min averaging period than with the 60 min period. In both cases, the difference between the levels decreases with increasing gust duration.

As already shown in section 4.1.2, stability affects the gust factor. G is highest in unstable conditions and lowest in stable ones and the difference in G between 10 and 100 m levels is smallest in unstable conditions and largest in stable ones. As shown in Figure 6(d), the decrease rate of the gust factor is similar in all stability conditions at 100 m level, but at 10 m level the rate varies with stability. In all cases, the decrease rate of G with increasing gust duration is larger at 10 m than at 100 m level, causing the difference between the 10 and 100 m curves to decrease with increasing gust duration. The decrease is strongest for stable conditions and smallest for unstable ones.

The gust duration also affects the peak factor, but not the turbulence intensity (Eq. (1)). Figures 7 and 8 show the observed median peak factors as a function of gust duration. In addition, theoretical estimates for the peak factors are presented. They were calculated using Eqs (8)–(10) and two different formulations for the empirical spectra, from Kaimal *et al.* (1972) and Højstrup *et al.* (1990).

Like the gust factors, the observed median peak factors are also higher and the difference between the 10 and 100 m levels is larger during the 60 min period than during the 10 min period (Figure 7). The observed difference between the levels also decreases with increasing gust duration. In near-neutral conditions, shown in Figure 8, the curves of the observed peak factor at 10 and 100 m levels follow closely the curves calculated from the whole dataset (the grey-shaded area). In stable conditions, the curves are also very similar to the curves of the whole data: the vertical difference is only a little larger and the decrease of g_x with increasing gust duration is slightly stronger than in neutral conditions. In unstable conditions, peak factors do not depend on height within the 100 m deep layer, as already found in section 4.1.2. Moreover, the decrease rate of the peak factor with increasing gust duration is smaller in unstable than in neutral or stable conditions.

The theoretical estimates for the peak factor in Figures 7 and 8 were calculated using Eqs (8)–(10). For the empirical spectra, we tested four different formulations: Kaimal *et al.* (1972), Kaimal (1978), Højstrup (1982) and Højstrup *et al.* (1990). We validated the results for both the shape of the curve and its separation from the observed curve. Two of the formulations outperformed the others. With the Kaimal *et al.* (1972) spectrum, the shape of the theoretical curve was closest to the observed one at the 100 m level, whereas at the 10 m level the closest form of the curve was provided by the Højstrup *et al.* (1990) spectrum. Contrary to observations, the difference between the 10 and 100 m curves with all empirical spectra increased with increasing gust duration. With the Højstrup *et al.* (1990) spectrum, the peak factor decreases with height, but only by about 0.04 units from 10 to 100 m level, whereas the observed decrease is about 0.20 units in the whole dataset. With the other spectra, the total change from 10 to 100 m

Table 3. Differences between 100 and 10 m levels in the median gust factor (first column), median peak factor (second column) and median turbulence intensity (fifth column) under different stability conditions and for all data. The relative contributions of the peak factor and the turbulence intensity to the vertical difference in the median gust factor (columns 3 and 6) were calculated, keeping either the turbulence intensity or the peak factor constant with height. As a constant, we used the median over all heights (columns 4 and 7).

	$G_{100m} - G_{10m}$	$g_{x,100m} - g_{x,10m}$	$(G_{100m} - G_{10m})\|_{I=\widetilde{I}}$ (%)	$\widetilde{I}$	$I_{100m} - I_{10m}$	$(G_{100m} - G_{10m})\|_{g_x=\widetilde{g_x}}$ (%)	$\widetilde{g_x}$
vs/s	−0.15	−0.27	−0.022 (15.3)	0.082	−0.047	−0.119 (81.7)	2.55
ns/n/nu	−0.13	−0.17	−0.019 (14.6)	0.112	−0.044	−0.110 (85.0)	2.52
u/vu	−0.10	0.01	0.001 (−1.0)	0.120	−0.040	−0.100 (97.0)	2.50
All	−0.13	−0.20	−0.021 (15.7)	0.102	−0.042	−0.107 (82.0)	2.53

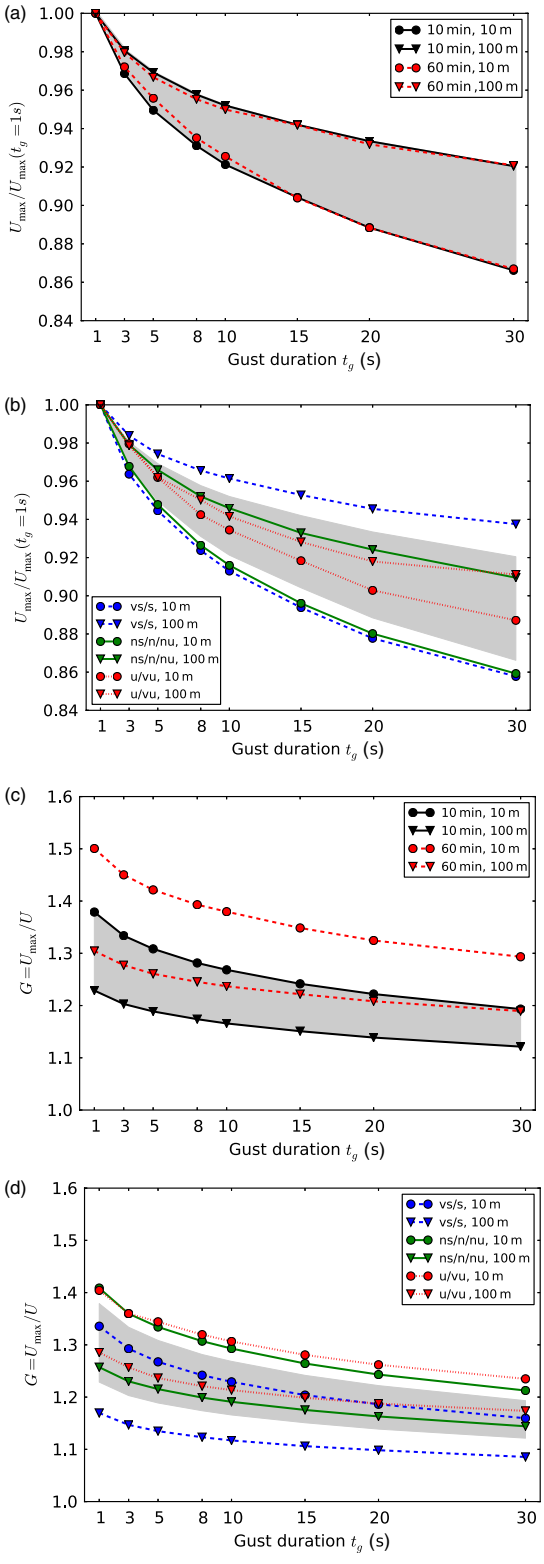

Figure 6. Medians of U_{max} (normalized by U_{max} with t_g = 1 s; panels (a) and (b)) and G (panels (c) and (d)) as a function of gust duration (t_g) at 10 and 100 m level with T = (10,60 min), using all data ((a) and (c)). In (b) and (d) the results are shown for different stability groups defined in Table 1; The grey shaded regions highlight the difference between the 10 and 100 m level curves including all data with 10 min averaging period.

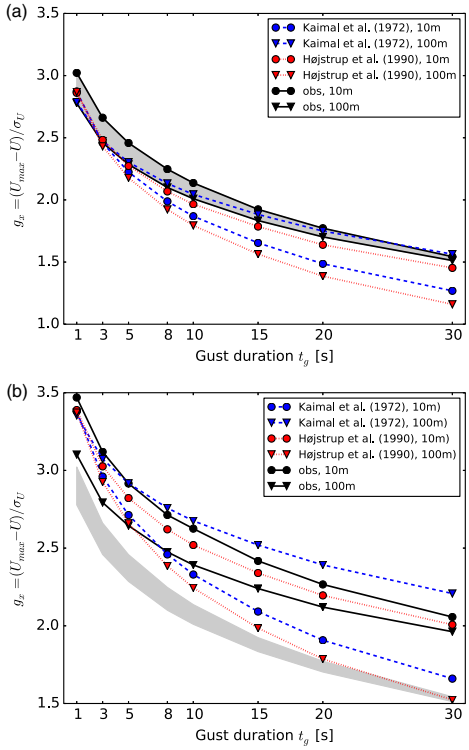

Figure 7. Median peak factor (g_x) in the east sector as a function of gust duration (t_g) with (a) T = 10 min and (b) T = 60 min at 10 and 100 m levels. The grey-shaded area represents the difference between 10 and 100 m levels with T = 10 min. The dashed (blue in the online article) and dotted (red in the online article) curves represent theoretical peak factor estimates using Kaimal *et al.* (1972) and Højstrup *et al.* (1990) spectra.

level is increasing, because the peak factor first increases with height from 10 to 40 m level, after which it starts to decrease slowly.

Both theoretical methods, one with the Kaimal *et al.* (1972) and the other with the Højstrup *et al.* (1990) spectrum, underestimated the peak factors at 10 m level with both 10 and 60 min sampling period lengths (Figure 7). The underestimation was largest with the Kaimal *et al.* (1972) spectrum. At 100 m level, the Kaimal *et al.* (1972) spectrum provided good results with T = 10 min, but overestimated the peak factor during the 60 min sampling period, even though the shape of the g_x curve was also realistic with T = 60 min.

4.1.4. *Application of peak factor estimates at other sites*

Suomi *et al.* (2013) compared gust factor profiles from two weather masts, Isosaari and Loviisa, located on the southern coast of Finland. The sites represented different surface roughness conditions, one marine (Isosaari) and the other inland (Loviisa). They both had a sector with similar surface conditions: some land in the direct vicinity of the mast and a coastline further away at about 500 m–1 km from the mast. Loviisa weather mast is surrounded by a forest, whereas at Isosaari there are mainly sparse bushes and small trees in the vicinity of the tower. Despite the orographically similar sector, direct comparison of the observations from the masts was, however, difficult because archived wind measurements consisted only of the wind gust speed and the mean wind speed and not the raw high-frequency data. Unfortunately, the gust time-scales were different: [t_g, T] = [1 s, 1 h] for Loviisa and [t_g, T] = [3 s, 10 min] for Isosaari. Figure 9 shows the profiles of the median gust factor of all data from orographically similar southwest sectors from

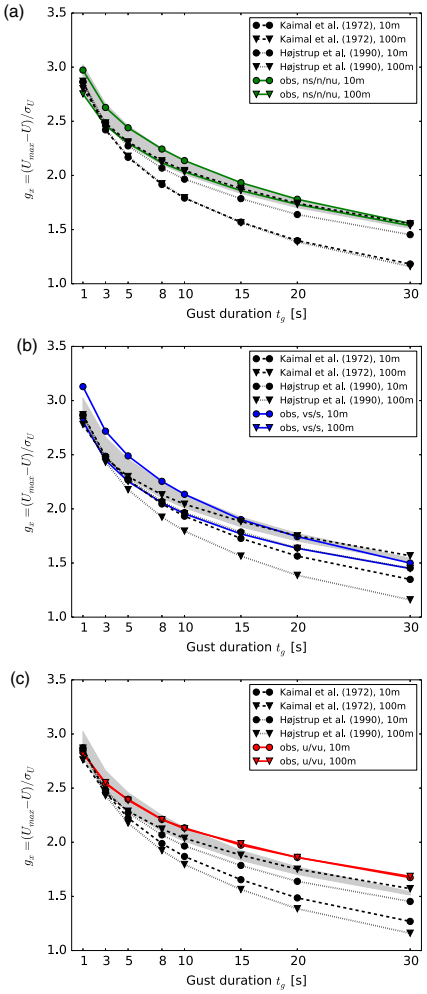

Figure 8. Observed median peak factor (g_x) as a function of gust duration (t_g) in (a) near-neutral (ns/n/nu), (b) stable (vs/s) and (c) unstable (u/vu) conditions with T = 10 min at 10 and 100 m levels. The grey-shaded area represents the observed median peak factor difference between 10 and 100 m levels, as shown in Figure 7. The black lines represent theoretical peak factor estimates, as in Figure 7, but here for different stability conditions.

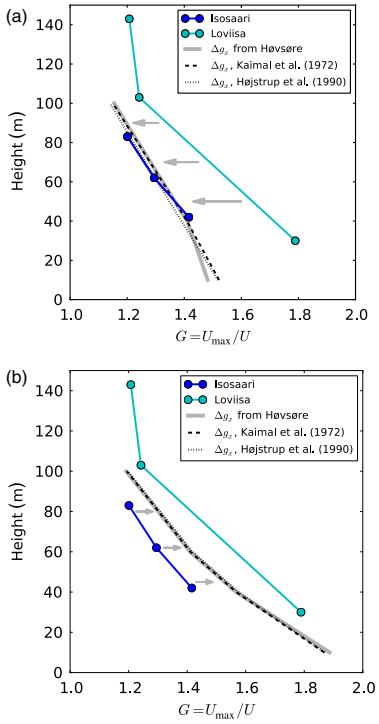

Figure 9. Observed median gust factor profiles (incl. all stability conditions) from two weather masts, Isosaari and Loviisa, located on the southern coast of Finland. Profiles represent gusts with different time-scales: Isosaari t_g = 3 s, T = 10 min; Loviisa t_g = 1 s, T = 1 h, as in Suomi *et al.* (2013). The thick grey, dashed and dotted profiles represent the potential gust factor profiles that could be attained if the sampling were the same for the measurements from both masts i.e. [t_g, T] = [3 s, 10 min] in panel (a) and [t_g, T] = [1 s, 1 h] in panel (b); see the detailed explanations for the curves in the text of section 4.1.4.

both masts, Isosaari and Loviisa. The thick grey curves represent the G to which the original gust factor profile would change if the changes in peak factor profile were similar to those observed at Høvsøre and the turbulence intensity is from the original data from both masts. The new estimated gust factor is then

$$G_{\text{new}} = G_{\text{local}} \pm |\Delta g_{x,\text{Høvsøre}}| I_{\text{local}}, \qquad (12)$$

where I_{local} is the turbulence intensity measured at Isosaari or Loviisa, which is interpolated and extrapolated to the heights of Høvsøre. $\Delta g_{x,\text{Høvsøre}}$ is the difference in peak factor between time-scales g_x(1 s, 1 h) and g_x(3 s, 10 min), as measured between 10 and 100 m at Høvsøre. In Figure 9(a), we see that, using the turbulence intensity from Loviisa, we would reach the profile of Isosaari with the peak factor difference from Høvsøre. When the turbulence intensity is taken from Isosaari, as was done in Figure 9(b), we will not reach the observed gust factor profile from Loviisa. This means that the differences in G between the Finnish weather mast sites cannot be fully explained by the different time-scales but there are also other factors generating differences, e.g. the surface roughness conditions.

For comparison, the dashed and dotted lines in Figure 9 represent the change between time-scales using theoretical peak factor differences instead of $|\Delta g_{x,\text{Høvsøre}}|$ in Eq. (12). With the Højstrup *et al.* (1990) spectrum, we assumed neutral conditions ($L = -10^5$ m, z_i = 1000.0 m). The differences between these profiles, the thick grey one calculated using Eq. (12) and the dashed and dotted ones using theoretical peak factor differences, are very small. This means that the theoretical peak factor model can be applied to convert gust durations between 1 and 3 s and sampling periods between 10 min and 1 h. The choice of model parameters like the type of spectrum becomes meaningful only with longer gust durations.

4.1.5. *Wind gust speed and the mean wind speed at 10 and 100 m levels*

Figure 10 shows the spectra for the mean wind and wind gust speed including all 10 min data (all sectors) from 2010. Results are shown for both 10 and 100 m levels. At 10 m level, there is a clear difference in energy between U and $U_{\max}$ at all scales. At 100 m level, the wind gust speed is only slightly larger and the mean wind speed has almost the same amount of energy. Moreover, the spectrum of the mean wind speed at the 100 m level coincides even better with the spectrum of wind gust speeds observed at the 10 m level. On scales from a few hours to half a day, $U_{\max}$ at 10 m level is less than U at 100 m level, but on a diurnal scale $U_{\max,10\text{m}}$ exceeds $U_{100\text{m}}$.

The distributions of the differences of these two variables are shown in Figure 10(b) separately for different stability conditions. The results were calculated using data from the east sector only. $U_{\max,10\text{m}}$ is clearly higher than $U_{100\text{m}}$ in unstable conditions, which is in line with the diurnal peak in the $U_{\max,10\text{m}}$ spectrum. Under neutral conditions, $U_{\max,10\text{m}}$ is on average slightly higher than $U_{100\text{m}}$, even though their difference is quite evenly distributed

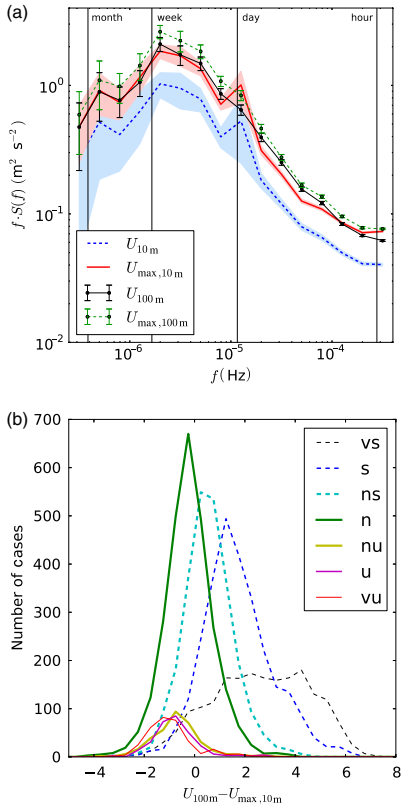

Figure 10. (a) Spectra of gust wind speed (3 s maximum gust) and mean wind speed (10 min mean) for 10 and 100 m levels. Data cover the whole of year 2010, with all sectors included. For the 10 m level, the standard error of the mean is given as a shaded area around the curves; for the 100 m level, errors are shown as error bars. (b) Difference between 100 m mean wind speed and 10 m wind gust speed under different stability conditions. Stability conditions are defined in Table 1. The data cover only the east sector.

around zero. In stable conditions, the mean wind speed at 100 m level is clearly higher than the wind gust speed at 10 m level.

4.1.6. *Summary of the results on gust profiles*

To summarize this section, we found that both the gust factor and the peak factor decrease with increasing gust duration and increase with increasing sampling period length. Stability has an effect on the decrease rate of the median gust factor, but only near the surface. At 100 m level, the decrease rate is similar in all stability conditions. The decrease at 10 m level is stronger than at 100 m level, which leads to a steeper gust factor profile with increasing gust duration. For the observed peak factor, there is some decrease with height, but only in neutral and stable conditions. In unstable conditions, the peak factors are of similar magnitude at all levels. Furthermore, in unstable conditions, the decrease rate of a peak factor as a function of gust duration is clearly less than in neutral and stable conditions. Theoretical peak factor models were unable to reproduce the height dependence of the median peak factors. The rate at which the peak factor decreases with increasing gust duration was quite realistic for theoretical gust models in stable and neutral conditions, but it was overestimated in unstable conditions. In addition, it depended greatly on the choice of empirical spectrum. However, none of the empirical spectra tested in the model performed well at both heights, i.e. at 10 and 100 m. Despite these inconsistencies in the theoretical peak factor estimates, the method performs well in estimating the differences between gust durations of 1 and 3 s with sampling period lengths of 10 min and 1 h. There was a peak on the diurnal scale in the spectrum of the 10 m level wind gust speed calculated over the whole dataset (including all sectors). It peaked over the mean wind speed at 100 m level. Comparing the distributions of $U_{max,10m}$ and U_{100m}, $U_{max,10m}$ was actually higher than U_{100m} in unstable conditions and vice versa for stable conditions. This result is in line with the idea of the profile method by Brasseur (2001), in which near-surface gusts result from eddies bringing fast-moving air parcels–and hence momentum–down towards the surface.

4.2. *Case studies on the vertical structure of individual gust events*

In this section, we will study, using a selection of strong wind cases presented in section 3.4, the timing of the wind velocity maximum at each measurement level relative to the time of the 10 or 100 m level maximum (3 s) gust. This could be done just by comparing the times of the maximum gusts at each level. However, it is not clear that the same eddy, intrusion or phenomenon that generates the maximum gust at one level also causes the maximum at the other levels. In fact, the average differences between the times of maxima at 10 and 100 m levels can be up to several minutes (not shown). To understand the structure of the wind flow in the context of maximum gusts and to study the interaction of maxima at different levels, we will use the following methodology.

- A strong wind case is selected: the case includes several 10 min periods (section 3.4).
- For each of the 10 min periods, the 10 and 100 m level maximum gust is detected (using a 3 s moving average window).
- Then, we consider only a period of ±1 min from the time of the maximum gust. If the gust occurred during the first or the last minute of the 10 min period, we also allowed wind velocity data from outside the 10 min period.
- At each measurement level of the mast, the highest 120 values (which correspond to 6 s with $f = 20$ Hz) of the horizontal wind velocity ($\sqrt{u^2+v^2}$) within the 2 min period are given a value 1, all other data points get a value 0. The choice of 120 values is somewhat arbitrary; other numbers of values can also be applied.
- Next, we calculate the ensemble mean over all 2 min periods, which gives the probability of a value 1 at each point in the 2 min time–height cross-section.
- Finally, it is possible to calculate from the resulting time–height average fields statistics like the median location, which is the position on the time axis where half of the maxima at that level occur before it and the other half after it. Similarly, it is possible to determine the locations in the time axis of the 25th and 75th percentiles (t_{P25} and t_{P75}) and the probability of maxima before the reference gust (P_0). It is noteworthy that these statistics do not include any effects due to averaging.

Following this approach, all 15 cases with strong easterly wind conditions presented in section 3.4 were analyzed, with respect to both 10 and 100 m level maximum gusts. To illustrate the results, we selected cases from two different periods. The first one is 10–11 January, which represents mainly stable winter conditions, and the second is 7–8 September, which includes a diurnal variation in the late summer. From the winter period, shown in Figure 11, we selected case C3. There the mean wind speed at 100 m level is higher than the wind gust speed at 10 m level. Gust factors are in general low, $G \approx 1.30$, and their vertical differences fairly small, $G_{100m} - G_{10m} \approx -0.10$. To compare this long-lasting stable case with nocturnal stable conditions, case C9 was selected from 7–8 September (Figure 12). During C9, the near-surface gust factor is higher than in C3 ($G \approx 1.37$) and it decreases more with height ($G_{100m} - G_{10m} \approx -0.19$). The mean wind speed at 100 m level is higher than the wind gust speed at

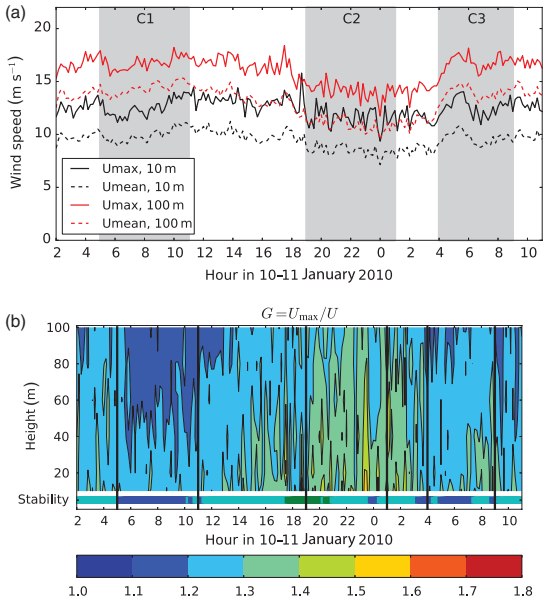

Figure 11. (a) Time series of U_{max} and U at 10 and 100 m levels on 10–11 January. The shaded areas show the cases included in the period. (b) Cross-section of gust factor. The colours below the cross-section refer to stability group: blue = s, light blue = ns and green = n.

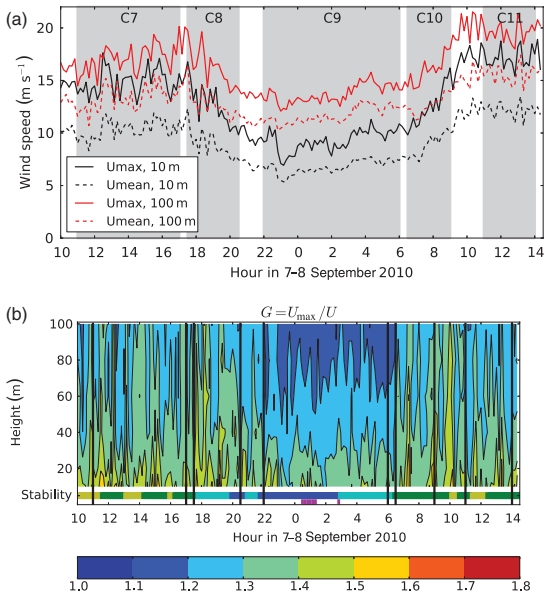

Figure 12. Same as Figure 11, but for 7–8 September. The colours designating the stability groups are yellow = nu, green = n, light blue = ns and blue = s. The pink colour below the stability group indicates rain.

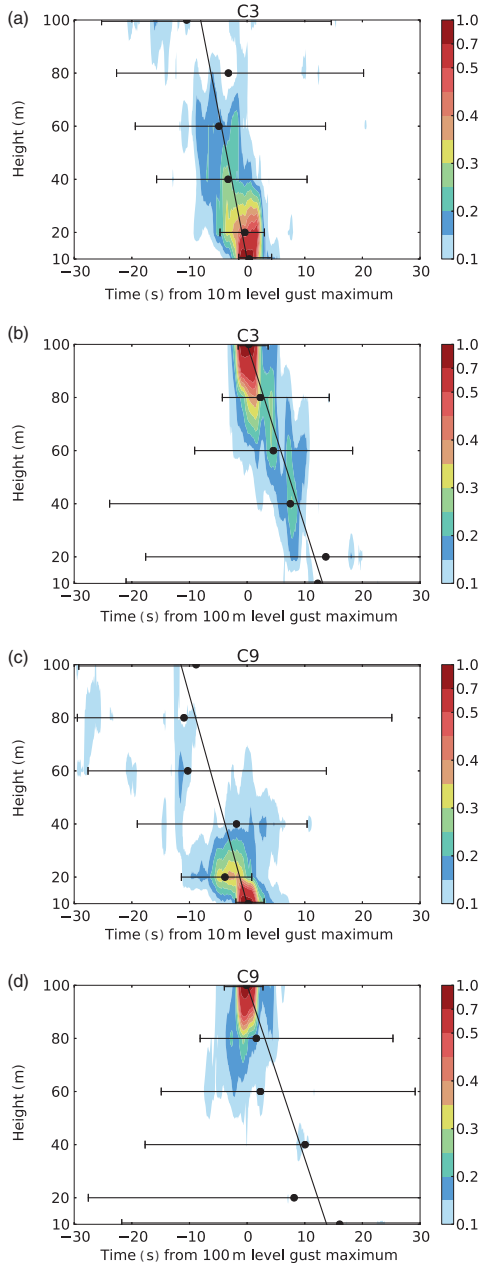

Figure 13. Cross-sections of the probability for a maximum in a time interval ±1 min around the reference gust (only ±30 s is shown) in cases C3 (panels (a) and (b)) and C9 (panels (c) and (d)). Panels (a) and (c) show the results for the 10 m level reference gust and panels (b) and (d) for the 100 m level reference gust. The slanting lines represent a linear fit introduced to the median locations (dots), with error bars showing the interval between the 25th and 75th percentiles. To get rid of the high-frequency structures in these probability fields, we calculated a moving average with a 1 s (20 values) window along the time axis. This was done only for plotting purposes; all statistics were calculated from the high-resolution (20 Hz) results.

10 m level, as in C3 (Figures 11 and 12). From the period 7–8 September, we also selected two other cases to be demonstrated. They are cases C8, with a decreasing trend in wind speed, and C11, which represents an unstable daytime case (Figure 12).

Figures 13 and 14 show the probability of a maximum in the sequence of ±30 s around the reference gust (calculated as a mean of values 1 and 0 at each height and time) in the four example cases C3, C9, C8 and C11. At the top of the cross-sections, the locations of the medians in the time axis are plotted for each height, together with the error bars representing the time difference between the 75th and 25th percentiles. In addition, the linear fits to the medians are shown.

In the long-lasting stable case C3 there is a clear signal of maxima organized along the linear fit applied to the median locations. The 10 m level maximum gust can be traced up to about 60 m height and the 100 m maximum down to 40 m level. The same cannot be seen in the case of nocturnal stable case C9, where both the 10 and 100 m maximum gusts are associated with

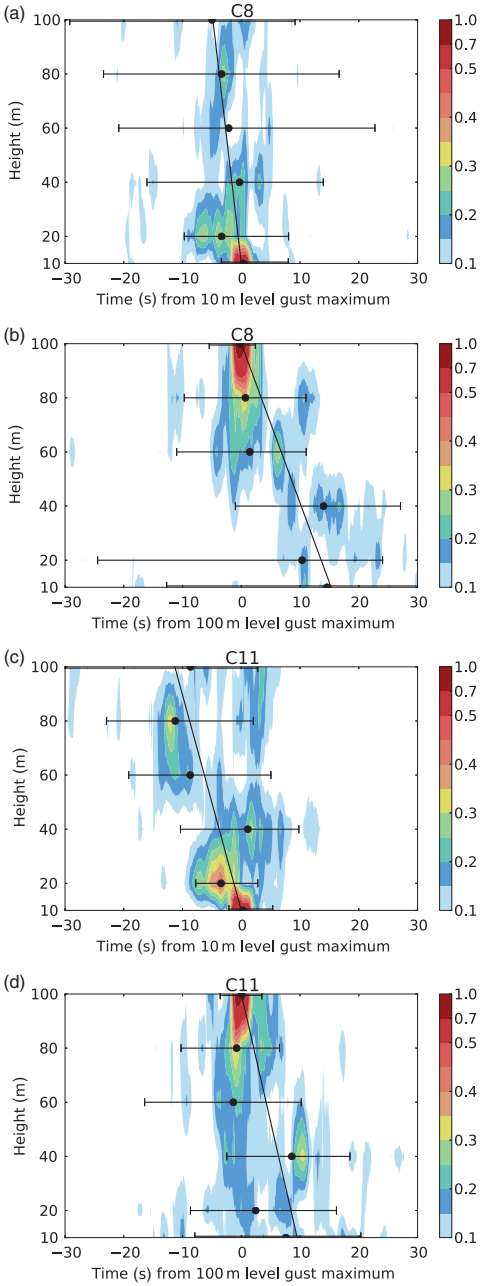

Figure 14. Same as Figure 13, but for cases C8 and C11.

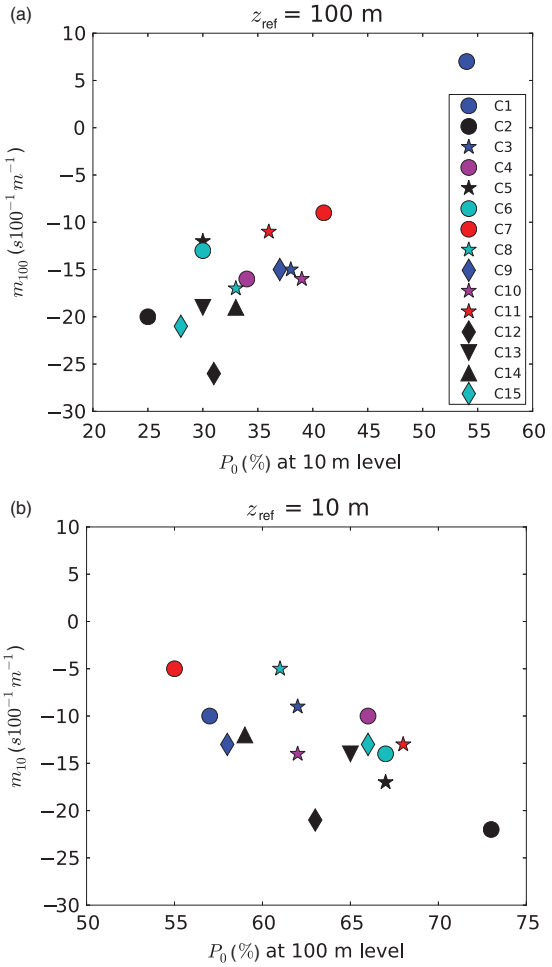

Figure 15. Slope in the timing of maxima relative to (a) 100 m and (b) 10 m level reference maximum gust (vertical axis) as a function of the probability of maxima observed before the reference gust at the most distant level from the reference, i.e. at 10 m level for the 100 m maximum gust and vice versa (horizontal axis). Colours refer to different case categories: blue = stable, red = unstable, light blue = decreasing trend, purple = increasing trend and black = stationary neutral/near-neutral stable cases.

clear maxima only at the nearest observation level. Also, the error bars in case C9 spread over a larger range than in case C3.

In cases C8 and C11 (Figure 14), there is less variation in the locations of maxima than in cases C3 and C9. In case C8, where the wind speed was decelerating, the maxima are vertically aligned, especially with the 10 m level reference gust. For the 100 m level gust, the linear fit is not a good approximation. The median locations down to 60 m level are very close to each other in time, but below this they are much further downwind. At 20 and 10 m, the error bars also spread to a wider range than above.

In unstable case C11, the time differences between the 75th and 25th percentiles were the smallest of all cases. Also, the median locations in this case are not organized exactly on the linear fit. With the 10 m reference gust, the median locations are placed in a fairly linear manner except at the 40 m height. The same level is also separated from the profile in the case of the 100 m reference gust maximum. This is seen as scattered areas of high probability, which are not connected to each other. Gusts are typically related to eddies that have a full three-dimensional structure. With a single instrumented mast, we can observe only a vertical cross-section of an eddy. Therefore, it is not possible to investigate with this dataset the reasons for the median location at the 40 m level being ahead of the other maxima.

Similar analyses were performed for each of the 15 cases of Table 2. The median location, 25th and 75th percentiles and percentage of maxima at each level before the time of the reference gust were calculated. The percentage of maxima before the reference gust is denoted as P_0, to distinguish it from the probability P in peak factor theory. In addition, a linear least-squares fit was applied to the median locations over all heights, as in Figures 13 and 14. The slope of the fit is denoted as $m_{z_{ref}} = \Delta t/\Delta z$, where z_{ref} is the reference height, either 10 or 100 m, and Δt is the time difference along the slope in layer Δz. These results and some other features of the cases are shown in the Appendix in Tables A1–A3; here we will discuss only the main features of the results.

As in the example cases above, in most of the cases a 10 m level maximum gust was preceded by a local maximum at higher levels and vice versa: local maxima were typically observed at lower levels after the 100 m level maximum gust. The slope m_{10m} varied from -22 to $-5\,s\,100^{-1}\,m^{-1}$ and m_{100m} from -26 to $-9\,s\,100^{-1}\,m^{-1}$. These slopes were plotted against the percentage of maxima before the reference gust at the most distant level from the reference, i.e. at 100 m level for 10 m maximum gust and vice versa. The results are shown in Figure 15. The portion of maxima before the 10 m level maximum gust varied from 55–73% and that before the 100 m level maximum gust from 25–41%, except in case C1, where $P_0 = 54\%$. Roughly, there is a linear dependence between the two. Some of the scatter in the plots is due to the linear fit applied to the median locations, which does not directly represent the time lag between the 100 and 10 m level maxima as P_0 does. With the 100 m reference gust, the most slanted slopes and the smallest probabilities P_0 are in stationary, near-neutral cases C2 and C12–C14 (black markers in Figure 15) and the most vertical slopes and highest probabilities in stable and unstable cases C1, C3, C7, C9 and C11 (red and blue markers). With the 10 m reference gust, the cases are in somewhat mixed order. In particular, one of the two unstable cases (C7) has a vertical slope with a small portion of maxima before the reference gust but the other (C11) has a more slanted slope and a larger portion of maxima. The cases with a trend lie in the middle of the ranges such that the cases with decreasing trend have a slightly more slanted slope than the cases with increasing trend.

The time difference between the 75th and 25th percentiles (Appendix) can be considered as a measure of the uncertainty in the slope. It was calculated for each height, but here we will consider only the difference at the most distant level from the reference gust. The percentile difference is largest in stable cases, especially at 10 m level when the 100 m level gust is considered. The smallest differences, 28 s for the 100 m reference and 34 s for the 10 m reference, are found in the unstable case C11, but in case C7, which is also unstable, they are 53 and 52 s, respectively, which are of the same order of magnitude as in stable conditions. The cases with an increasing trend have slightly larger percentile difference than the cases with a decreasing trend. The remaining stationary, near-neutral stable cases have similar differences to the cases with a trend.

The time difference between the maxima as measured by the slope m cannot be explained by the number of cross-sections (2 min samples) included in each case (Table 2 and Appendix). In stationary, near-neutral stable cases C2, C5 and C12, in which the slope is large, the correlation between $U_{max,10m}$ and U_{100m} is smaller than in the other cases. However, the correlation does not explain the slope differences in the other cases, although the correlation was found to be large in all those cases with a trend. Moreover, the slopes do not depend on the difference $U_{100m} - U_{max,10m}$ (Appendix).

5. Summary and conclusions

This study presented an overview of the vertical structure of gusts within a 100 m deep layer over a flat, fairly homogeneous land surface, where the median gust factor at 10 m level was about 1.4 and decreased to about 1.2 at 100 m level. New information about the behaviour of gusts with height and stability and with respect to different gust durations was obtained.

In a typical surface-layer parametrization, the gust factor is composed of two components, the peak factor and turbulence intensity, from which the turbulence intensity was found to rule over the peak factor in determining the effects of stability and height above the surface on gust factor. The peak factor was found to depend mostly on the time-scales of gusts, the gust duration and the sampling period length, whereas it did not vary much with height or stability.

Theoretical estimates for the peak factor were unable to reproduce the observed vertical decrease typical in near-neutral and stable conditions and near-constant peak factor with height in unstable conditions. Despite the inconsistencies between the theoretical and observed peak factor profiles, the theoretical method provides estimates for a peak factor within the 100 m layer in practical applications in which the aim is to convert gust factors between the time-scales $[t_g, T] = [1\,s, 1\,h]$ and $[t_g, T] = [3\,s, 10\,min]$.

The mean vertical velocities were on average negative during the maximum gust and positive during the minimum gust, a result that supports the idea that gusts are related to up- and downdraughts within the boundary layer. Comparison of spectra of mean wind speed and gust wind speed showed that gusts at 10 m level have an almost equal amount of energy to the mean wind speed at 100 m level. Moreover, there was a peak in $U_{max,10m}$ at the diurnal scale, which rose above the U_{100m} and $U_{max,100m}$ curves. The distributions of the difference $U_{100m} - U_{max,10m}$ revealed that, under unstable conditions, $U_{max,10m}$ is higher than U_{100m}. In near-neutral conditions it can be either higher or lower and in very stable conditions it is mostly lower.

The vertical structure of gust events was studied in a selection of 15 strong wind cases. They included three cases with stable and two with unstable conditions, two cases with increasing and three with decreasing trend in the wind speed, and five cases with near-neutral stationary conditions. A new methodology to detect maxima at all observation levels in a sequence of ± 1 min around the maximum gust at one level was developed. The method provides new information on the occurrence of maxima, without any effects due to the averaging of neighbouring points typically applied to high-resolution (here 20 Hz) turbulence data. The results showed that before a 10 m level maximum gust there was, on average, a local maximum at higher levels and after a 100 m level gust maximum there were typically maxima observed at lower levels. The time difference between the maxima at different levels was calculated by applying a linear fit to the median locations of maxima in the time axis. This time difference within a 100 m layer was 5–22 s for the 10 m level gusts and 9–26 s for the 100 m level gusts. The time difference was found to be largest for stationary, near-neutral or slightly stable conditions and smallest for the clearly stable or unstable cases or for cases with a trend in wind speed. However, a small time difference does not necessarily mean that a gust hits all levels almost simultaneously. There may be a large variability in the timing of maxima between levels, as was observed in stable conditions.

Acknowledgements

This research has received funding from the European Research Council under the European Community's Seventh Framework Programme (FP7/2007–2013)/ERC grant agreement number 227915, project PBL-PMES, Sergej Zilitinkevich, coordinator; from the Danish Council for Strategic Research, Sagsnr. 2104-08-0025 (Tall Wind project); and from Vilho, Yrjö and Kalle Väisälä Foundation and the Academy of Finland (contract 259537). The work has also been supported by two STSMs of the COST Action ES1002.

Appendix

Results of the case studies

Results of the 15 case studies were collected into Tables A1–A3. The data were grouped into these tables based on stability and stationarity. Table A1 shows the results for cases with a clear stable or unstable stratification, whereas Table A2 lists cases with a clear trend in the wind speed. Finally, Table A3 includes the remaining cases, which are mainly stationary with near-neutral or slightly stable conditions.

Table A1. Results of the statistical analysis of the location of maxima in stable cases C1, C3 and C9 and unstable cases C7 and C11.

Case	C1	C3	C7	C9	C11
N	36	30	36	48	18
G_{10m}	1.26	1.30	1.44	1.37	1.40
$G_{100m} - G_{10m}$	−0.09	−0.10	−0.16	−0.19	−0.15
$R^2(G_{100m}, G_{10m})$	0.1	0.1	0.1	0.0	0.4
$U_{100m} - U_{max,10m}$ (m s^{-1})	1.9	1.3	−1.5	2.4	−1.5
$R^2(U_{100m}, U_{max,10m})$	0.54	0.54	0.63	0.62	0.43
trend, U_{100m} (m s^{-1} h^{-1})	0.2	0.0	0.3	0.3	0.0
$t_{gust,100m} - t_{gust,10m}$ (s)	−4	−3	17	42	−43
$(t_{P75} - t_{P25})\|_{z_{ref}=10m}$ (s)	50	40	52	60	34
m_{10m} (s 100^{-1} m^{-1})	−10	−9	−5	−13	−13
$P_0\|_{z_{ref}=10m}$ (%)	57	62	55	58	68
$(t_{P75} - t_{P25})\|_{z_{ref}=100m}$ (s)	67	63	53	60	28
m_{100m} (s 100^{-1} m^{-1})	7	−15	−9	−15	−11
$P_0\|_{z_{ref}=100m}$ (%)	54	38	41	37	36
Stability	s	s	u/nu	s/ns	u/nu

N: number of 10 min samples; G_{10m}: mean gust factor at 10 m level; $G_{100m} - G_{10m}$ and $R^2(G_{100m}, G_{10m})$: mean difference between the 100 and 10 m level gust factors and their correlation; $U_{100m} - U_{max,10m}$ and $R^2(U_{100m}, U_{max,10m})$: mean difference and correlation of U_{100m} and $U_{max,10m}$; $t_{gust,100m} - t_{gust,10m}$: difference in the timing of the maximum 3 s gusts at 100 and 10 m levels; $(t_{P75} - t_{P25})$: difference between the locations of the 75th and 25th percentiles on the time axis at the level most distant to the reference level; $m_{z_{ref}} = \Delta t/\Delta z$: the slope of the linear fit applied to the median locations on the time axis; P_0: probability of maxima before the reference gust at the most distant level from the reference gust.

Table A2. Same as Table A1, but for cases with a trend: C4, C6, C8, C10 and C15.

Case	C4	C6	C8	C10	C15
N	36	42	18	15	30
G_{10m}	1.39	1.42	1.43	1.40	1.36
$G_{100m} - G_{10m}$	−0.12	−0.13	−0.15	−0.13	−0.09
$R^2(G_{100m}, G_{10m})$	0.12	0.54	0.06	0.04	0.11
$U_{100m} - U_{max,10m}$ (m s^{-1})	−1.0	−1.6	0.0	0.3	−0.5
$R^2(U_{100m}, U_{max,10m})$	0.73	0.78	0.73	0.73	0.85
trend, U_{100m} (m s^{-1} h^{-1})	0.5	−0.8	−0.9	0.9	−0.7
$t_{gust,100m} - t_{gust,10m}$ (s)	28	42	−49	1	−16
$(t_{P75} - t_{P25})\|_{z_{ref}=10m}$ (s)	43	38	38	49	37
m_{10m} (s 100^{-1} m^{-1})	−10	−14	−5	−14	−13
$P_0\|_{z_{ref}=10m}$ (%)	66	67	61	62	66
$(t_{P75} - t_{P25})\|_{z_{ref}=100m}$ (s)	51	38	48	56	44
m_{100m} (s 100^{-1} m^{-1})	−16	−13	−17	−16	−21
$P_0\|_{z_{ref}=100m}$ (%)	34	30	33	39	28
Stability	ns/n	u/nu→n	n→ns	ns→nu	n→ns

Table A3. Same as Table A1, but for stationary, neutral or near-neutral stable cases C2, C5, C12, C13 and C14.

Case	C2	C5	C12	C13	C14
N	36	24	60	48	36
G_{10m}	1.36	1.36	1.38	1.41	1.38
$G_{100m} - G_{10m}$	−0.07	−0.08	−0.11	−0.18	−0.10
$R^2(G_{100m}, G_{10m})$	0.01	0.28	0.13	0.03	0.00
$U_{100m} - U_{max,10m}$ (m s^{-1})	−0.7	−0.2	−0.4	0.1	−0.6
$R^2(U_{100m}, U_{max,10m})$	0.34	0.41	0.25	0.79	0.59
trend, U_{100m} (m s^{-1} h^{-1})	−0.2	0.2	0.0	−0.2	0.2
$t_{gust,100m} - t_{gust,10m}$ (s)	−1	−26	44	−18	13
$\Delta t(P75 - P25)\|_{z_{ref}=10m}$ (s)	39	58	47	45	43
m_{10m} (s 100^{-1} m^{-1})	−22	−17	−21	−14	−12
$P_0\|_{z_{ref}=10m}$ (%)	73	67	63	65	59
$\Delta t(P75 - P25)\|_{z_{ref}=100m}$ (s)	42	45	49	39	37
m_{100m} (s 100^{-1} m^{-1})	−20	−12	−26	−19	−19
$P_0\|_{z_{ref}=100m}$ (%)	25	30	31	30	33
Stability	ns/n	ns/n	ns/n	ns/n	ns/n

References

Ágústsson H, Ólafsson H. 2009. Forecasting wind gusts in complex terrain. *Meteorol. Atmos. Phys.* **103**: 173–185.

Beljaars ACM. 1987. The influence of sampling and filtering on measured wind gusts. *J. Atmos. Oceanic Technol.* **4**: 613–626.

Belusić D, Klaić ZB. 2004. Estimation of bora wind gusts using a limited area model. *Tellus* **56A**: 296–307.

Brasseur O. 2001. Development and application of a physical approach to estimating wind gusts. *Mon. Weather Rev.* **129**: 5–25.

European Centre for Medium-Range Weather Forecasts. 2012. 'Wind gusts'. In *IFS Documentation–Cy38r1, Operational Implementation 19 June 2012, Part IV: Physical Processes*: 51–52. ECMWF: Reading, UK. http://old.ecmwf.int/research/ifsdocs/CY38r1/IFSPart4.pdf (accessed 4 November 2014).

Goyette S, Brasseur O, Beniston M. 2003. Application of a new wind gust parametrization: Multiscale case studies performed with the Canadian regional climate model. *J. Geophys. Res.* **108**: 4374, doi: 10.1029/2002JD002646.

Gryning SE, Batchvarova E, Brümmer B, Jørgensen H, Larsen S. 2007. On the extension of the wind profile over homogeneous terrain beyond the surface boundary layer. *Boundary Layer Meteorol.* **124**: 251–268.

Højstrup J. 1982. Velocity spectra in the unstable planetary boundary layer. *J. Atmos. Sci.* **39**: 2239–2248.

Højstrup J, Larsen SE, Madsen PH. 1990. Power spectra of horizontal wind componenets in the neutral atmospheric surface boundary layer. In *Proceedings of 9th Symposium on Turbulence and Diffusion*, Jensen NO, Kristiansen L, Larsen SE. (eds.), Vol. 9: 305–308. American Meteorological Society: Roskilde, Denmark.

Kaimal JC. 1978. Horizontal velocity spectra in an unstable surface layer. *J. Atmos. Sci.* **35**: 18–24.

Kaimal JC, Wyngaard JC, Izumi Y, Cote OR. 1972. Spectral characteristics of surface-layer turbulence. *Q. J. R. Meteorol. Soc.* **98**: 563–589.

Kristensen L, Casanova M, Courtney MS, Troen I. 1991. In search of a gust definition. *Boundary Layer Meteorol.* **55**: 91–107.

Liu HP, Peters G, Foken T. 2001. New equations for sonic temperature variance and buoyancy heat flux with an omnidirectional sonic anemometer. *Boundary Layer Meteorol.* **100**: 459–468.

Rice SO. 1944. Mathematical analysis of random noice. *Bell Syst. Tech. J.* **23**: 282–332; **24**: 46–156.

Seity Y, Brousseau P, Malardel S, Hello G, Benard P, Bouttier F, Lac C, Masson V. 2011. The AROME-France convective-scale operational model. *Mon. Weather Rev.* **139**: 976–991.

Sheridan P. 2011. 'Review of techniques and research for gust forecasting and parameterisation forecasting', Forecasting Research Technical Report 570. UKMO: Exeter, UK. http://www.metoffice.gov.uk/media/pdf/e/3/FRTR570_Tagged.pdf (accessed 4 November 2014).

Suomi I, Vihma T, Gryning S-E, Fortelius C. 2013. Wind gust parametrizations at heights relevant for wind energy–a study based on mast observations. *Q. J. R. Meteorol. Soc.* **139**: 1298–1310.

Tammelin B, Vihma T, Atlaskin E, Badger J, Fortelius C, Gregow H, Horttanainen M, Hyvönen R, Kilpinen J, Latikka J, Ljungberg K, Mortensen NG, Niemelä S, Ruosteenoja K, Salonen K, Suomi I, Venäläinen A. 2013. Production of the Finnish wind atlas. *Wind Energy* **16**: 19–35, doi: 10.1002/we.517.

Thomas C, Foken T. 2005. Detection of long-term coherent exchange over spruce forest using wavelet analysis. *Theor. Appl. Climatol.* **80**: 91–104, doi: 10.1007/s00704-004-0093-0.

Van Dijk A, Moene AF, De Bruin HAR. 2004. 'The principles of surface flux physics: Theory, practice and description of the ECPACK library', Internal Report 2004/1. Meteorology and Air Quality Group, Wageningen University: Wageningen, the Netherlands.

Vickers D, Mahrt L. 1997. Quality control and flux sampling problems for tower and aircraft data. *J. Atmos. Oceanic Technol.* **14**: 512–526.

Wichers Schreur B, Geertsema G. 2008. Theory for a TKE based parametrization of wind gusts. *HIRLAM Newsl.* **54**: 177–188.

Wieringa J. 1973. Gust factors over open water and built-up country. *Boundary Layer Meteorol.* **3**: 424–441.

Wilczak JM, Oncley SP, Stage SA. 2001. Sonic anemometer tilt correction algorithms. *Boundary Layer Meteorol.* **99**: 127–150.

Woetmann Nielsen N, Petersen C. 2001. 'Calculation of wind gusts in DMI-HIRLAM', Scientific Report 01–03. Danish Meteorological Institute: Copenhagen.

World Meteorological Organization (WMO). 2008. Measurement of surface wind. In *Guide to Meteorological Instruments and Methods of Observation*, WMO No. 8 (7th edn). World Meteorological Organization: Geneva, Switzerland. http://www.wmo.int/pages/prog/gcos/documents/gruanmanuals/CIMO/CIMO_Guide-7th_Edition-2008.pdf (accessed 4 November 2014).

Reprinted, with permission, from
Quarterly Journal of Royal Meteorological Society, 142, 2985–3000,
doi:10.1002/qj.2880

III

Quarterly Journal of the Royal Meteorological Society Q. J. R. Meteorol. Soc. 142: 2985–3000, October 2016 B DOI:10.1002/qj.2880

RMetS
Royal Meteorological Society

Gust factor based on research aircraft measurements: a new methodology applied to the Arctic marine boundary layer

Irene Suomi,[a]* Christof Lüpkes,[b] Jörg Hartmann,[b] Timo Vihma,[a] Sven-Erik Gryning[c] and Carl Fortelius[a]

[a]*Meteorological Research, Finnish Meteorological Institute, Helsinki, Finland*
[b]*Climate Sciences, Alfred Wegener Institute for Polar and Marine Research, Bremerhaven, Germany*
[c]*DTU Wind Energy, Technical University of Denmark, Roskilde, Denmark*

*Correspondence to: I. Suomi, Finnish Meteorological Institute, PO Box 503, FI-00101 Helsinki, Finland. E-mail: irene.suomi@fmi.fi

There is as yet no standard methodology for measuring wind gusts from a moving platform. To address this, we have developed a method to derive gusts from research aircraft data. First we evaluated four different approaches, including Taylor's hypothesis of frozen turbulence, to derive the gust length-scales that correspond to the gust time-scales, namely the gust duration (s) and the sample period (typically 10 min). The novelty of our method lies in using peak factors (deviation of the gust from the mean wind speed normalized by the local turbulence) to convert between the scales. After devising a way to derive the gust length-scales, we calculated the gust factors from aircraft observations and tested them against those from four parametrizations originally developed for weather stations. Three of them performed well ($R^2 = 0.66$ or higher), while the fourth overestimated the gust factors in unstable conditions ($R^2 = 0.52$). The mean errors for all methods were low, from −0.02 to 0.05, indicating that wind gust factors can indeed be measured from research aircraft. Moreover, we showed that aircraft can provide gust measurements within the whole boundary layer, if horizontal legs are flown at multiple levels over the same track. This is a significant advance, as gust measurements are usually limited to heights reached by weather masts. In unstable conditions over the open ocean, the gust factor was nearly constant with height throughout the boundary layer, the near-surface values only slightly exceeding those at upper levels. Furthermore, we found gust factors to be strongly dependent on surface roughness conditions, which differed between the open ocean and sea ice in the Arctic marine environment. The roughness effect on the gust factor was stronger than the effect of boundary-layer stability.

Key Words: gust factor; marine atmospheric boundary layer; Arctic; aircraft measurements

Received 31 March 2016; Revised 17 June 2016; Accepted 11 July 2016; Published online in Wiley Online Library 20 September 2016

1. Introduction

An understanding of wind-speed maxima, or wind gusts, has important applications for various areas of human activity. Extreme gusts associated with storms can inflict damage on buildings and constructions and may become a safety risk in some fields of operation, such as navigation and aviation. For aviation, gusts are a risk, particularly in take-off and landing (Chan, 2012) but also during the flight (Shi *et al.*, 2015). On the other hand, aircraft can provide a platform to measure wind and potentially gusts in remote areas that cannot be reached by standard *in situ* measurement techniques, such as weather stations and meteorological masts. An example of such a remote location is the Arctic, which is of particular interest due to the accelerating effects of climate warming occurring there in recent decades (Overland *et al.*, 2015). The Arctic sea-ice thickness and late summer sea-ice extent have decreased by approximately 50% since the early 1980s (e.g. Vihma, 2014). Such changes affect the atmospheric boundary layer and thereby the wind and gust climatology.

A wind gust is, by definition, a wind-speed maximum of short duration, typically calculated as a maximum of the (moving) averaged wind-speed time series. The gust duration t_g is determined by the width of the moving average window. The magnitude of the gust depends on t_g and on the sample period T. The probability of a strong gust increases with increasing sample period. Wind gusts are typically expressed as a ratio of the wind gust to the mean wind speed, called the gust factor $G = U_{max}/U$, where U_{max} is the wind gust speed and U the mean wind speed calculated as a sample average.

Prediction of wind gusts in numerical weather prediction (NWP) models and the assessment of climate change effects on wind gust extremes in climate models are based on parametrizations, since even the highest resolution NWP models

do not resolve all the relevant scales of turbulence contributing to the gusts (e.g. Seity *et al.*, 2011; Honnert and Masson, 2014). The aim of these parametrizations is to provide an estimate for the maximum gust based on available model variables. The input variables typically include the effects of wind shear and buoyancy. In stable conditions, gusts are also generated by gravity waves and, in some cases, strong gusts may be related to orographically forced flow, including wakes, gap flows, etc. (e.g. Belušić and Klaić, 2004).

To develop and validate gust parametrizations, high-quality measurements of wind gusts from various environments are needed. However, the majority of gust studies relate to the midlatitudes (e.g. Wieringa, 1973; Beljaars, 1987; Woetman Nielsen and Petersen, 2001; Brasseur, 2001; Wichers Schreur and Geertsema, 2008; Suomi *et al.*, 2015). Gusts have been assessed over different surface types, including over land (Wieringa, 1973), near the coast and offshore (e.g. Hsu and Blanchard, 2004; Suomi *et al.*, 2013), in complex topography (Meyers *et al.*, 2003; Belušić and Klaić, 2004; Ágústsson and Ólafsson, 2004), over mountainous Iceland (Ágústsson and Ólafsson, 2004, 2009) and in the context of tropical cyclones (Harper *et al.*, 2010). Based on these studies, it has been found that G depends above all on surface roughness, static stability, height above the surface and orographic effects in the vicinity of high mountains. In the Arctic, gusts have received little attention. Over the Arctic marginal sea-ice zone, there are large variations in both surface roughness and stability. Ice ridges and other changes in ice thickness cause differences in the surface roughness, whereas the near-surface stability conditions may change abruptly due to leads and polynyas. Extreme wind gusts are typically observed during storms. Kolstad (2015) investigated extreme wind conditions over the Barents Sea during a 35 year (1979–2013) period and found that the 12 most severe extreme wind cases occurred in the context of polar lows formed during conditions of strong cold-air outbreak conditions.

Aircraft have been used extensively to measure turbulence (e.g. Hartmann *et al.*, 1997; Gryanik and Hartmann, 2002; Elvidge *et al.*, 2016). However, there exists no standard methodology for measuring wind gusts from an aircraft. The speed of the aircraft, V_a, relative to the Earth's surface is typically large compared with the mean wind speed, U, which allows sampling of a long distance during a short time period. Thus, gust measurements from an aircraft cannot be based on time averaging but must be based on spatial averaging.

Figure 1 shows an example of a turbulent wind-speed signal. The wind speed can be measured as a function of either time (at a fixed location, e.g. at a weather station) or distance (as in the case of a fast-moving platform). The sample length is expressed in terms of either time (T) or distance (X) and the prescribed gust length (the width of the moving average window) is either t_g in units of time or x_g in terms of distance. At weather stations, typically $t_g = 3$ s and $T = 10$ min. The first aim of this study is to define the length-scales x_g and X such that they match the time-scales t_g and T best.

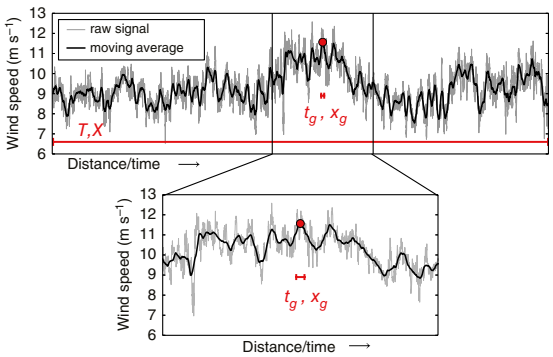

Figure 1. An example of a turbulent wind signal (thin line), which can be a function of time (t) or distance (x), depending on the data source. The wind gust speed (dot) is calculated as the maximum of the moving averages of the wind signal (thick line). The width of the moving average window determines the gust length (t_g or x_g) and the sample length is either T or X.

The comparison of turbulence measurements from a fixed point with those from a moving platform, such as an aircraft, is not straightforward. The most commonly used hypothesis to convert between temporal and spatial scales is Taylor's hypothesis of frozen turbulence, which assumes that the velocity by which the turbulent wind field is advected past the instrument is larger than the velocity scale of the turbulence (Taylor, 1938). With aircraft measurements, Taylor's hypothesis is typically valid, because aircraft can cover a long distance within a short time period (e.g. Samuelsson and Tjernström, 1999). According to Taylor's hypothesis, the time series can be expressed in terms of distance. This distance is called $\Delta x_{\mathrm{Taylor}}$ and it is the distance over which the 'frozen' turbulence is advected by the mean wind (U) in time Δt, i.e. $\Delta x_{\mathrm{Taylor}} = U\Delta t$. However, $\Delta x_{\mathrm{Taylor}}$ is different from the distance $\Delta x_{\mathrm{flight}}$ that the aircraft would cover if the wind speed in the flight direction were non-negligible. This distance $\Delta x_{\mathrm{flight}}$ can be measured by an aircraft in time $\Delta t_a = \Delta x_{\mathrm{flight}}/V_a$, where V_a is the speed of the aircraft relative to the Earth's surface. Taking into account the flight time Δt_a, the aircraft must fly a horizontal distance $\Delta x_{\mathrm{flight}} = \Delta x_{\mathrm{Taylor}} \pm U_x \Delta t_a$, where U_x is the mean (advection) wind speed along the flight track. This yields a flight distance

$$\Delta x_{\mathrm{flight}} = \frac{U\Delta t}{1 \pm \frac{U_x}{V_a}}, \tag{1}$$

where the plus sign is valid if U_x is towards the plane and the minus sign when the wind flow is directed in the flight direction. A special case is a wind field perpendicular to the flight track, i.e. $U_x = 0$. For advection perpendicular to the flight direction, the flow field is assumed isotropic. Usually the flight speed is large compared with the advection velocity, $V_a \gg U_x$, which means $\Delta x_{\mathrm{flight}} \approx \Delta x_{\mathrm{Taylor}} = U\Delta t$. However, research aircraft typically fly at a low speed and thus the ratio U_x/V_a can be large, 10% or even more. Then the flight speed may become important in the conversion between temporal and spatial scales.

Previous studies exist in which the length-scales for sample averaging have been estimated. For example, Tetzlaff *et al.* (2015) estimated minimum flight leg lengths required for calculation of the turbulent fluxes of momentum and heat over leads. The minimum leg length for the sensible heat flux was 2.5 km and that for the momentum flux 4 km. Their estimation was based on analysis of the fluxes, not on comparison with data from a weather station at a fixed point. Instead, Mahrt (1998) compared the fluxes measured by an aircraft with those from a tower, but his aim was not to define suitable sample lengths but to compare the flux measurements on board an aircraft with those measured at a weather mast.

There are three main goals in this study. Firstly, we will develop the methodology to derive gusts from turbulence measurements taken on board an aircraft, such that these gusts will be comparable with those measured at fixed locations such as weather stations and masts. For that, we will introduce and evaluate four different methods to define the gust length-scales (x_g, X), including Taylor's hypothesis as presented above (Eq. (1)). Then, as a second goal, we will test this methodology against data from a known and well-documented research aircraft campaign, the Arctic Radiation and Turbulence Interaction Study (ARTIST). The data have been used in several previous studies (Hartmann *et al.*, 1999; Kaleschke *et al.*, 2001; Garbrecht *et al.*, 2002; Gryanik and Hartmann, 2002; Vihma *et al.*, 2003, 2005), but none of these studies has addressed gusts. The methodology will be tested by comparing the observed gust factors with those from four different gust parametrizations originally developed for weather stations. Moreover, this will also allow an intercomparison of

the parametrization methods. Finally, as the third aim, this study will provide new information about gustiness conditions in the Arctic marine environment, on how the surface type (sea ice/open water), static stability and height above the surface affect the wind gusts.

The article is organized as follows. In section 2, we start with the gust definition as measured at weather stations and then extend that to aircraft data. We then briefly present four different parametrizations for gusts, originally developed for weather stations, and transform those to spatial averaging. The measurements are presented in section 3. The results of the study start in section 4 with the determination of gust length-scales and their effect on the gust factor. In section 5, we first study the gust factors along low-level flights over sea ice and open water and then investigate mean gust-factor profiles within the whole boundary layer based on shorter flights at multiple heights over the same flight track. These flights represent unstable marine conditions and also more extreme conditions during cold-air outbreaks. In section 6, we apply the four gust parametrizations to the aircraft measurements of this study. Finally, in section 7, a summary and conclusions are provided.

2. Theory

2.1. Gust definition

At weather stations, the wind gust speed ($U_{\max}$) is calculated as the maximum of short-term moving averages of the measured wind speed during a sampling period. Based on World Meteorological Organization (WMO) recommendations (WMO, 2010), the gust duration (the moving average window length) is $t_g = 3$ s and the sampling period is $T = 10$ min. The wind gust speed is

$$U_{\max} = \max\left(\left\{\frac{1}{n}\sum_{j=i}^{i+n-1} u_j\right\}_{i=1}^{N-n+1}\right), \qquad (2)$$

where $n = f_s t_g$ is the number of data points within the moving average window and f_s is the sampling frequency at a fixed point. $N = f_s T$ is the number of observations within each sample.

The aircraft data used in this study consist of turbulence measurements along nearly straight horizontal flight tracks (section 3.1), with only small variations (less than ± 15 m in 81% of cases) in the flight altitude. Therefore, we focus on the changes in wind speed along each flight track, which will represent the x-axis. Then, the sampling frequency is related to a wave number: $k_a = 2\pi f_a / V_a$, where the subscript 'a' refers to aircraft measurements and f_a is the sampling frequency of the anemometer carried by the aircraft. The number of data points in Eq. (2) then becomes

$$n = \frac{k_a}{2\pi} x_g \qquad \text{and} \qquad N = \frac{k_a}{2\pi} X,$$

where x_g is the gust length and X the sample length, both in metres. To calculate wind gusts from the aircraft measurements, we have to define the gust length-scales x_g and X. There are several options as to how the length-scales x_g and X corresponding to the time-scales t_g and T could be determined. Here we will discuss four possible methods, M1–M4.

(M1) Taylor's hypothesis of frozen turbulence introduced in section 1 provides a common theory for the relationship between the spatial and temporal changes in the turbulence measurements. According to the theory, a wind gust and the turbulence observed at a fixed point result from advection of the wind field past the instrument and the wind field is assumed to be unchanged (no sinks or sources of turbulence). Following Eq. (1), the gust length-scales become $[x_g, X] \approx [Ut_g, UT]$. The main disadvantage of the method is that the gust length x_g becomes a function of the mean wind speed, which depends on e.g. the height above the surface. In other words, the gust length will also depend on height. This will result in unwanted internal correlations in our analysis.

(M2) Another even simpler method is to choose the sampling strategy (measurement frequency, anemometer characteristics, flight speed) such that both anemometers, one at a fixed position and the other set up on an aircraft, give the same number of data within t_g and x_g respectively. Then, the gust length-scales become

$$x_g = \frac{f_s}{f_a} V_a t_g \qquad \text{and} \qquad X = \frac{f_s}{f_a} V_a T.$$

This definition is simple and straightforward to apply. One disadvantage is that the gust length-scales depend on the flight velocity; another is the assumption that the effects of the instrument characteristics (e.g. the instrument response, path-length averaging, aircraft upwash, flow distortion, etc.) and the sampling frequency are similar for both instrument set-ups, which may not be the case.

(M3) A very simple way of defining the gust length-scales is to first choose a fixed sample length X and then set the gust length using $x_g = (t_g/T)X$. This method has the disadvantage that we do not know what length-scale X corresponds to the time-scale T. This definition returns to M2 if we define $X = (f_s/f_a)V_a T$ and to M1 if $X = UT$.

(M4) One possibility is to choose the gust length-scales by comparing the actual structure of gust measurements from a weather mast with those observed from an aircraft. Traditionally, gust factors (G) have been used to convert between different sample periods (T) and gust durations (t_g) at weather stations. For example, Harper *et al.* (2010) provide a table of gust factors (their Table 1.1) that can be used to estimate wind gust speeds with different gust durations (t_g from 3–600 s) and sample periods (T from 60–3600 s) using observed gusts calculated with a certain known gust duration and sample period. This kind of table, however, must include gust factors for different surface types separately, because the gust factor depends on the surface roughness. Moreover, it depends on the stability (e.g. Woetman Nielsen and Petersen, 2001; Suomi *et al.*, 2015) and, by definition, on the mean wind speed. To eliminate the effect of local turbulence conditions at a particular site, we will use, instead of G, the peak factor $g_x = (U_{\max} - U)/\sigma_u$, which is the gust normalized by the standard deviation of the along-wind component of the horizontal wind speed (σ_u), i.e. by the local turbulence. This idea of comparing peak factors is based on the results of Suomi *et al.* (2015). They found that the shape of the observed peak factor as a function of gust duration behaves on average almost similarly in all stability conditions (Suomi *et al.*, 2015, their figure 8). Here, we assume that the shape of the curve is also similar for the aircraft measurements, but as a function of distance. Hence, by comparing the behaviour of the observed peak factors in time and space, it is possible to derive the optimal length-scale counterparts for the gust time-scales. This method is described in detail in Appendix A.

To summarize the above considerations on gust length-scales, we basically have three possibilities to define the gust length-scales, methods M1, M2 and M4. The requirement of method M3, i.e. the assumption that the time-scale ratios t_g/T and the length-scale ratios x_g/X are the same, can be met by all other methods. Methods M1–M4 will be tested and the sensitivity of the gust factor to the choice of length-scales will be investigated in section 4.

2.2. Gust parametrizations

Two types of gust parametrizations exist: those based on Monin–Obukhov (M–O) theory (Wieringa, 1973; Beljaars, 1987; Kristensen *et al.*, 1991; Woetman Nielsen and Petersen, 2001; Wichers Schreur and Geertsema, 2008; Suomi *et al.*, 2013), which we here call surface-layer parametrizations, and a second type called the profile method (Brasseur, 2001). In the profile method, gusts are assumed to result from turbulent eddies bringing fast-moving air parcels from aloft down to the surface while retaining their original speed. We will, however, not apply the profile method, as it requires data with high vertical resolution over the depth of the entire boundary layer.

Surface-layer gust parametrizations are typically derived by separating the wind gust speed into the components of the mean wind speed U and a maximum fluctuation $u'_{\max}$, so that

$$U_{\max} = U + u'_{\max}. \tag{3}$$

Further, the fluctuation $u'_{\max}$ can be related to the standard deviation of the along-wind velocity component: $u'_{\max} = C\sigma_u$, where C is a coefficient of proportionality, so that

$$U_{\max} = U + C\sigma_u. \tag{4}$$

The gust factor, $G = U_{\max}/U$, can be rewritten as

$$G = 1 + \frac{U_{\max} - U}{\sigma_u}\frac{\sigma_u}{U} = 1 + g_x I, \tag{5}$$

where

$$g_x = \frac{U_{\max} - U}{\sigma_u} \tag{6}$$

is the peak factor and $I = \sigma_u/U$ is the turbulence intensity of the horizontal wind speed. Using Eqs (4) and (5), it can be shown that $C = g_x$. Thus Eqs (5) and (6) provide the basis for the surface-layer gust parametrizations.

Four different formulations for G will be introduced here. The first method was proposed by Wieringa (1973). The original formulation includes the gust length as Ut_g, which will be replaced here by x_g:

$$G = 1 + \left[1.42 + 0.3013 \ln\left(\frac{990}{x_g} - 4\right)\right] \ln(z/z_0)^{-1}, \tag{7}$$

where z is the height above the surface and z_0 is the roughness length. Equation (7) is based on the assumption that the highest wind gust speeds are observed during near-neutral conditions and therefore the effect of stability is not included.

The second parametrization is based on Rice (1944, 1945). It has been applied in several studies (Beljaars, 1987; Kristensen *et al.*, 1991; Wichers Schreur and Geertsema, 2008). Wichers Schreur and Geertsema (2008) extended the parametrization to be used in NWP model environments where the turbulence kinetic energy (TKE) is provided. Thus, the method can potentially be applied to any height and stability conditions. Here, we will use the formulation by Wichers Schreur and Geertsema (2008):

$$G = 1 + g_{x,f} r_\sigma \frac{\sqrt{2\mathrm{TKE}}}{U}, \tag{8}$$

where $g_{x,f}$ is the peak factor of the moving averaged (filtered) wind signal and r_σ is the ratio of the filtered and true standard deviation of the along-wind velocity component. Both are determined by a statistical approach, described briefly in Appendix B, where the transformation of the equations into wave-number space is also provided.

The third parametrization was introduced by Woetman Nielsen and Petersen (2001):

$$G = 1 + c_t \frac{3.06u_{*0} + \gamma 0.85 w_*}{U}, \tag{9}$$

where c_t is an empirical constant that can be tuned by application. Woetman Nielsen and Petersen (2001) used $c_t = 1.7$. The parameter γ equals 1 when $L < 0$ and 0 otherwise. L is the Obukhov length: $L = -u_{*0}^3 \left[\kappa(g/\bar{\theta}_0)H_{v0}/(\rho_0 c_p)\right]^{-1}$, where u_{*0} is the friction velocity in the constant flux layer, κ is the von Kármán constant, g is the gravitational acceleration, $\bar{\theta}_0$ the mean surface potential temperature, H_{v0} the turbulent virtual heat flux, ρ_0 the air density and c_p the specific heat of dry air. In Eq. (9),

$$w_* = \left(\frac{g}{\bar{\theta}_0}\frac{H_{v0}}{\rho_0 c_p} h\right)^{1/3}$$

is the convective velocity scale (Deardorff, 1972).

The fourth method was proposed by Suomi *et al.* (2013). It was developed to account for the effects of both stability and height on the gust factor. Information about the behaviour of the gust factor as a function of height is important, for example for the safety and planning of high structures and the operation of wind turbines. Suomi *et al.* (2013) parametrize the gust factor as

$$G = 1 + g_{t,T}\frac{\sigma_u}{U},$$

where

$$\sigma_U = \begin{cases} u_{*0}\left[0.35\left(-\frac{h}{\kappa L}\right)^{2/3} + 4\left(1 - \frac{z}{h}\right)\right]^{1/2} & \text{if } L < 0, \\ 2u_{*0}\left(1 - \frac{z}{h}\right)^{1/2} & \text{if } L \geq 0, \end{cases} \tag{10}$$

where $g_{t,T}$ is the (median) peak factor, which is assumed to be constant and can be adjusted to the case considered, and h is the boundary-layer height. Equation (10) differs slightly from the formulation by Suomi *et al.* (2013) to avoid discontinuity at neutral conditions. In this reformulated version, at $|L| \to \infty$, $\sigma_u \to 2u_{*0}\left[1 - (z/h)\right]^{1/2}$.

Above, we have introduced four different surface-layer parametrizations for the gust factor, originally developed for weather stations and masts. In this study, we will investigate their applicability to aircraft data, which do not necessarily represent the conditions at the near-surface constant flux layer but rather above it, and the data are provided as a function of distance instead of time.

3. Measurements and methods

3.1. Aircraft measurements

Aircraft measurements were collected on board the Polar 2 aircraft during the ARTIST measurement campaign around Svalbard in March and April 1998 (Hartmann *et al.*, 1999). This fairly old data set was chosen because the data quality, meteorological conditions and atmospheric boundary layer (ABL) processes are known from previous studies.

The flight tracks used in this study are shown in Figure 2. The flights in March took place over sea ice and open water under different atmospheric and surface conditions. On 16 March (tracks L1, L2 in Figure 2(b)), the flow was from the open ocean towards sea ice, with slightly stable stratification over the open ocean and near-neutral conditions close to the coastline of Spitsbergen (Garbrecht *et al.*, 2002; Vihma *et al.*, 2003). The flights on 30 March (L3, L4) were carried out over the same area. The flow in the atmospheric boundary layer was parallel to the ice edge (Kaleschke *et al.*, 2001). There was one flight across the ice edge (L3 in Figure 2(b)) and several flight legs over the open water at multiple altitudes between 30 and 900 m on track L4.

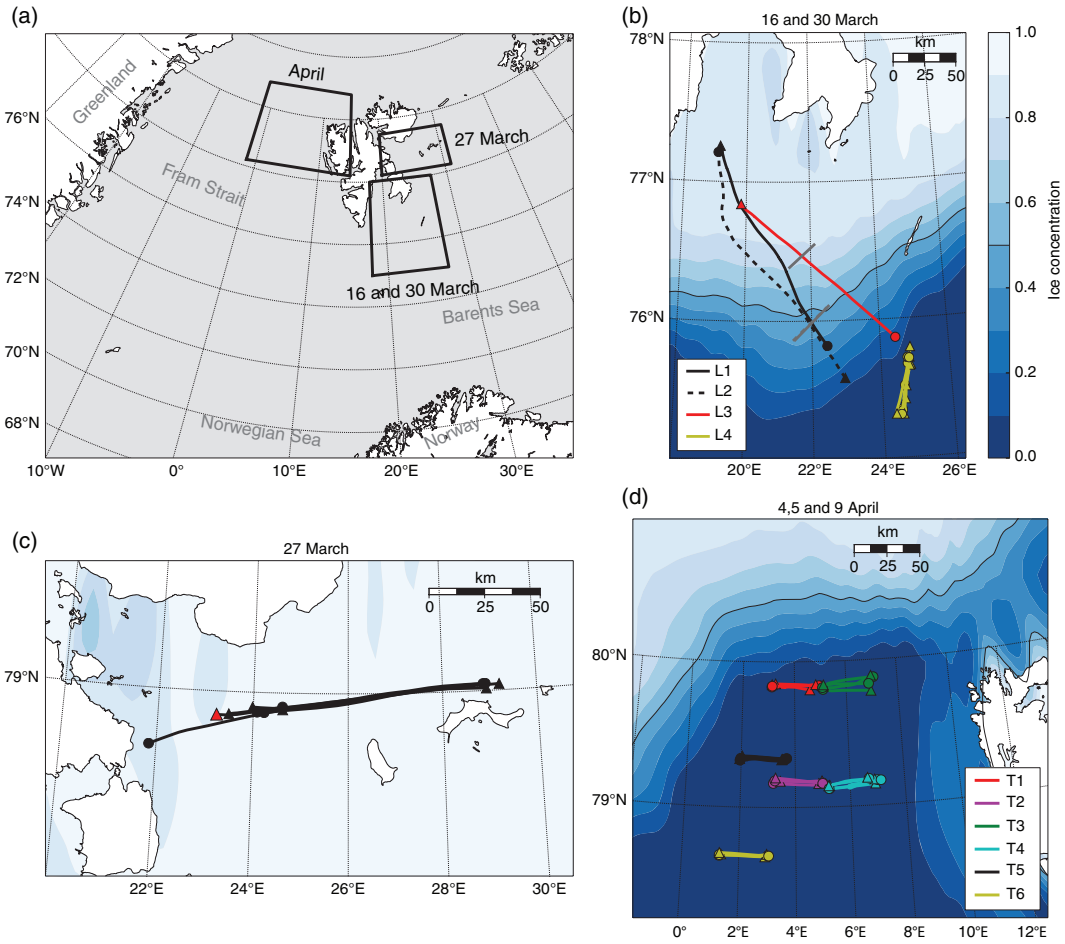

Figure 2. The study regions (a) and their flight tracks on 16, 27 and 30 March and during April 1998 (b)–(d). In each of the panels (b)–(d), the flight starts from the triangle and ends at a circle. In (b), the ice edge of each flight determined from surface radiation temperature measurements is shown as a grey line crossing the flight track. The blue colours show the sea ice concentration from Nimbus-7 SMMR and DMSP SSM/I-SSMIS Passive Microwave Data (National Snow and Ice Data Center, University of Colorado, Boulder, CO, USA) on (b) 30 March, (c) 27 March and (d) 5 April.

The case on 27 March 1998 is characterized by cold-air advection over the sea ice east of Svalbard (Vihma *et al.*, 2005). The flow was mainly from the east and the flight direction was parallel to the wind direction. The measurements consisted altogether of six low-level flights with a varying length (Figure 2(c)).

The flights in April were taken over open water during periods of cold-air outbreaks (Gryanik and Hartmann, 2002). Each flight track consisted of 4–5 flight legs at altitudes between about 35 and 1150 m. The lengths of the legs were 31–43 km, covering about 7–11 min each, the average flight speed (V_a) being about 60–75 m s^{-1}.

Turbulence measurements were taken at high frequency (120 Hz) by a five-hole probe. With a flight speed of $V_a \approx 70$ m s^{-1}, the spatial resolution is about $f_a/V_a = 1.7$ m^{-1}. During the flights used in this study, the flight speed relative to Earth's surface varied between about 50 and 80 m s^{-1}. The air temperature (T_a), relative humidity from a Väisäla humicap and specific humidity (q) from a Lyman-α hygrometer were also measured on board. The flight altitude (z) was determined as a barometric altitude based on local QNH (barometric pressure adjusted to sea level) and temperature profile and the aircraft location was determined using the Global Positioning System (GPS). Furthermore, the surface radiation temperature was measured. It will be used to distinguish open water from sea ice: over open water, the surface (radiation) temperature is close to the freezing point (−1.8 °C), while over sea ice it is much colder during this season and close to the low-level air temperature.

The boundary-layer height (h) was determined from profiles flown. In the case of flights L1–L3 and those on 27 March, the profiles were available at both ends of the horizontal flight tracks. These estimates of h were linearly interpolated to cover the whole flight leg except in case L3, where it was assumed that h over sea ice was equal to the h determined from the profile at the Svalbard end of the leg; over water we used the value derived from the profile measured over the open sea.

3.2. *Other measurements*

To relate the gust length-scales to the gust time-scales at a fixed point using the peak factor method (M4), we will need turbulence measurements from a fixed location, preferably from a weather mast. However, there were no such measurements available in the near environment of the aircraft observations. Comparison of gust factors from different environments is not meaningful, but using peak factors instead it is possible to compare turbulence measurements from different environments (method M4 in section 2.1 and Appendix A). Thus, we used measurements from a tower at the Danish National Test Station for Large Wind Turbines, which is located in Høvsøre, northwest Denmark. This site was chosen because it has already been extensively

investigated for gusts (Suomi *et al.*, 2015). The measurements at Høvsøre cover a full year (2010) and are available from several heights. Here we will use observations from 10, 40 and 60 m levels. Like Suomi *et al.* (2015), we will use data only from the eastern sector (50– 140°), because it represents homogeneous, flat grassland terrain without major obstacles disturbing the flow field. More detailed information about the data is provided by Suomi *et al.* (2015) and about the site by Peña *et al.* (2016).

To investigate the dependence of the peak factor on surface roughness, data from nine Finnish weather stations were used. The stations represent conditions in a marine environment (WMO stations 02964, 02981, 02761), on top of a fjeld (02705), over grassland (02974, 02753) and at sites surrounded by large roughness elements such as trees and bushes (02860, 02745, 02915).

3.3. Data processing

All high-frequency measurements (aircraft, weather mast) were checked for unphysical values and spikes. These values were replaced by linear interpolation of neighbouring data points. Then the data were divided into samples and only those with at least 99.9% of good data were included in further calculations. To define the gust length-scales using method M4, both data sets were divided into samples of variable length. For the sonic anemometers at Høvsøre, the sample lengths varied from T = 5–30 min and those for the aircraft data from X = 1–30 km.

For each sample, the mean horizontal wind speed U, standard deviation of the wind speed σ_u and gust $U_{\max}$ were calculated. For method M4, gusts were calculated by prescribing various durations and lengths, respectively. For the sonic anemometers the range was from $t_g = 1$ s to $t_g = 10$ s and for the aircraft data from $x_g = 1$ m to $x_g = 300$ m. These time- and length-scales are used to determine the length-scales that correspond to the time-scales of [$t_g = 3$ s, $T = 10$ min], hereafter referred to as [$x_{g,3}$, X_{600}], using the peak factor method M4 (section 2.1).

After defining the length-scale counterparts for the gust time-scales, the data were divided into bins using the optimal sample length X_{600}. The rotation of the wind coordinate system into streamline coordinates was done using the double rotation method (e.g. Rebmann *et al.*, 2012). The virtual potential temperature was calculated as $\theta_v = (1 + 0.61q)\theta$, where θ is the potential temperature and q is the specific humidity.

Friction velocity and the Obukhov length were calculated at flight height as $u_{*z} = -((\overline{u'w'})^2 + (\overline{v'w'})^2)^{1/4}$ and $L_z = -u_*^3 \left(\kappa \frac{g}{\theta_v} \overline{w'\theta_v'}\right)^{-1}$, respectively, where the subscript z refers to the flight height. The prime denotes the fluctuating part of a variable and the overbar represents the sample mean. g is the acceleration due to gravity.

The gust parametrization method by Wieringa (1973), Eq. (7), requires surface roughness as input. Because the flight altitude of the low-level flights varied from 20–70 m, the measurements do not necessarily represent the constant flux layer, especially in the case of stable conditions and a shallow boundary layer. To calculate the roughness length, the measured fluxes must first be extrapolated down to the surface values. For that, we assume a linear decrease of turbulent fluxes of momentum ($\tau_0 = -\rho u_{*0}^2$) and heat ($H_{v0} = \rho c_p \overline{w'\theta_{v0}'}$) from their surface values to zero at the top of the boundary layer ($z = h$), i.e.

$$\tau(z) = \tau_0 \left(1 - \frac{z}{h}\right)$$

and

$$H_v(z) = H_{v0} \left(1 - \frac{z}{h}\right),$$

respectively. The surface friction velocity and the Obukhov length then become

$$u_{*0} = u_{*z} \left(1 - \frac{z}{h}\right)^{-1/2}$$

and

$$L = L_z \left(1 - \frac{z}{h}\right)^{1/2},$$

respectively, and the roughness length is obtained as

$$z_0 = z / \exp\left(\frac{\kappa U(z)}{u_{*0}} + \psi_m\left(\frac{z}{L}\right)\right).$$

The similarity function ψ_m is defined as

$$\psi_m = -5\frac{z}{L} \text{ for stable } (L > 0)$$

and

$$\psi_m = \ln\left[\left(\frac{1+x^2}{2}\right)\left(\frac{1+x}{2}\right)^2\right] - 2\tan^{-1} x + \frac{\pi}{2}$$

for unstable ($L < 0$) conditions, where

$$x = \left(1 - 15\frac{z}{L}\right)^{1/4}$$

(e.g. Arya, 2001). Finally, the drag coefficient for neutral stratification at a height of 10 m is calculated as

$$C_{dn10} = \kappa^2 \left[\ln\left(\frac{10}{z_0}\right)\right]^{-2}.$$

We compared the present height-correction method with a correction method based only on M–O theory and with the method described by Garbrecht *et al.* (2002) and Vihma *et al.* (2005), which is based on mesoscale model results. We found that, for neutral conditions and $h = 100$ m, the latter method and the present method result in nearly the same correction coefficients (e.g. 1.62 for $z = 30$ m and $z_0 = 10^{-3}$ m), while this factor equals 1.3 for a correction based on the constant flux-layer assumptions without introducing linear flux profiles. The advantage of the present correction is that it accounts for the influence of the boundary-layer height. We stress, however, that the sensitivity of the main results in the present article (see sections 5–7) to the correction factor was small, because the height correction was only applied to derive a proper estimate for the surface roughness (z_0), which is required in the parametrization by Wieringa (1973), Eq. (7). All other parametrizations were tested only locally at the flight height (without any height corrections).

In this study, we use observed gust factors at different flight levels to assess the applicability of literature-based gust parametrizations and to quantify possible errors. Two of the parametrizations considered are height-dependent (the method by Wieringa (1973), Eq. (7), and the one by Suomi *et al.* (2013), Eq. (10)), so that comparison with aircraft measurements is straightforward. Note that the method by Suomi *et al.* (2013) even includes a similar height correction to that introduced above to derive z_0 from aircraft measurements. The gust parametrizations by Wichers Schreur and Geertsema (2008) (Eq. (8)) and by Woetman Nielsen and Petersen (2001) (Eq. (9)) do not depend on height and were constructed for the surface layer. Nevertheless, we apply them and compare their results with the aircraft measurements at flight height, which is possible since in most cases the latter is not far from the surface layer. However, one has to keep this in mind in the analysis of differences in section 6.

4. Determination of gust length-scales

In this section, we will apply the four methods introduced in section 2.1 to determine the gust length-scales and then compare the results to yield the optimal gust lengths $x_{g,3}$ and X_{600} to be applied in sections 5 and 6.

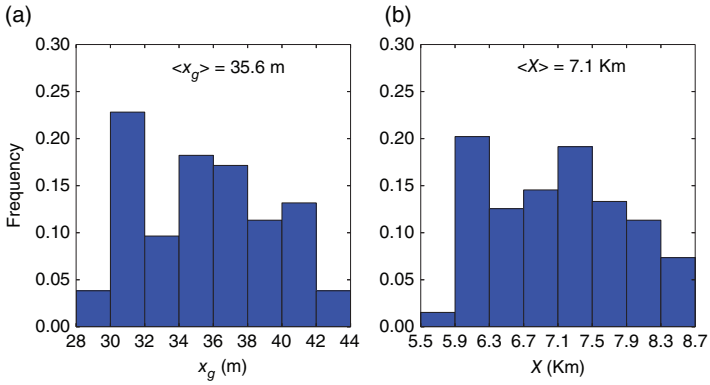

Figure 3. Distribution of (a) gust length x_g and (b) sample length X corresponding to the time-scales $[t_g, T] = [3\,\text{s}, 10\,\text{min}]$ using method M2. The median of the length-scales is $[x_{g,3}, X_{600}] = [35.6\,\text{m}, 7100\,\text{m}]$. The figure is based on data from all low-level flights.

Table 1. Gust length-scales and their sensitivity to g_x (in brackets) using the peak factor method M4.

z (m)	x_g (m)	X (km)
10	13.3 [6.4, 24.7]	6.0 [2.9, 11.6]
40	15.6 [8.1, 29.0]	4.7 [2.4, 9.2]
60	15.7 [8.0, 28.7]	4.2 [2.2, 8.5]

Sensitivity values show the range of length-scales for $g_x(3, 600\,\text{s}) \pm 0.2$ along the x_g and X axes of Figure 4.

In method M1, we assume a constant wind speed $U = 10\,\text{m s}^{-1}$ and a constant flight speed much higher than the advection speed along the flight track, i.e. $V_a \gg U_x$. Hence, following Eq. (1), the gust length-scales become $[x_{g,3}, X_{600}] \approx [30\,\text{m}, 6000\,\text{m}]$. In reality, however, the condition $V_a \gg U_x$ was not true. In the case of horizontal low-level flights, the ratio U_x/V_a varied from about -0.15 to about 0.2 (where the minus sign is for the cases where the flight direction is in the direction of the flow). However, the gust factor did not correlate with U_x/V_a, which means that other effects affecting the gust factor were more important than U_x.

Figure 3 shows the frequency distribution of the gust length-scales resulting from M2. Basically, both length-scales x_g and X depend on the speed of the aircraft ($X = (f_s/f_a)V_a T$ and $x_g = (f_s/f_a)V_a t_g$). Taking all low-level flights (flight altitude 20–70 m), the medians of these length-scales are $[x_{g,3}, X_{600}]$=[35.6 m, 7100 m]. The range of x_g is from 28–44 m and X varies from 5.5–8.5 km.

Figure 4 and Table 1 show the results for the peak factor method M4 (section 2.1 and Appendix A). A two-dimensional linear least-squares fit was made between the median peak factor field from the low-level (20–70 m) flights of the ARTIST campaign and three heights of the Høvsøre weather mast, 10, 40 and 60 m. In general, peak factors at 10 m level are higher than at 40 or 60 m levels of the mast (colour scale of Figure 4). The best fit with $[t_g, T] = [3\,\text{s}, 600\,\text{s}]$ at the 10 m level was found with $[x_{g,3}, X_{600}] = [13.3\,\text{m}, 6000\,\text{m}]$, at the 40 m level with $[x_{g,3}, X_{600}] = [15.6\,\text{m}, 4700\,\text{m}]$ and at the 60 m level with $[x_{g,3}, X_{600}] = [15.7\,\text{m}, 4200\,\text{m}]$. These x_g values are much smaller (by a factor of 2 or even more) than those obtained by methods M1 and M2. Nevertheless, the results for the sample length X are at least of the same order of magnitude for all methods M1, M2 and M4. The values with the peak factor method M4 (4.2–6.0 km) are on average somewhat lower than the median length (7.1 km) of M2 (Figure 3(b)). According to e.g. Emeis (2014), the turbulence length-scale is small close to the surface and increases with height. Therefore, in eddy covariance calculations, at higher altitudes a longer sampling period is typically required compared with lower altitudes, where more (small) eddies pass the instrument within a given period. In our results from the peak factor method (M4), the sample length X used in determining the gusts behaves in the opposite fashion: the sample length X decreases with height. Another important point is that the results of method M4 do not fulfil the criterion of M3, i.e.

$$\frac{x_{g,3}}{X_{600}} = \frac{3}{600}.$$

We have now determined the gust length-scales corresponding to the gust time-scales usually used for weather masts using three different methods. Still, we do not yet have evidence showing which of the methods is the most superior. For this, we study the sensitivity of the observed gust factors and peak factors to the length-scale results. Figure 5 shows the observed median gust factor G and observed median peak factor g_x as a function of various gust lengths x_g from 10–50 m (x-axes) and sample lengths X from 4–12 km (different curves). These were calculated using data from all low-level (20–70 m) horizontal flights. At first the data were divided into bins of length X and then, for each bin, the gust factor and the peak factor were calculated using different values for x_g. The calculation was repeated for several sample lengths X. For each combination of $[x_g, X]$, the median and the standard error of the mean for G and g_x were calculated from all flights and the results are shown in Figure 5. Over these results, we have plotted (as dashed lines) the optimum values of $[x_{g,3}, X_{600}]$ according to methods M1, M2 and M4. These optimum length-scales give almost the same median gust factor, about 1.22, except for M4 with a 6 km sample length, which provides a slightly higher G than the others.

M1 and M2 result in almost the same peak factor g_x (about 2.26, Figure 5(b)), whereas the values generated by method M4 are slightly larger, around 2.4. Only M4 is based on the comparison of peak factors from the aircraft and the weather mast. The difference in the results between M4 and M1/M2 could be due to the differences in the environments where the data were collected. At Høvsøre, the terrain was flat grassland, while the aircraft measurements in this study were taken in a marine environment over sea ice and open water. The dependence of the peak factor on surface roughness is not well known. Therefore, we calculated peak factor distributions for nine Finnish weather stations with different terrain types including sea, the top of a field, flat grassland and rougher environments such as forest. The results showed that over the sea and at the top of the fjeld the median peak factors were typically around 2.2, whereas over grassland (e.g. airports) they were about 2.5 and even higher (up to 3.0) over more rough terrain. Therefore, the higher peak factor resulting from method M4 in Figure 5 may be due to differences in the surface type. Furthermore, the results of method M4 do not satisfy the condition of M3, $x_{g,3}/X_{600} = 3/600$, whereas those of methods M1 and M2 do. For these reasons, we will not use M4 to

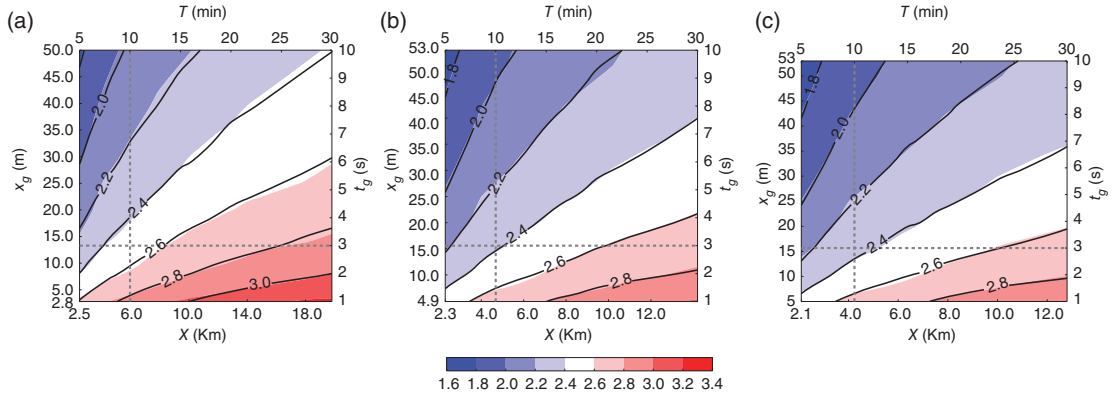

Figure 4. Peak factor fields from the ARTIST campaign (colours) and Høvsøre weather mast (black lines) at (a) 10 m, (b) 40 m and (c) 60 m levels. The fields from different data sources were fitted using the least-squares method by changing the gust length-scale ranges on the axis on the left and below the figure, while the time-scale ranges above and on the right of the figure were kept unchanged. A detailed description of the method is provided in Appendix A. The dashed horizontal and vertical lines represent the time-scales $[t_g, T] = [3\,\text{s}, 600\,\text{s}]$ corresponding to the length-scales shown in Table 1.

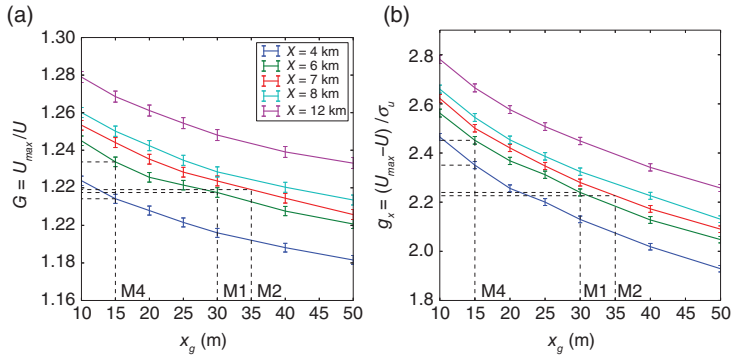

Figure 5. (a) Median gust factor and (b) peak factor as a function of gust length x_g with sample lengths X from 4–12 km (curves). The error bars show the standard error of the mean. The optimum length-scales $[x_{g,3}, X_{600}]$ by methods M1, M2 and M4 are shown as dashed lines.

determine the gust length-scales in this study. However, this does not mean that M4 could not be applied to derive the optimum length-scale counterparts for the gust time-scales. It may give very good results if parallel observations from an aircraft and a weather mast are available.

The differences between the length-scales obtained with methods M1 and M2 are small. With M1 they are $[x_{g,3}, X_{600}] = [30\,\text{m}, 6000\,\text{m}]$ and with M2 $[x_{g,3}, X_{600}] = [35.6\,\text{m}, 7100\,\text{m}]$. Here, we choose to apply only the results of method M1 from here on. However, it can be seen from Figure 5 that practically the same results in terms of G and g_x would also have been obtained with M2 and, moreover, with all other combinations of x_g and X satisfying the condition of M3, which is $x_{g,3}/X_{600} = 3/600$. For example, with $x_{g,3} = 20\,\text{m}$ we have $X_{600} = 4000\,\text{m}$, which in Figure 5 gives approximately the same results as with M1 and M2.

5. Gust factors in the Arctic marine boundary layer

In this section, we will first investigate the gustiness conditions during the horizontal low-level flights, including all flight tracks shown in Figure 2. The main focus will be on flights L1–L3 (16 and 30 March) and on those during 27 March. They were taken over sea ice or its near vicinity. Then, in the second part of this section, we will analyse the vertical gust profiles from the flight tracks that included horizontal legs at multiple heights. These flights have been carried out mainly over open water with strong unstable stratification in the ABL.

5.1. *Low-level flights over sea ice and open water*

Figures 6 and 7 show the meteorological variables during the low-level horizontal flights on 16 and 30 March (flights L1–L4) and on 27 March 1998, respectively. During L1 and L2, the prevailing wind direction was from the southeast from open ocean across the ice edge towards Spitsbergen. The flight direction was parallel to the flow (Figure 2). During L3, the flow direction was from the east/northeast, i.e. parallel to the ice edge, while the flight direction was perpendicular to the flow. The flights during 27 March (Figure 7) were parallel to the wind direction.

In the case of L1 and L2 (Figure 6), the boundary layer was stably stratified throughout both flights. Over the open ocean, $1/L$ (L is the Obukhov length) and thus the stable stratification decreased slightly towards the ice edge but increased dramatically a few kilometres downwind, north of the ice edge. Further downwind, it gradually decreased towards Spitsbergen. The changes in the neutral drag coefficient were quite opposite to those of $1/L$. Over the open ocean and across the ice edge, C_{dn10} increases. When the stability started to increase over sea ice a few kilometres downwind of the ice edge, C_{dn10} became extremely low. The behaviour of the surface roughness and thus C_{dn10} in the Storfjorden region has been described by Garbrecht *et al.* (2002) and Vihma *et al.* (2005). The gust factor was smallest over the open ocean and some kilometres north of the ice edge and largest near Spitsbergen. Even though the flight legs L1 and L2 were not exactly from the same track (Figure 2) and there was almost a 2 h time lag between the measurements on the open water side (the flight time of one flight leg was about 50 min), the measurements from both flights were in good agreement. Standard deviations in the wind velocities

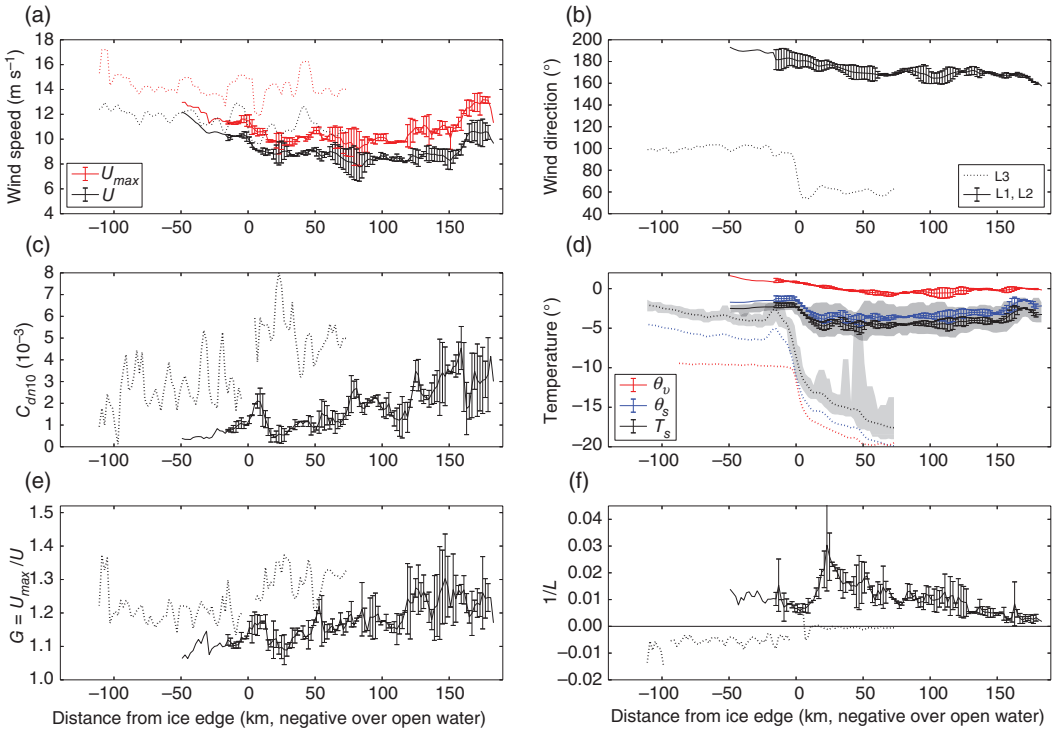

Figure 6. (a) Mean wind speed and wind gust speed, (b) wind direction, (c) neutral drag coefficient at 10 m height, (d) air and surface temperatures, (e) gust factor and (f) the inverse of the Obukhov length as a function of distance from the ice edge for three horizontal low-level flight legs: L1 and L2 on 16 March (solid lines with error bars) and L3 on 30 March 1998 (dotted lines). Each data point represents a 6 km sample centred at the midpoint of the sample and all parameters were (calculated and) plotted by 2 km intervals. In the temperature plot (d), the shaded areas represent the intervals between the maximum and minimum surface temperatures. The results of the flight legs L1 and L2 are combined and the error bars show the standard deviation of the two passes for each bin.

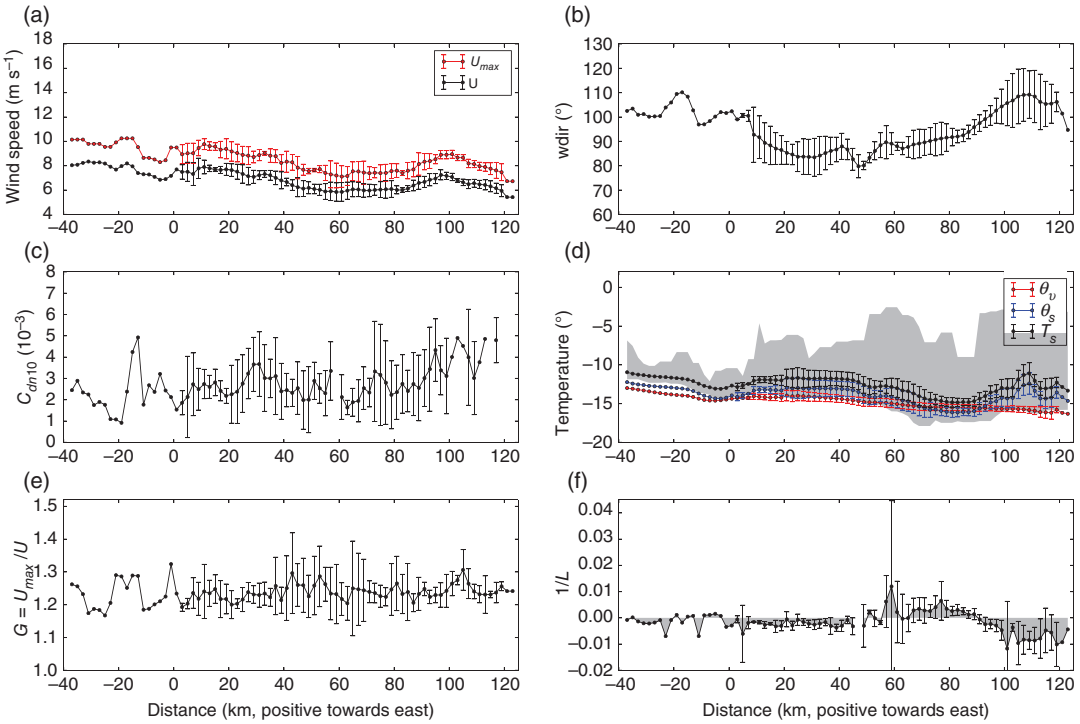

Figure 7. As Figure 6, but for the flight legs on 27 March 1998. The distance is given relative to the reference point shown in Figure 2(c). The error bars show the standard deviation of all the passes for each bin. At the western end of the flight track, there was only one pass available.

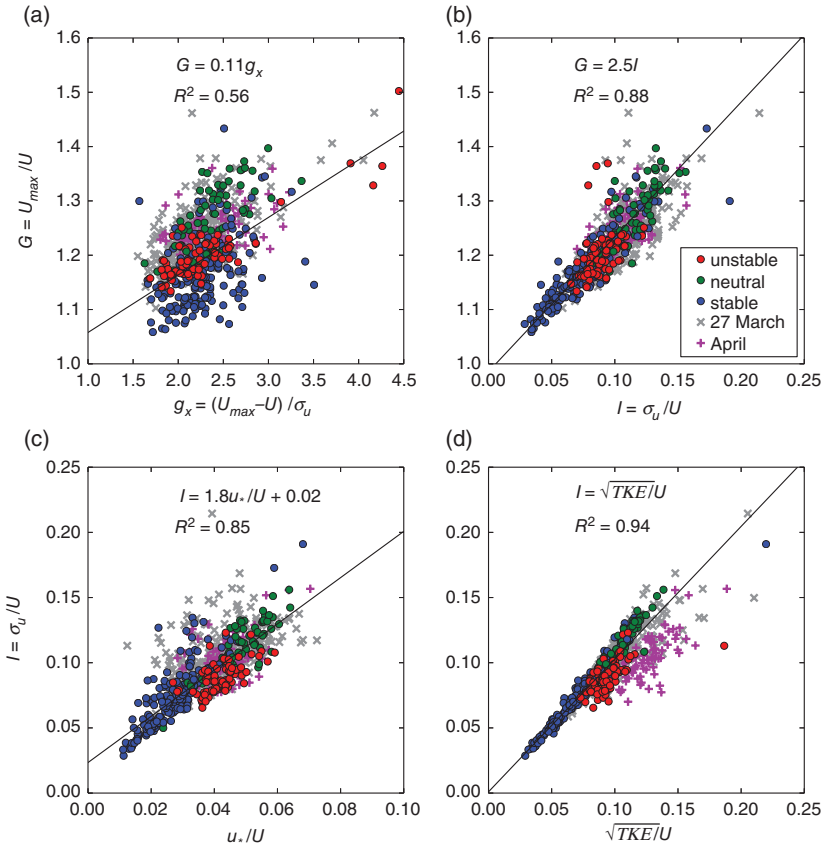

Figure 8. Gust factor as a function of (a) peak factor and (b) turbulence intensity, and turbulence intensity as a function of (c) u_*/U and (d) $\sqrt{\mathrm{TKE}}/U$ for low-level ($z < 70$ m) flights. Flights L1–L4 are shown by stability class (unstable: $0 > L > -250$ (red), neutral: $|L| > 250$ (green), stable: $0 < L < 250$ (blue)). In each plot, the linear fit and the correlation coefficient (R^2) are based on L1–L4; the results of flights on 27 March and in April are shown for illustration only.

were largest between about 60–90 km, but the drag coefficients and gust factors differed most between the legs in the Spitsbergen end of the track.

During flight leg L3, conditions were unstable over the open ocean and near-neutral over sea ice (Figure 6(f)). Surface roughness and accordingly C_{dn10} were clearly larger over sea ice than over the open ocean, which was reflected as a larger gust factor G (Figure 6(c) and (e)). C_{dn10} over ice is also much larger than during L1 and L2. After 16 March (L1, L2), the ice conditions changed. During 30 March at L3, there was extremely rough sea ice in Storfjorden with new, chaotically distributed pressure ridges, explaining the extremely high C_{dn10} over ice. Near the ice edge, there was a belt of rough pancake ice with nearly 100% cover and the diameter and the thickness of these ice floes decreased towards the open water.

Conditions during the flights on 27 March were variable in space and time (Figure 7). In the western part, where only one flight was available, the stability conditions were near-neutral but there were large fluctuations in C_{dn10} along the flight track. The differences in C_{dn10} between different flight passes in other parts of the track were clearly larger than during 16 March (L1 and L2, Figure 6), indicating that the roughness conditions also changed in time. The same is also seen in the observed gust factors.

Although the flights on 27 March were over sea ice (broken by leads), the stratification was mostly unstable between 0 and 50 km. However, at about 50–90 km there was a stable region, co-located with a surface temperature minimum. In these two regimes, the standard deviations of the stability parameter calculated over all flight legs were large at around 60 km, indicating that the stability changed in time. According to Vihma *et al.* (2005), the sky was cloudy at both ends of the flight track but clear in the middle, where the surface temperature had its minimum. The western side cloud edge in the middle of the track moved westwards during the course of the flight legs, which caused non-stationarity in the results, especially in the stability parameter $1/L$ shown in Figure 7(f). In the east, there was a region of small leads covering about 5% of the surface area, which can be seen as surface (radiation) temperature maxima close to the freezing point. The sea ice surface was relatively rough, because easterly winds had prevailed for a few days and the ice was packed against the east coast of Spitsbergen. The air mass also had a long fetch (at least 1000 km) over the sea ice (Vihma *et al.*, 2005).

Overall, the conditions during the flights on 27 March varied in space and time. The surface roughness was non-homogeneous due to ridges, flow edges and leads. Leads also caused heterogeneity in surface heat fluxes and the evolving cloud cover amounted to the non-stationarity in the surface energy balance.

As discussed in section 2.2, the gust factor is composed of two components, the peak factor g_x and the turbulence intensity I (Eq. (5)). Figure 8(a) and (b) shows the observed G as a function of g_x and I, respectively. The correlation between G and g_x ($R^2 = 0.56$) is lower than that between G and I ($R^2 = 0.88$), showing that G is dominated by the variability in I. A linear fit to the results of flight legs L1–L4 shows only a weak dependence of G on g_x, by a factor of 0.11, whereas G depends on I by factor of 2.5. Hence, the variation in the gust factor is mainly determined by the variations in the turbulence intensity, not those in the peak factor. This conclusion is in line with the findings of Suomi *et al.* (2015) based on mast measurements in Denmark. However, it should not

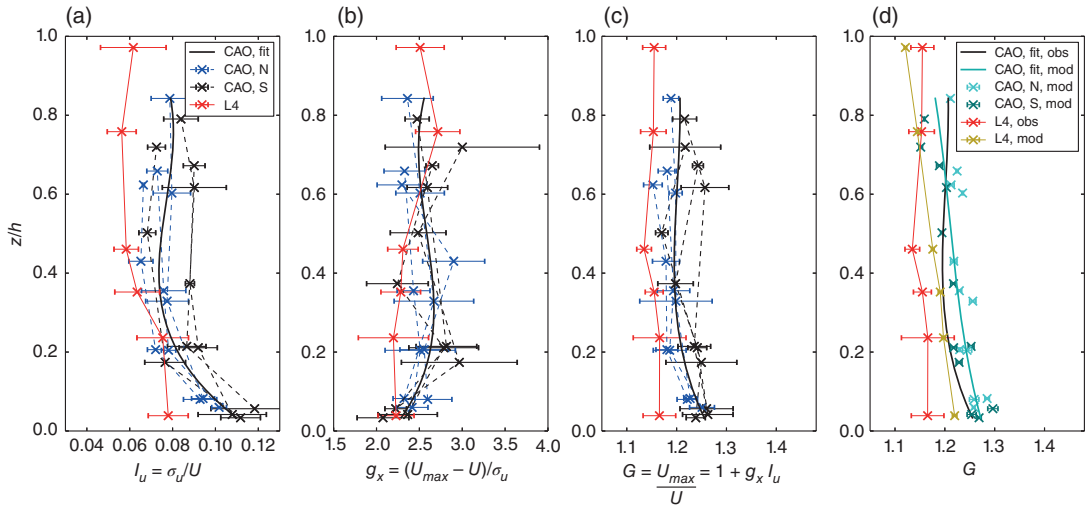

Figure 9. Profiles of the observed median (a) turbulence intensity, (b) peak factor and (c) gust factor and (d) the parametrized median gust factor using the method by Suomi *et al.* (2013). The error bars show the standard error of the mean. The flights on 30 March (L4) are shown in red and those in April (cold-air outbreak, CAO) in blue and black. Blue markers (CAO, N) indicate flights closer to the ice edge in the north than those in black (CAO, S), which are further downstream in the south on each day. A cubic fit to the April data is shown as a thick black line. For comparison, the gust factor profiles from (c) (red and black curves) are also shown in panel (d), where 'obs' in the legend refers to observed values and 'mod' to parametrized ones.

be forgotten that only the peak factor – not the turbulence intensity – determines the effects of the gust length-scales on the gust factor. This means that, once the gust length-scales are fixed, the turbulence intensity is the main component that determines the gust factor.

Figure 8(c) and (d) shows how I depends on u_*/U and on $\sqrt{\mathrm{TKE}}/U$. These parameters were chosen because they are included in the parametrizations of Eqs (8)–(10) (Woetman Nielsen and Petersen, 2001; Wichers Schreur and Geertsema, 2008; Suomi *et al.*, 2013). Moreover, the mean wind speed U is in the denominator of both parameters and therefore a linear relationship between these parameters and $I = \sigma_u/U$ can be expected. R^2 is high in both Figure 8(c) and (d), but it is higher between I and $\sqrt{\mathrm{TKE}}/U$, as expected, because σ_u is included on both sides. The best fit between I and $\sqrt{\mathrm{TKE}}/U$ has a slope of 1.0 instead of $\sqrt{2}$ as in Eq. (8). However, Figure 8(d) also shows that unstable conditions are mainly below this fitted line, especially those in April during cold-air outbreaks, and the near-neutral conditions with high I (due to rough surface) are above the fitted line. We also investigated the dependence of g_x on u_*/U and $\sqrt{\mathrm{TKE}}/U$, but it was weaker than the dependence of I on u_*/U and $\sqrt{\mathrm{TKE}}/U$. Moreover, the dependence of I on w_*/U (Eq. (9)) and $[-h/(\kappa L)]^{1/3}$ (Eq. (10)) in unstable conditions was in general weak, with a very low correlation.

The strong dependence of G on the surface roughness might allow its parametrization as a function of drag coefficients over sea ice. Possible candidates are the parametrizations by Lüpkes *et al.* (2012) (neutral) and Lüpkes and Gryanik (2015) (non-neutral conditions). Their formulations of C_d include the effect of topography caused by floe and lead/melt pond edges, which was parametrized as a function of the sea-ice concentration. Thus, with given sea-ice concentration maps, an Arctic-wide distribution of G could be obtained in the future, accounting at least for the topography effect of floe and lead/pond edges.

The data from 27 March alone show no clear dependence of G on I, or I on u_*/U or $\sqrt{\mathrm{TKE}}/U$, even though the data in Figure 8 fit well into the range of values from flights L1–L4. Sometimes gust factors are used to determine surface roughness when no other information on turbulence is available (e.g. Verkaik, 2000). In the case of flights on 27 March, for which the atmospheric and surface conditions were highly variable in time and space, one cannot obtain reliable estimates for the roughness length along the flight track based on the measured G.

In this section, we have investigated the dependence of the gust factor along the horizontal low-level flights in various atmospheric and surface conditions. The gust factor was found to depend mainly on the surface roughness with a high C_{dn10}, whereas the effect of stability on G was found to be less important.

5.2. *Vertical profiles of the gust factor in unstable conditions over open sea*

In this section we will derive gust profiles based on horizontal flights at multiple heights over the same flight track. Such data were available from 30 March (L4) and from the flights on 4, 5 and 9 April. Figure 9 summarizes the results of these flights. On 30 March, the profiles represent unstable conditions over the open sea near the sea-ice edge when the flow was parallel to the ice edge (a long fetch over open sea). This flight took place on the same day as flight L3 (Figures 2 and 6). According to Figure 9, the observed G was fairly constant with height. In the lower part of the boundary layer, I was slightly larger than in the upper part. On the other hand, g_x was somewhat smaller in the lower part of the boundary layer compared with the upper part. These effects partly compensated for each other in the G profile, which is nearly vertical.

The flights on 4, 5 and 9 April represent conditions in cold-air outbreaks, where the atmospheric flow was directed from sea ice to the open sea in the Fram Strait. There were two flight tracks on each day at different distances from the ice edge. In Figure 9, those closer to the ice edge are marked in blue whereas the ones further downstream in the south are in black. In general, the blue profiles have slightly smaller G and I values compared with the black ones, as expected. In g_x, no such systematic difference between the profiles can be seen. Instead, g_x varied significantly from track to track, especially between about $z/h = 0.1$ and $z/h = 0.6$. At the lowest measurement level, I was high and decreased strongly to the second observation level. In contrast, g_x exhibited the opposite behaviour, which led to a situation where the G profile decreased only marginally with height.

In Figure 9(a)–(c), a third-order polynomial fit is applied to the April data. During these cold-air outbreaks, gust factors were slightly higher than on 30 March (L4) throughout the profile. At L4, the peak factor did not change much with height in the lower

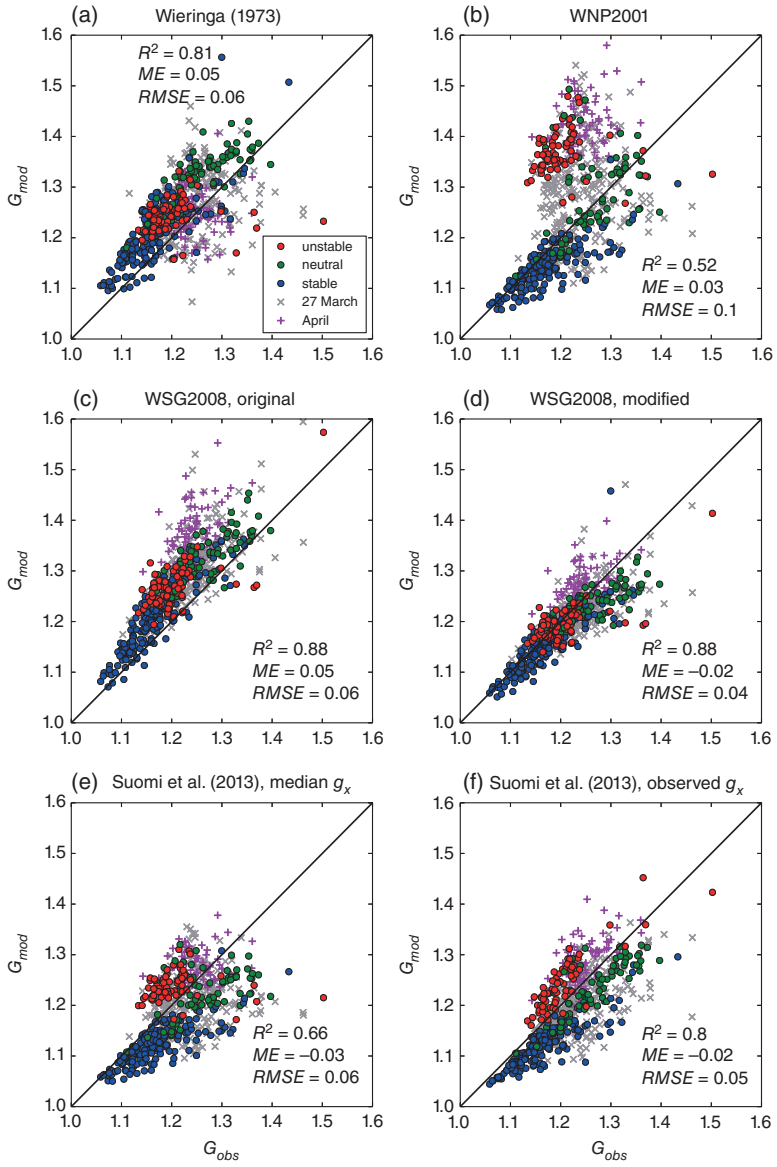

Figure 10. Parametrized gust factor obtained by several different methods, (Wieringa, 1973; Woetman Nielsen and Petersen, 2001 (WNP2001); Wichers Schreur and Geertsema, 2008 (WSG2008); Suomi *et al.*, 2013). The gust factors using the method by Wichers Schreur and Geertsema (2008) were calculated using g_x from observations (b) and by calculating $g_x r_\sigma$ using the spectrum from observations (d) and the empirical spectrum from Kaimal (1978) (f). Colours and markers indicate the same as in Figure 8.

half of the boundary layer. During cold-air outbreaks, the near-surface g_x was similar to the one at L4, but above that it clearly became larger than at L4. The turbulence intensity was clearly higher near the surface during April cold-air outbreaks than at L4. Because of that, the differences between the gust factors in cold-air outbreaks and at L4 were largest near the surface.

6. Validation of gust parametrizations

In this section, we will compare the four different gust parametrizations presented in section 2.2, i.e. Eqs (7)–(10). The results are shown in Figure 10. The highest correlations with observations were found with the Wichers Schreur and Geertsema (2008) method (Eq. (8)). With the original formulation, there was a clear positive bias (ME) because of the formulation $G = f(\sqrt{2\mathrm{TKE}}/U)$ instead of $G = f(\sqrt{\mathrm{TKE}}/U)$, which is supported by Figure 8(d). The latter is applied in Figure 10(d). After this modification, there was, however, a small negative bias, which was caused by the peak-factor formulation. The peak factor in Figure 10(c) and (d) was calculated using the formulation of Appendix B by applying the spectrum $F(k)$ calculated from observations. Figure 11 shows the peak-factor distributions for observed g_x and for g_x resulting from the statistical peak-factor method (Appendix B). The range of observed values is quite large, from about 1.6 to above 3.0, with a median of 2.26. The ones calculated using the observed spectrum correspond well with observations at the low end of values, but they underestimate the highest values and this is seen as a negative bias in Figure 10(d). Values for g_x calculated using the empirical spectra are nearly constant, from about 2.3–2.6, representing conditions typical for flat grassland.

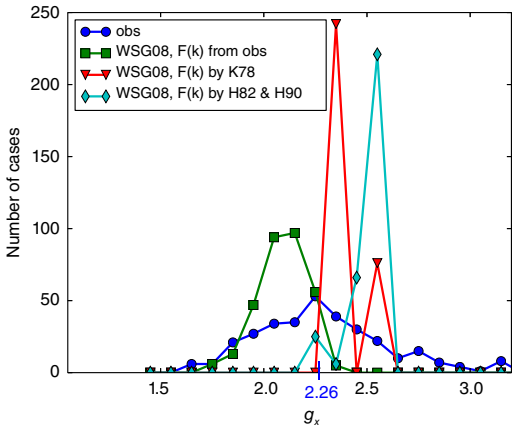

Figure 11. Peak factor ($g_x = (U_{max} - U)/\sigma$) distributions calculated from observations (obs) and by using Eqs (B6) and (B9) as $g_{x,f}r_\sigma$ (WSG08). Spectra in the latter method were determined from observations (obs) and using empirical spectra by Kaimal (1978, K78), Højstrup (1982, H82) and Højstrup *et al.* (1990, H90).

In Figure 10, the method by Wieringa (1973) clearly overestimates the gust factors at the flight height. The method was originally developed for the constant-flux layer, which did not reach the flight heights (20–70 m), especially in stable conditions with a shallow boundary layer ($h < 150$ m). There was also a general overestimation of gust factors by the method of Woetman Nielsen and Petersen (2001). This was mainly due to the unrealistically high G in unstable conditions, whereas in stable and neutral conditions G was even slightly underestimated. These results are in agreement with those of Suomi *et al.* (2013).

The method by Suomi *et al.* (2013) has a small negative overall bias in Figure 10(e). The model performs well in near-neutral conditions, but underestimates G in stable conditions over rough surfaces (high observed G). In unstable conditions, the method gives a G value that is slightly too high. In Figure 10(e), we have used the median g_x (2.26). If the observed g_x is used instead, as in Figure 10(f), the results are improved, with a higher R^2 and smaller ME and root-mean-square error (RMSE).

Overall, all gust parametrization methods that were originally developed for 10 m winds observed at weather stations performed well when applied to the aircraft data. This means that the derivation of the gust length-scales in section 4 was successful. Moreover, it shows that gusts measured in very different conditions, such as at weather stations in the midlatitudes, behave similarly to those over Arctic sea ice and open sea.

The parametrization by Suomi *et al.* (2013) provides a possibility of estimating G within the entire boundary layer. The results are shown in Figure 9(d). The profiles were calculated using a constant peak factor ($g_x = 2.26$). For comparison, the observed profile on 30 March (L4) and the cubic fit to the observed April profiles are also shown. For both, there is an overestimation within the lower half of the boundary layer, except near the surface, where the fitted April profiles meet. The overestimation in the median profiles is as high as 0.06, which corresponds to about 1.0 m s^{-1} if the observed wind gust speed is 20.0 m s^{-1}. In the upper part of the boundary layer, G is underestimated both at L4 and during April. This may be related to the entrainment processes near the boundary-layer top, which are not represented in the parametrization.

7. Summary and conclusions

We have derived the optimal length-scales that should be used to calculate the gust factor from research aircraft measurements and have shown that these length-scales result in gust factors comparable with those measured at weather stations. Moreover, we have shown that the gust parametrizations originally developed for the 10 m winds observed at weather stations are applicable to gusts observed by research aircraft. In other words, the choice of gust length-scales was successful.

Optimal gust length-scales were determined using four different approaches, M1–M4. The aim was to find the length-scale counterparts [$x_{g,3}$, X_{600}] for the gust time-scales widely used at weather stations: [t_g, T] = [3 s, 10 min]. All methods provided very similar results in terms of the median gust factor, which was 1.22. Sample lengths (X_{600}) varied from 4.2 km to nearly 8.5 km. Method M4 gave the shortest distance for X_{600} and the longest values resulted from M2. Gust lengths ($x_{g,3}$) were about 30 and 35 m for M1 and M2, respectively. Method M4 resulted in a gust length that is only half that of M1 and M2 at about 15 m. However, the results of M4 did not meet the condition of M3, which is $x_g/X = t_g/T$. This does not necessarily mean that M4 could not be used to estimate gust length-scales. It may give very good results when there are available parallel measurements from an aircraft and a weather mast, which was not the case here. As a summary, we decided to use the length-scale values of M1, which were [$x_{g,3}$, X_{600}] = [30 m, 6000 m]. However, using the criteria of M3, it was shown that any combination of x_g from 20–50 m and X from 4–10 km would have led to approximately the same results in terms of the median gust factor and the median peak factor in this study.

Gustiness conditions were analyzed based on low-level horizontal flights over sea ice and open water and on profiles derived from horizontal flights at multiple levels over the same track over open water. In a typical surface-layer gust parametrization, the gust factor is composed of a peak factor and turbulence intensity. The first of these defines the effects of the gust length-scales on the gust factor and the latter was found to determine the effects of stability and surface roughness. Gust factors were higher over sea ice than over open ocean in similar stability conditions, due to the higher surface roughness over sea ice caused by ice ridges and floe edges. However, when the atmospheric conditions were highly variable with large changes in the surface energy balance, both along the flight track and during the duration of the flight, the gust factors were highly variable and no clear connection to the surface roughness or turbulence intensity was found. From such data, it is not recommended to use the observed G to estimate the surface roughness.

Overall (through the entire boundary layer), gust factors measured during a cold-air outbreak were slightly larger than those during unstable conditions over open sea, when the flow was parallel to the ice. The peak factor (g_x) typically either decreases or is constant with height within the lowest hundred metres (e.g. Suomi *et al.*, 2013, 2015). During a cold-air outbreak, however, it was found that the median g_x increased strongly with height within the lowest 200 m (up to about $z/h = 0.2$), although the turbulence intensity decreased substantially. This means that, even though the overall turbulence conditions in terms of velocity variance decreased with height, strong deviations (gusts) from the mean occasionally occurred. This feature can be important, for example, for wind turbine operations and/or aircraft safety during take-off and landing.

Four different gust parametrizations originally developed for weather stations were tested against the aircraft data. All of them performed well, with a correlation to the observed gust factor of about $R^2 \approx 0.5$ or more and with biases (in terms of ME) from −0.02 to 0.05. This means that the gust length-scales determined in this study resulted in gust factors comparable with those observed at weather stations. The highest correlations between observed and parametrized G were obtained with the Wichers Schreur and Geertsema (2008) method, but the method had a clear positive bias, i.e. it overestimated G. The bias was related to an overestimation of the variance of the horizontal wind speed by the assumption $\sigma_u = \sqrt{2\mathrm{TKE}}$. The method by Woetman Nielsen and Petersen (2001) had a large positive bias in unstable conditions over the sea, but otherwise it performed

well. A similar positive bias has also been observed before by Suomi *et al.* (2013). The method by Wieringa (1973) somewhat overestimated G at the flight heights. The method is strictly based on M–O theory, which is valid only within the constant-flux layer. The measurements analyzed in this study were taken at heights between 20 and 70 m. These were mostly above the constant-flux layer, especially in stable conditions with a shallow boundary layer ($h < 150$ m).

The method by Suomi *et al.* (2013) provides the possibility of parametrizing G within the entire boundary layer. It was applied to data where measurements were available from several heights over the same flight track. These represented unstable conditions with a long fetch over the open sea and conditions of off-ice flow during cold-air outbreaks. In both, the method slightly overestimated G in the lower half of the boundary layer, but underestimated it near the top of the boundary layer. The underestimation may be related to the entrainment processes in the upper part of the boundary layer, which are not included in the method by Suomi *et al.* (2013). Gust measurements have so far been limited to the heights reached by meteorological masts, i.e. up to a couple of hundred metres. We showed that research aircraft can also provide high-quality observations at higher altitudes.

Acknowledgements

This research has received funding from the Academy of Finland via the TWASE project (contract 283101) and from the Vilho, Yrjö ja Kalle Väisälä Foundation.

Appendices

Appendix A: Peak-factor method to determine gust length-scales

Here we introduce a new method to convert between gust time and length-scales. Instead of a gust factor, the method is based on the peak factor, which is defined as $g_x = (U_{\max} - U)/\sigma_u$ (Eq. (6)). In other words, g_x is the deviation of the wind gust speed ($U_{\max}$) from the mean wind speed (U) normalized by the standard deviation of the along-wind velocity component (σ_u). It is assumed that this normalization makes the peak factor invariant with respect to the local turbulence conditions (determined by the surface roughness and static stability of the atmosphere) and the type of data (wind speed as a function of time or as a function of flight distance).

Theoretically, the peak factor is only a function of the gust time-scales (t_g, T) or the gust length-scales (x_g, X) if the turbulent wind-speed signal is stationary, ergodic and Gaussian (Appendix B). Even though these conditions are not necessarily fulfilled in real turbulence data, we can still assume that, in an ensemble of samples, the median peak factor is only a function of the gust time or length-scales (Suomi *et al.*, 2015). Then, by comparing the median peak factors, a match between the gust time and length-scales can be accomplished. The methodology is presented in the following six steps.

(1) Peak factors are first calculated from both data sets using various combinations of time- (t_g, T) and length- (x_g, X) scales. At first, the calculations are performed separately for each sample, but the comparison is only based on the median g_x of each combination of $[x_g, X]$ or $[t_g, T]$. For simplicity, 'peak factor' in this Appendix hereafter refers to the median peak factor.
(2) The peak factors are collected together to form two two-dimensional fields, one as a function of time-scales, $g_x(t_g, T)$, and the other as a function of length-scales, $g_x(x_g, X)$. The time-scales are determined by the range of scales of interest: for example, in this study t_g is given values from 1–10 s and T from 5–30 min. The range of chosen length-scales (x_g, X) must be large enough such that the peak factors from the aircraft data will cover the range of peak-factor values in the $g_x(t_g, T)$ field.
(3) Both fields, $g_x(t_g, T)$ and $g_x(x_g, X)$, are then linearly interpolated on to an equidistant grid, with exactly the same amount of grid points on the t_g axis as on the x_g axis and on the T axis as on the X axis.
(4) The squared difference of the interpolated fields is taken as $\left(g_{x,\mathrm{interp}}(t_g, T) - g_{x,\mathrm{interp}}(x_g, X)\right)^2$ and its grid mean is calculated.
(5) Then, the range of values of gust length-scales of the interpolated $g_{x,\mathrm{interp}}(x_g, X)$ field is changed a little, while the range of gust time-scales of the $(g_{x,\mathrm{interp}}(t_g, T)$ field is kept fixed.
(6) Finally, steps (3)–(5) are repeated by varying the minimum and maximum values of x_g and X in the interpolated $(g_{x,\mathrm{interp}}(x_g, X)$ field until the minimum of the grid mean least-squares difference $\left\langle (g_{x,\mathrm{interp}}(t_g, T) - g_{x,\mathrm{interp}}(x_g, X))^2 \right\rangle$ is found.

When the best possible match between the peak factor fields $g_{x,\mathrm{interp}}(t_g, T)$ and $g_{x,\mathrm{interp}}(x_g, X)$ is found, the length-scale counterparts $[x_{g,3}, X_{600}]$ for the time-scales $[t_g, T] = [3\ \mathrm{s}, 10\ \mathrm{min}]$ are determined by

$$X_{600} = \min(X) + \frac{10\ \mathrm{min} - 5\ \mathrm{min}}{30\ \mathrm{min} - 5\ \mathrm{min}}(\max(X) - \min(X)),$$
$$x_{g,3} = \min(x_g) + \frac{3\ \mathrm{s} - 1\ \mathrm{s}}{10\ \mathrm{s} - 1\ \mathrm{s}}(\max(x_g) - \min(x_g)), \qquad \text{(A1)}$$

where the min and max values are the end points of x_g and X in the resulting least-squares fitted $g_{x,\mathrm{interp}}(x_g, X)$ field.

Appendix B: Statistical peak factor method and its transformation into wave-number space

Here we first review the statistical theory to determine the peak factor. It is based on work by Rice (1944, 1945) and has later been applied in several studies (e.g. Beljaars, 1987; Kristensen *et al.*, 1991; Wichers Schreur and Geertsema, 2008; Suomi *et al.*, 2015). The probability of a maximum (g_x) that is not up-crossed in an ensemble of turbulence samples can be assumed to be Poisson-distributed:

$$P\left(\frac{u(t) - U}{\sigma_u} < g_x, T\right) = \mathrm{e}^{-N_x(g_x, T)}, \qquad \text{(B1)}$$

where N_x is the number of up-crossings of the level g_x in an ensemble of samples of duration T. When $N_x = 0$, the probability is $P = 1$. The probability for one up-crossing is then $P = \mathrm{e}^{-1} \approx 0.37$ and the median g_x in a set of samples is obtained with a probability $P = 0.5$.

Following Kristensen *et al.* (1991), the number of up-crossings N_x during T can be approximated by integration:

$$N_x = 2\pi T \int_0^\infty \dot{u} p(u, \dot{u})\, \mathrm{d}\dot{u}, \qquad \text{(B2)}$$

where $\dot{u}$ is the time derivative of the wind speed u and the probability $p(u, \dot{u})$ can be approximated as a joint Gaussian distribution of $u(t)$ and $\dot{u}$, assuming that u and $\dot{u}$ are statistically independent, which yields $p(u, \dot{u}) = p(u)p(\dot{u})$. Assuming a stationary u, the probability of a maximum becomes

$$p(U_{\max}, \dot{u}) = \frac{1}{2\pi\sigma_u\sigma_{\dot{u}}} \mathrm{e}^{-[g_x^2/2] - [\dot{u}^2/(2{\sigma_{\dot{u}}}^2)]}, \qquad \text{(B3)}$$

where ${\sigma_u}^2$ and ${\sigma_{\dot{u}}}^2$ are the variances of u and $\dot{u}$. Substituting Eq. (B3) into Eq. (B2) and by integration, we obtain

$$N_x = \frac{T}{\sqrt{2\pi}\tau} \mathrm{e}^{-g_x^2/2}, \qquad \text{(B4)}$$

where

$$\tau = \frac{1}{\sqrt{2\pi}}\frac{\sigma_u}{\sigma_{\dot{u}}}$$

is the turbulent time-scale. Combining Eqs (B4) and (B1) and solving for g_x yields

$$g_x = \left[2\ln\left(\frac{T}{\tau}\frac{1}{\sqrt{2\pi}\ln\frac{1}{P}}\right)\right]^{1/2}, \tag{B5}$$

which is the final peak-factor equation. The turbulent time-scale (τ) can be determined using the one-sided power spectrum $S(f)$ of the horizontal wind velocity as

$$\tau = \left[\frac{\int_0^\infty S(f)\,\mathrm{d}f}{2\pi\int_0^\infty f^2 S(f)\,\mathrm{d}f}\right]^{1/2}. \tag{B6}$$

Above, we have shown the derivation of Eq. (B5) to determine g_x as a function of time-scale. Next we will transform this equation into wave-number space by applying Taylor's hypothesis, by which the wave number can be expressed as $k = 2\pi f/U$. Kaimal *et al.* (1972) have shown that $fS(f) = kF(k)$, where $F(k)$ is the one-sided power spectrum as a function of the wave number. From that, it follows that $S(f) = (2\pi/U)F(k)$ and $f^2S(f) = [U/(2\pi)]k^2F(k)$. Substituting these into Eq. (B6) gives

$$\tau = \frac{\sqrt{2\pi}}{U}\left[\frac{\int_0^\infty F(k)\,\mathrm{d}k}{\int_0^\infty k^2F(k)\,\mathrm{d}k}\right]^{1/2} = \frac{\sqrt{2\pi}}{U}l, \tag{B7}$$

where l is the turbulent length-scale:

$$l = \left[\frac{\int_0^\infty F(k)\,\mathrm{d}k}{\int_0^\infty k^2F(k)\,\mathrm{d}k}\right]^{1/2}. \tag{B8}$$

Further, substituting Eq. (B7) into Eq. (B5) and using Taylor's hypothesis to define the sample length as $X = UT$, the peak factor will become

$$g_x = \left[2\ln\left(\frac{X}{l}\frac{1}{2\pi\ln\frac{1}{P}}\right)\right]^{1/2}. \tag{B9}$$

This equation provides an estimate for a peak factor based on a theoretical wind spectrum. In reality, the measured spectrum and the peak-factor estimate depend on the characteristics of the instrumentation and on the gust length x_g. These can be taken into account by multiplying the spectra $F(k)$ in Eq. (B8) by a filter function $|H(k)|^2$. The filter function has been determined e.g. by Wichers Schreur and Geertsema (2008, their eq. (22)) for cup anemometers as a function of frequency:

$$|H(f)|^2 = \left(\frac{\sin(\pi f t_g)}{\pi f t_g}\right)^2\left(\frac{\sin(\pi f\Delta t_{obs})}{\pi f\Delta t_{obs}}\right)^2\frac{1}{1+(2\pi f\frac{l_{cup}}{U})^2}, \tag{B10}$$

where the components on the right-hand side represent (i) the moving average filter with a window length equal to the gust duration t_g, (ii) the discretization filter with Δt_{obs}, which is the time interval between two consecutive data points, and finally (iii) the anemometer response filter, where l_{cup} is the cup anemometer response length. Again, we apply Taylor's hypothesis ($k = 2\pi f/U$) to convert $|H(f)|^2$ into wave-number space. The gust duration t_g will be defined here as x_g/U and the spacing between two neighbouring data points is $\Delta x_{obs} = U\Delta t_{obs}$. The third term on the right-hand side of Eq. (B10) is considered small compared with the other two components, because the anemometer (five-hole probe) used on board the research aircraft is a fast-response instrument with very small physical dimensions. Therefore, we can omit the last term, yielding

$$|H(k)|^2 = \left(\frac{\sin(\frac{1}{2}kx_g)}{\frac{1}{2}kx_g}\right)^2\left(\frac{\sin(\frac{1}{2}k\Delta x_{obs})}{\frac{1}{2}k\Delta x_{obs}}\right)^2. \tag{B11}$$

After filtering (i.e. multiplication of spectra $F(k)$ by $|H(k)|^2$ in both the numerator and the denominator) Eq. (B8) and using it in Eq. (B9), we obtain the peak-factor estimate $g_{x,f}$ of the measured and moving averaged (filtered) signal. In practical applications, we are interested in a gust relative to the true turbulent time series. Therefore, $g_{x,f}$ from Eq. (B9) (after filtering) must be multiplied by the ratio of the standard deviations of the filtered (σ_f) and true (σ) signals:

$$r_\sigma = \frac{\sigma_f}{\sigma} = \left[\frac{\int_0^\infty |H(k)|^2F(k)\,\mathrm{d}k}{\int_0^\infty F(k)\,\mathrm{d}k}\right]^{1/2}. \tag{B12}$$

References

Ágústsson H, Ólafsson H. 2004. Mean gust factors in complex terrain. *Meteorol. Z.* **13**: 149–155.

Ágústsson H, Ólafsson H. 2009. Forecasting wind gusts in complex terrain. *Meteorol. Atmos. Phys.* **103**: 173–185.

Arya SP. 2001. *Introduction to Micrometeorology* (2nd edn). Academic Press: San Diego, CA.

Beljaars ACM. 1987. The influence of sampling and filtering on measured wind gusts. *J. Atmos. Oceanic Technol.* **4**: 613–626.

Belušić D, Klaić B. 2004. Estimation of bora wind gusts using a limited area model. *Tellus* **56A**: 296–307.

Brasseur O. 2001. Development and application of a physical approach to estimating wind gusts. *Mon. Weather Rev.* **129**: 5–25.

Chan PW. 2012. An event of tail strike of an aircraft due to terrain-induced wind shear at the Hong Kong International Airport. *Meteorol. Appl.* **19**: 325–333.

Deardorff JW. 1972. Theoretical expression for the countergradient vertical heat flux. *J. Geophys. Res.* **77**: 5900–5904, doi:10.1029/JC077i030p05900.

Elvidge A, Renfrew I, Weiss A, Brooks I, Lachlan-Cope T, King J. 2016. Observations of surface momentum exchange over the marginal ice zone and recommendations for its parametrisation. *Atmos. Chem. Phys.* **16**: 1545–1563, doi: 10.5194/acp-16-1545-2016.

Emeis S. 2014. Review: Current issues in wind energy meteorology. *Meteorol. Appl.* **21**: 803–819.

Garbrecht T, Lüpkes C, Hartmann J, Wolff M. 2002. Atmospheric drag coefficients over sea ice – validation of a parameterisation concept. *Tellus* **54A**: 205–219.

Gryanik V, Hartmann J. 2002. A turbulence closure for the convective boundary layer based on a two-scale mass-flux approach. *J. Atmos. Sci.* **59**: 2729–2744.

Harper BA, Kepert JD, Ginger JD. 2010. *Guidelines for Converting between Various Wind Averaging Periods in Tropical Cyclone Conditions*, WMO/TD-No.1555. World Meteorological Organization: Geneva, Switzerland.

Hartmann J, Kottmeier C, Raasch R. 1997. Boundary layer development and roll vortex structure during a cold-air outbreak. *Boundary Layer Meteorol.* **84**: 45–65.

Hartmann J, Albers F, Argentini S, Bochert A, Bonafe U, Cohrs W, Conidi A, Freese D, Georgiadis T, Ippoliti A, Kaleschke L, Lüpkes C, Maixner U, Mastrantonio G, Ravegnani F, Reuter A, Trivellone G, Viola A. 1999. 'Arctic Radiation and Turbulence Interaction Study (ARTIST)'. Reports on Polar Research 305. Alfred-Wegener-Institute for Polar and Marine Research: Bremerhaven, Germany.

Højstrup J. 1982. Velocity spectra in the unstable planetary boundary layer. *J. Atmos. Sci.* **39**: 2239–2248.

Højstrup J, Larsen SE, Madsen PH. 1990. Power spectra of horizontal wind components in the neutral atmospheric surface boundary layer. In *9. Symposium on turbulence and diffusion*: Jensen NO, Kristensen L, Larsen SE. (eds.) American Meteorological Society: Boston, MA; 305–308.

Honnert R, Masson V. 2014. What is the smallest physically acceptable scale for 1D turbulence schemes? *Front. Earth Sci.* **2**: 27, doi: 10.3389/feart.2014.00027.

Hsu S, Blanchard B. 2004. Estimating overwater turbulence intensity from routine gust-factor measurements. *J. Appl. Meteorol.* **43**: 1911–1916.

Kaimal JC. 1978. Horizontal velocity spectra in an unstable surface layer. *J. Atmos. Sci.* **35**: 18–24.

Kaimal JC, Wyngaard JC, Izumi Y, Cote OR. 1972. Spectral characteristics of surface-layer turbulence. *Q. J. R. Meteorol. Soc.* **98**: 563–589.

Kaleschke L, Lüpkes C, Vihma T, Haarpaintner J, Bochert A, Hartmann J, Heygster G. 2001. SSM/I sea ice remote sensing for mesoscale ocean–atmosphere interaction analysis. *Can. J. Remote Sens.* **27**: 526–536.

Kolstad E. 2015. Extreme small-scale wind episodes over the Barents Sea: When, where and why? *Clim. Dyn.* **45**: 2137–2150, doi: 10.1007/s00382-014-2462-4.

Kristensen L, Casanova M, Courtney MS, Troen I. 1991. In search of a gust definition. *Boundary Layer Meteorol.* **55**: 91–107.

Lüpkes C, Gryanik VM. 2015. A stability-dependent parametrization of transfer coefficients for momentum and heat over polar sea ice to be used in climate models. *J. Geophys. Res. – Atmos.* **120**: 552–581, doi: 10.1002/2014JD022418.

Lüpkes C, Gryanik VM, Hartmann J, Andreas EL. 2012. A parametrization, based on sea ice morphology, of the neutral atmospheric drag coefficients for weather prediction and climate models. *J. Geophys. Res. – Atmos.* **117**: D13112, doi: 10.1029/2012JD017630.

Mahrt L. 1998. Flux sampling errors for aircraft and towers. *J. Atmos. Oceanic Technol.* **15**: 416–429.

Meyers MP, Snook JS, Wesley DA, Poulos GS. 2003. A Rocky Mountain storm. Part II: The forest blowdown over the west slope of the northern Colorado mountains – observations, analysis and modeling. *Weather and Forecasting* **18**: 662–674.

Overland J, Hanna E, Hanssen-Bauer I, Kim S-J, Walsh JE, Wang M, Bhatt US, Thoman RL. 2015. 'Air temperature', In *Arctic Report Card: Update for 2015*. http://www.arctic.noaa.gov/report15/air_temperature.html (accessed 24 August 2016).

Peña A, Floors R, Sathe A, Gryning S-E, Wagner R, Courtney MS, Larsen XG, Hahmann AN, Hasager CB. 2016. Ten years of boundary-layer and wind-power meteorology at Høvsøre, Denmark. *Boundary Layer Meteorol.* **158**: 1–26, doi: 10.1007/s10546-015-0079-8.

Rebmann C, Kolle O, Heinesch B, Queck R, Ibrom A, Aubinet M. 2012. Data Acquisition and Flux Calculations. In *Eddy Covariance: A Practical Guide to Measurement and Data Analysis*, Aubinet M, Vesala T, Papale D. (eds.): 59–84. Springer Atmospheric Sciences, doi: 10.1007/978-94-007-2351-1_3.

Rice SO. 1944. Mathematical analysis of random noice. *Bell Syst. Technol. J.* **23**: 282–332, doi:10.1002/j.15387305.1944.tb00874.x.

Rice SO. 1945. Mathematical Analysis of Random Noise. *Bell Syst. Technol. J.* **24**: 46–156, doi:10.1002/j.1538-7305.1945.tb00453.x.

Samuelsson P, Tjernström M. 1999. Introduction to the in situ airborne meteorological measurements in NOPEX. *Agric. For. Meteorol.* **98–99**: 181–204.

Seity Y, Brousseau P, Malardel S, Hello G, Benard P, Bouttier F, Lac C, Masson V. 2011. The AROME-France convective-scale operational model. *Mon. Weather Rev.* **139**: 976–991.

Shi X, Liu J, Li Y, Huang B, Tan Y. 2015. A diagnostic method for aircraft turbulence based on high-resolution numerical weather prediction products. *Nat. Hazards* **77**: 867–881.

Suomi I, Vihma T, Gryning S-E, Fortelius C. 2013. Wind-gust parametrizations at heights relevant for wind energy: A study based on mast observations. *Q. J. R. Meteorol. Soc.* **139**: 1298–1310.

Suomi I, Gryning S-E, Floors R, Vihma T, Fortelius C. 2015. On the vertical structure of wind gusts. *Q. J. R. Meteorol. Soc.* **141**: 1658–1670, doi: 10.1002/qj.2468.

Taylor GI. 1938. The spectrum of turbulence. *Proc. R. Soc. London* **164**: 476–490.

Tetzlaff A, Lüpkes C, Hartmann J. 2015. Aircraft-based observations of atmospheric boundary-layer modification over Arctic leads. *Q. J. R. Meteorol. Soc.* **141**: 2839–2856, doi: 10.1002/qj.2568.

Verkaik JW. 2000. Evaluation of two gustiness models for exposure correction calculations. *J. Appl. Meteorol.* **39**: 1613–1626.

Vihma T. 2014. Effects of Arctic sea ice decline on weather and climate: A review. *Surv. Geophys.* **35**: 1175–1214, doi: 10.1007/s10712-014-9284-0.

Vihma T, Hartmann J, Lüpkes C. 2003. A case study of an on-ice air flow over the Arctic marginal sea-ice zone. *Boundary Layer Meteorol.* **107**: 189–217.

Vihma T, Lüpkes C, Hartmann J, Savijärvi H. 2005. Observations and modelling of cold-air advection over Arctic sea ice. *Boundary Layer Meteorol.* **117**: 275–300.

Wichers Schreur B, Geertsema G. 2008. Theory for a TKE based parametrization of wind gusts. *HIRLAM Newsl.* **54**: 177–188.

Wieringa J. 1973. Gust factors over open water and built-up country. *Boundary Layer Meteorol.* **3**: 424–441.

Woetmann Nielsen N, Petersen C. 2001. Calculation of wind gusts in DMI-HIRLAM. Scientific Report 01-03:1-32. Danish Meteorological Institute: Copenhagen, Denmark.

World Meteorological Organization (WMO). 2010. Measurement of surface wind. In *Guide to Meteorological Instruments and Methods of Observation*, WMO No. 8 (7th edn): I.5-1-15. World Meteorological Organization: Geneva, Switzerland. http://library.wmo.int/pmb_ged/wmo_8-2012_en.pdf (accessed 24 August 2016).

RMetS
Royal Meteorological Society

Methodology for obtaining wind gusts using Doppler lidar

Irene Suomi,[a]* Sven-Erik Gryning,[b] Ewan J. O'Connor[a,c] and Timo Vihma[a]
[a]*Meteorological Research, Finnish Meteorological Institute, Helsinki, Finland*
[b]*Department of Wind Energy, Technical University of Denmark, Roskilde, Denmark*
[c]*Meteorology, University of Reading, UK*

*Correspondence to: I. Suomi, Meteorological Research, Finnish Meteorological Institute, PO Box 503, FI-00101 Helsinki (Erik Palménin aukio 1, 00560 Helsinki), Finland. E-mail: irene.suomi@fmi.fi

A new methodology is proposed for scaling Doppler lidar observations of wind gusts to make them comparable with those observed at a meteorological mast. Doppler lidars can then be used to measure wind gusts in regions and heights where traditional meteorological mast measurements are not available. This novel method also provides estimates for wind gusts at arbitrary gust durations, including those shorter than the temporal resolution of the Doppler lidar measurements. The input parameters for the scaling method are the measured wind-gust speed as well as the mean and standard deviation of the horizontal wind speed. The method was tested using WindCube V2 Doppler lidar measurements taken next to a 100 m high meteorological mast. It is shown that the method can provide realistic Doppler lidar estimates of the gust factor, i.e. the ratio of the wind-gust speed to the mean wind speed. The method reduced the bias in the Doppler lidar gust factors from 0.07 to 0.03 and can be improved further to reduce the bias by using a realistic estimate of turbulence. Wind gust measurements are often prone to outliers in the time series, because they represent the maximum of a (moving-averaged) horizontal wind speed. To assure the data quality in this study, we applied a filtering technique based on spike detection to remove possible outliers in the Doppler lidar data. We found that the spike detection-removal method clearly improved the wind-gust measurements, both with and without the scaling method. Spike detection also outperformed the traditional Doppler lidar quality assurance method based on carrier-to-noise ratio, by removing additional unrealistic outliers present in the time series.

Key Words: Doppler lidar; wind gust; wind profile; atmospheric boundary layer; spike removal; data quality

Received 09 December 2016; Revised 13 April 2017; Accepted 14 April 2017; Published online in Wiley Online Library

1. Introduction

Wind gusts are typically used as the main weather parameter in the assessment of wind-induced damage (e.g. Pasztor *et al.*, 2015; Jung *et al.*, 2016). Therefore, accurate wind-gust forecasts will enhance preparedness planning, with, for example, rescue services and power companies able to allocate resources when strong, damaging gusts are expected. Numerical weather prediction models do not resolve wind gusts and gust forecasts are based on parametrizations. These parametrizations have typically been developed for a reference height of 10 m, which is the standard measurement height for surface winds (e.g. Brasseur, 2001; Woetmann Nielsen and Petersen, 2001; Wichers Schreur and Geertsema, 2008). However, the measured gustiness at the reference height is not always representative of the surrounding area because of the spatial variation in the aerodynamic roughness of the surrounding environment, which can have a significant impact on wind gusts (Wieringa, 1973; Suomi *et al.*, 2013, 2015). Hence, a fair comparison of model gust forecasts and observations is challenging, because the roughness in the model grid cell may differ from the conditions at the measurement site (e.g. Wieringa, 1986; Vihma and Savijärvi, 1991; Bou-Zeid *et al.*, 2007). For this reason, Wieringa (1986, 1996) and Verkaik (2000) proposed methods for deriving representative wind measurements at non-ideal weather stations based on extrapolation of the wind profile up to altitudes where the wind is representative of larger horizontal scales; Wieringa (1986) suggested 50–100 m above the surface. Forecast validation with measurements at altitudes above the roughness sublayer, or even above the surface layer, is therefore sought, as this would enable direct verification. Doppler lidars can potentially provide wind-gust measurements from these heights, enabling direct validation of wind-gust forecasts.

Wind gust measurements have traditionally been available only from weather stations and meteorological masts where the wind

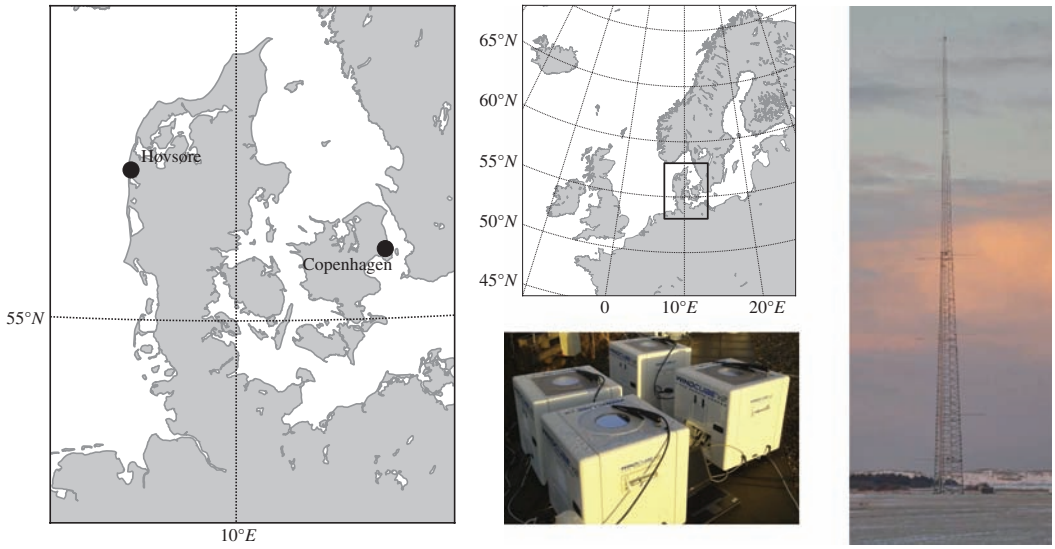

Figure 1. The National Test Site for Large Wind Turbines is located at Høvsøre, near the western coast of Denmark. At the site, a WindCube V2 Doppler lidar manufactured by Leosphere was placed next to the meteorological mast. The mast is equiped with sonic anemometers at six levels between 10 and 100 m and the range of lidar measurements covers heights from 40–290 m.

can be measured at high temporal resolution (>1 Hz). Hence, continuous wind-gust time series are usually only available at the standard 10 m measurement height and at altitudes reachable by meteorological masts (up to about 300 m). Recently, Suomi *et al.* (2016) developed a methodology to derive gusts based on research aircraft data to measure gusts from various heights, but these datasets are typically limited to short-term measurement campaigns and are therefore not suitable for operational model evaluation. Tall weather masts are rather sparse, so another possibility for obtaining continuous wind-gust records above the standard weather station height is Doppler lidar. Certain Doppler lidar instrument versions are capable of measuring to altitudes above tall masts, but the challenge is in measuring the high-frequency changes in wind speed. The main aim of this study is to develop a methodology for scaling wind gusts derived from the Doppler lidar wind-speed distribution, so that they are comparable with the standard wind-gust measurements obtained from meteorological masts and weather stations. Then, the Doppler lidar technique can be applied to regions and heights where traditional meteorological measurements do not reach.

Doppler lidar technology for measuring wind has matured rapidly in recent years, with the first small (<100 kg) commercial wind lidars becoming available less than a decade ago (Emeis *et al.*, 2007). Profiles of the mean wind speed can be measured effectively and accurately at high vertical resolution within the boundary layer and up to a couple of kilometres in altitude, depending on the weather situation.

To measure the 3D wind vector requires information from at least three different lines of sight pointing towards different directions (e.g. Lane *et al.*, 2013). The instrument sensitivity depends on the amount of aerosol present and the velocity measurement uncertainty is related to the strength of the backscattered signal (Pearson *et al.*, 2009). It typically takes a second or more to measure each line of sight with sufficient sensitivity and therefore the temporal resolution of the wind measurement is often of the order of tens of seconds, which is not sufficient for gusts (e.g. Suomi *et al.*, 2015). However, Doppler lidars can also provide high-resolution turbulent measurements, in both the vertical direction (O'Connor *et al.*, 2010) and, potentially, the horizontal direction (Vakkari *et al.*, 2015).

In this study, we will first investigate how the wind-speed maxima measured by a Doppler lidar compare with those measured at a meteorological mast and then introduce a new method to scale the Doppler lidar measurements to provide estimates for short-duration (1–19 s) wind-speed maxima. Finally, we will show that the Doppler lidar can also provide good wind-gust observations above the mast measurement heights. We use a commercial short-range pulsed Doppler lidar, which is commonly used in wind-energy applications and has already been shown to be applicable for measuring extreme winds (Sathe *et al.*, 2011). The advantage of this lidar type is the relatively high temporal resolution of the measurements, which is very important for gusts. In section 2, we introduce the data, which include coincident meteorological mast and Doppler lidar measurements from the western coast of Denmark, and describe the data processing steps, including the methods to assure and assess the quality of lidar data. In section 3, the gust measurements from the lidar are compared with those from the meteorological mast and in section 4 we introduce a new method to scale the lidar measurements so that they match the wind gusts that would be measured by in situ measurement systems. The scaling method can be applied to derive gusts with different durations, including gusts for durations that are shorter than the temporal resolution of the lidar measurements. The resulting scaled Doppler lidar wind gusts are compared with the mast observations in section 5, together with a discussion on the applicability of the profile of the scaled lidar wind-gust measurements above the mast measurement levels. In section 5, we conclude with a summary of the main results and provide suggestions for further development of the method.

2. Measurements and data processing

Doppler lidar and meteorological mast measurements were collected at the Danish National Test Station for Large Wind Turbines, located at Høvsøre, near the western coast of Denmark (Figure 1). A thorough description of the site and its instrumentation is provided by Peña *et al.* (2015). The long-term wind-gust conditions at this site have been investigated by Suomi *et al.* (2015). Here, the study period covers 2 days, 10 and 11 October 2015, during which there were easterly winds of 4–10 m s^{-1} at the 100 m level and the surface layer stability underwent a clear diurnal cycle: unstable conditions during the day and stable conditions at night. The first day selected exhibits

ideal conditions for the Doppler lidar, with good sensitivity up to 250 m or more. The second day was more challenging, with precipitation present and reduced sensitivity, but this provided an opportunity to investigate the impact of data with larger uncertainties, test the post-processing applied to the Doppler lidar data and check the data-quality assessment. We now briefly present the lidar and sonic anemometers used in this study and describe the data post-processing applied to both sets of instrumentation.

2.1. Doppler lidar measurements

The Doppler lidar instrument used in this study is a Windcube V2 Doppler lidar manufactured by Leosphere. It was operated next to the meteorological mast at Høvsøre (Figure 1). The lidar measures radial wind velocities along four inclined and one vertical line of sight. The four inclined measuring beams are at $\phi = 28^\circ$ from zenith, with azimuth angles at 90° relative to each other. The radial wind-velocity measurements were taken along each line of sight at ten levels (40, 60, 76, 80, 100, 116, 160, 200, 250 and 290 m). One scan sequence is defined as a set of sequential measurements covering all five lines of sight, which takes about 3.8 s. We will consider this as the resolution of the lidar wind measurements, i.e. the radial wind velocity vector ($\mathbf{V_r}$) is updated once each scan sequence is completed. The radial velocities ($\mathbf{V_r} = [V_{r0}, V_{r90}, V_{r180}, V_{r270}, V_{rz}]^{\mathrm{T}}$) were transformed into orthogonal geographical coordinates ($\mathbf{v} = [v_1, v_2, v_3]^{\mathrm{T}}$, where the superscript 'T' denotes the transpose) using the methodology from Päschke *et al.* (2015). For this instrument, the rotation matrix $\mathbf{A}$ from geographic coordinates to radial velocities ($\mathbf{V_r} = \mathbf{Av}$) includes five lines of sight

$$A = \begin{bmatrix} 0 & \sin(\phi) & \cos(\phi) \\ \sin(\phi) & 0 & \cos(\phi) \\ 0 & -\sin(\phi) & \cos(\phi) \\ -\sin(\phi) & 0 & \cos(\phi) \\ 0 & 0 & 1 \end{bmatrix}, \tag{1}$$

where the first four rows represent the four inclined lines of sight with a zenith angle $\phi = 28^\circ$ and azimuth angle at 90°. The fifth row represents the vertical beam for which $\phi = 0^\circ$. According to Päschke *et al.* (2015), the geographic wind components can be derived using the matrix operation

$$\mathbf{v} = \mathbf{A}^{+}\mathbf{V_r}, \tag{2}$$

where $\mathbf{A}^{+}$ denotes the Moore–Penrose pseudoinverse of $\mathbf{A}$ because the system is overdetermined, i.e. there are more rows (5) in the matrix $\mathbf{A}$ (Eq. (1)) than required (3) to solve the wind velocity components $[v_1, v_2, v_3]$. The resulting horizontal wind components in geographic coordinates are

$$v_1 = \frac{v_{r90} - v_{r270}}{2\sin(\phi)}, \tag{3}$$

$$v_2 = \frac{v_{r0} - v_{r180}}{2\sin(\phi)}, \tag{4}$$

for the west-to-east and south-to-north components, respectively. The horizontal wind velocity is then $u_{\mathrm{L}} = \sqrt{v_1^2 + v_2^2}$. After the coordinate transformation, the dataset was divided into 10 min periods; for each period, the mean horizontal wind speed (U_{L}), wind direction (θ_{L}), standard deviation of the wind speed ($\sigma_{u_{\mathrm{L}}}$), wind-gust speed ($U_{\mathrm{max,L}}$) and gust factor

$$G_{\mathrm{L}} = U_{\mathrm{max,L}}/U_{\mathrm{L}} \tag{5}$$

were calculated. The subscript 'L' refers to lidar measurements. The gust factor is the ratio of the wind-gust speed to the mean wind speed and is the most commonly used measure of gustiness.

Since $U_{\mathrm{max,L}}$ was calculated as the maximum of the horizontal wind speed u_{L}, this means that the wind gust corresponds roughly to a wind gust with a duration (t_{g}) equal to the temporal resolution of the measurement ($\Delta t = 3.8$ s for this Doppler lidar instrument). To compare lidar gusts with sonic anemometer gusts in section 4, we also calculated gusts with varying durations by applying a moving average to the measured horizontal wind-speed time series before taking the maximum. The moving average was taken over n measurements, which corresponds to a gust duration of $t_{\mathrm{g}} = n\Delta t$. In this study, we allowed n to vary from 2–8, which means that t_{g} varied from 7.6–30.4 s.

2.2. Doppler lidar data quality

Doppler lidar data quality can be quantified in terms of the lidar carrier-to-noise ratio (CNR), a measure of the relative strength of the heterodyne backscattered Doppler signal over the inherent unavoidable noise level of the detection chain. The factors affecting CNR are related to the characteristics of the lidar and the atmosphere. For a pulsed wind lidar, such as the one used in this study, the CNR is proportional to the aerosol cross-sectional area and, at the longest measurement distances, inversely proportional to the square of the measurement range. Therefore, the wind-data availability decreases with measurement range when using a constant CNR value to filter the measurements. The four most significant atmospheric factors influencing the wind lidar performance are aerosol backscatter, atmospheric refractive turbulence, relative humidity and precipitation. When the air is clean (low concentrations of aerosols), the retrieved wind data from power spectra measurements are associated with generally lower CNR values.

The uncertainty in the radial Doppler velocities along each line of sight is obtained from the associated CNR value for each measurement volume, following the methodology from O'Connor *et al.* (2010). The resulting error estimate σ_{e} as a function of CNR is presented in Figure 2. Typically, a threshold of −22 or −23 dB is used as a limit for the accepted uncertainty in the lidar measurements (e.g. Gryning *et al.*, 2016), which corresponds to an uncertainty of about $0.15\,\mathrm{m\,s^{-1}}$. The uncertainty is calculated for each radial velocity component separately and propagated into the geographic wind components calculated using the formulations from Päschke *et al.* (2015). The error in the radial winds is represented by a diagonal $[5 \times 5]$ matrix $C_{\mathbf{V_r V_r}}$ with the (squared) errors on its diagonal $[\sigma_{\mathrm{e}0}^2, \sigma_{\mathrm{e}90}^2, \sigma_{\mathrm{e}180}^2, \sigma_{\mathrm{e}270}^2, \sigma_{\mathrm{eZ}}^2]$. The errors in the geographic coordinates $\mathbf{C_{vv}}$ are then provided by

$$\mathbf{C_{vv}} = \mathbf{A}^{+} C_{\mathbf{V_r V_r}} (\mathbf{A}^{+})^{\mathrm{T}}, \tag{6}$$

from which the errors in v_1, v_2 and v_3 are obtained from the diagonal components of $C_{\mathbf{vv}}$. For the horizontal wind components, they are

$$\sigma_{\mathrm{e},v_1}^2 = \frac{\sigma_{\mathrm{e}90}^2 + \sigma_{\mathrm{e}270}^2}{4\sin^2(\phi)}, \tag{7}$$

$$\sigma_{\mathrm{e},v_2}^2 = \frac{\sigma_{\mathrm{e}0}^2 + \sigma_{\mathrm{e}180}^2}{4\sin^2(\phi)} \tag{8}$$

and the error of the horizontal wind is $\sigma_{\mathrm{e},u_{\mathrm{L}}} = \sqrt{\sigma_{\mathrm{e},v_1}^2 + \sigma_{\mathrm{e},v_2}^2}$. Thus, the error in the wind-gust speed $\sigma_{\mathrm{e},U_{\mathrm{max,L}}}$ is the error in the horizontal wind speed at the time of the maximum gust. The error propagation into the mean wind speed (U_{L}) is calculated in terms of the root-mean-squared error (RMSE):

$$\sigma_{\mathrm{e},U_{\mathrm{L}}} = \left[\frac{1}{N}\sum^{N}\sigma_{\mathrm{e},u_{\mathrm{L}}}^2\right]^{0.5}, \tag{9}$$

where N is the number of observations in a sample.

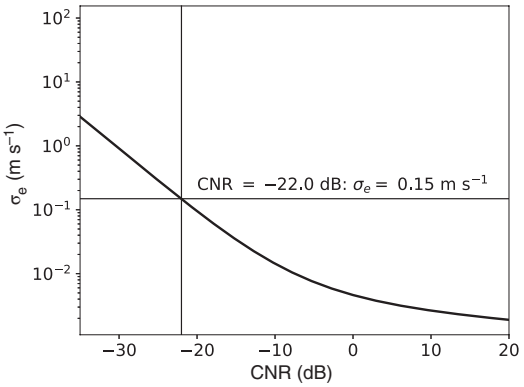

Figure 2. Lidar measurement error as a function of CNR. A CNR of −22 dB corresponds to an error of about 0.15 m s^{-1}.

Manninen *et al.* (2016) have shown, however, that an instrument's internal calculation of CNR is not always correct, due to issues in calculating a reliable 'background' value, so that post-processing of the instrument data may be required. For the instrument used in this study, the background value used to determine CNR is calculated on a profile-by-profile basis; therefore there are occasional profiles with unrealistic CNR values. This has little impact when calculating mean wind profiles from a large set of samples, but is crucial when deriving the wind gust from a time series of wind values, since the gust-factor value is highly dependent on the uncertainty of a single wind measurement in the time series (Eq. (5)). When the signal strength is very weak (low CNR), velocity estimates derived from the Doppler shift are dominated by random noise and thus subject to estimation errors (the wind estimate can have any value within 0–60 m s^{-1} for this instrument); the resulting spikes in the signal lead to unrealistically high gust factors.

To mitigate this impact, we apply an approach called despiking to remove unrealistically high u_{L} values. It is usually applied as standard to turbulence measurements from sonic anemometers, in order to detect malfunctioning of the instrument (Højstrup, 1993; Vickers and Mahrt, 1997; Floors, 2013). Here, despiking was implemented following the recommendation by Højstrup (1993). It is based on two-point statistics, using the previous data point $(i-1)$ to predict the next data point in the time series as

$$u_{\mathrm{fcst},i} = \mathrm{cov}_i(\tau)u_{\mathrm{L},i-1} + (1 - \mathrm{cov}_i(\tau))\bar{u}_{\mathrm{L},i}, \qquad (10)$$

where $\mathrm{cov}(\tau)$ is the autocovariance with a time lag τ equal to the resolution of the measurements ($\tau = \Delta t$) and $\bar{u}_{\mathrm{L},i}$ is the observed mean wind speed. Højstrup (1993) calculated the mean and the two-point correlation ($\mathrm{cov}(\tau)$) using a memory size concept, which allows automated operational detection of spikes without the requirement of a large memory size for the data-processing system. Here, we are not limited by the recording nor by the data-processing systems, because we are applying the spike detection to data that have already been collected. Therefore we calculate $\mathrm{cov}(\tau)$ and $\bar{u}_{\mathrm{L},i}$ using a fixed number of data points, which is the last $N = 100$ values of the time series. Based on artificial turbulence data, Højstrup (1993) tested different memory sizes from 10–10 000 data points. With a 10 Hz sampling frequency, these represent time-scales from 1–1000 s. Our fixed $N = 100$ corresponds to 380 s (the lidar measuring interval being $\Delta t = 3.8$ s) and thereby fits into the range of values discussed by Højstrup (1993).

When the prediction for the next value in a time series is obtained, a possible spike is detected using the criterion

$$|u_{\mathrm{fcst},i} - u_{\mathrm{L},i}| > C_{\mathrm{spike}}\sigma_i, \qquad (11)$$

where || refers to the absolute value, σ_i is the standard deviation of the last N observations and C_{spike} is the threshold for the spike detection. Following Højstrup (1993), we assume a Gaussian distribution of the difference $u_{\mathrm{fcst},i} - u_{\mathrm{L},i}$ and, based on the results, we applied a threshold of $C_{\mathrm{spike}} = 3.5$ to detect spikes. This threshold corresponds to a probability of about 5×10^{-5}. The same threshold was also used by Vickers and Mahrt (1997) and Floors (2013) and it also fits within the range of discrimination levels provided by Højstrup (1993), which was 3.3–4.9, associated with detection levels from 10^{-6}–10^{-3}. The spike detection was performed as a moving window over the whole data set. All detected spikes were replaced by linear interpolation using the neighbouring non-spike values. Similarly to Vickers and Mahrt (1997) and Floors (2013), we repeated the spike detection-removal procedure until no more spikes were found and after each iteration the threshold C_{spike} was increased by 0.1, which accounts for the reduced σ_i after spike removal. Visual inspection showed that this method removes spikes efficiently when only a few spikes exist, but not once unrealistically high wind-speed values begin to dominate the time series. In this study, a maximum of 29 spikes were detected within a 10 min period of data, which consists of about 156 values. This corresponds to about 19% of data. The effect of the filtering on the results is discussed in section 5.2.

2.3. *Meteorological mast measurements*

Sonic anemometer measurements were available from six levels of the meteorological mast: at 10, 20, 40, 60, 80 and 100 m heights. This provides coincident measurements from the mast and the lidar at four heights: 40, 60, 80 and 100 m. In this study, we consider sonic anemometers as the reference instruments for wind-gust measurements, because they provide wind-speed measurements with a high temporal resolution, here at 20 Hz. Moreover, as will be shown in section 4, sonic anemometers provide wind-gust measurements that fit well with the expected theoretical behaviour of short wind gusts as a function of the gust duration.

To ensure data quality of the sonic anemometer measurements, unphysical values and spikes were detected and replaced by linear interpolation using neighbouring points. Spikes were removed using the same approach as for the lidar data (Eqs (10) and (11)). Data were then divided into 10 min periods and only those periods with more than 99.9% of acceptable data were included in further analysis. Sonic temperature was corrected for crosswind effects and the wind coordinate system was rotated into streamwise coordinates using the double rotation method (e.g. Rebmann *et al.*, 2012).

The mean horizontal wind speed, its standard deviation, wind direction and wind-gust speed were calculated for each 10 min period, similarly to the lidar measurements. The wind-gust speed $U_{\mathrm{max,S}}$ was calculated with $t_{\mathrm{g}} = 3.8$ s (corresponding to an average of 76 values) and this will represent the sonic anemometer wind gust throughout the article, unless mentioned otherwise. In section 4, we derive a theoretical method for estimating gusts of different durations from Doppler lidar measurements. To compare the resulting gusts with those from the meteorological mast, we will also calculate gusts from the sonic anemometer data with durations varying in range $t_{\mathrm{g}} = 1$–30 s.

Data from the sonic anemometer at 20 m level were used to derive stability conditions based on the Obukhov length (L). The Obukhov length was calculated as

$$L = -\frac{u_*^3}{\kappa \frac{g}{\theta}\overline{w'\theta'}},$$

where $\kappa = 0.4$ is the von Karman constant, g is the gravitational acceleration and $\overline{w'\theta'}$ is the kinematic heat flux, with θ the potential temperature and w the vertical velocity. The prime denotes the deviation of a variable from its mean and the overbar

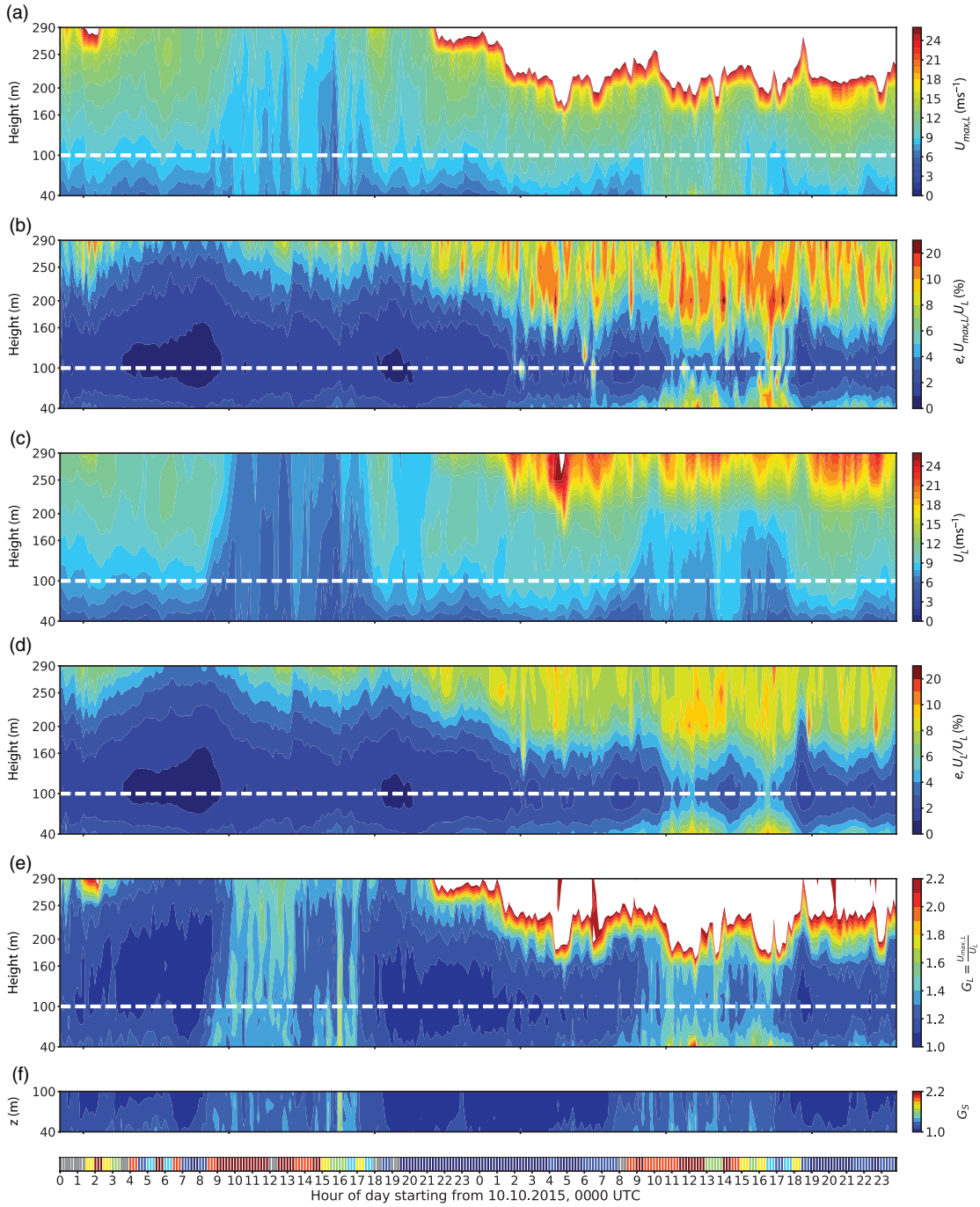

Figure 3. Despiked time–height cross-sections of (a) the wind-gust speed ($U_{\mathrm{max,L}}$) and (b) its relative error ($\sigma_{\mathrm{e},U_{\mathrm{max,L}}}/U_{\mathrm{L}}$), (c) mean wind speed ($U_{\mathrm{L}}$) and (d) its relative error ($\sigma_{\mathrm{e},U_{\mathrm{L}}}/U_{\mathrm{L}}$) and (e) the gust factor (G_{L}) from the lidar measurements after applying the despiking procedure. Panel (f) shows the corresponding sonic anemometer gust factor (G_{S}) for the heights covered by the weather mast. The bottom panel shows the stability conditions during each 10 min sample, as follows: dark red: very unstable ($-0.01 > L^{-1} \geq -0.02$), orange: unstable ($-0.005 > L^{-1} \geq -0.01$), yellow: near-neutral unstable ($-0.002 > L^{-1} \geq -0.005$), green: neutral ($|L^{-1}| \leq 0.002$), light blue: near-neutral stable ($0.005 \geq L^{-1} > 0.002$), blue: stable ($0.02 \geq L^{-1} > 0.005$) and dark blue: very stable ($0.1 \geq L^{-1} > 0.02$). The criteria for stability groups are based on Gryning *et al.* (2007).

denotes the sample mean. u_* is the friction velocity calculated as $u_* = (\overline{u'w'}^2 + \overline{v'w'}^2)^{1/4}$, where u' and v' are the fluctuating parts of the wind components along and perpendicular to the mean wind in the horizontal direction, respectively, and w' in the vertical.

3. Comparison of wind gusts from lidar and meteorological mast

Figure 3 shows the time–height cross-sections of (a) wind-gust speed, (c) mean wind speed and (e) gust factor as measured by

lidar. For comparison, the corresponding gust factors from the meteorological mast are presented in Figure 3(f) and the height of the mast is indicated by a white dashed line in panels (a)–(e). The diurnal cycle is clearly seen, with high gust factors during the day and lower gust factors during the night. The gust-factor patterns are very similar for both measuring systems below 100 m (Figures 3(e) and (f)). For example, the peak G values in the transition period on the evening of 10 October near sunset are found in both lidar and mast measurements. This means that, in good signal conditions, the Doppler lidar measures reliable wind gusts and potentially provides good information on the gustiness above the mast heights. Also clear is that the wind gust is more uncertain than the mean wind speed (compare the relative errors shown in Figures 3(b) and (d)); unrealistically high wind gust maxima often occur at lower altitudes than the mean wind speed, even though spikes have been removed.

Figure 4 shows the distributions of the gust factor from (a) lidar and (b) sonic anemometers as a function of the relative error based on the CNR from the lidar. Panel (c) shows the difference between (a) and (b), from where we see that lidar systematically overestimates the gust factors (bias = 0.08) compared with the sonic anemometer gust factors calculated with a gust duration of 3.8 s. In Figure 4, we have applied the filter based on spike detection described in section 2.2 to the lidar measurements. This filter removes outliers efficiently and therefore it is recommended for use when measuring wind gusts by a lidar.

So far, we have shown that Doppler lidar measurements yield wind-gust patterns comparable to those measured by sonic anemometers and, in addition, the lidar can reach above the meteorological mast. However, there exists a positive bias in the lidar gust factor, even after filtering of the outliers (Figure 4(c)). If the aim is to measure gusts comparable to those from a meteorological mast, this bias must be understood and accounted for.

4. A new scaling methodology for lidar gusts

Standard operational measurements of wind gusts are calculated from high temporal resolution anemometer measurements, with a standard wind-gust duration defined in terms of a 3 s moving average (WMO, 2010). In this section, we present a theoretical approach for scaling measured lidar gusts obtained at a lower temporal resolution and show that they correspond with high-resolution measurements from sonic anemometers across a range of gust durations. The previous section highlighted that wind-gust maxima, and hence gust factors, from lidar measurements are overall higher than those from sonic anemometers. There are a number of reasons for this bias. The main reason is that the wind lidar combines measurements from four lines of sight that are separated spatially, whereas the sonic anemometer measurement is a point measurement. Therefore the lidar measurements are effectively providing an average of the spatially distributed wind field. Moreover, we introduced a moving average for sonic anemometer data (averaging over 76 observations, 3.8 s), while the lidar gust represents only one time-averaged value. This means that, compared with sonic anemometer results, lidar gusts are more prone to a single unrealistically high value in the data. Here, we develop a method to estimate wind gusts from lidar measurements as they would be measured by sonic anemometers reliably, to extend observations of wind-speed maxima above a mast measurement height.

The wind gust ($U_{\max}$) can be expressed in terms of the mean wind speed (U) and a positive fluctuation from it, which is assumed to be proportional to the standard deviation of the horizontal wind speed (σ). The coefficient of proportionality is called the peak factor g_{t_g}, where the subscript t_g refers to the gust duration determined by the sampling frequency and/or the moving average window applied to the high-frequency turbulence data in the calculation of the maximum gust. Since these are different for each instrument, we have two equations for $U_{\max}$:

$$U_{\max,S} = U_S + g_{t_g,S}\sigma_S, \tag{12}$$

$$U_{\max,L} = U_L + g_{t_g,L}\sigma_L, \tag{13}$$

where the subscript 'S' refers to sonic anemometers and the subscript 'L' to the Doppler lidar.

The scaling will enable the wind-gust speed estimation as it would be measured by an anemometer with a high temporal resolution, i.e. the sonic anemometer $U_{\max,S}$ (Eq. (12)) in terms of the parameters available from the lidar in Eq. (13). Therefore, we will start the derivation of this scaling by evaluating the different components of Eqs (12) and (13). Doppler lidar measures the mean wind speed with a high and known accuracy; Floors (2013) and Peña *et al.* (2013) found good agreement between wind lidar and cup-anemometer measurements at 100 m for a CNR > -22 dB, with agreement deteriorating as the CNR threshold is lowered (as expected from Figure 2). The relationship between the long-term wind speed and the CNR threshold value is further discussed in Gryning *et al.* (2016). In other words, we can assume $U_S \approx U_L \approx U$. This assumption gives

$$U_{\max,S} = U_L + g_{t_g,S}\sigma_S. \tag{14}$$

Next, we will compare the peak factors from lidar and sonic anemometers, i.e. $g_{t_g,L}$ and $g_{t_g,S}$, respectively. Figure 5 shows the median peak factor as a function of the gust duration for both lidar and sonic anemometers. The observed peak factors are calculated by applying Eqs (12) and (13), with

$$g_{t_g} = \frac{U_{\max} - U}{\sigma}.$$

Figure 5(a) shows that lidar and sonic anemometer peak factors match at about $t_g = 15$ s, but there is an overestimation by lidar at shorter gust durations and a small underestimation at longer gust durations. The overestimation is caused by the difference in how each instrument samples the atmospheric turbulence. The sonic anemometer provides pointwise measurements with a high temporal resolution and thus covers all temporal scales contributing to short gusts, whereas the lidar combines information on short-duration averages of radial wind speed from spatially separated measuring volumes. Thus, the shortest lidar gusts are higher than the respective gusts from the sonic anemometer. Moreover, the higher individual values in the high-frequency part of the lidar signal are reflected in the lidar Doppler velocity standard deviation σ_L, causing it to be higher overall than σ_S. This in turn leads to lower $g_{t_g,L}$ than $g_{t_g,S}$ at low gust durations. If we scale $g_{t_g,L}$ by σ_L/σ_S as in Figure 5(b), the peak factors from both data sources agree at gust duration $t_g \approx 19$ s and longer.

To overcome the mismatch between the median g_{t_g} curves from sonic anemometer and lidar measurements for gust durations shorter than 19 s (Figure 5(b)), we use information about the known theoretical behaviour of the peak factor as a function of the gust duration and thereby force the lidar peak factor curve to follow the sonic anemometer curve for short gust durations. This is illustrated by the red curve in Figure 5. The mathematical description of the scaling of the lidar peak factor is given by

$$\begin{cases} g_{t_g,S} = \frac{g_{t_g,\text{theory}}}{g_{t_{g,\text{ref}},\text{theory}}} g_{t_{g,\text{ref}},L} & \text{for } t_g < t_{g,\text{ref}}, \\ g_{t_g,S} = g_{t_g,L} & \text{for } t_g \geq t_{g,\text{ref}}, \end{cases} \tag{15}$$

where $g_{t_g,\text{theory}}$ is the theoretical expression for the peak factor and $g_{t_{g,\text{ref}},L}$ and $g_{t_{g,\text{ref}},\text{theory}}$ are the observed and theoretical peak factor, respectively, corresponding to the gust duration $t_{g,\text{ref}}$, which is the shortest gust duration for which the observed median peak factor curves from the lidar and the sonic anemometer match. In this case, it is $t_{g,\text{ref}} \approx 19$ s. Theoretically, if the time series are stationary

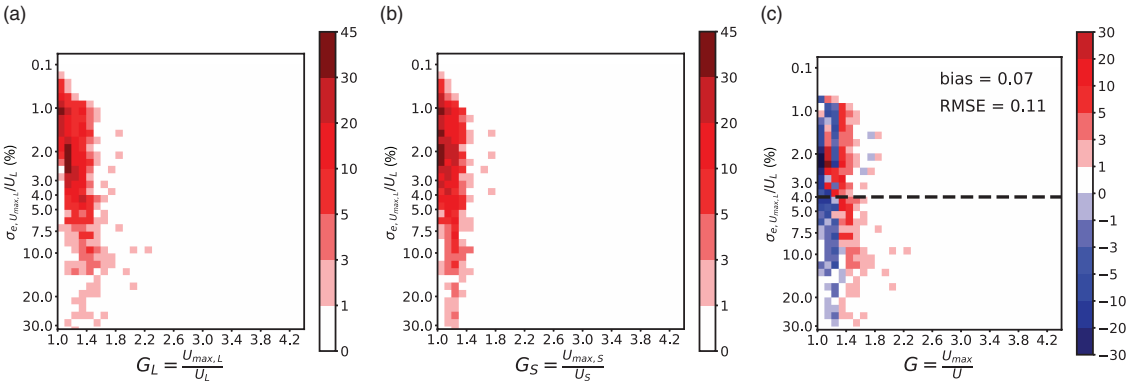

Figure 4. Two-dimensional histograms of the gust factor for (a) despiked lidar data, (b) sonic anemometer data and (c) their difference as a function of the relative error of the wind-gust speed ($\sigma_{e,U_{max,L}}/U_L$). In panel, (c) the bias and RMSE are provided.

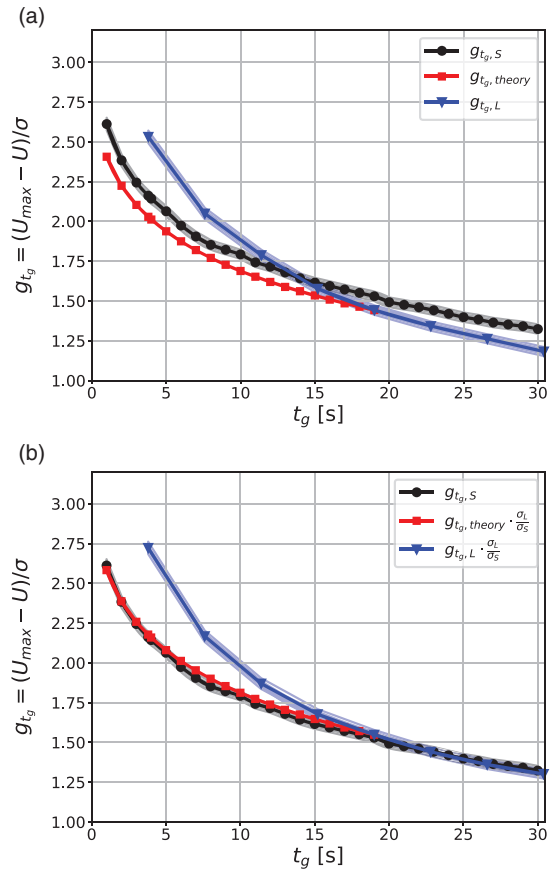

Figure 5. (a) Median peak factor as a function of gust duration as observed by sonic anemometers (black), lidar (blue) and the theoretical peak factor (red; Eqs (15)) derived from the parallel measurements from lidar and sonic anemometers between 40 and 100 m during 10 October 2015. (b) The same as (a), but the lidar peak factor and the theoretical one are scaled by the ratio σ_L/σ_S. In both panels, the standard error of the mean is given by the shadowed region underlying the points in each median curve.

and Gaussian, this point should only be a function of the lidar instrument set-up, because the peak factor is the deviation of the gust from the mean normalized by the standard deviation. The normalization makes the time series independent of the local turbulence conditions at the measurement site. However, in real turbulence data the time series is not always stationary or Gaussian, but the method can still be applied using median peak factors as seen in Figure 5. We also found that, in this real turbulence data, $t_{g,ref}$ varies with the Doppler lidar measurement uncertainty (CNR) and also the measurement height. However, based on this dataset only, it is not possible to evaluate the reasons for the dependence of $t_{g,ref}$ on measurement height, because it may be caused by the growing integral length-scale (the time/distance after which the autocorrelation function of the wind speed decreases below e^{-1}) of turbulence by height or by the lidar measurement set-up (e.g. the growing horizontal distance between the lidar measuring volumes by height, or by the changes in CNR by height).

The theoretical peak factor $g_{t_g,\mathrm{theory}}$ can be derived from statistical considerations (Rice, 1944, 1945; Beljaars, 1987; Kristensen *et al.*, 1991; Wichers Schreur and Geertsema, 2008; Suomi *et al.*, 2015). The theoretical peak factor equation is

$$g_{t_g,\mathrm{theory}} = \left[2\ln\left(\frac{T}{\tau}\frac{1}{\sqrt{2\pi}\ln\frac{1}{P}}\right)\right]^{1/2}, \tag{16}$$

where T is the sample length and P the desired probability of a gust in the ensemble of samples. For the median peak factor, it is $P = 0.5$. τ is the turbulent time-scale, which also determines the effect of the gust duration on the peak factor and is expressed as

$$\tau = \frac{1}{\sqrt{2\pi}}\frac{\sigma_u}{\sigma_{\dot{u}}} = \left[\frac{\int_0^\infty |H(f)|^2 S(f)\,\mathrm{d}f}{2\pi\int_0^\infty f^2|H(f)|^2 S(f)\,\mathrm{d}f}\right]^{1/2}, \tag{17}$$

where $S(f)$ is the one-sided power spectrum of the horizontal wind speed, for which we used the formulation by Kaimal *et al.* (1972) with a constant $U = 10\,\mathrm{m\,s^{-1}}$ and $z = 10\,\mathrm{m}$. The spectrum is filtered by a function $|H(f)|^2$, determined by

$$|H(f)|^2 = \left(\frac{\sin(\pi f t_g)}{\pi f t_g}\right)^2, \tag{18}$$

which represents the moving average filter determining the desired gust length (t_g).

Equations (16)–(18) provide an estimate for the peak factor of the filtered turbulence time series, but usually we are interested in the peak factor relative to the true turbulence. Therefore, Eq. (16) must be multiplied by the ratio of the standard deviations of the filtered and true turbulent wind speeds, expressed in terms of the turbulence spectrum:

$$r_\sigma = \frac{\sigma_{\mathrm{filtered}}}{\sigma_{\mathrm{true}}} = \frac{\int_0^\infty |H(f)|^2 S(f)\,\mathrm{d}f}{\int_0^\infty S(f)\,\mathrm{d}f}. \tag{19}$$

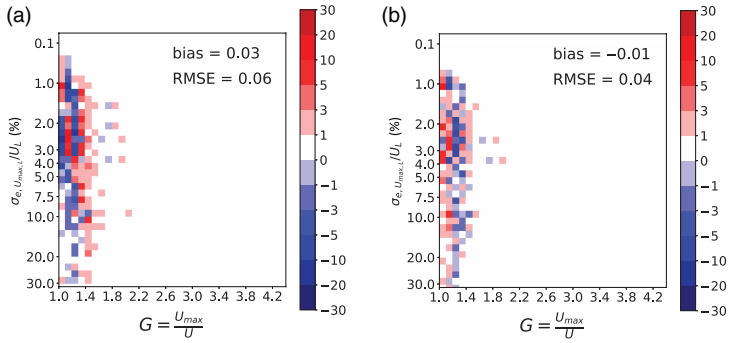

Figure 6. Difference in the gust factor distributions as a function of the relative error ($\sigma_{e,U_{max,L}}/U_L$) as in Figure 4(c). Here, Doppler lidar G is derived using the scaling method with the observed standard deviation from (a) lidar measurements (assuming $\sigma_S = \sigma_L$) and (b) sonic anemometer measurements.

Now we have derived the equations to estimate the peak factor from lidar measurements for any gust duration using a statistical scaling approach. The advantage of using Eq. (15) to scale the lidar peak factors is that they use information about the observed lidar wind-speed maxima of each sample ($g_{t_{g,ref},L}$) and the scaling coefficient $g_{t_g,theory}/g_{t_{g,ref},theory}$ scales that to correspond to the value observed by a sonic anemometer with some defined gust duration t_g. Since $g_{t_{g,ref},L} = (U_{max,L} - U_L)/\sigma_L$ varies from sample to sample, it retains the natural scatter of the peak-factor values as in the original lidar data set.

Now that we have derived the expression for the peak factor $g_{t_{g,S}} = f(g_{t_{g,L}})$ (Eq. (15)), the wind-gust equation can be written as

$$\begin{cases} U_{max,S} = U_L + \frac{g_{t_g,theory}}{g_{t_{g,ref},theory}} g_{t_{g,ref},L}\sigma_S & \text{for } t_g < t_{g,ref}, \\ U_{max,S} = U_L + g_{t_g,L}\sigma_S & \text{for } t_g \geq t_{g,ref}. \end{cases} \quad (20)$$

There is one more component to be estimated, σ_S. Turbulence estimation from lidar measurements has received a lot of attention in the literature and a summary is provided by Sathe and Mann (2013). Here, we require a pragmatic and robust method for scaling the Doppler lidar wind gusts independent of meteorological mast measurements. Therefore, we will test the method using the standard deviation of velocity obtained directly from lidar measurements (assuming $\sigma_S = \sigma_L$). The resulting gusts will then naturally deviate from those obtained from the meteorological mast. To evaluate the effect of this assumption, we also applied the scaling method using the best possible estimate for σ_S, i.e. that from the meteorological mast. This, of course, can only be applied at the mast measurement heights, i.e. here up to 100 m. The evaluation of the assumption is presented at the beginning of the following section, followed by a comparison of mean gust-factor profiles up to 290 m derived independently from Doppler lidar measurements using the scaling method (Eq. (20) with the assumption $\sigma_S = \sigma_L$) and up to 100 m based on meteorological mast measurements.

5. Results

5.1. *Validation of the scaling method*

We now test the scaling method derived in section 4 to measure wind gusts. In Figure 6(a), we applied Eq. (20) with $\sigma_S = \sigma_L$, i.e. turbulence directly from the lidar measurements. Comparison with Figure 4(c) shows that both the mean error and RMSE have clearly decreased, but there is still an overestimation by the lidar. In Figure 6(b), using σ_S observed by sonic anemometers, the positive bias in the gust measurements is reduced (leaving a very small negative bias) and RMSE reduces to 0.04. Hence, this novel scaling method for estimating wind gusts from lidar measurements performs well and demonstrates that the method clearly benefits from a reliable estimation of turbulence (in terms of velocity variance).

Figure 7 shows the performance of the scaling method during the two-day period at heights covered by both mast and Doppler lidar. There is a clear overestimation of the gust factor by the original lidar measurements and the overestimation is largest where G is highest, i.e. during turbulent daytime conditions. During early morning and in the evening of 10 October, the gust factors from Doppler lidar and mast measurements compare well even without scaling, whereas the scaling method improves the results most during daytime on 10 October and in the precipitating conditions on 11 October.

So far, our evaluation of the scaling method has been based on the heights where there are coincident Doppler lidar and meteorological mast measurements. The gust factor profiles have been extended above the mast height in Figure 8. For comparison, G values from the mast are shown as dashed lines in (a) and (c). The results are shown separately for 10 and 11 October, to distinguish between non-rainy (10 October) and rainy (11 October) conditions. On 10 October, the estimated lidar wind gust using assumption $\sigma_S = \sigma_L$ provides gust factors that fit the sonic anemometer gust factors exactly in stable conditions, but in unstable and near-neutral conditions the estimated gust factors are slightly overestimated (probably due to the impact of higher turbulence). Above the meteorological mast heights, the question is whether the lidar gust-factor measurements are reliable. Since we do not have reference sonic anemometer measurements above 100 m, we have to use other information to assess the quality of the measurements. In Figures 8(b) and (d), we highlight an error level of 4% in terms of relative error of the wind-gust speed $\sigma_{e,U_{max,L}}/U_L$ as an indicator of data quality. This choice for the acceptable error level is discussed in section 5.2. Here, with a threshold of 4%, Figure 8(b) indicates good-quality measurements at least up to 200 m and potentially even higher.

On 11 October (Figures 8(c) and (d)), the shape of the profiles clearly differs from those on 10 October (Figures 8(a) and (b)). Compared with the sonic anemometer measurements, the scaled Doppler lidar G is slightly high at all mast levels. Doppler lidar G is almost constant up to 160 m, above which it increases strongly. The relative errors are below 4% only near 100 m level; below and above that the errors are larger.

Precipitating conditions pose an additional challenge for obtaining reliable Doppler lidar wind retrievals. Aerosol and cloud droplets are ideal targets for Doppler lidar wind retrievals, as they have negligible terminal fall velocities ($< 5\,\mathrm{cm\,s^{-1}}$) and are effective tracers of the air motion, whereas precipitating particles have an appreciable terminal fall velocity. For widespread precipitation that is all falling at similar velocities, there is little impact on the wind retrieval; however, in patchy or evaporating precipitation there could be variations of $5\,\mathrm{m\,s^{-1}}$ or more in the vertical component of the radial Doppler

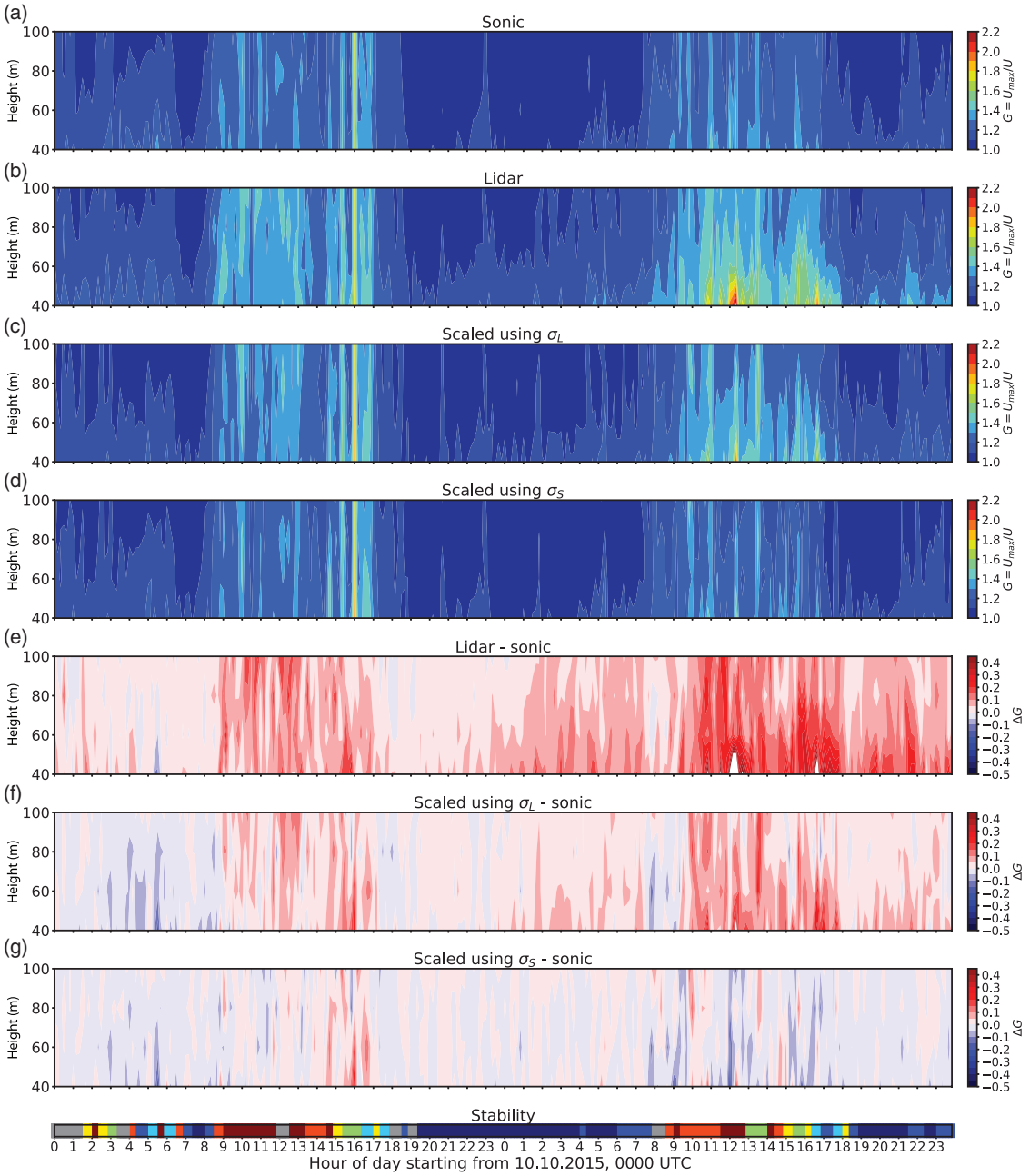

Figure 7. Time–height cross-sections of the gust factor from (a) sonic anemometer, (b) Doppler lidar with no scaling, (c) Doppler lidar with scaling using σ_L, (d) Doppler lidar with scaling using σ_S, (e) difference between sonic anemometer and Doppler lidar with no scaling, (f) difference between sonic anemometer and Doppler lidar with scaling using σ_L, (g) difference between sonic anemometer and Doppler lidar with scaling using σ_S. The lowest panel shows the same stability index for each 10 min sequence as in Figure 3.

velocities measured by each beam within a single scan (i.e. one beam encounters precipitation, another beam in the opposite direction only encounters aerosol), which then propagates through to the wind retrieval. This may be an additional reason for the reduced performance of the scaling method using σ_L on 11 October, together with the reduction in sensitivity increasing the uncertainty. Even though the Doppler lidar raw radial measurements are more prone to errors in precipitating conditions, the scaling can still provide reasonable wind-gust estimates after spikes are removed from the wind-speed time series (section 3 and Figure 6; section 5.2). Although there are larger uncertainties in the Doppler lidar wind measurements (Figures 3 and 7), the gust factor is probably representative up to 160 m on 11 October (Figure 8(c)).

5.2. *Sensitivity tests of the scaling method*

In section 2.2, it was shown that wind gusts from a Doppler lidar are sensitive to outliers in the data and that spike removal is effective in improving the quality of the wind-gust measurements.

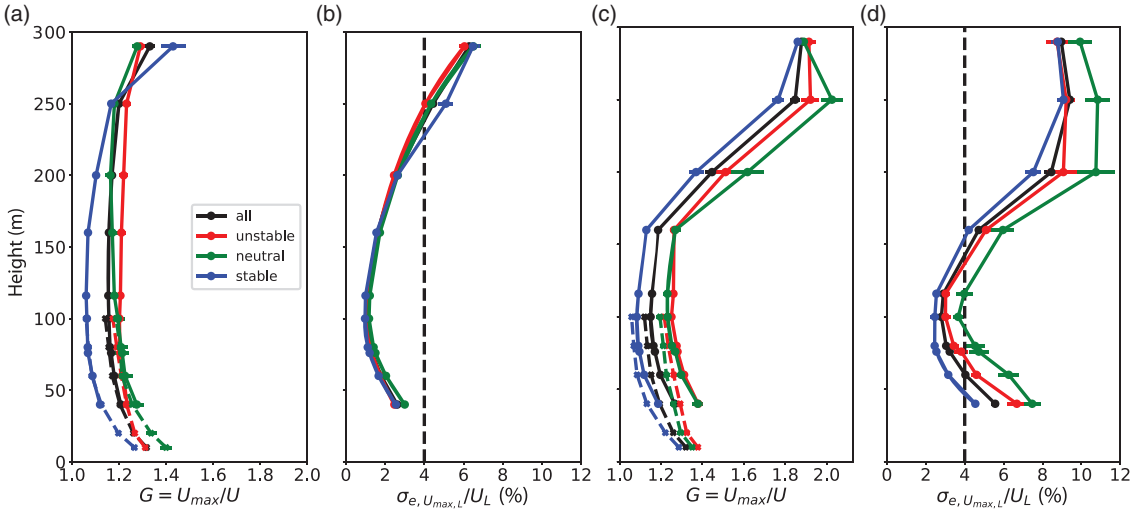

Figure 8. Mean profiles of (a) scaled Doppler lidar gust factor and (b) relative error in the scaled Doppler lidar gust factor for 10 October, plus mean profiles of (c) scaled Doppler lidar gust factor and (d) relative error in the scaled Doppler lidar gust factor for 11 October. The mean gust factor from the meteorological mast is shown by dashed lines. The standard error of the mean is shown by error bars. The line colour indicates grouping by stability: all profiles (black), unstable (red, $L^{-1} < -0.005$), neutral (green, $|L^{-1}| \leq 0.005$) and stable (blue, $L^{-1} > 0.005$).

The effectiveness of the spike removal is illustrated in Figure 9, where the G_L distribution is calculated from the raw lidar measurements without spike removal. Comparison with Figure 4, where the spikes have been removed, shows a clear impact on the results, especially for relative errors higher than 4%. The bias of the raw lidar data is 0.23 and the RMSE 0.6 (Figure 9(b)); after spike removal this is reduced to 0.07 and 0.11, respectively (Figure 4(c)). When the spikes are removed, the data quality improves such that, after scaling, it becomes acceptable to include gust factors with relative errors also above 4% (Figure 6) and hence potentially provide reliable gust-factor profiles from lidar measurements up to 290 m in non-precipitating conditions on 10 October and up to 160 m in precipitating conditions on 11 October (Figure 8).

In addition to spike removal, we also tested filtering based on CNR during the maximum gust. Figure 10 shows the CNR during the maximum gust as a function of the lidar gust factor. The mean of the five radial CNR values is shown in black and the minimum in red. Based on sonic anemometer measurements, all gust factors during this period were smaller than 2 and therefore all G_L values exceeding this threshold are erroneous. From Figure 10, we see that there are unrealistically high gust factors at mean CNR values below about −21 to −22 dB and at minimum CNR below −24 dB. Either of these thresholds could be used to filter out unreliable data. However, when the lidar is used to measure gusts operationally, it is easiest to assess data quality without any averaging operations, i.e. without taking the mean of the radial CNR values, and therefore we tried using a threshold based on the minimum CNR. In other words, all **v** measurements for which any of the five radial CNR values was < -24 dB were flagged. Flagged data were then filtered out of the time series before the gust calculations; the filtering replaced bad values by linear interpolation using neighbouring non-flagged points. We tested the effectiveness of this approach to filter out unreliable data, but found that not all unrealistically high wind-speed (u_L) values were removed, i.e. spikes were still present at CNR values above the threshold. We associate this with occasional issues in the automated calculation of the CNR within the instrument, i.e. an incorrect determination of the instrument noise level generates a CNR profile that is biased high or low. In cases where the CNR was biased high, a constant CNR threshold would not then filter out all potentially unreliable values.

6. Summary and discussion

We have derived a methodology for scaling Doppler lidar wind-gust estimates so that they are comparable with those observed by sonic anemometers on a meteorological mast. Thereby, profiles of wind gusts can potentially be measured by Doppler lidars at many more locations without the need for the costly and challenging deployment of a tall meteorological mast. This novel method not only scales the lidar gusts but also provides estimates for wind gusts with variable gust durations, including shorter durations (of the order of a second) that are beyond the limits of the lidar measurement frequency. The input parameters for the scaling method are the wind-gust speed as well as the mean and standard deviation of the horizontal wind speed from the Doppler lidar. The wind-gust speed is calculated as the maximum of the moving-averaged horizontal wind speed. For the WindCube V2 Doppler lidar used in this study, an average over five samples (corresponding to gust duration $t_g = 19$ s) was found to be adequate, but this depends on the lidar type and the scanning technique and must be tuned separately for each lidar set-up. As the scaling method is based on peak factors, which represent the maximum turbulent deviations from the mean in the normalized (by its standard deviation) wind-speed time series, the method does not depend on the measurement site, provided that the wind-speed time series is stationary and Gaussian. Instead, the measured (and scaled) wind-gust speeds and gust factors are site-specific, i.e. they depend on the local turbulence conditions determined by the surface roughness and the static stability of the atmosphere (e.g. Suomi *et al.*, 2013, 2016).

Using Doppler lidar data only, the novel scaling method will provide reasonable gust factor estimates, with a small positive bias (0.03) and RMSE of about 0.06, but it is possible to reduce the bias by better estimates of the velocity variance. The added performance of the scaling method was most noticeable in turbulent daytime conditions, but also improved the estimation of gustiness in precipitating conditions.

The data quality is crucial for successful wind-gust measurements, both with and without the scaling method. Here we applied a spike-detection method similar to that typically used in sonic anemometer data processing and found that it removes outliers from the data effectively. The spikes were replaced by linear interpolation using neighbouring non-spike values. This

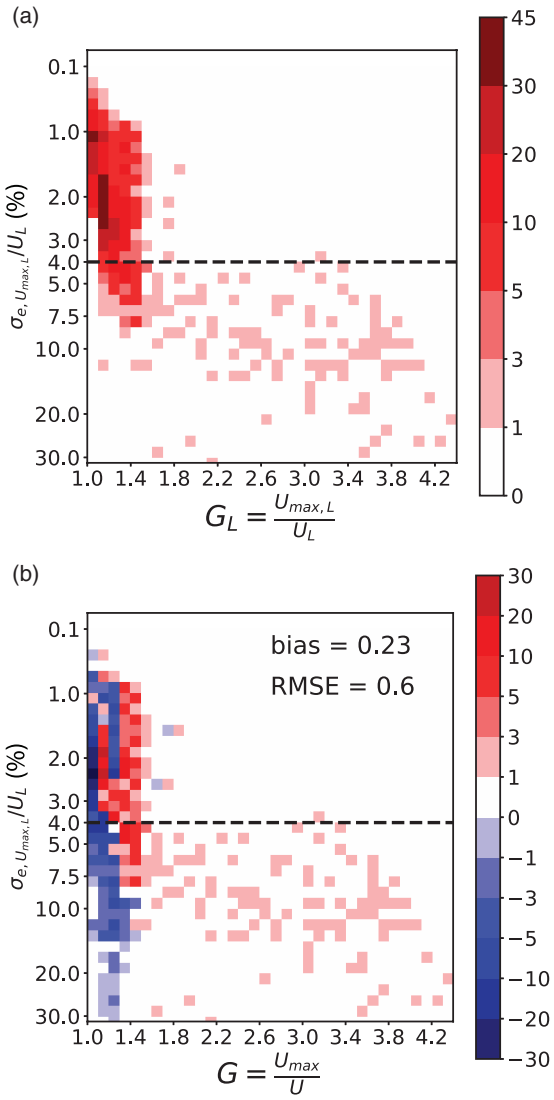

Figure 9. Similar to Figure 4; two-dimensional histograms of the gust factor for (a) raw Doppler lidar data and (b) the difference between Doppler lidar and sonic anemometer data as a function of the relative error of the wind-gust speed ($\sigma_{e,U_{max,L}}/U_L$). In (b), the bias and RMSE are provided.

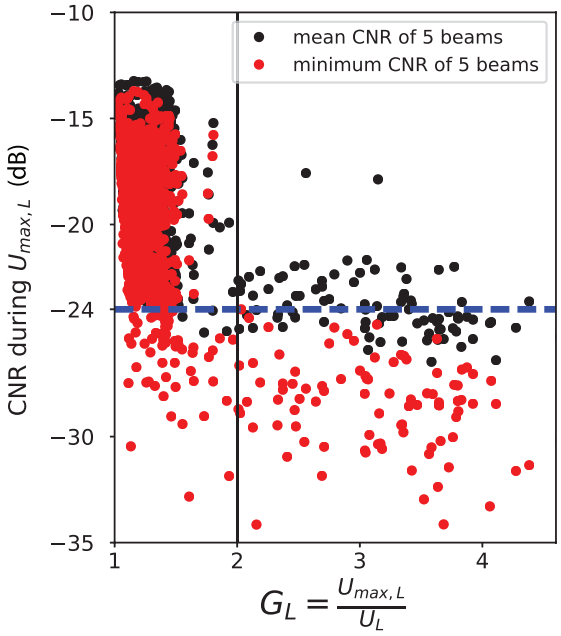

Figure 10. CNR during the wind gust as a function of the gust factor from lidar. CNR is provided as a mean of five radial components (black dots) and as the minumum of five radial components (red). A threshold of CNR = −24 dB is shown as a blue horizontal dashed line.

removal of spikes improves the gust-factor estimation most in cases when only a few outliers exist. When unrealistically high wind-speed values (poor data quality) start to dominate the time series, the performance of the spike detection decreases. We also tested a spike-detection method based on instantaneous CNR values, but it did not remove all unrealistically high wind-speed values. Therefore, our conclusion is that, when using Doppler lidar to measure gusts, better data quality is achieved using a filtering technique based on spike detection and removal than filtering based on instantaneous CNR. Instead, CNR is a good tool for overall data-quality assessment, such as when estimating the relative error of the measurement (O'Connor *et al.*, 2010).

The scaling methodology presented here was developed for one particular lidar type and scanning sequence. To develop this methodology further, the next step is to test the applicability of the method to other lidar types and other scanning sequences, such as conical scans with many more beams. One open question is as follows: what is a sufficient Doppler lidar measurement frequency in order to obtain reliable wind-gust estimates? Also to be examined is the effect of the horizontal variability of the wind on the scaling method. In this study, we concentrated on removing the effect of horizontal variability in the time-scales of the lidar scan sequence (3.8 s) and length-scales of the volume between the lidar measuring beams (up to about 300 m). Smoothing the turbulent measurements with a 19 s moving average reduced the temporal and spatial variability in the wind field, so that the lidar measurements matched the sonic anemometer measurements. Moreover, in the theoretical method we used only one formulation for the turbulence spectrum, that by Kaimal *et al.* (1972) with a fixed mean wind speed and height. This choice provided good results in this study, but the sensitivity of the results to different spectral formulations will be investigated in the future.

Here, the aim was to scale Doppler lidar wind-gust measurements to match the sonic anemometer measurements from a tall meteorological mast. We have shown that this particular lidar instrument provides good wind-gust estimates up to heights of about 160–250 m, typically well above the roughness sublayer and often also above the surface layer. This is exceedingly useful when assessing wind-gust parametrizations in numerical weather prediction models, since we are no longer limited by the mismatch between the roughness at the model grid point and the conditions at the observation site, as is the case for weather stations where the wind measurements are usually made at 10 m reference height. With model evaluation based on observed profiles of gusts, there are now possibilities of developing gust forecast methods further.

In wind-energy applications, it is not only the pointwise measurement of the wind-gust speed that is important for estimating the extreme instantaneous loads on wind turbines. As seen in this study, lidar wind-gust measurements without the scaling method are affected by wind-speed variability on the scale of the volume between the lidar measuring beams. This information could be useful for wind turbine operations and is therefore an aspect that should also be investigated in the future.

Acknowledgements

This research has received funding from Vilho, Yrjö ja Kalle Väisälä Foundation, from the Academy of Finland via the TWASE project (contract 283101) and from EU COST Action ES1303 TOPROF (Towards operational ground based profiling with ceilometers, Doppler lidars and microwave radiometers for improving weather forecasts) in the form of two Short Term Scientific Missions (STSMs).

References

Beljaars ACM. 1987. The influence of sampling and filtering on measured wind gusts. *J. Atmos. Oceanic Technol.* **4**: 613–626.

Bou-Zeid E, Parlange M, Meneveau C. 2007. On the parametrization of surface roughness at regional scales. *J. Atmos. Sci.* **64**: 216–227. https://doi.org/10.1175/JAS3826.1.

Brasseur O. 2001. Development and application of a physical approach to estimating wind gusts. *Mon. Weather Rev.* **129**: 5–25.

Emeis S, Harris M, Banta RM. 2007. Boundary-layer anemometry by optical remote sensing for wind-energy applications. *Meteorol. Z.* **16**: 337–347. https://doi.org/10.1127/0941-2948/2007/0224.

Floors R. 2013. *Measuring and Modelling of the Wind on the Scale of Tall Wind Turbines*. DTU Wind Energy PhD-0034(EN) Report. DTU Wind Energy: Denmark, 112 pp.

Gryning SE, Batchvarova E, Brümmer B, Jørgensen H, Larsen S. 2007. On the extension of the wind profile over homogeneous terrain beyond the surface boundary layer. *Boundary Layer Meteorol.* **124**: 251–268.

Gryning S-E, Floors RR, Peña A, Batchvarova E, Brümmer B. 2016. Weibull wind-speed distribution parameters derived from a combination of wind-lidar and tall-mast measurements over land, coastal and marine sites. *Boundary Layer Meteorol.* **159**: 329–348. https://doi.org/10.1007/s10546-015-0113-x.

Højstrup J. 1993. A statistical data screening procedure. *Meas. Sci. Technol.* **4**: 153–157. https://doi.org/10.1088/0957-0233/4/2/003.

Jung C, Schindler D, Albrecht AT, Buchholz A. 2016. The role of highly-resolved gust speed in simulations of storm damage in forests at the landscape scale: A case study from Southwest Germany. *Atmosphere* **7**: 7.

Kaimal JC, Wyngaard JC, Izumi Y, Cote OR. 1972. Spectral characteristics of surface-layer turbulence. *Q. J. R. Meteorol. Soc.* **98**: 563–589.

Kristensen L, Casanova M, Courtney MS, Troen I. 1991. In search of a gust definition. *Boundary Layer Meteorol.* **55**: 91–107.

Lane SE, Barlow JF, Wood CR. 2013. An assessment of a three-beam Doppler lidar wind profiling method for use in urban areas. *J. Wind Eng. Ind. Aerodyn.* **119**: 53–59.

Manninen AJ, O'Connor EJ, Vakkari V, Petäjä T. 2016. A generalised background correction algorithm for a Halo Doppler lidar and its application to data from Finland. *Atmos. Meas. Tech.* **9**: 817–827. https://doi.org/10.5194/amt-9-817-2016.

O'Connor E, Illingworth A, Brooks I, Westbrook C, Hogan R, Davies F, Brooks B. 2010. A method for estimating the turbulent kinetic energy dissipation rate from a vertically pointing Doppler lidar, and independent evaluation from balloon-borne in situ measurements. *J. Atmos. Oceanic Technol.* **27**: 1652–1664.

Päschke E, Leinweber R, Lehmann V. 2015. An assessment of the performance of a 1.5 μm Doppler lidar for operational vertical wind profiling based on a 1-year trial. *Atmos. Meas. Tech.* **8**: 2251–2266. https://doi.org/10.5194/amt-8-2251-2015.

Pasztor F, Matulla C, Zuvela-Aloise M, Rammer W, Manfred JL. 2015. Developing predictive models of wind damage in Austrian forests. *Ann. For. Sci.* **72**: 289. https://doi.org/10.1007/s13595-014-0386-0.

Pearson G, Davies F, Collier C. 2009. An analysis of the performance of the UFAM pulsed Doppler lidar for observing the boundary layer. *J. Atmos. Oceanic Technol.* **26**: 204–250.

Peña A, Gryning S-E, Hahmann AN. 2013. Observations of the atmospheric boundary layer height under marine upstream flow conditions at a coastal site. *J. Geophys. Res. Atmos.* **118**: 1924–1940. https://doi.org/10.1002/jgrd.50175.

Peña A, Floors R, Sathe A, Gryning S-E, Wagner R, Courtney MS, Larsen XG, Hahmann AN, Hasager CB. 2015. Ten years of boundary-layer and wind-power meteorology at Høvsøre, Denmark. *Boundary Layer Meteorol.* **158**: 1–26. https://doi.org/10.1007/s10546-015-0079-8.

Rebmann C, Kolle O, Heinesch B, Queck R, Ibrom A, Aubinet M. 2012. Data acquisition and flux calculations. In *Eddy Covariance: A Practical Guide to Measurement and Data Analysis*, Aubinet M, Vesala T, Papale D. (eds.): 59–84. Springer Atmospheric Sciences. https://doi.org/10.1007/978-94-007-2351-1_3.

Rice SO. 1944. Mathematical analysis of random noise. *Bell Syst. Tech. J.* **23**: 282–332. https://doi.org/10.1002/j.1538-7305.1944.tb00874.x.

Rice SO. 1945. Mathematical analysis of random noise. *Bell Syst. Tech. J.* **24**: 46156. https://doi.org/10.1002/j.1538-7305.1945.tb00453.x.

Sathe A, Mann J. 2013. A review of turbulence measurements using ground-based wind lidars. *Atmos. Meas. Tech.* **6**: 3147–3167. https://doi.org/10.5194/amt-6-3147-2013.

Sathe A, Courtney M, Mann J, Wagner R. 2011. 'How good are remote sensors at measuring extreme winds?'. In *Proceedings, 2011, European Wind Energy Association (EWEA)*. Brussels.

Suomi I, Vihma T, Gryning S-E, Fortelius C. 2013. Wind-gust parametrizations at heights relevant for wind energy: A study based on mast observations. *Q. J. R. Meteorol. Soc.* **139**: 1298–1310.

Suomi I, Gryning S-E, Floors R, Vihma T, Fortelius C. 2015. On the vertical structure of wind gusts. *Q. J. R. Meteorol. Soc.* **141**: 1658–1670. https://doi.org/10.1002/qj.2468.

Suomi I, Lüpkes C, Hartmann J, Vihma T, Gryning S-E, Fortelius C. 2016. Gust factor based on research aircraft measurements: A new methodology applied to the Arctic marine boundary layer. *Q. J. R. Meteorol. Soc.* **142**: 2985–3000. https://doi.org/10.1002/qj.2880.

Vakkari V, O'Connor EJ, Nisantzi A, Mamouri RE, Hadjimitsis DG. 2015. Low-level mixing height detection in coastal locations with a scanning Doppler lidar. *Atmos. Meas. Tech.* **8**: 1875–1885. https://doi.org/10.5194/amt-8-1875-2015.

Verkaik JW. 2000. Evaluation of two gustiness models for exposure correction calculations. *J. Appl. Meteorol.* **39**: 1613–1626.

Vickers D, Mahrt L. 1997. Quality control and flux sampling problems for tower and aircraft data. *J. Atmos. Oceanic Technol.* **14**: 512–526.

Vihma T, Savijärvi H. 1991. On the effective roughness length for heterogeneous terrain. *Q. J. R. Meteorol. Soc.* **117**: 399–407.

Wichers Schreur B, Geertsema G. 2008. Theory for a TKE based parametrization of wind gusts. *HIRLAM Newsl.* **54**: 177–188.

Wieringa J. 1973. Gust factors over open water and built-up country. *Boundary Layer Meteorol.* **3**: 424–441.

Wieringa J. 1986. Roughness-dependent geographical interpolation of surface wind speed averages. *Q. J. R. Meteorol. Soc.* **112**: 867–889.

Wieringa J. 1996. Does representative wind information exist? *J. Wind Eng. Ind. Aerodyn.* **65**: 1–12. https://doi.org/10.1016/S0167-6105(97)00017-2.

Woetmann Nielsen N, Petersen C. 2001. 'Calculation of wind gusts in DMI-HIRLAM', Danish Meteorological Institute Scientific Report 01-03. Danish Meteorological Institute: Copenhagen, Denmark, 1–32.

World Meteorological Organization (WMO). 2010. Measurement of surface wind. In *Guide to Meteorological Instruments and Methods of Observation*, WMO No. 8 (7th edn): I.5-1-15. World Meteorological Organization: Geneva, Switzerland. http://library.wmo.int/pmb_ged/wmo_8-2012_en.pdf (accessed March 2017).

FINNISH METEOROLOGICAL INSTITUTE
Erik Palménin aukio 1
P.O. Box 503
FI-00101 HELSINKI
tel. +358 29 539 1000
WWW.FMI.FI

FINNISH METEOROLOGICAL INSTITUTE
CONTRIBUTIONS No. 134
ISBN 978-952-336-024-2 (paperback)
ISSN 0782-6117
Erweko
Helsinki 2017

ISBN 978-952-336-025-9 (pdf)
Helsinki 2017